Université catholique de Louvain
Faculté des Sciences, Ecole de Géographie
Georges Lemaître Centre for Earth and Climate Research
Earth and Life Institute

Analysis of the Holocene climate variability using a data assimilation method in the model LOVECLIM

Doctoral Dissertation presented by

Aurélien Mairesse

in fulfillment of the requirements
for the degree of Doctor in Sciences

Thesis committee:

Prof. Hugues Goosse (Supervisor)	Université catholique de Louvain
Prof. Thierry Fichefet	Université catholique de Louvain
Prof. Kristof Van Oost	Université catholique de Louvain
Prof. Hans Renssen	Vrije Universiteit Amsterdam
Prof. Marit-Solveig Seidenkrantz	Aarhus University
Prof. Marie-Laurence De Keersmaecker (Chair)	Université catholique de Louvain

Louvain-la-Neuve
December 2014

Ce long cheminement, qui m'a amené à réaliser cette thèse, n'aurait sans aucun doute été possible sans l'aide, le soutien, les encouragements et la bienveillance de celles et ceux que je remercie ci-après.

Merci Hugues, de m'avoir proposé de faire une thèse avec toi et de m'avoir donné les moyens nécessaires à sa réalisation. Ton honnêteté scientifique, ta patience, ta rigueur, ta créativité, ta disponibilité et ta bonne humeur quotidienne sont autant de qualités que j'apprécie chez toi. Je te remercie de tout cœur pour la formation que tu m'as donnée et aussi de m'avoir fait voyager. C'est un réel plaisir que j'ai eu de passer ces quatre années sous ta supervision.

Merci Thierry, d'avoir été le promoteur de mon mémoire et d'avoir partagé avec moi ton enthousiasme pour la science et pour la perfection. Merci aussi d'avoir été membre de mon jury. Tes commentaires avisés, ta rigueur et ta précision enrichissent ma thèse.

I also wish to warmly thank my other jury members, Kristof Van Oost, Hans Renssen and Marit-Solveig Seidenkrantz, for your knowledge, your time and for the discussions we had to improve my manuscript. Merci Marie-Laurence De Keersmaecker d'avoir été la présidente de mon jury.

This thesis has also given me the opportunity to travel and learn about proxies from brilliant scientists. I thank Marit-Solveig Seidenkrantz and Anne de Vernal for the very useful discussions about the oceanic proxy-based reconstructions as well as Eric Wolff and Joël Guiot for their help concerning the ice core and the pollen proxies, respectively.

Merci Marie-France, d'avoir passé de longues heures, au début de ma formation, à m'expliquer les bases pratiques de la science du climat et d'avoir décortiqué et exploré avec moi les moindres recoins de notre modèle.

Merci à mes deux collègues de bureau, Pierre et François, d'avoir partagé mon quotidien et d'avoir rendu mes journées si agréables. Merci Dominique et Monique pour tout le boulot que vous faites qui nous permet d'être si sereins. Merci aux copains du bureau et en particulier à Olivier, Violette, Elisabeth, Pierre, Alice, Antoine, Svetlana, Yoann, Pierre-Yves, Sébastien et aux deux François pour tous ces moments que nous avons partagés ensemble. Les discussions geek, les soirées de Noël, ou soirées tout court, le vin chaud hivernal sur le toit du monde, le badminton, les vacances à Sérigny, les fameuses LAN et les pauses-café resteront à jamais gravées dans ma mémoire.

Merci à Geneviève et Céline pour leur relecture rapide et efficace de mon anglais. Vous m'avez ôté une belle épine du pied.

Merci à mes parents et à ma famille de m'avoir permis d'en arriver là aujourd'hui. Merci, papa et maman, de m'avoir fait persévérer et de m'avoir entouré. Sans vous, rien de tout cela n'aurait été possible. Merci Adrien, Antonin, Marie, Marie-Astrid, Dominique, Denis, Pascale, Simon, Stéphanie, Guillaume, Geneviève et les nièces d'avoir été là pour moi et pour votre joie de vivre. Merci Papy et les cousins pour les dîners du jeudi.

Merci à mes copains de toujours, ceux de Lauzelle, de la 42e et du Kap Vert. Être bien entouré, et surtout bien se détendre est la clé de la réussite. Merci à François, Franc et Eliot, pour être vous-même et être là pour moi. Un merci tout particulier à la bande des docteurs, et des pas docteurs, pour ces nombreuses discussions, où l'on refait le monde et qui ne s'arrêtent jamais parce qu'on est "beaucoup trop intelligent" !

Enfin, merci Delphine. Tu es ma joie de vivre. Tu es mon inspiration au quotidien. Tu es mon équilibre. Tu me rends patient. Tu me fais me sentir bien. Tu es un exemple de générosité. Tu es mon épouse. Tu es la promesse d'une vie exceptionnelle.

Table of contents

List of abbreviations

^{137}Cs	Caesium 137
^{90}Sr	Strontium 90
AABW	Antarctic Bottom Water
AD	Anno Domini
AGISM	Antarctic and Greenland Ice Sheet Model
ALL	Simulation of the mid-Holocene period in which ALL the proxy-based surface temperature available are assimilated
AMOC	Atlantic Meridional Overturning Circulation
AOD	Aerosol Optical Depth
BCC-CSM1-1	Beijing Climate Center Climate System Model version 1.1
BP	Before Present, before 1950 AD
CCSM2	Community Climate System Model version 2
CCSM3	Community Climate System Model version 3
CH_4	Methane
CLIMBER	CLIMate and BiosphERe model
CLIO	Coupled Large-scale Ice-Ocean
CMIP5	Coupled Model Inter-comparison Project phase 5
CO_2	Carbon dioxide
CON	Simulation of the mid-Holocene period in which only the CONtinental proxy-based surface temperature available are assimilated
CSIRO-Mk3L-1-2	Commonwealth Scientific and Industrial Research Organisation MarK 3L climate system model v1.2
DAMEAN13	Simulation of the period 2.8 to 2.6 kyBP in which the mean value of 13 proxy-based surface temperatures are assimilated
DAMIN11	Simulation of the period 2.8 to 2.6 kyBP in which the minimum value of 11 proxy-based surface temperatures are assimilated
DAMIN13	Simulation of the period 2.8 to 2.6 kyBP in which the minimum value of 13 proxy-based surface temperatures are assimilated

DJF	December, January, February
ECBILT	A dynamic atmospheric model
EDML	European Project for Ice Coring in Antarctica at Dronning Maud Land
EMIC	Earth system Model of Intermediate Complexity
ENSO	El Niño-Southern Oscillation
GCM	General Circulation Model
GISP2	Greenland Ice Sheet Project Two
HadCM3	Hadley Centre Coupled Model version 3
HOCLAT	A web-based Holocene Climate Atlas
JJA	June, July, August
KNMI	Koninklijk Nederlands Meteorologisch Instituut, Nederlands
LGM	Last Glacial Maximum
LIA	Little Ice Age
LMALL	Last millennium simulation that use the PMIP3 forcing. LMALL5, LMALL with 5 members. LMALL12, LMALL with 12 members.
LOCH	Liège Ocean Carbon Heteronomous model
LOVECLIM	LOch-Vecode-Ecbilt-CLio-agIsM model
LOWESS	LOcally WEighted Scatterplot Smoothing. LOWESS500 or LOWESS3000 stand for the LOWESS filter with a cut-off frequency of 500 years or 3000 years, respectively
MARGO	Multiproxy Approach for the Reconstruction of the Glacial Ocean surface
MAT	Modern Analog Technique
MoBidiC	Modèle Bidimensionnel du Climat
MPI-ESM-P	Max Planck Institut Earth System Model running in low resolution grid and Paleo mode
N_2O	Nitrous oxide
NADW	North Atlantic Deep Water

NAO	North Atlantic Oscillation
NEEM	North Greenland Eemian Ice Drilling project
NODATA	Simulation of the mid-Holocene period with NO DATA assimilation
NOVOLC	Holocene simulation with NO VOLCanic activity
OCE	Simulation of the mid-Holocene period in which only the OCEanic proxy-based surface temperature available are assimilated
P4F	Past4Future european project
PFT	Plant Functional Types
PIK	Potsdam Institute for Climate Impact Research
PMIP	Paleoclimate Modelling Intercomparison Project
PMIP3	Paleoclimate Modelling Intercomparison Project third phase
REF	Simulation of 96 members covering the period 2.8 to 2.6 kyBP without data assimilation
RMSE	Root Mean Square Error
SMOW	Standard Mean Ocean Water
SST	Sea Surface Temperature
ST	Surface air Temperature
Sv	Sverdrup
TF	Transfer Function
Tg	Teragram
TSI	Total Solar Irradiance
UCL-ASTR	Université Catholique de Louvain, institut d'ASTRonomie et de Géophysique G. Lemaître
VECODE	VEgetation COntinuous DEscription model
VOLC	Holocene simulation with VOLCanic activity
y	year. ky, thousand y
yAD	year Anno Domini
yBP	year Before Present. kyBP, thousand yBP

CHAPTER 1

Introduction

This Chapter aims to provide a general overview of Holocene climate and of the tools used to understand its evolution. It also defines the objectives of this thesis and the path followed to meet them.

1.1 The Holocene: the current interglacial

Over the last 3 million years, the Earth underwent several glaciations during which the ice sheets of the Northern Hemisphere high-and-mid latitudes have advanced (Joussaume and Duplessy, 2013). These glaciations have been interrupted by warmer interglacial periods marked by ice sheet retreat, letting those confined to the Antarctic and Greenland. The current interglacial period is called the Holocene and covers the period from 11.7 thousand years before present (kyBP) until today (Walker et al., 2009).

The Holocene is commonly divided into three subperiods (Walker et al., 2012). The Early-Holocene, that spans from 11.7 to 8.2 kyBP, is characterized by the remains of the large Laurentide ice sheet over North America and by high Northern Hemisphere summer insolation (see Fig 1.1). The Middle-Holocene (hereafter mid-Holocene) is the period that covers 8.2 to 4.2 kyBP, during which the Northern mid-to-high latitudes experience relatively warm conditions. The Late-Holocene is the period from 4.2 kyBP to the present day. During this period, the summer insolation is declining in the Northern Hemisphere which favors the advance of glaciers.

Several important events have occured during the last 11.7 kyBP. Around 8,470 years ago, the melt of the remaining Laurentide ice sheet has produced

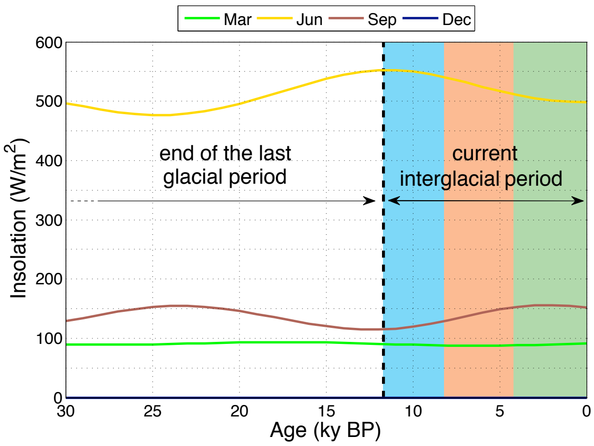

Figure 1.1: Evolution of the insolation at the top of the atmosphere (W/m^2) at 75°N according to Berger (1978) for the following months: March, June, September and December. The insolation at 75°N is zero during December. The black vertical dashed line separates the end of the last glacial period from the current interglacial. The three vertical shaded areas limit the Early-Holocene (blue), the Mid-Holocene (orange) and the Late-Holocene (green). The data have been provided by Marie-France Loutre.

the catastrophic drainage of the glacial lakes Agassiz and Ojibway that were originally dammed by ice (Barber et al., 1999). This has released more than 10^{14} m^3 of fresh water into the Labrador Sea, leading to a freshening of the surface ocean and therefore to an altered ocean circulation. The result is a temperature drop by 4 to 8°C in central Greenland and 1.5 to 3°C at marine and continental sites surrounding the North Atlantic Ocean. According to Barber et al. (1999), this is the most abrupt and widespread cold event that has occurred during the Holocene, known as the 8.2 kyBP event.

Another major event that has occurred during the mid-Holocene is the disappearance, around 6 to 5 kyBP, of the vegetation that covered the Sahara (Kutzbach and Liu, 1997; Demenocal et al., 2000; Renssen et al., 2003) triggered by the summer insolation decrease. The transition is explained by the following positive feedback process (Charney et al., 1975): The summer insolation decrease led to a decrease of the Sahara surface temperature and thus to a decrease of the summer African monsoon. As a consequence, precipitations were reduced over Sahara, which induced a decrease of the vegetation cover, leading to an increased surface albedo and therefore to a lower surface temperature.

Around 4.2 kyBP, several records indicate an aridification of the mid to low latitudes. This aridification event might have caused the fall of the Mesopotamia's Akkadian empire (Weiss et al., 1993; Gibbons, 1993) . According to deMenocal (2001), this aridification may have been related to colder conditions that prevailed over the North Atlantic at that time. Indeed, Cullen and deMenocal (2000) suggest using modern instrumental data that when the subpolar northwest Atlantic sea surface temperature is colder, the precipitations are reduced over the Mesopotamia.

The interest of studying past climates and particularly the Holocene, is to provide a long period of climate evolution during which the climatic conditions were similar to the pre-industrial ones, and therefore give a broader perspective to the actual global warming (Box 2.2 of Hartmann et al., 2013). Indeed, the climate of the last 10,000 years is close to the one we are experiencing, in comparison to the one of a glacial period (see Fig. 1.2). The current interglacial is then a perfect period to improve our knowledge about the climate mechanisms that drive the climate evolution in conditions that are near to the ones of the last centuries. The Holocene has thus been widely studied these last decades and consequently numerous climate data that reflect the climate of this period have been produced.

Paleoclimates are usually studied following two approaches: the production and analysis of reconstructions based on proxy data (e.g. Fig 1.2) and the development and use of climate models. The former are indirect observations of the past climate, while the latter are mathematical representations of the climate system based on physical, biological and chemical principles. The advantages and disadvantages of these two complementary sources of information are reviewed in the next sections.

1.2 The indirect observations of past climates

A proxy data is a natural archive influenced by climate (Bradley, 1999) from which a physical variable describing the climate of the past can be reconstructed. For instance, the past sea surface temperature can be reconstructed from informations embedded in a marine core. To this end, a method is used to link the core material, the proxy data (e.g the foraminifera, that are single-celled organisms, or the alkenone which is an organic compound), to the past sea surface temperature variations. Two families of method exist according to Masson-Delmotte and Guiot (2013) – the transfer function and the modern analog – that are both based on the same strong hypotheses:

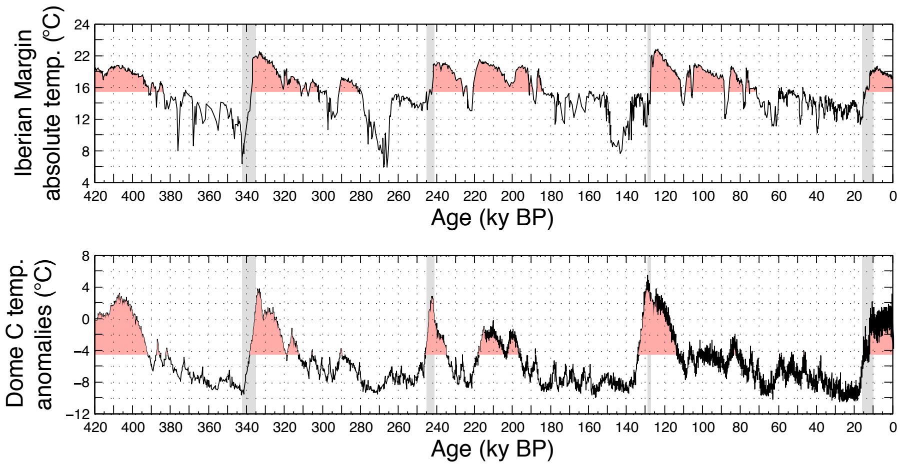

Figure 1.2: Top panel: Composite Iberian Margin sea surface temperature reconstructed from an organic compound, named alkenone, retrieved in two marine cores (MD01-2443 and MD01-2444) (Martrat et al., 2007). The sea surface temperature is calculated with the relation found by Muller et al. (1998): $\mathrm{U}_{37}^{\mathrm{K'}} = 0.033 \times \mathrm{SST} + 0.044$ where $\mathrm{U}_{37}^{\mathrm{K'}}$ is the alkenone unsaturation index and SST the past Sea Surface Temperature. Please refer to the section about marine sediments to have more information about alkenones and this function. **Bottom panel**: Dome C air surface temperature anomalies w.r.t the last 1000 year mean (Jouzel et al., 2007). The temperature curve is derived from the measure of the Dome C ice core deuterium variations: δD_{ice} (in ‰) $= [(D/H)_{\mathrm{sample}}/(D/H)_{\mathrm{SMOW}} - 1] \times 1000$, where H is the amount of hydrogen and D is the amount of deuterium, an isotope of the hydrogen with a neutron (Petit et al., 1999). SMOW is the standard mean ocean water. The relation between the Dome C δD and the Dome C temperature is estimated to 6.04 ‰/°C (Jouzel et al., 2007). **Both panels**: Grey shaded areas show transitions between the climate cycles according to Martrat et al. (2007). Red shaded areas show the values above the average.

1. The climate is the ultimate cause of the changes observed in the proxy data. The influence of any other factors is supposed to be negligible and included in the uncertainty. This implies that a climate archive which includes too much non-climatic noise should not be used.

2. The relationship between the proxy data and climate has not changed through time.

3. The modern observations contain all the necessary informations to allow the proxy data interpretation.

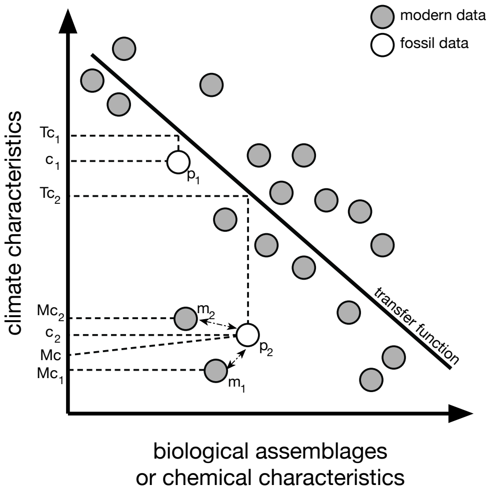

Figure 1.3: Schematic representation of the two families of methods used for paleoclimate reconstructions. This figure is adapted from Masson-Delmotte and Guiot (2013).

A transfer function (TF) is a statistical relation that links the modern biological assemblage or the modern chemical characteristics to the modern climate. Schematically, the TF can be represented as a regression that fits all the modern data displayed in a two dimensional space, where the ordinate represents the climate characteristics and the abscissa shows the biological assemblage or the chemical characteristics of the proxy (see Fig. 1.3). Based on this relation, the past climate variable c_1 of the proxy p_1 can be estimated by Tc_1, even if this proxy falls in an area with no modern data. In this case, the use of a TF provides a relatively plausible estimate of the past climate characteristic as Tc_1 and c_1 are close. At the opposite, since the TF follows the dominant gradient depicted by the modern data, the TF is not able to provide a reliable estimation of climate for the marginal proxy data p_2, as Tc_2 is not close to the value of the climate characteristic c_2.

The Modern Analog Technique (MAT) attributes to a fossil assemblage (p_2) the actual climatic conditions (Mc with $Mc_1 \leq Mc \leq Mc_2$) corresponding to the modern biological assemblages (m_1 and m_2) that are the most similar to the fossil assemblage (p_2). Unlike the TF, the MAT can provide an estimation of climate for the marginal data p_2. However, the MAT can not attribute a climate that does not exist in the modern data. The MAT is usually applied to biological assemblages but, theoretically, this method could also use chemical characteristics.

The schematic representation of the two families of methods illustrates that there is no perfect way to estimate past climate. To obtain a robust reconstruction of past climate, it is thus necessary to compare the results of several different methods (Masson-Delmotte and Guiot, 2013) that belong to the TF and MAT families. A description of the different methods used in paleoclimate studies can be found in Guiot and de Vernal (2007).

Proxy records provide indirect observations of past climate that are subject to uncertainties. The first type of uncertainty is related to the physical interpretation of the variable inferred from the proxy record. This physical variable can be incorrectly determined. For instance, it happens when the sea surface temperature is estimated from foraminifera species that lived between 50 m and 100 m depth since, in this case, the temperature rather represents the subsurface. Also, the value of this physical variable can varies within a wide range depending on the reconstruction method used. Moreover, the proxy record may have been more influenced by many factors in addition to the direct physical climate variable that is estimated. For instance, the development of some species of foraminifera can be more influenced by nutriment availability than by temperature. Finally, for a given proxy record, as the alkenones for instance, the reconstructed sea surface temperature can represent an annual or a summer temperature. Another type of uncertainty is related to the domain that the proxy signal is supposed to represent. Depending on the type of proxy, the area can be more or less large, varying from a very local to regional. This information is not always estimated in the original studies describing the proxies. Assumptions must thus be made for model-data comparison, often leading to a basic comparison at the model grid scale. A final type of uncertainty is associated to the temporal resolution of the reconstruction and the dating of the records. The temporal resolution depends on the sedimentation rates (for ice, marine and lake cores) or on the growth rates (for speleothem, a mineral formation located in cave and created by drip-water). For a core or a speleothem of a fixed length, the faster they grow, the higher the resolution. The temporal resolution of the proxy also relies on analytical issues, as the amount of samples used for the analysis. This amount mainly depends on the sample quality and on the total time and/or money that the scientist is able to spend. This is why, according to Bartlein et al. (2014), most terrestrial and marine records that span many thousands or millions of years generally could not be analyzed at annual or decadal resolutions.

1.2.1 Marine sediments

Marine sediments are deposits of insoluble material formed of rocks, soil particles, marine organisms, products of submarine volcanism, etc. that accumulate on the seafloor. A marine core is a cylinder of marine sediment. Such a core, contains among others several proxies of the sea surface temperature that are reviewed below. In the Ocean Drilling Program, an international scientific project that aims to conduct basic research about the ocean, each core is cut in two half cylinders (Fig. 1.4). One is the working-half and the other the backup that is stored in plastic tubes and refrigerated (Blum, 1997).

Figure 1.4: Opened section (0.16 to 1.17 m) of the gravity core DA12-11-GC01 from south of Iceland. Courtesy of Christof Pearce, Department of Geoscience, Aarhus University, Denmark.

1.2.1.1 Foraminifera

The planktic foraminifera, hereafter forams, are unicellular eukaryotic organisms that mainly live in the marine mixed layer and the upper thermocline (Dowsett, 2007; Kucera, 2007). Forams present passive floating lifestyles. There are about 40 species in the ocean today. Each species lives in particular condition of temperature. Therefore the identification of the foraminifera species that are present in the marine core, i.e. the remaining shell, can lead to a reconstruction of the sea surface temperature. To obtain the forams remaining shell from marine sediments, the working-core is cut in slices. A part of each slice is washed with water over piled up sieves that have different sizes (Fig. 1.5). The goal is to sort the material of the marine core from the coarser sediment located in the top sieve to the finest one retrieved in the bottom sieve. As the forams size ranges from 100 μm to 1 mm, the material that should be examined is the one dried from the sieve that includes these sizes. The forams of each working-core slice, are counted and classified into species with the help of a microscope. The result is a faunal assemblage diagram, i.e. the amount of each species versus depth. A method that is part of the modern analog family is then used to interpret this diagram in term of sea surface temperature.

In the case of forams, the MAT has some limitations. First, it is only applicable to the 40 modern species. This means that all the species found in the marine core that are not part of these 40 species could not be used to reconstruct

Figure 1.5: Separate sieves that have different sizes. They can be piled up in order to separate the sediments of different sizes. The sieve with the smaller mesh size, that contains the smaller sediments, is on the right of the picture. Courtesy of Joe Kistel from the "Think It Sink It Reef It" non-profit organization.

the sea surface temperature. Second, the present climate that is linked to the modern forams is more likely associated with the forams of the last centuries. Indeed, the modern forams are retrieved from the top of the marine core, that often don't reach the recent years, as the few first centimeters of the marine core are often not preserved during the sampling. Third, each foraminifera species can live at different depths depending on their age and on the water mass stratification (Kucera, 2007). Depending on the species used to reconstruct oceanic temperature, the temperature could be more representative of the surface, or the first 50 m depth, or of the depth between 50 m and 100 m, for instance (Dowsett, 2007).

Depending on the proxies, the surface temperature reconstruction can represent a particular month of the year, a season or the whole year. The sea surface temperature derived from forams could either corresponds to the hottest month of the year or the summer, which, according to Fraile et al. (2009) is often the case at high latitudes. At low latitudes, the sea surface temperature more often corresponds to the winter months (Came et al., 2007; Fraile et al., 2009).

1.2.1.2 Magnesium-Calcium ratio and oxygen isotope composition

The Magnesium-Calcium ratio ($\frac{\mathrm{Mg}}{\mathrm{Ca}}$) and the oxygen isotope composition (δ^{18}O) are usually measured from the calcite that forms the forams shell. The sea surface temperature can be derived from both the $\frac{\mathrm{Mg}}{\mathrm{Ca}}$ and the δ^{18}O by the use of different empirical formula (Rostek et al., 1993; Elderfield and Ganssen, 2000; Schmidt et al., 2004b). Reconstructing the sea surface temperature can, in principle, be done with any of the forams species of the core. But, generally, $\frac{\mathrm{Mg}}{\mathrm{Ca}}$ and the δ^{18}O are calculated for only one species, the one that is dominant in the sample and that lives near the ocean surface, i.e. until 30 m depth. Also, as $\frac{\mathrm{Mg}}{\mathrm{Ca}}$ and δ^{18}O are measured from the forams calcite shell, the derived temperature should be representative of the period in which the shell has formed and of the depth at which it was formed. However the forams calcification can occur at different times of the year and at different depths (Kucera, 2007). All these parameters should be taken into account for the interpretation of the temperature reconstruction.

1.2.1.3 Alkenone

An alkenone is an organic compound that is synthesized by coccolithophores – an unicellular eukaryotic phytoplankton – and is preserved in the marine sediments (Hönisch and Hall, 2007; Grimalt and Lopez, 2007).

The simplified form of the alkenone unsaturation index $\mathrm{U}_{37}^{\mathrm{K'}}$ (Prahl and Wakeham, 1987) varies linearly with the sea water temperature (Prahl et al., 1988), at least over the range 8-25°C such as:

$$\mathrm{U}_{37}^{\mathrm{K'}} = \frac{[C_{37:2}]}{[C_{37:2} + C_{37:3}]} \tag{1.1}$$

$$= 0.033 \times \mathrm{SST} + 0.043 \tag{1.2}$$

where $[C_{37:2}]$ and $[C_{37:3}]$ are concentrations of diunsaturated and triunsaturated C_{37} alkenones, respectively, and SST is the sea surface temperature. Muller et al. (1998) have refined this relation based on the calibration of 370 sites in the Atlantic, Indian and Pacific Oceans: $\mathrm{U}_{37}^{\mathrm{K'}} = 0.033 \times \mathrm{SST} + 0.044$. This result perfectly agrees with Prahl and Wakeham (1987), confirming that this calibration based on the *E. huxleyi* coccolithophores leads to the most plausible sea surface temperature estimates in most regions of the present oceans. The *E. huxleyi* species has been used in plankton studies for the following reasons: it may compose 60-80% of the coccolithophorid assemblage and it tolerates a large range of temperatures, salinities, nutrients levels, and light availability (Winter et al., 1994; Herbert, 2003). The *E. huxleyi* species is therefore present in waters of nearly all temperatures except those of the polar oceans (Herbert, 2003). Since the 1980s, the alkenone proxy has thus been widely used to estimate the sea surface temperature (Grimalt and Lopez, 2007). As the maximum alkenone production mainly occurs during summer months, during the bloom of the *E. huxleyi*, it is assumed that the reconstructed sea surface temperature based on this proxy mainly corresponds to the summer conditions (Herbert, 2003; Came et al., 2007). Nevertheless, according to Bendle and Rosell-Melé (2007) most of the paleoceanographers assume that the alkenone signal reflects the annually average sea surface temperature. So, there is no broad consensus on this issue.

1.2.2 Ice cores

The snow falling over locations facing low temperatures forms glaciers and ice sheets if the ablation is smaller than the accumulation. Glaciers and ice sheets are persistent mass of continental ice that are constantly moving under their own weight. An ice core is a cylinder of ice drilled out of an ice sheet or glacier (Fig. 1.6).

Figure 1.6: Ice cores drilled out of the Greenland ice sheet, by the NEEM ice core drilling project (http://www.neem.ku.dk). Photographer: Sune Olander Rasmussen, 2009.

An ice core is an excellent record of past climatic conditions. Firstly because it often provides an excellent temporal resolution due to the high accumulation rate (Brook, 2007) and secondly because multiple studies can be performed over it: carbon dioxyde and methane studies (Petit et al., 1999), stable isotope studies (δ^{18}O and δD) (Jouzel et al., 2007; Steig et al., 2013), volcanism studies (Gao et al., 2008), etc. Only the stable isotopic composition of ice measured by the δ^{18}O will be described here.

The two most abundant isotopes of the oxygen are ^{16}O and ^{18}O. ^{18}O has two more neutrons than the ^{16}O. The mass of the water molecule $H_2{}^{18}O$ is thus higher than the mass of $H_2{}^{16}O$. Because of this difference in weight, there is a difference in the evaporation rate, since the lightest water molecule evaporates first. As a consequence, the relative amount of ^{18}O compared to ^{16}O ($\frac{^{18}\mathrm{O}}{^{16}\mathrm{O}}$) in the ocean is higher, while for the water vapor presents in the atmosphere, this ratio is lower. As the air cools by rising in the atmosphere or by moving towards the poles, the water vapor condensates and precipitates. The atmospheric $\frac{^{18}\mathrm{O}}{^{16}\mathrm{O}}$ ratio thus decreases, while the water vapor is getting closer to the poles, since the water molecules that first condensate and fall are the heaviest. When climate changes, the $\frac{^{18}\mathrm{O}}{^{16}\mathrm{O}}$ ratio of the water present in the ocean and ice sheets varies. This is measured by:

$$\delta^{18}O = \left(\frac{\left(\frac{^{18}\mathrm{O}}{^{16}\mathrm{O}}\right)_{\mathrm{sample}}}{\left(\frac{^{18}\mathrm{O}}{^{16}\mathrm{O}}\right)_{\mathrm{SMOW}}} - 1 \right) * 1000 \tag{1.3}$$

where SMOW (Standard Mean Ocean Water) is a reference sample used to allow the comparison of isotopic measurements of different laboratories (Craig, 1961; Bradley, 1999). In a warmer climate, the ice core $\delta^{18}O$ is then smaller than in colder climate. This $\delta^{18}O$ measurement is very accurate, as a reproducibility between 0.01‰ and 0.03‰ is possible (Barkan and Luz, 2005). Based on this $\delta^{18}O$ series, a surface temperature can be derived. For instance, Vinther et al. (2009) found that the relation between the uplift-corrected Agassiz ice cap $\delta^{18}O$ record and the air surface temperature is 2.1°C/‰ associated with an uncertainty of 0.2°C/‰ as temperature/$\delta^{18}O$ slopes range from 1.9°C/‰ to 2.3°C/‰. Regarding the Antarctic ice cores, the relation of 0.08‰/°C has been found by Masson-Delmotte et al. (2008).

To date, the longest ice core record has been drilled in dome C Antarctica and represents about 800,000 years (see Fig. 1.2 for the more recent 420,000 years). Such a record allows us to understand that (1) climate changes that occurred during the Holocene are rather weak compared to the ones that have occurred during the transition between the last glaciation and the present interglacial period, and (2) other past periods have been warmer than the Holocene, for instance the period between 120 and 125 kyBP.

1.2.3 Pollen

An hectare of forest produces several billions of pollens according to Seppä (2007) that cites Pohl (1937). While most of them are deposited in the vicinity of the source – between 10^1 and 10^3 m – some can be transported in the atmosphere over longer distances (Prentice, 1988; Seppä, 2007). The majority of these pollens decay, unless they are deposited in an anoxic sedimentary environment, where they can be preserved for millions of years (Hedges et al., 1999; Seppä, 2007). From such an environment, it is difficult to precisely distinguish the pollens that come from the surrounding from those which come from more distant plants (Davis, 2000). However, it is known that large basins, as lakes, mainly receive well-mixed and wind-transported pollens from the air (Seppä, 2007). The size of the source area from which the pollens are coming is proportional to the lake size (Davis, 2000). Large lakes thus reflect the regional vegetation (Jacobson Jr and Bradshaw, 1981) and could be used to monitor regional vegetation and climate changes (Davis, 2000). A core drilled in such a lake is generally represented by a pollen diagram which shows for each depth the amount of pollen grains of each species expressed as a pourcentage of the plant group to which the pollen species belongs: trees, shrubs or herbs. This diagram does not reflect directly the plant abundance because some plants produce more pollens than others, or because some pollens are better preserved than others. It is thus necessary to apply correction factors that are specific for each plant species (Seppä, 2007).

Climate influences the vegetation distribution because each type of vegetation has a different tolerance to extreme temperatures, humidities or droughts (Brewer et al., 2007a). To convert the pollen diagram into temperatures, it is assumed that the information required to understand past climate could be obtained from the relationship existing between the modern taxa and the modern climate as for the marine sediments. Knowing the climate associated to numerous different modern distributions of pollens leads to attribute to the fossil pollen a particular climate. A detailed overview of different transfer functions can be found in Birks (2007). The air surface temperature reconstruction based on pollens usually span the Holocene or the late glacial period (Bradley, 1999). In 1999, Bradley pointed out that the temporal resolution of the reconstructions based on pollens was generally an order of magnitude greater than the one provided by the marine sediments because of the lake's high sedimentation rates. Using 145 recent Holocene surface temperature data, coming from the database built within this thesis (see section 1.6 for more information), it seems that this is not true anymore. The average temporal resolution of surface temperature reconstructions based on pollens is about 12 values for one thousand years, while the reconstructions based on marine sediments are close to 11 values for one thousand years.

1.2.4 Speleothems

A speleothem is a mineral formation located in a cave and created by dripwater. A speleothem thus reflects the environmental changes at the surface above the cave since its growth rate and composition are directly linked to the water that seeps from the surface through the bedrock into the cave (Lauritzen and Lundberg, 1999b). The focus on speleothems is very recent as speleothems are sensitive to the external changes that are often climate-related. This means that the oxygen isotopes measured in speleothems can be used as climate proxies (Lauritzen and Lundberg, 1999a,b). Because the cave environment is well protected from the erosion, speleothems may remain undamaged for a long period of time. Finally, a very accurate and absolute chronology of the speleothem stratigraphy can be established with the Thorium/Uranium ($^{230}Th/^{234}U$) dating technique (Lauritzen, 1998; Lauritzen and Lundberg, 1999b).

1.2.5 The global and regional surface temperature reconstructions based on proxies

So far, we have viewed that past surface temperatures, for specific areas, can be derived from proxies preserved in climate archives. The main strength of these surface temperature reconstructions is that the information reconstructed is derived from a climate archive, which is the imprint of the climate evolution. One weakness of these reconstructions is that the information is often only representative of the area that surrounds the proxy location. To overcome this, a few regional and global past air and sea surface temperature reconstructions have been made.

The most recent one focusing on the sea surface temperature is the Multi-proxy Approach for the Reconstruction of the Glacial Ocean surface (MARGO) (Kucera et al., 2005). This reconstruction of the Last Glacial Maximum (the period between 23 and 19 kyBP) sea surface temperature is based on different records derived from alkenones and foraminifera (Kucera et al., 2005; Waelbroeck et al., 2009).

The regional air surface temperature reconstructions based on proxies are more numerous. However, at the time when the database used by this thesis was built, only two reconstructions, both based on pollen data, provides a continuous record through the Holocene: the reconstruction of Viau and Gajewski (2009) for North America and the one of Davis et al. (2003) for Europe. The reconstruction of Bartlein et al. (2011) is also based on pollen data but only provides air surface temperatures for the Last Glacial Maximum and 6 kyBP. Very recently, a reconstruction of regional and a global Holocene temperatures from 73 globally distributed records has been proposed by Marcott et al. (2013). This reconstruction is not used in this thesis as it has been released to late to be included in our simulations with data assimilation.

1.3 Mathematical modelling of past climate

In climatology, a model is a mathematical representation of climate. The degree of simplification of this representation is the key to distinguish the Earth system Model of Intermediate Complexity (EMIC) (Claussen et al., 2002; Claussen, 2005), including a simpler representation of physical processes and a coarser grid (see Fig. 1.7), than the state-of-the-art climate General Circulation Models (GCMs).

Models are used to perform simulations. To start a simulation, each model needs initial conditions that reflect the state of the climate at the beginning of

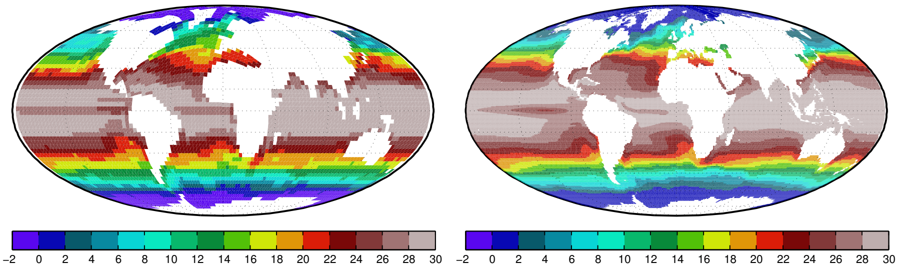

(a) LOVECLIM (b) BCC-CSM1-1

Figure 1.7: Raw (not interpolated) annual 6 kyBP sea surface temperature (°C) of the Earth Model of Intermediate Complexity LOVECLIM and the General Circulation Model BCC-CSM1-1

the experiment, i.e. the value of each state variables for each location in which they are defined. Additionally, boundary conditions should be defined, i.e. a set of data that influences the behavior of the modeled climate. It could be for instance the definition of the continents. Commonly, boundary conditions are called forcings if they have an impact on the climate changes at the scale investigated. For instance, it can be the Earth motion around the Sun, the greenhouse gases evolution, the effect of volcanism, the melting of ice sheet, the vegetation changes, etc. If the forcing used is constant through time, the simulation results represent the state of the climate at a particular time (time-slice simulation). If the forcing is time-dependent then the results depict the evolution of climate over a period (transient simulation).

In 1994, influenced by the Cooperative Holocene Mapping Project (COHMAP-Members, 1988), the Paleoclimate Modeling Intercomparison Project (PMIP) was launched (Joussaume et al., 1999). The aim of this project is to provide guidelines for the modelers in order to, for instance, facilitate the model evaluations (Braconnot et al., 2012). It intends to improve our understanding of mechanisms that drive the climate evolution, as the climate feedbacks (Braconnot et al., 2007a, 2012). Today, the PMIP project is a reference for the paleoclimate modeling community (Joussaume et al., 1999; Bonfils et al., 2004; Gladstone et al., 2005; Braconnot et al., 2007a,b; Crespin et al., 2013), providing common forcings and recommandations to simulate the past climates. Every two years, a conference is organized in order to share results and discuss future work.

Computing resources are a limiting factor for paleoclimate simulations. In the first phase of PMIP, it was decided to focus on a few key past periods for which there were evidences that regional climates were significantly different from today (Joussaume et al., 1999). The first period studied was the mid-Holocene. Later comes the Last Glacial Maximum and the Last Millennium. Now, multiple simulations of the whole Holocene performed by EMICs exist. For instance, simulations have been realized with MoBidiC by Crucifix et al. (2002), with LOVECLIM by Renssen et al. (2005) or Timm and Timmermann (2007) and with CLIMBER by (Brovkin et al., 2002). Some GCM transient simulations also exist. Because these model are more complex, an acceleration technique that reduces by a factor 10 to 100 the cost of such a simulation have been developed by Lorenz and Lohmann (2004). For instance, Varma et al. (2012) applied this acceleration technique to produce with CCSM3 a simulation of the Holocene. Recently, a multi-model-data comparison based on 9 model transient Holocene simulations has been carried out by Bakker et al. (2014). Within this thesis, we have conducted Holocene simulations with the LOVECLIM model and compared these results to available simulations from three GCMs: MPI-ESM-P, CSIRO-Mk3L-1-2 and BCC-CSM1-1.

The beginning of my PhD thesis has been devoted to implement in the LOVECLIM model the forcing for the last millennium proposed in the PMIP third phase (PMIP3). Detailed explanations about the implementation, as well as a list of the forcings involved are available in section 1.3.2. This work has led to the production of a five member reference simulation for the last millennium, called LMALL5, that spans the years AD 850 to 2000. The five member wording means that five simulations, which have slightly different initial conditions, have been run to represent a range of possible climate states for the last millennium. This ensemble of simulations (or the update version using 12 member, LMALL12) has been used in several recent studies (Mathiot et al., 2013; Mairesse et al., 2013; Shi et al., 2013; Klein et al., 2014). All simulations include the same forcings. The orbital parameters are calculated according to Berger (1978). The other forcings are detailed in section 1.3.2 and listed in table 1.1. Furthermore, the implementation of the last millennium forcings has helped E. Crespin in her work which has led to a publication about the response of the Arctic climate to external forcings (Crespin et al., 2013). It has also been used by Goosse et al. (2012a) in their evaluation of the simulations and the reconstructions of the last millennium Antarctic temperature changes.

1.3.1 Description of LOVECLIM1.2

LOVECLIM version 1.2 (Goosse et al., 2010a) is a three dimensional EMIC that is composed of five components: the atmospheric model ECBILT (Opsteegh et al., 1998), the sea ice-ocean model CLIO (Goosse and Fichefet, 1999), the terrestrial biosphere model VECODE (Brovkin et al., 1997), the ocean carbon cycle model LOCH (Mouchet and François, 1996) and the ice sheet model AGISM (Huybrechts, 2002).

Originally, only ECBILT and CLIO were coupled in the late 1990s (version used in Goosse et al., 2001, 2002). This version is followed by the ECBILT-CLIO-VECODE model that includes the terrestrial biosphere (version used in Renssen et al., 2003, 2005). The LOVECLIM acronym (LOch-Vecode-Ecbilt-CLio-agIsM) has been used when LOCH and AGISM were part of the system. To date, according to Goosse et al. (2010a), more than 100 papers have been published with the various versions of this model.

LOVECLIM is based on a simplified representation of the dynamics of the climate system. It has a coarse horizontal and vertical resolution which enables low computational requirements. In about 4 hours of calculation, 100 years of simulation are performed on a Intel Xeon E5649 processor. It can thus be used to run large ensembles of simulations, which is useful to test the influence of parameters (Roche et al., 2007; Loutre et al., 2011; Goelzer et al., 2012), to study the climate variability (Goosse et al., 2001, 2002; Nikolova et al., 2013), and is very convenient in the framework of data assimilation (see next section).

The LOCH and AGISM components are not activated within this thesis because (1) they are not necessary for the processes investigated here and (2) they are not public and their use is subject to permission. Therefore, these two components will not be explained here. For a complete description of LOVECLIM1.2, please refer to Goosse et al. (2010a).

1.3.1.1 ECBILT

Developed at the Koninklijk Nederlands Meteorologisch Instituut (KNMI), ECBILT models the atmosphere dynamics through the use of the quasi-geostrophic potential vorticity equation (Opsteegh et al., 1998). The geostrophic approximation being not valid at the equator, an ageostrophic term and a term representing the advection of heat by ageostrophic winds have been introduced within the equation in order to, among other things, improve the simulation of the Hadley circulation.

The equation is solved using a spectral method with a horizontal truncation T21 (Opsteegh et al., 1998), corresponding to an horizontal resolution of about 5.625° in latitude and longitude, and three vertical levels: 800 hPa, 500 hPa and 200 hPa.

The humidity in the atmosphere is represented by the total precipitable water content between the surface and 500 hPa (Opsteegh et al., 1998). Above

500 hPa, the atmosphere is assumed to be completely dry. There are two ways to form precipitation in ECBILT. Precipitation occurs if water vapor is transported above the 500 hPa level or if the total precipitable water between the surface and 500 hPa is above a threshold.

The longwave radiative scheme is based on a Green's function method (Chou and Neelin, 1996). In ECBILT, the longwave flux is calculated for all the model levels (Goosse et al., 2010a). To calculate the longwave flux, two anomalies are applied to a reference value of the flux. The first is function of the vertical profile of temperature and of the greenhouse gases in the atmosphere. The second is function of the humidity.

The shortwave fluxes (downward and upward) are also computed using a linearised scheme. This is achieved at 3 different levels, at the surface and at the top of the atmosphere. The transmissivity of the atmosphere varies with location and season. The surface albedo depends on the fraction of grid covered by ocean, sea ice, trees, desert and grass. The insolation at the top of the atmosphere is obtained using the calculation of Berger (1978).

Additionally, ECBILT includes a land-surface model. The land contains a single soil layer. The heat budget of this layer influences the surface temperature and the snow cover. The layer's moisture is computed with a bucket model. Its maximum water content is function of the vegetation cover. When the water content of the layer exceeds its maximum value, the water is transferred to the closest ocean grid that corresponds to the mouth of the river that drains the model grid box.

1.3.1.2 CLIO

Developed at the Université catholique de Louvain, Institut d'Astronomie et de Géophysique G. Lemaître (UCL-ASTR), the Coupled Large-scale Ice-Ocean model (CLIO) is an oceanic general circulation model coupled to a comprehensive sea ice model (Goosse and Fichefet, 1999; Goosse et al., 2000). It has a horizontal resolution of $3° \times 3°$ and 20 unequally spaced vertical levels ranging from 10 m near surface to 500 m at 5500 m depth. To avoid the singularity at the North Pole, the grid of CLIO is composed of two subgrids (Deleersnijder et al., 1997). The first one, based on classical latitude and longitude coordinates, covers all the oceans except the North Atlantic and the Arctic. The second grid, which covers the North Atlantic and the Arctic ocean is rotated by 90° anticlockwise and thus has its pole at the equator, the "North Pole" being located in the Pacific (111°W), while the "South Pole" is in the Indian Ocean (69°E). These two subgrids are connected in the equatorial Atlantic.

The oceanic component is governed by the primitive equations derived from the Navier-Stokes equations (Goosse et al., 2000). Three classical approximations are used to formulate these equations. First, the Boussineq approximation states that the density (ρ) variability is negligible compared to its mean value (ρ_0), except in the expression of the gravitational force. Second, the depth of the ocean is supposed negligible compared to the Earth radius, so that the distance between each location of the ocean and the Earth center is constant. Third, the ocean is supposed to be in the hydrostatic equilibrium leading to $\partial p/\partial z = -\rho g$ with p the pressure, z the depth, ρ the density and g the gravitational acceleration. Moreover, physical parameterization are applied to represent subscale phenomena that have impact on large scale. For more information, please refer to Goosse et al. (2000).

The sea ice component uses the same grid as the oceanic component. Each grid cell is partly covered by sea ice that has within each cell the same thickness (Fichefet and Morales Maqueda, 1997). The physical processes that rule its evolution can conceptually be divided into two parts. The first deals with the thermodynamic sea ice growth and melt, that depend on the vertical response of the sea ice layer to the exchanges with the atmosphere and ocean. The second physical process deals with sea ice dynamic and transport assuming a constant horizontal sea ice velocity over its thickness. The behavior of sea ice is the one of a two-dimensional viscous fluid when its deformation rate is low, and the one of a plastic fluid when its deformation rate is high.

The oceanic and sea ice components exchange momentum, heat, and mass (Goosse et al., 2000). The momentum exchanges are proportional to the difference between oceanic surface velocity and the one of the sea ice. The heat flux is proportional to the difference between the temperature of the first oceanic layer and its freezing temperature. The mass exchanges can either be represented by an equivalent salt flux or as a realistic freshwater flux (Tartinville et al., 2001). A freshwater flux is used if liquid or solid water is added or extracted from the ocean-ice system, through precipitation or evaporation for instance. An equivalent salt flux is used when the surface process affects the salinity without a net gain or loss of water within the ocean-ice system, through ice melting or freezing for instance.

1.3.1.3 VECODE

Developed by the Potsdam Institute for Climate Impact Research (PIK), VECODE (VEgetation COntinuous DEscription model) is the continental biosphere component that describes the distribution of trees, grass and desert at the same resolution as ECBILT (Brovkin et al., 1997; Fichefet et al., 2007; Goosse et al., 2010a). VECODE is composed of three submodels. The first models the vegetation structure, the second is a biogeochemical model and the third simulates the vegetation dynamics. VECODE has been specifically designed to be coupled to a coarse resolution atmospheric model and to be run over period ranging from decades to millennia (Brovkin et al., 1997).

Coupling a vegetation model with a climate model requires the transformation of vegetation characteristics into bioclimatic parameters such as, for instance, the surface albedo or the leaf area index (Brovkin et al., 1997). The model of the vegetation structure only takes into account two types of vegetation: grass and trees. This strong approximation has been made since Dickinson et al. (1993) have demonstrated that the sets of bioclimatic parameters only differ significantly for these two main Plant Functional Types (PFT). The other biomes, such as savannah for example, are characterized by intermediate values of these bioclimatic parameters. Within a land grid cell, the tree (f_t) and grass (f_g) fractions are controlled by the climate and their sum is equal to the vegetation fraction (f_v); the rest corresponding to the desert fraction (f_d) so that $f_v + f_d = 1$ for a given climate. The tree fraction depends on the growing degree-days above 0 (i.e. the sum of the surface air temperature for all the days with a mean daily temperature higher than 0°C) and on the mean annual precipitation. This fraction is determined as follows: in cold climates, the forest growth is mainly limited by the temperature, while in a warm climate, the major limiting factor is precipitation. Moreover, if the precipitation amount is smaller than the minimum quantity required to sustain vegetation, or if the temperature is below a critical threshold of about -15°C, the tree fraction is equal to 0 or nearly inexistant, respectively. The desert fraction is divided into two types of desert: the warm desert where the vegetation growth is limited by precipitation and the cold desert where the main limiting factor is temperature. The grass fraction is deduced from the tree and desert fractions. This first model aims to update the vegetation structure in response to climate evolutions.

The biogeochemical component models the vegetation and the organic matter carbon cycle. Four carbon pools are considered: a fast one composed of the green biomass (leaves), a slow one composed by the structural biomass (stems and roots) and two pools that gather the soil organic matters: a fast one (woody residues) and a slow one (humus). The equations describing the carbon dynamics into those pools mainly depend on the carbon disintegration rate and are integrated annually. Finally, the net primary productivity, i.e. the net flux of carbon from the atmosphere into green plants per unit time, is also simulated annually through the parametrization of Lieth (1975).

The third component models the vegetation dynamics. It simulates the subgrid-scale processes of the vegetation succession and thus the dynamics of the PFT fractions (Brovkin et al., 1997). The first submodel calculates the equilibrium structure of the vegetation with respect to the climate state. This third sub-model evaluates the transition speed between the previous vegetation structure and the new one.

1.3.1.4 Coupling the ocean and atmosphere

CLIO and ECBILT are running on two different grids. To transfer information between the two components, an interpolation is necessary. To ensure that this interpolation is conservative, each grid is divided into the three following categories, such as the total surface of each category is the same in the two sub-models: land, ocean and sea ice. In practice, this is accomplished by decomposing the ECBILT grid in function of the CLIO grid. It is therefore CLIO which determines the land/sea mask between the two components (Fig. 1.8). This mask is fixed. This implies that the coastline changes, that could be due, for instance, to a sea level rise, cannot be taken into account. Besides, this land/sea mask can be changed between two different simulations.

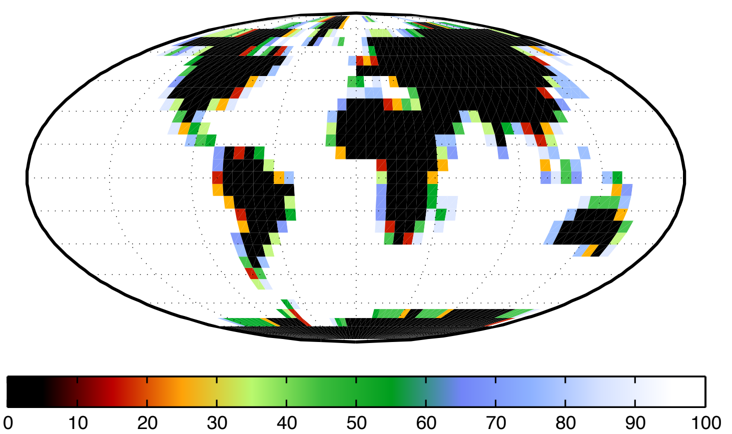

Figure 1.8: Fraction of ocean surface for each grid cell of ECBILT (in %).

The information exchanged between CLIO and ECBILT is the following. CLIO gives to ECBILT the sea surface temperature, the sea ice fraction and the sea ice and snow thicknesses. ECBILT provides CLIO with the wind stress, the shortwave radiation and net heat flux over the ocean, the solid and liquid precipitation and the runoff.

1.3.1.5 The model performance

The LOVECLIM model simulates a present-day climate that agrees reasonably well with the observations (Goosse et al., 2010a). For instance, the model is able to reproduce, in a satisfactory way, the large-scale oceanic circulation and surface temperature patterns, the atmospheric near-surface circulation and the sea-ice extent in both hemispheres. LOVECLIM also succesfully simulates the climate changes over the last decades, the last millennium, the mid-Holocene and the last glacial maximum, when it is driven by estimates of forcings variations over those periods.

Nevertheless, the model has clear biases. For instance, the Atlantic and Arctic precipitations are overestimated in comparison to modern estimates, while they are underestimated in the North Pacific. To overcome this issue, the precipitations in the Artcic and the Atlantic are reduced by 25% and 8.5%, respectively, and the excess water is dumped into the North Pacific allowing to conserve mass. Another bias of LOVECLIM is an overestimation of the tropical temperatures, particularily, in the Eastern Pacific. Consequently, the temperature gradient between the Eastern and Western Pacific is underestimated. This, in addition to the impact of simplification of tropical dynamics in the model, leads to a very weak ENSO-like activity in the model.

Additionaly, the model does not include an interactive representation of stratospheric dynamics. Such a dynamics influence the variability of the North Atlantic Oscillation (NAO) and, for instance, is necessary to generate the Europe winter warming that follows some strong volcanic eruptions (see section 3.1 for more information).

Finally, climate sensitivity of LOVECLIM, is of about 1.9°C (Goosse et al., 2010a). It is in the lower end of the range of values obtained from EMICs (1.9-4.0°C) and GCMs (2.1-4.7°C) (Flato et al., 2013). This metric indicates that LOVECLIM is less sensitive than most of the models to a doubling of the atmospheric CO_2 concentration, and more generally, to the forcings.

1.3.2 The forcing used within this thesis and their implementation in LOVECLIM

In the simulations described in this thesis, various forcings have been taken into account: the astronomical parameters, the Total Solar Irradiance (TSI), the volcanism, the greenhouse gases, the anthropogenic land cover change, the topography and the surface albedo of the Laurentide ice sheet, the freshwater fluxes resulting from the melting of the ice sheets. Below, these forcings and their implementation are described. The forcings utilized to simulate the last millennium have been distributed in the framework of PMIP3 (Schmidt et al., 2011, 2012) and are listed in Tab. 1.1. For the Holocene and 6 kyBP, the forcings implemented slightly differ from PMIP protocol and have been provided in the framework of the European project Past4Future. These forcings are listed in Tab. 1.2.

Last millennium forcings

Forcing type	File name	Covered period (yAD)
Total Solar Irradiance	`TSI_NB.dat` `TSI_WB.dat`	850-2000 850-2000
Volcanism	`VOL_GAO.dat` `VOL_CRO.dat`	501-2000 800-2001
Greenhouse gases	`GHG.dat`	1-2000

The anthropogenic land cover change	`VG.nc`
	`VG_MIN.nc`
	`VG_MAX.nc`
		850-1992
		850-1992
		850-1992

Table 1.1: Summary of the available PMIP3 last millennium forcings for LOVECLIM. These forcing files are available online: `http://www.climate.be/mairesse/forcing/pmip3_lm`

Holocene and 6 kyBP forcings

Forcing type	Covered period (yBP)	Reference
Total Solar Irradiance	8050 to -50	Steinhilber et al. (2009)
Volcanism	11495 to -50	Vinther's dataset; Gao et al. (2008). See chapter 3.
Greenhouse gases	10250 to -50	Flückiger et al. (2002); Schmidt et al. (2012)
Laurentide Ice Sheet topography and surface albedo	10000 to 125	Renssen et al. (2009); Peltier (2004)
Freshwater fluxes	10000 to 1	Pollard and DeConto (2009)

Table 1.2: Summary of the available Holocene forcings for LOVECLIM.

1.3.2.1 Astronomical parameters

The three astronomical parameters, also called orbital parameters, describe the Earth motion around the Sun (eccentricity and climatic precession) and the position of its rotation axis (obliquity). The eccentricity is a measure of the shape of the Earth's orbit around the Sun. The climatic precession is related to the Earth-Sun distance at the summer solstice. The obliquity is the tilt of the equator plane with respect to the plane of the Earth's orbit. These three parameters have quasi-periodic oscillations and their value is calculated within LOVECLIM following the work of Berger (1978). This forcing is used in all the simulations realized with LOVECLIM in the present framework.

1.3.2.2 Total solar irradiance

"The total solar irradiance is the amount of solar radiation received outside the Earth's atmosphere on a surface normal to the incident radiation, and at the Earth's mean distance from the Sun" (IPCC, 2007). Its mean value for LOVECLIM is 1365 Wm^{-2}. In LOVECLIM, the TSI forcing is implemented as an anomaly added to this constant value that evolves through time and represents the variations of the solar radiation.

For the last millennium, the TSI forcing used is the stacked reconstruction of Delaygue and Bard (2009) for 850 to 1609 yAD and Wang et al. (2005) for 1610 to 2000 has been implemented. Two versions of the Wang et al. (2005) forcing exist: one that has TSI variations similar to those seen over a solar cycle today, called no-background (`TSI_NB.dat`), and one with longer-term trends in the solar minimum, named with background (`TSI_WB.dat`).

For the Holocene simulations, the longer TSI reconstruction of Steinhilber et al. (2009) have been used. It is represented in the Fig. 1.9.

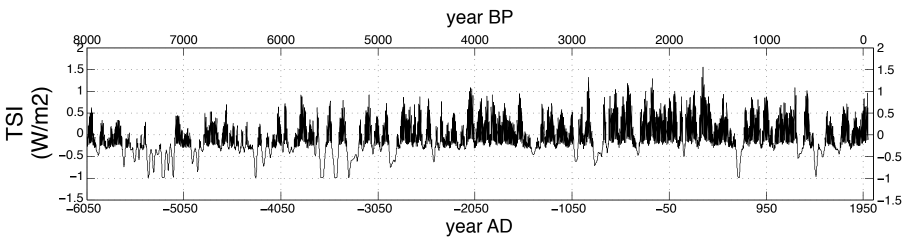

Figure 1.9: The Total Solar Irradiance (Wm^{-2}) reconstruction of Steinhilber et al. (2009).

1.3.2.3 Volcanism

The volcanism is taken into account in LOVECLIM as a negative anomaly of the TSI (Wm^{-2}). The goal is to represent the decrease of the amount of solar radiation that reaches the Earth surface in response to the sulfates injected in the atmosphere by a volcanic eruption. This forcing has a monthly resolution and is function of the latitude. Four equal-area latitude bands are considered: from 90°S to 30°S, from 30°S to the equator, from the equator to 30°N, from 30°N to 90°N. The text file that contains the forcing has thus six columns: yAD, month, and the four equal-area latitude bands in the order described above.

In the PMIP3 framework, two datasets are used: the one of Crowley et al. (2008) and the one of Gao et al. (2008). Below, the procedure to convert these datasets in TSI anomaly is described. The resulting LOVECLIM files are named `VOL_CRO.dat` and `VOL_GAO.dat`, respectively. The chapter 3 provides the procedure to produce a volcanic forcing that covers the Holocene. For more details about this forcing, please refer to this chapter.

Crowley et al. (2008) provide Aerosol Optical Depth (AOD) for the four equal-area latitude bands of LOVECLIM, where AOD is a local measurement of how opaque the atmosphere is in a single column.

Gao et al. (2008) provide the total sulfate loading (kg/km^2) for 18 latitude bands. It represents the amount of sulfate present in the atmosphere per km^2 at a monthly resolution for 43 different altitudes. The objective is to obtain AOD from the total sulfate loading and then to convert it in TSI forcing. Firstly, the sulfate loadings (kg/km^2) are summed over the altitude. The output is weighted, for each 10° latitude band, by the area of the 10° latitude band. The result (in kg per 10° latitude band) is summed over the four equal-area latitude bands and converted in Tg. Afterwards, following Stothers (1984), the amount of sulfate (in Tg) of each of the four equal-area latitude bands, is converted in AOD by dividing it by $\left(150 \times \frac{1}{4}\right)$. The $\frac{1}{4} = \left(\frac{\text{band area}}{\text{Earth area}}\right)$ factor is used to take into account the area of the considered band compared to the whole Earth.

At this stage, both forcings (Gao et al. (2008) and Crowley et al. (2008)) are in the same format (AOD) and can be converted by the same procedure. The conversion from AOD to Wm^{-2} at the top of the atmosphere implies the multiplication of the AOD by -20 according to Wigley et al. (2005). To convert the Wm^{-2} at the top of the atmosphere to TSI equivalent, they should be multiplied by $\frac{4}{0.7}$. The numerator is used to transfer the value from a sphere to a plane, and the denominator is to take into account the Earth albedo.

Finally, the global averaged monthly forcing of the considered period is added for each month and each latitude so as to provide in average a nul forcing for the period considered.

1.3.2.4 Greenhouse gases

"Greenhouse gases are gaseous constituents of the atmosphere, both natural and anthropogenic, that absorb and emit radiation at specific wavelengths within the spectrum of thermal infrared radiation emitted by the Earth's surface, the atmosphere itself, and by clouds. This property causes the greenhouse effect." (IPCC, 2007).

PMIP3 provides the annual evolution of three greenhouse gases (CO_2, CH_4 and N_2O) compiled by Schmidt et al. (2012). In LOVECLIM, the file where this information is stored contains 20 columns (`GHG.dat`). The first column contains the yAD, while the CO_2 (ppmv), CH_4 (ppbv) and N_2O (ppbv) values are stored in the columns 2 to 4, respectively. The other columns contain the values corresponding to the CFCs concentrations provided by the Intergovernmental Panel on Climate Change Special Report on Emissions Scenarios A1B for the period 1749 to 2000 yAD.

An additional greenhouse gases forcing has been used to perform Holocene simulations. It is a data set based on the reconstruction of Flückiger et al. (2002) from -8300 to -50 yAD, stacked with the PMIP3 last millennium values (Schmidt et al., 2011) from 0 to 2100 yAD. To fill in the gap between the two data sets, a linear interpolation is realized between -50 and 0 yAD. A graphical respresentation is provided in the Fig. 1.10. The data set based on the reconstruction of Flückiger et al. (2002) has been provided by Cedric Van Meerbeeck in the framework of the HOLOCLIP project.

1.3.2.5 Anthropogenic land cover changes

The anthropogenic land cover changes are taken into account in LOVECLIM through deforestation. Annually, and for each grid of VECODE, a fraction of the forest is changed into grassland. These changes are derived from the reconstruction of the global agricultural areas and land cover reconstruction of Pongratz et al. (2008) from 850 to 1700 yAD, stacked with the reconstruction of Ramankutty and Foley (1999) from 1700 to 1992 yAD (see Fig. 3 of Schmidt et al., 2011 for an illustration). The file that contains these values is `VG.nc`. Additionally, two alternative scenarios, a maximum (`VG_MAX.nc`) and minimum (`VG_MIN.nc`) reconstruction, can be used to test the uncertainties.

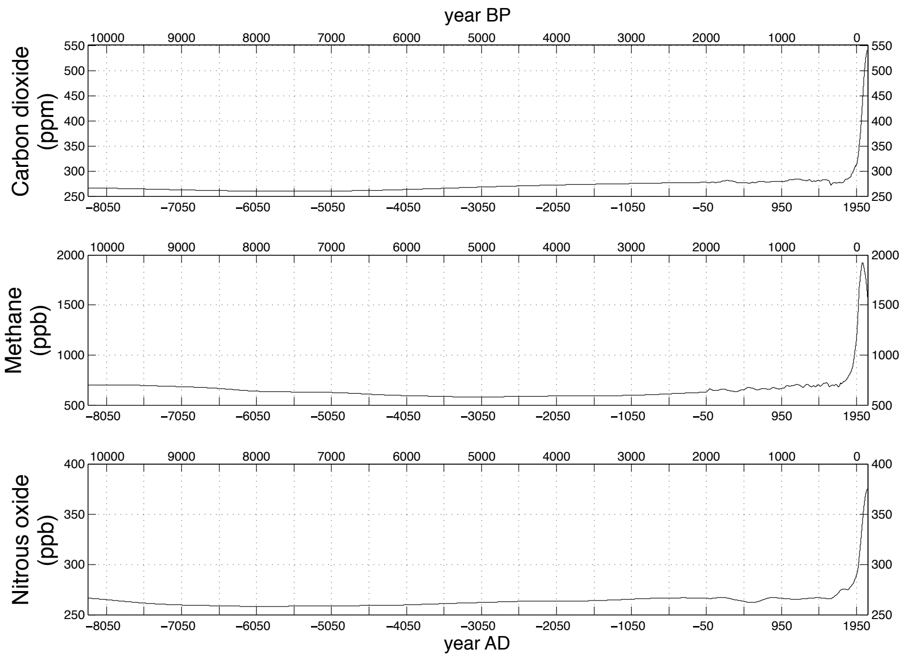

Figure 1.10: The greenhouse gas concentrations based on the data of Flückiger et al. (2002) and the PMIP3 last millennium values (Schmidt et al., 2011).

1.3.2.6 Laurentide Ice Sheet topography and surface albedo

The Laurentide Ice Sheet topography (in m) and surface albedo have been adapted for LOVECLIM by Renssen et al. (2009) from the reconstruction of Peltier (2004). The file contains a value each 25 years between -8050 yAD and 1825 yAD. The figure 1.11 represents the topography for three different periods and illustrates that the Laurentide ice sheet almost nearly totally vanished at 6 kyBP.

To take into account the Laurentide ice sheet presence, the surface albedo value is modified to correspond to an area covered by ice. The area where this modification is applied is defined by a mask shown in the Fig. 1.12 for the same period than the Fig. 1.11. As for the topography, a value is provided each 25 years between -8050 yAD and 1825 yAD.

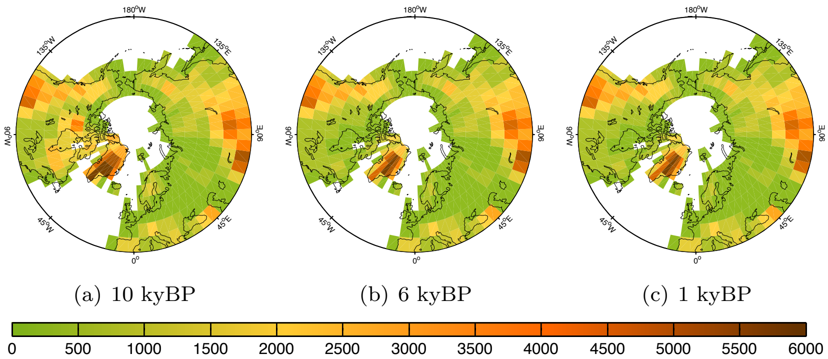

(a) 10 kyBP (b) 6 kyBP (c) 1 kyBP

Figure 1.11: The topography forcing (in m) for three different periods: 10, 6 and 1 kyBP.

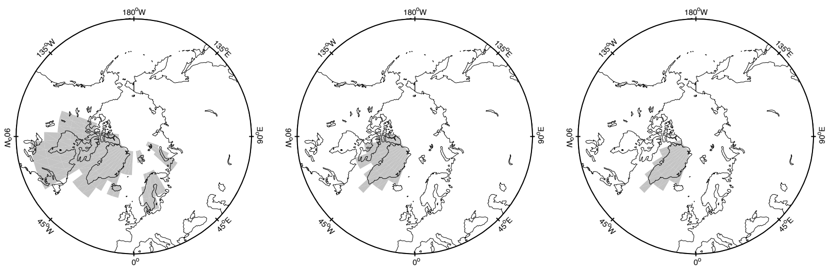

(a) 10 kyBP (b) 6 kyBP (c) 1 kyBP

Figure 1.12: Mask (in grey) that defines the area covered by the Laurentide Ice Sheet at three different times: 10, 6 and 1 kyBP.

1.3.2.7 Freshwater fluxes

This forcing has been provided by Cedric Van Meerbeeck and is based on the reconstruction of Pollard and DeConto (2009). The freshwater fluxes (in Sv, with $1\text{Sv}=10^6\text{m}^3\text{s}^{-1}$) that are resulting from the melting of the Laurentide ice sheet are injected in the north-east part of the Labrador Sea and close to the mouth of the Gulf of St Lawrence. The freshwater fluxes resulting from the melting of the Antarctic ice sheet are injected in the Weddell Sea, Bellingshausen Sea, Amundsen Sea and Ross Sea. The three time series corresponding to those three regions are shown in the Fig. 1.13.

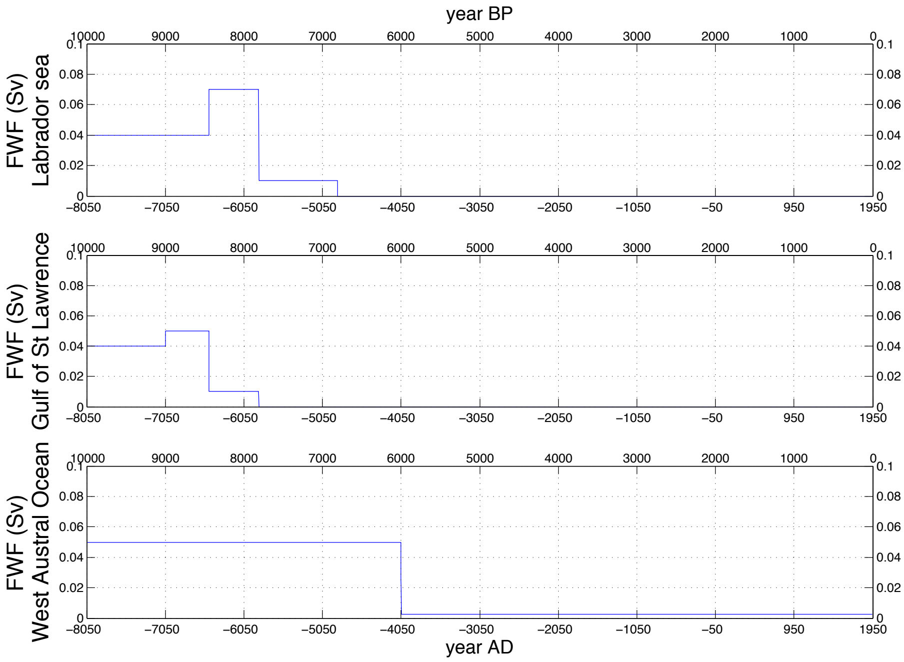

Figure 1.13: The freshwater fluxes (Sv) based on the work of Pollard and DeConto (2009) and Renssen et al. (2009). The fresh water is injected in the North-East part of the Labrador Sea, in the mouth of the Gulf of St Lawrence and in the Weddell Sea, Bellingshausen Sea, Amundsen Sea and Ross Sea.

1.4 Comparing model results and proxy-based reconstructions

So far, we have seen that paleoclimates can be studied with climate models and with proxy data. The models provide an information available everywhere and for any time. This knowledge depends only on the understanding of the physical phenomena that influence the climate. With the proxies, the reconstructed information is sparse in time and space, but is directly derived from an archive that has been influenced by climate.

The purpose of this section is to highlight that these two approaches are complementary (Mock, 2007). Indeed, the information inferred from the proxies often serve to validate climate model results (Braconnot et al., 2012), while the models allow to understand the physical processes responsible for the recorded climate changes. For instance, Renssen et al. (2002) have studied the 8.2 kyBP event with LOVECLIM and have shown the influence of different freshwater pulses. They have established that the simulated changes are realistic compared to proxy evidence. The different simulations have highlighted that the number of years to recover the initial state is unpredictable since, for a fixed freshwater pulse, the time of recovery can be longer and shorter than 200 years.

Applying jointly these two approaches can also highlight systematic biases. For instance, Brewer et al. (2007b), analyzing the mid-Holocene climate over Europe, have concluded that the models are not able to simulate the magnitude of the reconstructed changes based on pollens. Lohmann et al. (2013) have made a model-data comparison of the Holocene sea surface temperature evolution. They also concluded that models tend to underestimate the amplitude of the changes. Braconnot et al. (2007a,b) compared the results of the mid-Holocene and the Last Glacial Maximum (LGM) in PMIP2 coupled simulations, to several proxy-based reconstructions. The comparison with data also allowed them to conclude that the mid-Holocene changes in precipitation over the west Africa are underestimated in most of the simulations.

1.5 Data assimilation: the particle filter with resampling

Recently, data assimilation methods have been applied in paleoclimatology (Widmann et al., 2010). The idea is to constrain climate model results using the information derived from multiple proxies to produce a reconstruction of the past climate that is consistent with the physics and forcings of the climate model and the information inferred from proxies. Among the data assimilation methods, the selection of ensemble members consists to approximate the statistical behavior of the model with a finite ensemble of random model states (Widmann et al., 2010; Dubinkina et al., 2011) and estimate which of those states are the most likely with respect to observations. The random model states are the result of variations of the initial conditions, the model parameters or the forcings in a plausible range (Widmann et al., 2010; Dubinkina et al., 2011). These ensemble methods are used because (i) they are relatively easy to implement in comparison to other techniques, (ii) they do not require any information about the model and (iii) because the model may have a strong non-linear behavior. The particle filter with resampling of van Leeuwen (2009) is one of the ensemble member methods and is the filter that has been implemented in LOVECLIM by S. Dubinkina (Dubinkina et al., 2011).

The particle filter method with resampling consists in running an ensemble of several simulations, also called particles (Fig. 1.14). In the default version, the ensemble is generated by adding a small perturbation to the air surface temperature in the initial conditions. Due to the relatively chaotic nature of the climate system, the propagation of these particles results in trajectories that quickly deviate from each other. After a fixed period of simulation (called the assimilation step), the particles are stopped. The climate state of each particle is then evaluated and a likelihood is attributed to each particle. The likelihood is estimated as a function of the difference between the climate state of the particle and the observations.

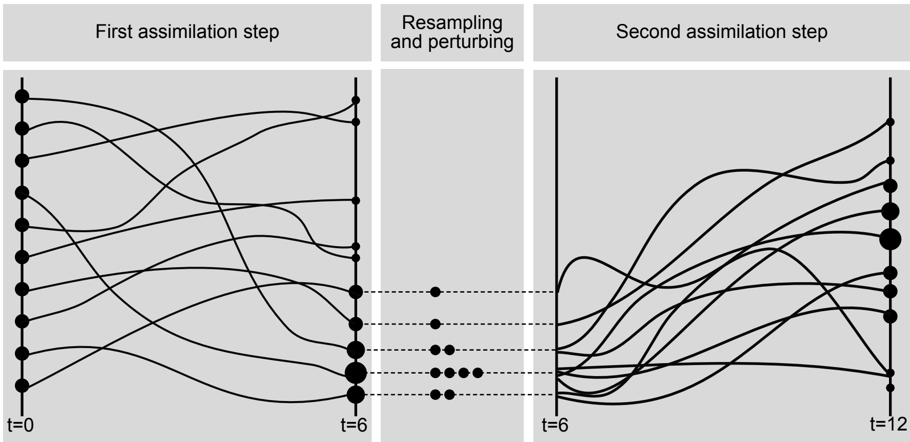

Figure 1.14: Schematic illustration of the particles filter for two assimilation steps of 6 months. The curves show the trajectories of the particles, while the size of the points corresponds to the likelihood of the particles. The figure is adapted from van Leeuwen (2009).

Various types of observations can be used in the process of assimilation. The only requirement is that a quantitative estimate of the agreement with model results can be estimated. Such observation can be a categorical variable as the presence or the absence of sea ice if a quantitative variable can be inferred from it. It also might be a variable directly comparable as the surface temperature, the freshwater fluxes due to ice sheet melting, the sea ice concentration, etc.

Knowing which particles are the closest to observations and have thus a high likelihood, a new ensemble is setup (Fig. 1.14). The particles with the highest likelihood are continued, while the particles with a low likelihood are stopped. The remaining particles are then resampled a number of times proportional to their likelihood so that the total number of particles is kept constant. The initial conditions of the particles that have been resampled are slightly perturbed by adding a small perturbation to the air surface temperature. Finally, all the particles are restarted until the next assimilation step. This procedure is repeated until the end of the simulation. This resampling step is necessary to avoid a collapse of an ensemble of particles to one single particle.

The amount of particles needed for the data assimilation process depends on the number of proxy-based reconstructions that are used and on their independence. The more complex the target as described by the proxy-based reconstructions, the larger the ensemble. This can be illustrated with the following reasoning. First, it is assumed that, for each proxy-based reconstruction, five simulations are needed to be sure to have at least one simulation that is consistent with the proxy-based reconstruction. Second, it is supposed that all the proxy-based reconstructions are independent. Therefore, the amount of simulations needed to get one simulation that is consistent with the variations of n proxies is 5^n. For 50 proxy records, this means that more than 8×10^{34} simulations are needed. Fortunately for us, the reconstructions inferred from the proxies are not truly independent as proxies have been influenced by the same climate. The amount of 96 particles has been chosen because it provides a satisfactory large-scale climate reconstruction at an affordable computing cost (Dubinkina et al., 2011; Goosse et al., 2006).

The advantage of the data assimilation is to provide a better estimate of past climates combining the proxy-based reconstructions with the physical understanding of the climate models. The inconvenience of such a methodology is the very expensive costs in terms of computing resources. If the data assimilation is performed with an ensemble of 96 simulations, it takes, in theory, about 96 times more resources than a single simulation performed without data assimilation. In practice, it takes more time due to cluster communication issues which leads to about 1 day of computation for 100 years of simulation with 48 processors, as all the 96 simulations should wait for each other to communicate informations.

Data assimilation is performed with LOVECLIM since less than a decade, but the way it is performed has quickly evolved. At the beginning, the filter was only keeping the best simulation (Goosse et al., 2006). Goosse et al. (2009) have demonstrated that the assimilation of a unique variable (the surface temperature) was sufficient to influence other variables, such as the sea ice area. Crespin et al. (2009) and Goosse et al. (2010b) have assimilated the homogeneous surface temperature reconstruction of Mann et al. (2008). This has highlighted the existence of a prominent Arctic warm event between the late 15th and the early 16th century. This has also produced a faithful representation of the Northern Hemisphere signal at both regional and grid-box scales, except in the areas where no data were available such as the North Atlantic Ocean. In 2011, Dubinkina et al. have implemented the version of the filter described here. This new filter has been used by Goosse et al. (2012b) and Goosse et al. (2012c) to improve the understanding of the Medieval Climate Anomaly in Europe (around 950-1250 yAD). In this framework, I have for the first time assimilated two different variables together: the air and sea surface temperatures. This has been done for the mid-Holocene period (see chapter 2) and has led to an objective demonstration of the existence of incompatibilities between some proxy-based reconstructions that represent different variables. Those tools have been used by Mathiot et al. (2013). They have shown that data assimilation can also be used to reconstruct past forcings (the freshwater fluxes) that maximize the consistency between proxy-based reconstructions and model results. I also have contributed to the studies of Klein et al. (2014) and Renssen et al. (2014, in prep.) focussing on the sea ice during the mid-Holocene and the causes of the Younger Dryas cold event, respectively.

1.6 Objectives and outline of the thesis

This introduction has highlighted that the current paleoclimate knowledge is based on the one hand, on the climate models results and, on the other hand, on the reconstruction of physical variables derived from paleoclimate observations. It has also been emphasized that these two types of information are complementary. Indeed, the past climate characteristics derived from proxies often serve to validate climate model results, while the model results allow to investigate the climate mechanisms that have influenced the evolution of characteristics retrieved from proxies. The data assimilation methodology combines these two sources of information. This is promising to reconstruct the past climates since both model results and proxy-based reconstructions have their own limitations and biases.

The purpose of this thesis is to analyse the Holocene climate variability using a data assimilation method in the model LOVECLIM. The data assimilation method applied here is a particles filter. It is based on the selection of the members of an ensemble of simulations performed with LOVECLIM that have the best agreement with the reconstructions. One of the main data assimilation strenght is to provide a reconstruction that is both consistent with the model physics, the forcings and the proxy-based reconstructions. This gives a reconstruction of the climate variables evolution from which the mechanisms that explain the proxy-based reconstructions can be deduced. In other words, the data assimilation allows to select the mechanisms that explain best the proxies variations.

The chapter 2 is based on the paper published on 6 December 2013 by Mairesse et al. (2013). It is focussed on the ability of LOVECLIM to reproduce the long-term local surface temperature variability derived from proxies for the mid-Holocene, i.e. the difference between the mean surface temperature of the period 6 ± 0.5 kyBP and the mean surface temperature of the first half of the last millenium. To do so, LOVECLIM is forced by the data assimilation methodology, to represent the proxy-based signal difference between two fixed time slices. This chapter examines in details the output of the data assimilation and highlight the difficulties encountered when performing assimilation of paleoclimate data.

Chapters 3 and 4 have been developped in parrallel and are connected by a common goal: studying the centennial and multi-centennial fluctuations that are superimposed on the long-term trends over the Holocene. Chapter 3 deals with the Holocene volcanism. The volcanism is known to be one of the main natural climate forcings at annual to centennial timescales. Investigating its impact over the Holocene appears thus justified. Such an analysis has never been performed before, because of the lack of an adequate forcing. Here the beta-version of a forcing obtained in the framework of Past4Future is applied.

In chapter 4, the ability of LOVECLIM to reproduce the observed variations at the multi-centennial timescale is investigated. The signal assimilated is obtained by removing high- and low-frequency variability to the temporal series of surface temperature reconstructions derived from proxy records. In contrast to the simulations presented in chapter 2 that were using a constant forcing, the analysis of multi-centennial variability requires transient experiment. The focus is a cold period in the Arctic around 2.7 kyBP.

In order to be able to perform simulations with data assimilation, the first contribution to this thesis has been to built a database that contains available reconstructions of surface temperature in the Northern Hemisphere. To do so, the following steps have been realized. The proxy-based reconstructions have been collected. The consistency between the published and online data have been verified. The database have been filled and the scripts used to easily get informations from this database have been built. The proxy-based reconstructions of this database that are used within this thesis are listed and shown in the appendix A.

To assimilate the proxy-based reconstruction of air and sea surface temperature that are included in the database a few modifications of the data assimilation methodology have been required. First, we have chosen to adapt the assimilation step in function of the characteristics of the observations. Because the proxy-based reconstructions mostly represent seasonal data, i.e. a month or a particular season (instead of an annual average), an interval of 6 months was used. This means that the simulations constrained by data assimilation are stopped and restarted every 6 months. In addition, to manage the assimilation of proxy-based reconstructions that represent different variables at the same time, i.e. the air and sea surface temperatures, some technical modifications have been done. For each particle, this is handled by calculating separately the likelihood for each variable and by multiplying the different likelihoods to obtain the final particle's likelihood. Another change has been done to take into account the proxy-based reconstructions that correspond to an area larger than the model grid, as the ones of Viau and Gajewski (2009) and Davis et al. (2003). This issue is solved by averaging the model results at the right spatial resolution before comparing them to the proxy-based reconstructions.

An estimation of the uncertainty of each reconstructions is required in data assimilation, as it is used in the likelihood computation. This information is frequently not available, and when it is, these uncertainties are often upper bounds and thus sometimes of the same order of magnitude as the signal itself (Ohlwein and Wahl, 2011). We have not used those values in order to provide a sufficiently strong constrain on model results through data assimilation. Consequently, we likely underestimate the uncertainty of the proxies (see table 2.1). By facility, we have chosen only one error for each archive type based on values provided in previous studies (e.g., Heikkilä and Seppä, 2003; Martrat et al., 2007; Mathiot et al., 2013; Muller et al., 1998; Seppä and Birks, 2001). This underestimation affect weakly the spatial patterns but influence the magnitude of the changes induced by the data assimilation processes (Goosse et al., 2012b). Therefore, this should be taken into account in the interpretation of the results of our experiments.

Finally, the following key scientific questions will be treated during this thesis and answers will be proposed in the chapter 5 that concludes the thesis and sums up the most important findings and perspectives: Do the model limitations affect the reconstruction of the past climate that is produced with and without the data assimilation method? What are the potential and limitations of the information brought by the proxies? What are the characteristics of ideal data to be used for data assimilations? What is the ideal number of data for data assimilation? Is quality more important or quantity? Does the data assimilation highlight the same mechanism to explain a particular phenomenon? If yes, is the mechanism robust or does its selection only due to the use of a model with a too simple physics? Is LOVECLIM able to reproduce in Europe the 6 kyBP summer temperature gradient that is indicate by the proxy-based reconstruction of Davis et al. (2003)?

Chapter 2

Investigating the consistency between proxy-based reconstructions and climate models using data assimilation: a mid-Holocene case study

This Chapter is based on the paper published by Mairesse et al. (2013).

The period around 6 kyBP is a key period to study the consistency between model results and proxy-based reconstructions as it corresponds to a standard test for models and a reasonable number of proxy-based records are available. Taking advantage of this relatively large amount of information, we have compared a compilation of 50 air and sea surface temperature reconstructions with the results of three simulations performed with general circulation models and one carried out with LOVECLIM, a climate model of intermediate complexity. The conclusions derived from this analysis confirm that models and data agree on the large-scale spatial pattern but the models underestimate the magnitude of some observed changes and that large discrepancies are observed at the local scale. To further investigate the origin of those inconsistencies, we have constrained LOVECLIM to follow the signal recorded by the proxies selected in the compilation using a data assimilation method based on a particle filter. In one simulation, all the 50 proxy-based records are used, while in the other two, only the continental or oceanic proxy-based records constrain the model results. As expected, data assimilation leads to improving the consistency between model results and the reconstructions. In particular, this is achieved in a robust way in all the experiments through a strengthening of the westerlies at the northern midlatitude that warms up northern Europe. Furthermore, the comparison of the LOVECLIM simulations with and without data assimilation has also objectively identified 16 proxy-based paleoclimate records whose reconstructed signal is either incompatible with the signal recorded by some other proxy-based records or with model physics.

2.1 Introduction

The Holocene, our current interglacial, has been the subject of a large number of studies based on reconstructions derived from proxy records (e.g., Bartlein et al., 2011; Davis et al., 2003; Leduc et al., 2010; Marcott et al., 2013; Viau and Gajewski, 2009; Vinther et al., 2009) and on simulations performed with climate models of various complexities (e.g., Braconnot et al., 2007a,b; Claussen et al., 1999; Crucifix, 2008; Renssen et al., 2012; Zhao et al., 2005). The two approaches are complementary (Mock, 2007) as the information inferred from the proxies often serves to validate the climate model results (Braconnot et al., 2012), while the models allow the exploration of the physical processes responsible for the recorded climatic changes.

In particular, the period around 6 kyBP (within this chapter referred to as the mid-Holocene) is a standard period in the Paleoclimate Modelling Intercomparison Project (PMIP) for which boundary conditions have been specified to facilitate the comparison between model results and proxy-based reconstructions (hereafter often referred to as reconstructions, for simplicity). One of the most robust conclusions of those model studies is that the summer of the mid to high latitudes of the Northern Hemisphere is warmer during the mid-Holocene compared to the pre-industrial conditions (Braconnot et al., 2007a). This is consistent with the trends of the regional pollen-based reconstructions of Bartlein et al. (2011) and Davis et al. (2003) for northern Europe and with several other proxy-based records (e.g., Andreev et al., 2003; Clegg et al., 2010; Marcott et al., 2013; Seppä and Birks, 2002, 2001; Vinther et al., 2009).

The model–data comparisons have nonetheless underlined some major differences between reconstructions and simulation results. Brewer et al. (2007b) have highlighted that PMIP2 models are able to capture the large-scale surface temperature patterns over Europe reconstructed from pollen records, but they tend to underestimate the magnitude of the observed changes, which is also in agreement with the conclusion of Braconnot et al. (2007a). Previous studies (e.g., Lohmann et al., 2013; Lorenz et al., 2006; Schneider et al., 2010) have found similar results when analyzing the trends of the Holocene sea surface temperature obtained mainly from alkenone data: data and models are in relatively good agreement regarding the sign of the trend, while the models underestimate the magnitude of the changes. Furthermore, Hargreaves et al. (2013) have shown that, at the local scale, models fail to reproduce the difference between mid-Holocene and pre-industrial temperatures reconstructed by Leduc et al. (2010) for sea surface temperature and Bartlein et al. (2011) for land temperature.

Our goal here is to further investigate the origin of those inconstancies between model results and reconstructions using simulations with data assimilation. Data assimilation evaluates which state of the system is the most consistent with all the sources of information, derived here from a climate model, the forcings and the proxy-based records. By performing different experiments, driven by different subsets of proxy-based records, we plan to identify the ones that are compatible with model physics, the ones that are not, and those that are incompatible with other proxy-based reconstructions.

We focus on the mid-Holocene as this is a well-documented period. LOVECLIM1.2 (Goosse et al., 2010a), a three-dimensional Earth system model of intermediate complexity, is constrained to follow a compilation of 50 air and sea surface temperature reconstructions located in the Northern Hemisphere by means of a particle filter with resampling (Dubinkina et al., 2011). These simulations with data assimilation will be compared with a simulation performed with LOVECLIM without data assimilation and with three GCM (general circulation model) simulations following the PMIP3–CMIP5 framework (Paleoclimate Models Intercomparison Project phase 3 – Coupled Model Intercomparison Project phase 5) in order to assess the dependence of model–data differences on the model selected.

2.2 Methodology

2.2.1 Description of LOVECLIM1.2

LOVECLIM1.2 is based on a simplified representation of the dynamics of the climate system and has a coarse horizontal and vertical resolution that enables low computational requirements. Therefore, the large ensembles of simulations required by data assimilation can be performed at a reasonable cost. This model includes three main components named ECBILT2, CLIO3 and VECODE, which represent the atmosphere, the ocean and the vegetation, respectively. ECBILT2 is a spectral T21 (corresponding to about 5.625° in latitude and longitude) global three-level quasi-geostrophic model (Opsteegh et al., 1998). CLIO3 is an ocean general circulation model coupled to a comprehensive sea ice model (Goosse and Fichefet, 1999). It has a horizontal resolution of $3^\circ \times 3^\circ$ and 20 unequally spaced vertical levels ranging from 10 m near surface to 500 m at 5500 m depth. VECODE is the continental biosphere component that describes the distribution of trees, grass and deserts at the same resolution as ECBILT2 (Brovkin et al., 1997). For a complete description of LOVECLIM1.2 please refer to Goosse et al. (2010a).

2.2.2 Data assimilation method

The results of a simulation performed with a climate model depend on (i) the physics of the climate model, (ii) the initial conditions used to initialize the simulation and (iii) the forcings used to drive the model such as, for instance, the amount of solar radiation received by Earth. Here, in order to obtain an ensemble of simulations that represents possible mid-Holocene climate states, we change only the initial conditions by adding a small noise to the sea surface temperature, while the physics and the forcings are kept unchanged.

Due to the relatively chaotic nature of the climate system, even small perturbations in initial conditions result in trajectories that quickly deviate from each other. These different trajectories are called particles or ensemble members. Starting from different initial conditions and using the LOVECLIM climate model, we propagate 96 particles forward in time for an interval of six months: from December until May and then from July until November, thus with a restart each 1 December and 1 July. This is repeated during 400y. The interval of six months (the assimilation frequency) has been chosen to follow more precisely the seasonal signal embedded in reconstructions as more than 60 % of the selected proxy-based records represent a month or a particular season (mainly winter and summer, the coldest or the hottest month). The amount of 96 particles has been chosen because it provides a satisfactory climate range at an affordable computing cost (Dubinkina et al., 2011; Goosse et al., 2006).

After the propagation step and before another restart, the 96 climate states are evaluated according to their agreement with the air and sea surface temperature reconstructions inferred from proxies. This evaluation is derived from the comparison of a likelihood of each particle estimated as a function of the difference between the climate state of the particle and the proxy-based reconstructions. It is based on the surface air and sea surface temperature anomalies obtained from both the model and proxy-based reconstruction as the difference between mid-Holocene (the period 6 ± 0.5 kyBP) and nearly modern conditions (the period 950–450 yBP). This difference is computed for all the locations and months for which proxy-based reconstructions are available (Table 2.1). For instance, during a "winter" step of data assimilation (when the model is propagated from December until May), one of the proxy-based reconstructions that is taken into account in the computation of the likelihood is the reconstruction number 21 (hereafter N21) for which its mean winter anomaly value is compared to the anomaly of the winter (December–February) sea surface temperature of the corresponding LOVECLIM grid point, while the proxy-based reconstruction N20 is not taken into account at this step because it represents a summer anomaly. As the methodology does not allow taking into account different time resolutions (Mathiot et al., 2013), the annual proxy-based reconstructions are compared to model values twice a year: to the mean value of December–May during a "winter" step of assimilation, and to the mean value of June–November during a "summer" step of assimilation (when the model is propagated from July until November).

The particles that have highest likelihood are retained, while the particles with small likelihood are eliminated. The remaining particles are resampled a number of times proportional to their likelihood so that the total number of particles is kept constant. This resampling step is necessary to avoid a collapse of an ensemble of particles to one single particle. Then, a small perturbation of the surface temperature is added to the initial conditions of the ensemble members and the particles are propagated forward in time for the next 6 months of assimilation using the climate model. For more details about the methodology, which has been applied in several recent studies (e.g., Goosse et al., 2012b; Mathiot et al., 2013), please refer to Dubinkina et al. (2011).

2.2.3 The proxy-based data set

Numerous surface and sea surface temperature reconstructions derived from proxies are available for the Holocene. These reconstructions are derived from marine, continental and ice archives using different methods such as, among others, the alkenone paleothermometry (Grimalt and Lopez, 2007; Herbert, 2003), the modern analog technique (Brewer et al., 2007a) or the stable isotope analysis (Brook, 2007). Each quantitative reconstruction has its strengths and weaknesses (Birks et al., 2010; Juggins, 2013; Telford and Birks, 2005). For instance, almost all of them are influenced by the confounding effects, which means that environmental variables other than the climate variable of interest influence the reconstruction (Birks et al., 2010; Ortiz, 2007). For instance, a summer temperature derived from pollen records could include a signal related to winter temperature or precipitation (Birks et al., 2010). Furthermore, attributing the signal to a particular period of the year is not always straightforward as, for instance, the sedimentary alkenone signal is usually assumed to reflect the annually averaged sea surface temperature, while at high latitudes, the alkenone signal is likely phased to the summer months (Bendle and Rosell-Melé, 2007; Herbert, 2003; Samtleben and Bickert, 1990; Thomsen et al., 1998). In this study, we decided to follow the interpretation proposed in the original studies describing the proxy-based reconstructions. For instance, if the reconstructed signal represents the summer surface air temperature according to the authors of those studies, this is also the case for us.

Table 2.1: Surface air (ST) and sea surface (SST) mid-Holocene temperature proxy-based reconstructions (hereafter in the table, Proxy. recons.) used in the simulations with data assimilation. Winter corresponds to December–February (DJF) and summer to June–August (JJA). The column's name "Temporal interp." stands for Temporal interpretation. The anomalies and their error are in °C.

ID	Lat	Lon	Site or core name	Area	Archive type	Proxy. recons.	Temporal interp.	6 kyr BP ano	Error	Reference
1	61.48	26.07	Laihalampi Lake	Southern Finland	Pollen	ST	Annual	1.86	0.60	Heikkilä and Seppä (2003)
2	69.20	21.47	Toskaljavri Lake	Northern Finland	Pollen	ST	Jul	1.06	0.60	Seppä and Birks (2002)
2'	68.68	22.08	Tsuolbmajavri Lake	Northern Finland	Pollen	ST	Jul	1.14	0.60	Seppä and Birks (2001)
3	55.65	−13.98	Feni Drift	North Atlantic	Alkenone – U_k^{37}	SST	Annual	0.47	0.80	Esparza (2005)
4	40.50	4.03	Minorca	Mediterranean	Alkenone – U_k^{37}	SST	Annual	2.38	0.80	Martrat (2007)
5	43.88	−62.80	OCE326-GGC30	Northwest Atlantic	Alkenone – U_k^{37}	SST	Annual	4.15	0.80	Sachs (2007)
6	43.48	−54.87	OCE326-GGC26	Northwest Atlantic	Alkenone – U_k^{37}	SST	Annual	2.81	0.80	Sachs (2007)
7	37.56	−10.14	MD01-2444	Iberian Margin	Alkenone – U_k^{37}	SST	Annual	0.63	0.80	Martrat et al. (2007)
8	66.60	−17.58	JR51-GC35	Nordic Seas	Alkenone – U_k^{37}	SST	Annual	−1.10	0.80	Bendle and Rosell-Melé (2007)
9	30.85	−10.27	GeoB 6007-02	Northwest Africa	Alkenone – U_k^{37}	SST	Annual	1.02	0.80	Kim et al. (2007)
10	38.63	−9.45	D13882	Iberian Margin	Alkenone – U_k^{37}	SST	Annual	2.27	0.80	Rodrigues et al. (2009)
11	62.09	−17.82	RAPiD-12-1k	Sub-polar North Atlantic	Mg/Ca and $\delta^{18}O$ (bulloides)	SST	May, Jun	−1.12	0.80	Thornalley et al. (2009)
12	60.08	15.83	Stora Gilltjarnen	Sweden	Pollen	ST	Annual	1.01	0.60	Antonsson et al. (2006)
13	60.58	24.08	Lake Arapisto	Finland	Pollen	ST	Annual	3.04	0.60	Sarmaja-Korjonen and Seppä (2007)
14	58.55	13.67	Lake Flarken	Sweden	Pollen	ST	Annual	2.04	0.60	Seppä et al. (2005)
15	66.97	7.63	JM97-948/2A and MD95-2011	Norwegian Sea	Forams (planktic)	SST	Aug	−1.77	0.80	Risebrobakken et al. (2003)

Continued on next page

Table 2.1 – continued from previous page

ID	Lat	Lon	Site or core name	Area	Archive type	Proxy. recons.	Temporal interp.	6 kyr BP ano	Error	Reference
16	74.47	98.63	Levinson-Lessing Lake	Russia	Pollen	ST	Annual	2.06	0.60	Andreev et al. (2003)
17	41.68	−124.93	ODP1019C	North Pacific	Alkenone – U_k^{37}	SST	Annual	−0.84	0.80	Barron et al. (2003)
18	20.75	−18.58	ODP658C	Northwest Africa sea	Forams (planktic)	SST	Aug	−3.05	0.80	deMenocal et al. (2000)
19	20.75	−18.58	ODP658C	Northwest Africa sea	Forams (planktic)	SST	Feb	−1.07	0.80	deMenocal et al. (2000)
20	31.48	128.52	Core B-3GC	Northwestern Pacific Ocean	Forams (planktic)	SST	Summer	−0.54	0.80	Jian et al. (2000)
21	31.48	128.52	Core B-3GC	Northwestern Pacific Ocean	Forams (planktic)	SST	Winter	−1.59	0.80	Jian et al. (2000)
22	66.55	13.92	SG93	Norway (Soylegrotta)	Speleothem	ST	Annual	−0.19	0.80	Lauritzen and Lundberg (1999a)
23	58.58	26.65	Raigastvere Lake	Estonia	Pollen	ST	Annual	2.63	0.60	Seppä and Poska (2004)
24	36.03	141.78	KR02-06 St.A MC/GC and MD01-2421	Northwestern Pacific	Alkenone – U_k^{37}	SST	Summer	2.08	0.80	Isono et al. (2009)
25	20.12	117.38	GIK17940-2	South China Sea	Alkenone – U_k^{37}	SST	Annual	−0.19	0.80	Pelejero et al. (1999)
26	52.78	108.12	Kotokel Lake	Russia	Pollen	ST	Jan	3.30	0.60	Tarasov et al. (2009)
27	52.78	108.12	Kotokel Lake	Russia	Pollen	ST	Jul	−0.07	0.60	Tarasov et al. (2009)
28	80.70	−73.70	Agassiz Ice Cap	Greenland	ice core – $\delta^{18}O$	ST	Annual	2.00	0.40	Vinther et al. (2009)
29	71.27	−26.73	Renland Ice Cap	Greenland	ice core – $\delta^{18}O$	ST	Annual	2.00	0.40	Vinther et al. (2009)
30	50 to 70	−65 to −50	Labrador region	Canada	Pollen	ST	Jan	−2.28	0.60	Viau and Gajewski (2009)
31	50 to 70	−65 to −50	Labrador region	Canada	Pollen	ST	Jul	−0.48	0.60	Viau and Gajewski (2009)
32	50 to 70	−120 to −80	Central Canada region	Canada	Pollen	ST	Jan	0.68	0.60	Viau and Gajewski (2009)
33	50 to 70	−120 to −80	Central Canada region	Canada	Pollen	ST	Jul	0.49	0.60	Viau and Gajewski (2009)
34	50 to 70	−140 to −120	Mackenzie region	Canada	Pollen	ST	Jan	0.46	0.60	Viau and Gajewski (2009)

Continued on next page

Table 2.1 – continued from previous page

ID	Lat	Lon	Site or core name	Area	Archive type	Proxy. recons.	Temporal interp.	6 kyr BP ano	Error	Reference
35	50 to 70	−140 to −120	Mackenzie region	Canada	Pollen	ST	Jul	0.17	0.60	Viau and Gajewski (2009)
36	44.53	145.00	MD01-2412	Okhotsk Sea	Alkenone – U_k^{37}	SST	Autumn	−0.82	0.80	Harada et al. (2006)
37	71.34	−113.78	KR02 lake	Victoria Island (Canada)	Pollen	ST	Jul	0.00	0.60	Peros and Gajewski (2008)
38	55 to 72	−12 to 15	Northwest region	Europe	Pollen	ST	Winter	−0.71	0.60	Davis et al. (2003)
39	55 to 72	−12 to 15	Northwest region	Europe	Pollen	ST	Summer	1.00	0.60	Davis et al. (2003)
40	45 to 55	−12 to 15	Central-west region	Europe	Pollen	ST	Winter	−0.51	0.60	Davis et al. (2003)
41	45 to 55	−12 to 15	Central-west region	Europe	Pollen	ST	Summer	0.47	0.60	Davis et al. (2003)
42	30 to 45	−12 to 15	Southwest region	Europe	Pollen	ST	Winter	−0.98	0.60	Davis et al. (2003)
43	30 to 45	−12 to 15	Southwest region	Europe	Pollen	ST	Summer	−1.49	0.60	Davis et al. (2003)
44	55 to 72	15 to 50	Northeast region	Europe	Pollen	ST	Winter	0.22	0.60	Davis et al. (2003)
45	55 to 72	15 to 50	Northeast region	Europe	Pollen	ST	Summer	0.60	0.60	Davis et al. (2003)
46	45 to 55	15 to 50	Central-east region	Europe	Pollen	ST	Winter	0.24	0.60	Davis et al. (2003)
47	45 to 55	15 to 50	Central-east region	Europe	Pollen	ST	Summer	−0.11	0.60	Davis et al. (2003)
48	30 to 45	15 to 50	Southeast region	Europe	Pollen	ST	Winter	−0.25	0.60	Davis et al. (2003)
49	30 to 45	15 to 50	Southeast region	Europe	Pollen	ST	Summer	−0.66	0.60	Davis et al. (2003)

Our goal is not to include all the available local proxy-based reconstructions. When a choice has to be made, we prefer to use regional-scale reconstructions such as the ones of Davis et al. (2003) and Viau and Gajewski (2009) rather than the individual records that were included in those reconstructions.

The proxy-based reconstruction data set used in the simulations with data assimilation results then from a selection among more than 300 Holocene records according to the following criteria: (i) the record represents the air or sea surface temperature, (ii) comes from archives located between 20 and 90°N, (iii) covers the full mid-Holocene time-slice (6 ± 0.5 kyBP) and the reference period (950–450 yBP) with a resolution of at least 250y, as we work with anomalies related to this period (Sect. 2.2.2). (iv) If multiple reconstructions with different temporal interpretations are located within the same model grid, the seasonal reconstructions are retained, as we consider that they provide more information on the system. On the basis of these criteria, we have selected 50 proxy-based records of air and sea surface temperatures for the mid-Holocene (Table 2.1). For each selected record, an anomaly is calculated between the mean value of the period of interest (6 ± 0.5 kyBP) and the mean value of the reference period (950–450 yBP) (Fig. 2.1). As we perform averages over periods that are longer than the dating uncertainties of the records, we neglect any potential biases related to those dating uncertainties.

Furthermore, if two reconstructions that represent the same physical variable at the same period of the year are located in the same model grid, they are averaged. This is the case for the proxy-based reconstructions N2 and N2′, which are merged under the identifier N2. In the evaluation of the likelihood, we assume that a proxy-based reconstruction represents the climate at the scale of the model grid, except for the reconstructions of Davis et al. (2003) and Viau and Gajewski (2009), which explicitly refer to a larger scale and, therefore, the average over the corresponding region for the model is performed before computing the model–data difference. Therefore, the signal reconstructed from the proxies is representative of a 3° grid box for CLIO3 and a 5.625° grid box for ECBILT2.

Finally, an estimation of the uncertainty for each reconstruction derived from proxies is required for data assimilation. This information is frequently not available, and when it is, these uncertainties are often very large and thus sometimes of the same order as the signal itself (Ohlwein and Wahl, 2011). As in Mathiot et al. (2013), we have thus deliberately selected here lower bounds for those uncertainties in order to provide a strong constraint on the model during the data assimilation process. By simplicity, we have also chosen only one error for each archive type (Table 2.1) based on values provided in previous studies (e.g., Heikkilä and Seppä, 2003; Martrat et al., 2007; Mathiot et al.,

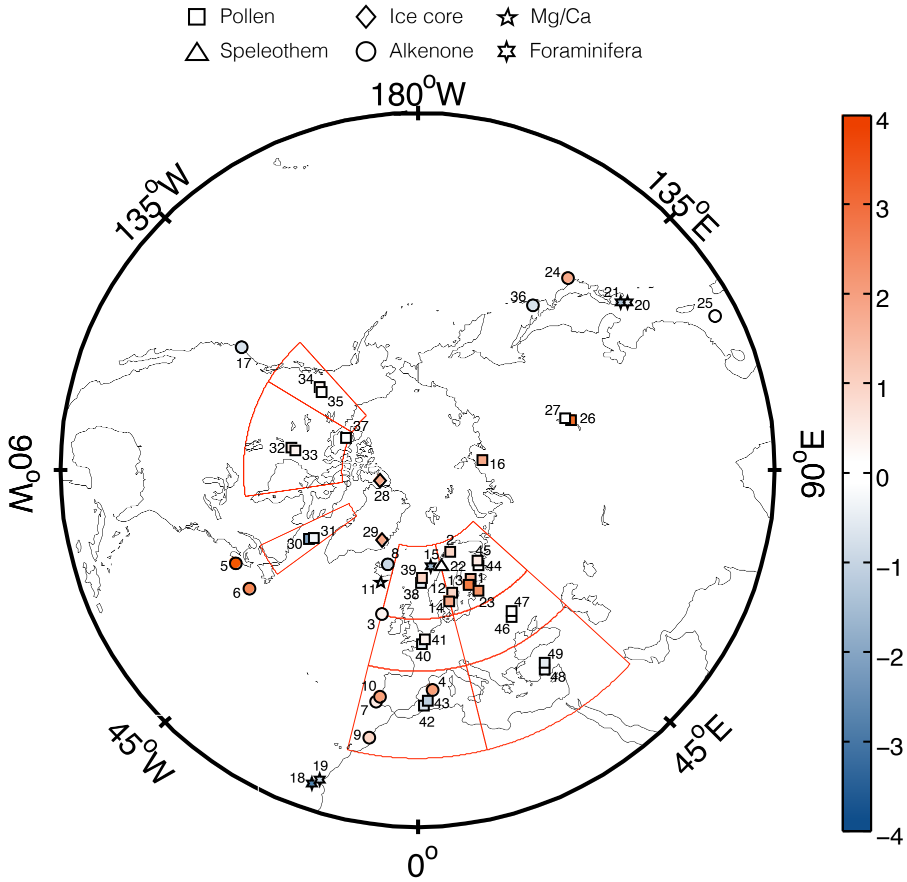

Figure 2.1: Mean air and sea surface temperature anomalies (°C) for all the proxy-based reconstructions selected for the mid-Holocene. Each marker type corresponds to a different proxy-based reconstruction group. Each anomaly represents a month or a particular period (Table 2.1). The red boxes display the areas that correspond to the proxy-based reconstructions of Davis et al. (2003) and Viau and Gajewski (2009). If more than one proxy-based reconstruction is given at the same location, the markers representing the proxy-based reconstructions are slightly shifted for improved readability. The reference period is 950–450 yBP.

2013; Muller et al., 1998; Seppä and Birks, 2001). Those uncertainty values affect weakly the spatial patterns but influence the magnitude of the changes induced by the data assimilation processes (Goosse et al., 2012b). This will be taken into account in the interpretation of our results.

Table 2.2: List of the simulations analyzed in this study.

Model name	Simulation period	Simulation name	Forcing	Data assimilation	Reference
LOVECLIM	reference	LMALL	Crespin et al. (2013)	no	Goosse et al. (2010a)
	mid-Holocene	ALL	this study	yes	
	mid-Holocene	CON	this study	yes	
	mid-Holocene	OCE	this study	yes	
	mid-Holocene	NODATA	this study	no	
MPI-ESM-P	reference	past 1000	PMIP3	no	Raddatz et al. (2007);
	mid-Holocene	mid-Holocene	PMIP3	no	Marsland et al. (2003)
CSIRO-Mk3L-1-2	reference	past 1000	PMIP3	no	Phipps et al. (2011)
	mid-Holocene	mid-Holocene	PMIP3	no	
BCC-CSM1-1	reference	past 1000	PMIP3	no	`http://bcc.cma.gov.cn/`
	mid-Holocene	mid-Holocene	PMIP3	no	`bcccsm/web/?ChannelID=43`

2.2.4 Experimental design

Three mid-Holocene simulations with data assimilation are performed and compared to a mid-Holocene reference simulation conducted with LOVECLIM, named NODATA (Table 2.2). In two simulations either the continental or oceanic proxy-based reconstructions are assimilated and in, one simulation, these proxy-based reconstructions are assimilated together. They are named CON, OCE and ALL, respectively. The objective is to propose two extreme cases in which we either constrain the model by only the continental reconstructions or by only the signal inferred from oceanic ones in order to identify the information brought by each subset as well as the compatibility between model physics and the proxy-based reconstructions, and between the proxy-based reconstructions themselves. In addition, a simulation spanning the reference period (950–450 yBP) is required as the likelihood in the data-assimilation process compares proxy-based reconstruction anomalies with modeled anomalies (Sect. 2.2.2). This simulation is driven by both natural and anthropogenic forcings as in Crespin et al. (2013).

We also analyze simulations performed with GCMs to allow the comparison of the LOVECLIM results with the ones from three state-of-the-art models: BCC-CSM1-1, CSIRO-Mk3L-1-2 and MPI-ESM-P. For details about these models, please refer to the references listed in Table 2.2. These models were chosen because, at the time of our analysis, they were the only ones on the CMIP5 data portal that provided the variables needed for our diagnostics over the period 950–450 yBP and the mid-Holocene.

The four mid-Holocene simulations performed with LOVECLIM are either 200 (NODATA) or 400 year long (ALL, CON and OCE). The length of the simulation NODATA is smaller because it is the prolongation of an equilibrium simulation in the same conditions. The four simulations are driven by the same constant forcings as done in Mathiot et al. (2013). The orbital parameters follow Berger (1978). The greenhouse gas concentrations are based on the data of Flückiger et al. (2002). The Laurentide Ice Sheet topography and surface albedo have been adapted for LOVECLIM by Renssen et al. (2009) from the reconstruction of Peltier (2004). In comparison to the present, the changes in topography and surface albedo are extremely small. As in Mathiot et al. (2013) small freshwater fluxes (26 mSv) coming from the Antarctic Ice Sheet are added in the Amundsen, the Bellingshausen and the west part of Weddell Sea, based on Pollard and DeConto (2009). For the Northern Hemisphere, there are no freshwater fluxes resulting from the melt of the Laurentide Ice Sheet for this period (as in Renssen et al., 2009). This design is slightly different from the PMIP3 protocol used in GCMs as the latter assumed a similar ice sheet topography as the present one and no additional freshwater fluxes from ice sheet melting. But this has only a very marginal effect on our results at 6 kyBP.

2.3 Results and discussion

2.3.1 Simulations without data assimilation

The climate anomalies simulated by LOVECLIM and the selected GCMs for mid-Holocene conditions display similar large-scale patterns (Fig. 2.2) and are consistent with previous modeling studies (e.g., Braconnot et al., 2007a). They all depict warmer air and sea surface temperatures during the mid-Holocene summer and cooler air surface temperatures during winter, except in the Arctic. The mid-Holocene seasonal cycle amplitude is then more pronounced than the one of the reference period for most of the locations in the Northern Hemisphere. This signal is mainly caused by the higher (lower) summer (winter) insolation for mid-Holocene (Braconnot et al., 2007a; Wanner et al., 2008). The winter Arctic warming is due to a memory effect associated with the summer insolation as the latter induces a decrease in ice thickness, which leads to larger oceanic heat fluxes during autumn and winter, and then to a surface temperature increase during these seasons (Renssen et al., 2005).

In comparison with the first half of the last millennium, the westerlies are slightly weakened during the mid-Holocene in LOVECLIM during winter (Fig. 2.3). This appears consistent with a smaller meridional gradient in temperature due to the Arctic warming and leads to a tendency towards a more negative NAO state in the model for that period. BCC-CSM1-1 also shows a weakening of the westerlies in the Pacific during the mid-Holocene, while MPI-ESM-P and CSIRO-Mk3L-1-2 show a slight strengthening. These results are consistent with an analysis of PMIP2 simulations performed by Gladstone et al. (2005) showing that many models display anomalies similar to either positive or negative NAO phases during the mid-Holocene compared

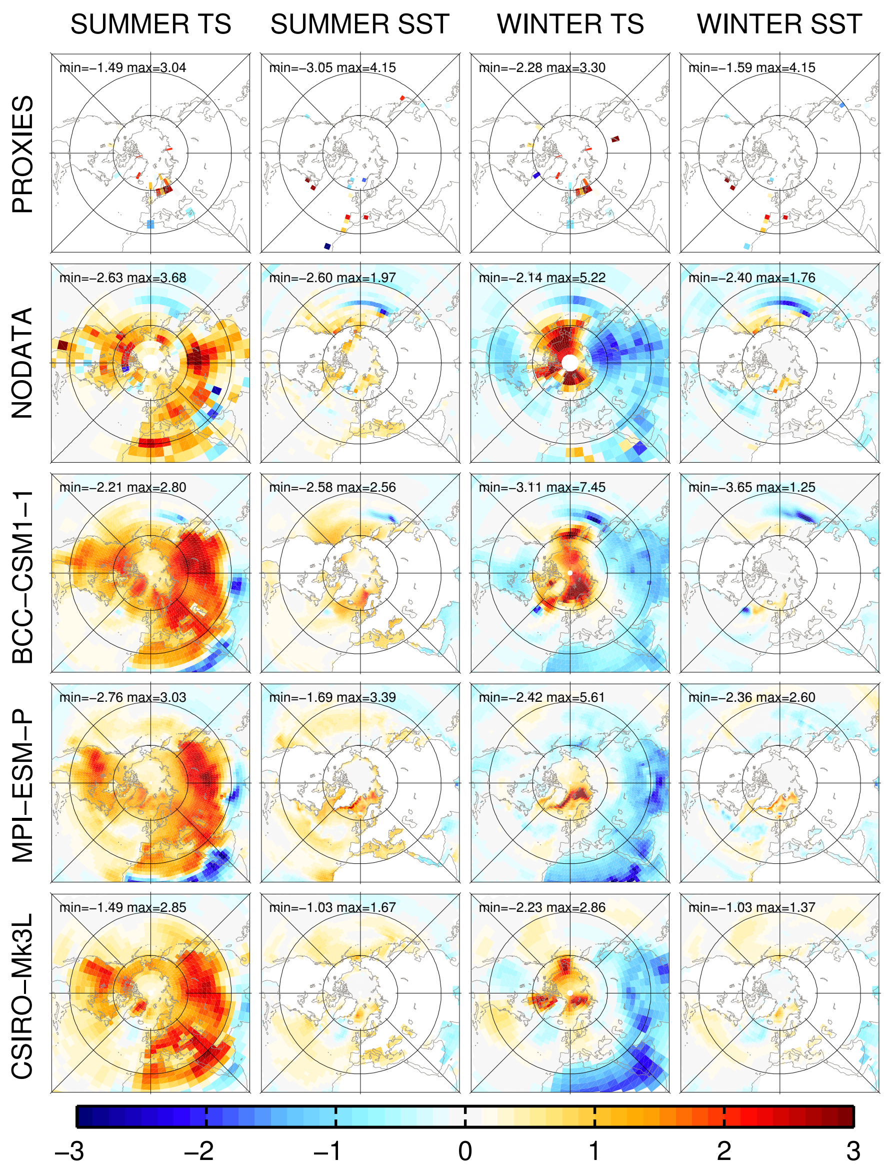

Figure 2.2: Mid-Holocene air (ST) and sea (SST) surface temperature anomalies (°C) for the proxy-based reconstructions, LOVECLIM without data assimilation (NODATA) and the GCMs. Winter corresponds to December–February (DJF) and summer to June–August (JJA). The reference period is 950–450 yBP.

to present day but without a clear and robust signal common between the different models.

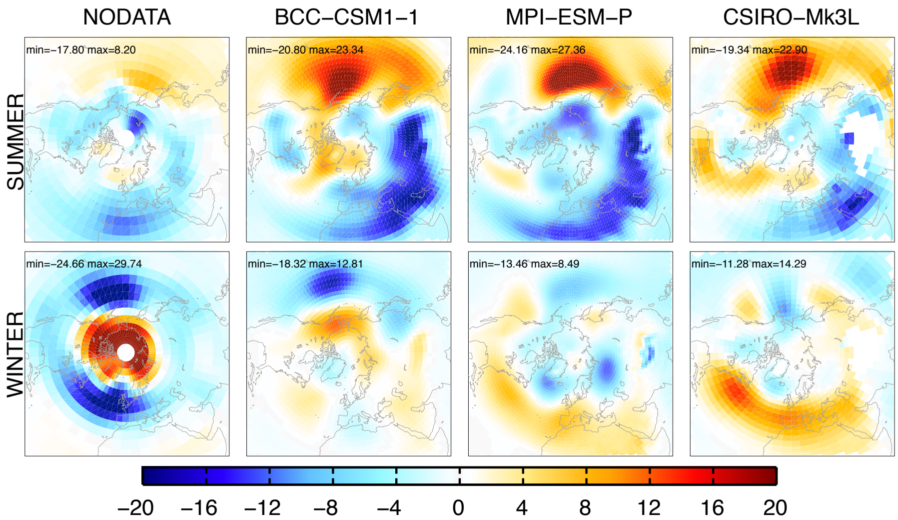

Figure 2.3: Mid-Holocene geopotential height anomalies (in m) at 800 hPa for LOVECLIM without data assimilation (NODATA) and at 850 hPa for the GCMs. Winter corresponds to DJF and summer to JJA. The reference period is 950–450 yBP.

The mid-Holocene reconstruction based on proxies (Fig. 2.2) depicts a less homogeneous pattern than the modeled one. The Arctic and northern Europe surface air temperatures are warmer during the summer and the winter, which is in agreement with model results, while the Norwegian sea surface temperature is colder in the selected proxy-based reconstruction for the same seasons, in contrast to model results. Risebrobakken et al. (2003) argue that this reconstructed cooling in the Norwegian Sea may rather represent a subsurface signal, explaining the discrepancy with other estimates of surface temperature in the region. Over Europe, the northern part is warmer during the mid-Holocene and the southern one is colder all year long in the proxy-based reconstructions. Those changes are relatively consistent with the simulation results in winter, although the signal at high latitudes appears underestimated in many models, but no model is able to reproduce a cooling in summer over southern Europe. In the western North Atlantic, the reconstructed sea surface temperatures are warmer, which is consistent in summer but not with the winter signal simulated by LOVECLIM and BCC-CSM1-1. In North America, surface temperature is slightly warmer in the reconstructions over the western part, while it is colder over the eastern part, a signal that appears thus weaker than the one simulated by models.

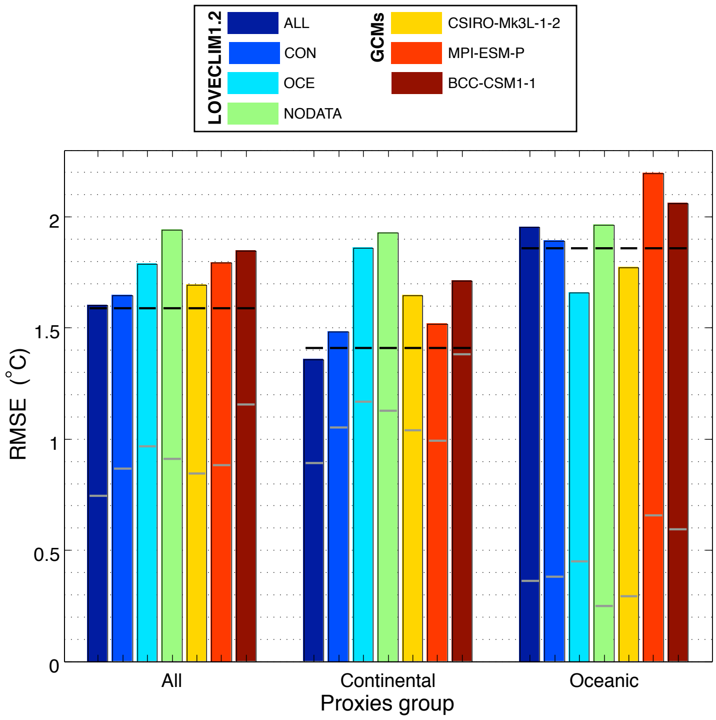

Figure 2.4: From left to right: RMSE between the mid-Holocene anomalies of each simulation (LOVECLIM with and without data assimilation and the GCMs) and the proxy-based reconstruction anomalies for three groups of proxy-based reconstructions: all the proxy-based reconstructions, the continental proxy-based reconstructions only and the oceanic proxy-based reconstructions only. The mean mid-Holocene signal (estimated as the standard deviation of the anomalies) for the proxy-based reconstructions and the model are the black and the grey horizontal bars, respectively.

A more quantitative model–data comparison shows that the magnitude of the signal (estimated here by the standard deviation of the anomalies) is much weaker in models, with a mean value of 0.9 °C, than in reconstructions based on proxies, which reach a value of 1.6 °C (Fig. 2.4). The difference is seen both for continental and oceanic proxy-based reconstructions, but is more marked over the ocean where the signal in the proxy-based reconstructions is 4.5 times greater than one of models, a result consistent with the recent findings of Lohmann et al. (2013). According to Fig. 2.4, the mean signal recorded by the selected proxies is larger over the ocean that over land by about 0.5 °C. This might appear surprising as the oceanic response to many forcings is expected to be smaller than the one over continents because of the larger thermal inertia

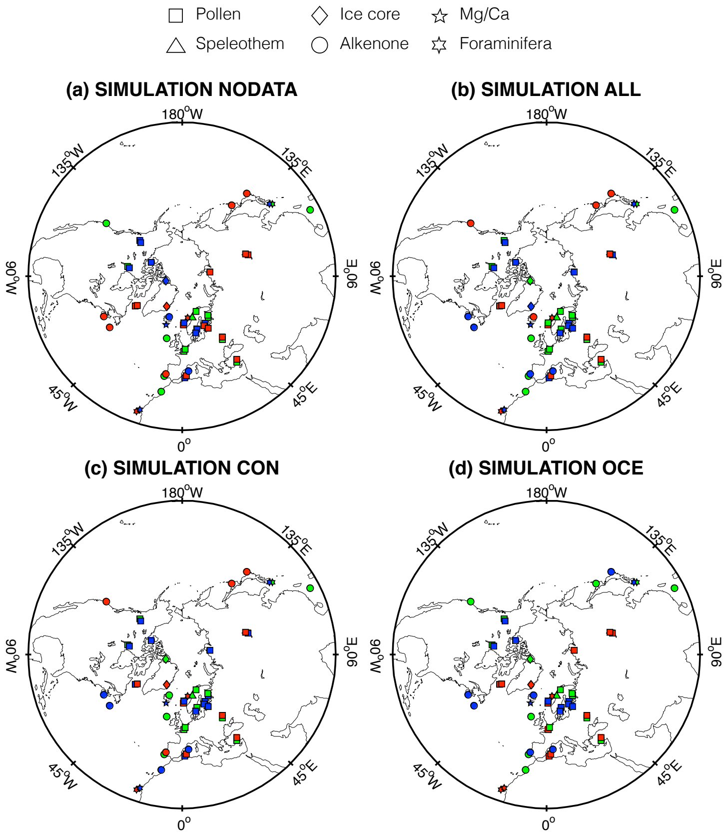

Figure 2.5: Agreement between the mid-Holocene surface air and sea surface temperature anomalies in LOVECLIM and in the proxy-based reconstructions. Each marker type corresponds to a different proxy-based reconstruction group. It is in green when the model agrees with the proxy-based reconstruction record within the error bars; in blue, when the model agrees only with the sign of the anomaly; in red, when the model does not agree on the sign of the anomaly. If more than one proxy-based reconstruction is given at the same location, the markers representing the proxy-based reconstructions are slightly shifted for improved readability.

of the ocean and of various feedbacks (e.g., Boer, 2011; Joshi et al., 2013). Investigating this issue in detail is out of the scope of this study, but it might be related to the too small number of proxy-based reconstructions used here to estimate precisely the mean over oceans and continents or to the location of oceanic proxy-based reconstructions that represent relatively local–regional phenomena in coastal areas or close to fronts and thus not the mean open ocean conditions.

Additional information on the local agreement between model results and proxy-based reconstructions can be obtained by computing the root mean square error (RMSE) defined as

$$\mathrm{RMSE} = \sqrt{\frac{\sum_{i=1}^{n} \left(\Delta T_i^{\mathrm{mod}} - \Delta T_i^{\mathrm{obs}}\right)^2}{n}} \tag{2.1}$$

where n is the number of proxy-based reconstructions, $\Delta T_i^{\mathrm{obs}}$ is one particular mid-Holocene air or sea surface temperature anomaly derived from a proxy-based reconstruction and $\Delta T_i^{\mathrm{mod}}$ is the corresponding modeled value. The minimum RMSE value for the different models is 1.7 °C (Fig. 2.4). This is larger than the mean signal, showing that the models have nearly no skill at the local scale as discussed in Hargreaves et al. (2013). Furthermore, the RMSE is larger for the oceanic proxy-based reconstructions than for continental proxy-based reconstructions in all the models. Actually, the models' results are in much better agreement between themselves than with the proxy-based reconstructions as the root mean square difference between different models, at locations for which proxy-based reconstructions are available, is close to 0.6 °C on average (i.e., about a third of the RMSE shown in Fig. 2.4).

Nevertheless, this quantitative evaluation of model performance based on results at the grid scale could be considered as a too-strong test on several aspects. First, it does not take into account proxy-based reconstruction uncertainties. Second, any small spatial shift in the model response compared to data would lead to large errors (e.g., Guiot et al., 1999). Third, model results and proxy-based reconstructions do not necessarily represent the climate at the same scale, leading to differences in the recorded signal, in particular on its magnitude. As a consequence, we have divided in Fig. 2.5a all the proxy-based reconstructions into three categories: (i) LOVECLIM agrees with the reconstructions with error bars, (ii) LOVECLIM agrees only with the sign of the reconstruction anomaly, and (iii) it does not agree with the sign of the reconstruction anomaly. This is displayed for the LOVECLIM model, but the results are similar for the three GCMs (not shown). As this analysis is much less strict since it is less influenced by the magnitude of the anomaly, it leads to much more encouraging results than the conclusions derived from the analysis of the RMSE: the LOVECLIM mid-Holocene simulation agrees with the sign of the anomaly of about two thirds of the proxy-based reconstructions (see the blue and the green markers in Fig. 2.5a). This agreement displays no clear dependence on the season, on the location of the reconstructions or on the type of the proxy-based reconstructions and no dominant spatial pattern can be defined from Fig. 2.5a.

2.3.2 Simulations with data assimilation

Although the results of simulations constrained by data assimilation will be presented in a quantitative way, our interpretation will often be more qualitative for the two following reasons. First, as mentioned in the methodology section, the proxy-based reconstruction uncertainty selected here has a potential influence on the amplitude of the difference between the simulations with and without data assimilation. Second, the disagreement between LOVECLIM without data assimilation and proxy-based reconstructions is large. Although some improvements are due to data assimilation, the obtained model state is still not fully consistent with all the proxy-based reconstructions. This would require including additional control parameters in the data assimilation process, for instance perturbation of some model parameters, or alternative estimates of the uncertainty of the proxy-based reconstructions. This specific experimental design is out of the scope of this paper, as we would like to focus, in this first study of the mid-Holocene climate, on an estimate of compatibilities between models and proxy-based reconstructions using the standard model configuration and interpretation of the proxy-based reconstructions.

By construction, the data assimilation method applied in LOVECLIM for the mid-Holocene period provides with results that are locally more consistent with the proxy-based reconstructions that are assimilated than with any other simulation performed without data assimilation selected in this study (Fig. 2.4). Indeed, the simulation constrained by all the proxy-based reconstructions displays a RMSE of 1.6 °C, which is 15 % closer to the proxy-based reconstruction anomalies compared to the model without data assimilation. The RMSE between this simulation and the reconstructions is thus of the same magnitude as the mean signal of the proxy-based reconstructions from the mid-Holocene (1.6 °C). The assimilation of the continental reconstructions alone gives a RMSE of 1.5 °C, which corresponds to model results that are 22 % closer to the proxy-based reconstructions that are assimilated compared to the model results without data assimilation. Finally, the data assimilation of the oceanic proxy-based reconstructions alone provides results that are 15 % closer to those oceanic proxy-based reconstructions, inducing almost a doubling of the simulated oceanic signal compared to the simulation without data assimilation.

Figure 2.4 shows also that the assimilation process in ALL leads LOVECLIM to be more consistent with the continental proxy-based reconstructions than with the oceanic ones, which is due to the combination of two effects. First, the estimated error of the continental proxy-based reconstructions is smaller than the oceanic proxy-based records error (Table 2.1), which means that in the computation of the likelihood a larger weight is given to the continental archives. Second, the model's atmospheric fields and the surface temperature

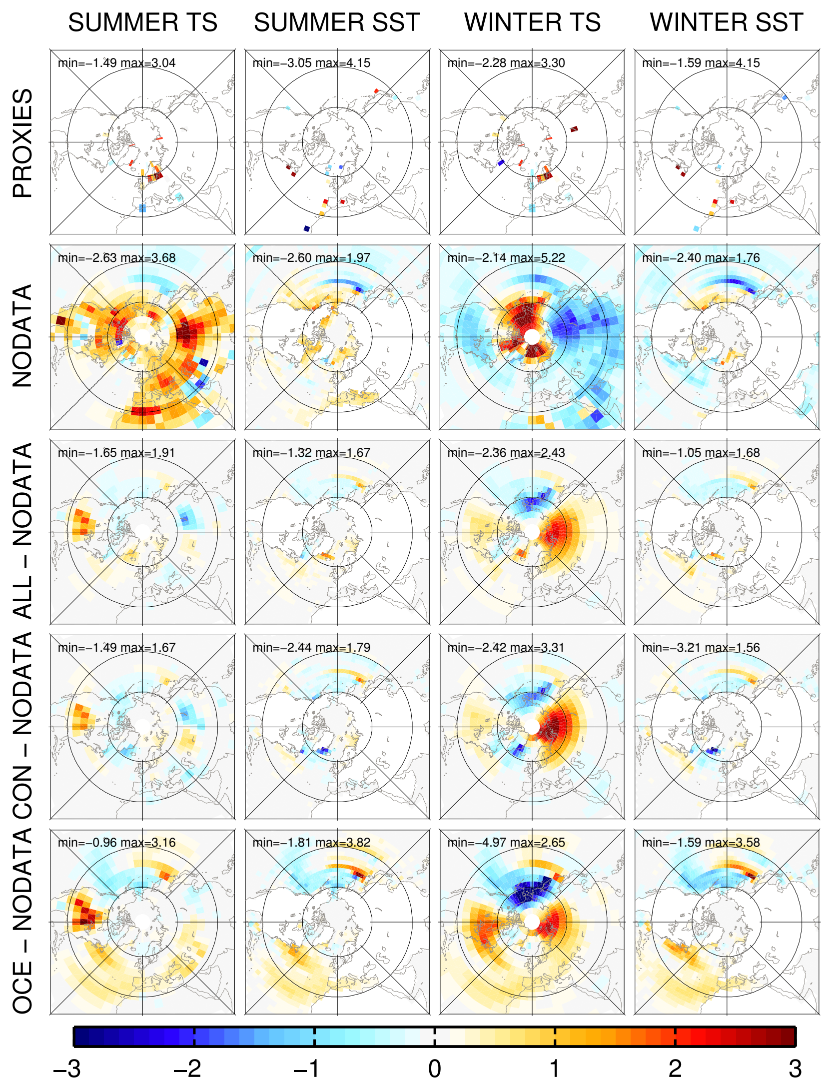

Figure 2.6: Mid-Holocene air and sea surface temperature anomalies (°C) for the proxy-based reconstructions and the LOVECLIM simulation performed without data assimilation (NODATA). The reference period is 950–450 yBP. Differences between the three simulations performed with data assimilation (ALL, CON and OCE) and the simulation NODATA (°C). Winter corresponds to DJF and summer to JJA.

over land have a greater variance than the oceanic ones. Among the ensemble of simulations, it is thus more common to have members that are in agreement with continental proxy-based reconstructions. This leads to a larger impact from the continental proxy-based reconstructions if both domains are assimilated together and to strong similarities between the simulation constrained by all the proxy-based reconstructions and the one that is based on the continental proxy-based reconstructions only.

Although data assimilation only marginally reduces the RMSE between model and reconstructions, the amount of proxy-based reconstructions for which LOVECLIM does not agree with the sign of the anomalies decreases by about 20 % in OCE and about 30 % in CON and ALL compared to NODATA (Fig. 2.5). This is mainly caused in CON and ALL by a slight summer warming over northeastern Europe, the Barents Sea and the Kara Sea and by a summer cooling around Lake Baikal as well as by a winter warming from northeastern Europe to Lake Baikal, over the north of Greenland and over the central part of North America (Fig. 2.6). In these simulations, the improvement of sea surface temperature is mainly related to a warming along the coast of North America at about 40°N. In the simulation OCE, the higher number of proxy-based reconstructions that have the same anomalies as the model is mainly due to an annual warming of the North Atlantic and a summer warming in the North Pacific close to the west coast at 45°N (Fig. 2.6). Consequently, data assimilation drives the LOVECLIM model to a state that is maybe still not in the range of the anomalies derived from the proxies but that is at least more consistent with the sign of their changes.

The three experiments with data assimilation also allow us to test the influence of the data assimilation over the different domains (continent and ocean) on all the proxy-based reconstructions by grouping them in three categories (Fig. 2.7), but on different basis compared to Fig. 2.5. The first category consists in the proxy-based reconstructions for which LOVECLIM results without data assimilation were already consistent with the reconstructed signal, i.e., the difference between model results and proxy-based reconstructions is smaller than the error assigned here. Moreover, assimilation of these proxy-based reconstructions does not deteriorate the consistency between the model results with data assimilation and the signal recorded by the proxy. This category concerns 22 % of all the proxy-based reconstructions used in this study. These reconstructions can be identified individually on the basis of the numbers in Fig. 2.1, using Table 2.1. The second category (45 % of all the proxy-based reconstructions) deals with the reconstructions that satisfy the two following criteria: (i) at least in one of the two simulations performed with data assimilation, in which these proxy-based reconstructions are used, they are more consistent with the results with data assimilation than with the results without data assimilation. (ii) These proxy-based reconstructions are not less consistent with the results with data assimilation than with the results without data assimilation if they do

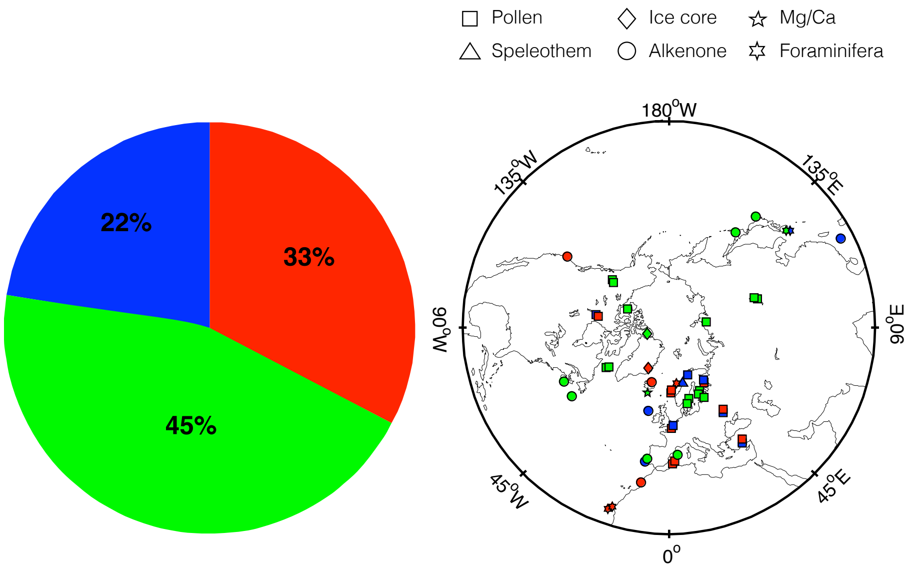

Figure 2.7: Percentage and location of mid-Holocene proxy-based reconstructions for which (i) the modeled anomalies without data assimilation and in the three simulations with data assimilation are always within the estimated uncertainty of a particular proxy-based reconstruction (in blue); (ii) the modeled anomaly of at least one simulation with data assimilation is more consistent with the proxy-based reconstruction at the same location if it is assimilated and is not less consistent in the other simulations with data assimilation (in green); (iii) at least one of the three simulations with data assimilation is less consistent with the proxy-based reconstructions than the simulation without data assimilation or that no improvement is brought when they are assimilated (in red). On the map, if more than one proxy-based reconstruction is given at the same location, the markers representing those reconstructions are slightly shifted for improved readability. Each marker type corresponds to a different proxy-based reconstruction group.

not comply with the first rule. This corresponds to all the continental (oceanic) proxy-based reconstructions for which the anomaly difference in absolute value decreases by at least 5 % in ALL and/or CON (ALL and/or OCE) and does not increase by more than 5 % in the other(s) simulation(s) with data assimilation. For 66 % of the proxy-based reconstructions included in this category (28 % of all the reconstructions), the anomalies in the three simulations with data assimilation are closer to the proxy-based reconstruction anomaly than in the model without data assimilation. This implies that the model dynamics is able to propagate the signal brought by the assimilated proxy-based reconstructions towards the locations where no data is assimilated and also that the information brought by this 28 % of reconstructions is coherent. The third category (33 % of all the proxy-based reconstructions) includes the reconstructions that are either (i) less consistent (5 % threshold) in at least one of the three simulations with data assimilation compared with the simulation without data assimilation, or that are (ii) not more consistent with any simulation with data assimilation than with the simulation without data assimilation. In the majority of the cases (70 % of the proxy-based reconstructions of this category), this corresponds to reconstructions on land (ocean) whose differences with model results are larger in OCE (CON) than in NODATA. As a consequence, the model dynamics suggests an incompatibility between the signal reconstructed from the different types of proxies as improving one realm (land or ocean) deteriorates the results in the other one. This could be due to several processes such as a bias in the teleconnections simulated by the models, in the interpretation of the signal recorded by the proxy, in the way models and proxy-based reconstructions are compared. Our experimental design does not allow us to determine which of those is dominant for each proxy-based reconstruction but it indicates that a special attention has to be given to those regions to understand the causes of this disagreement. This is the case, for instance, for the continental proxy-based reconstruction N42 whose signal is opposite to the one depicted by the oceanic proxy-based reconstructions N4, N7, N9 and N10. Another example is the oceanic proxy-based reconstruction N15 whose signal shows a summer negative anomaly opposite (i) to the positive one illustrated by the nearby continental proxy-based reconstructions and (ii) to the alkenone-based sea surface temperature reconstruction derived from the same core, which depicts a positive anomaly (Calvo et al., 2002). This incompatibility consolidates the interpretation of Risebrobakken et al. (2003) that this proxy-based reconstruction should not be considered as an estimate of surface temperature. Finally, the proxy-based reconstructions that are never more consistent with the simulations performed with data assimilation, indicate a profound disagreement between their information and the model physics. For instance, the model is not able to reproduce the summer (winter) cooling over southwestern (northwestern) Europe depicted by the proxy-based reconstructions N43 (N38) with data assimilation as already mentioned for LOVECLIM and the GCMs without data assimilation.

The improvement brought by data assimilation can be related to modifications of both winds and ocean currents. The atmospheric circulation changes associated with data assimilations in ALL, CON and OCE have a lower magnitude than the one in response to the forcings in NODATA for the summer, while for the winter, these changes are at least of the same magnitude as the model response to forcings (Fig. 2.8). All the experiments constrained by data assimilation display a decrease in geopotential height at high latitudes and an increase at midlatitudes in winter compared to NODATA, the signal in summer being weaker. This strengthens the westerlies over the North Atlantic inducing a winter warming from northern Europe to Lake Baikal as well as over North America (Fig. 2.6). This is consistent with the findings of Rimbu et al. (2003), who indicate, using alkenone data, that the NAO was more likely in a positive pattern phase during the mid-Holocene with respect to our reference period. The induced surface temperature changes are more pronounced during winter since, during these months, the atmospheric circulation endures the stronger changes. Furthermore, changes in atmospheric circulation are stronger in the OCE simulation than in the simulations ALL and CON (Fig. 2.8). This induces stronger westerlies over the Pacific and, therefore, a stronger warming over North America (Fig. 2.6). In winter the pattern over the North Atlantic is more complex in OCE than in the other experiments, with stronger westerlies northward of 50°N and weaker ones between 40 and 50°N.

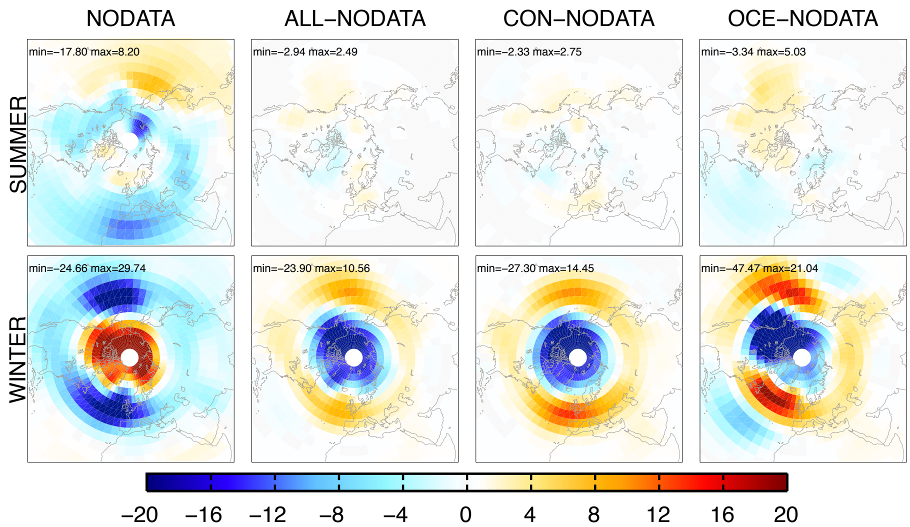

Figure 2.8: Mid-Holocene geopotential height anomalies at 800 hPa (in m) for the simulation NODATA. The reference period is 950–450 yBP. Difference between the three simulations performed with data assimilation (ALL, CON and OCE) and the simulation NODATA. Winter corresponds to DJF and summer to JJA.

The spatial structure of the changes in annual mean sea surface temperature and surface current between each simulation performed with data assimilation and the simulation NODATA are similar, both in the North Atlantic and the North Pacific. Therefore, the figures are shown only for ALL (Fig. 2.9). In the Pacific, the strengthening of the westerlies produces an intensification of the northern branch of the North Pacific Gyre, which is stronger on the eastern part compared to the western part. This tends (i) to transport the warmer water from the northern extension of the Kuroshio eastward (around 45°N).

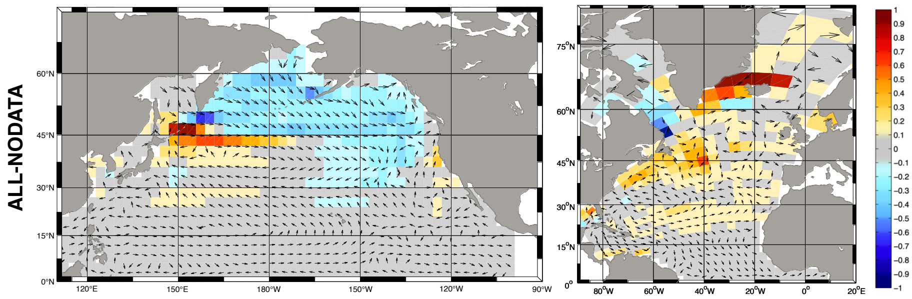

Figure 2.9: Mean annual mid-Holocene differences of sea surface temperature (°C) and surface oceanic current for the Pacific and the Atlantic Oceans between the simulations ALL and NODATA. The size of the arrows is not proportional to their velocity in order to improve the readability of the maps since the objective is to show the current direction and not its strength.

It leads to warmer sea surface temperature and a warming of the atmosphere by the ocean. (ii) This also transports the colder western and northern Pacific water (cooled by the Siberian winds) toward the warmer eastern Pacific following the gyre cycle. The pattern is most marked in the simulation OCE than in the other two (Fig. 2.6) as the westerlies are more intensified in this simulation. Additionally, the northward shift of the westerlies slows down the winds around 30°N in the western Pacific, which induces a reduced heat loss by evaporation and, therefore, a warmer sea surface temperature at this location. These two processes occur also in the Atlantic Ocean. The first is associated with an intensification of the Gulf Stream current at around 40°N due to stronger winds at this location (Fig. 2.8), which leads to a warming of the western Atlantic between 40 and 50°N. The second one leads to a warming of the Atlantic between 20 and 30°N induced by weaker winds. Finally, around 65°N, a localized warming results from a shift of the sea ice front. This feature is not robust as it is not present in all our experiments. The meridional overturning circulation is also slightly stronger in the Atlantic in the simulations with data assimilation compared to NODATA. The difference between the maximum in ALL-CON-OCE and the maximum in NODATA is, however, smaller than 1 Sv, which corresponds to an increase of between 2 (5 TW) and 8 % (18 TW) in the meridional heat transport at 30°S compared to the mean value in NODATA, contributing to some extent to the large-scale warming of the North Atlantic.

2.4 Conclusions

The conclusions derived from our analysis of simulations performed with GCMs and with LOVECLIM with and without data assimilation for the mid-Holocene can be summarized as follows.

1. In agreement with previous studies, a direct evaluation of the mean error of mid-Holocene simulations performed without data assimilation suggests that models have nearly no skill at the local scale compared to proxy-based reconstructions and that the models agree much better between themselves than with proxy-based reconstructions. A comparison of the dominant patterns and of the sign of the changes, taking into account the uncertainties in proxy-based reconstructions, leads to a much better consistency between models and data although clear disagreements remain in some regions.

2. The simulations with data assimilation are more consistent with the sign of the proxy-based reconstruction anomalies and the spatial pattern of the changes than the simulation without data assimilation.

3. However, for a third of the proxy-based reconstructions, data assimilation does not bring any improvement to the agreement with proxy-based reconstructions. For some reconstructions, this is due to a fundamental inconsistency with model physics, but for the majority of the proxy-based reconstructions in this case, this is due to an incompatibility between the various proxy-based reconstructions according to the model physics; i.e., the model is not able to follow the signal recorded in all of them simultaneously. One clear strength of our methodology is to identify objectively those proxy-based reconstructions.

4. The methodology has also allowed identifying the mechanisms that lead to a better consistency between the model results and the proxy-based reconstructions. The dominant one, which is robust in all our experiments, is the strengthening of the westerlies at midlatitudes that warm up northern Europe.

5. The LOVECLIM physics is not compatible with the 6 kyBP summer temperature gradient obtained in the pollen-based surface temperature reconstructions of Davis et al. (2003), which indicates a colder southern Europe and a warmer northern Europe (Fig. 2.6). The problem is mainly in southern Europe which is always warmer in LOVECLIM at 6 kyBP than over the past millennium because of the stronger insolation. This result is in agreement with others proxy-based reconstructions (Martrat, 2007; Martrat et al., 2007; Rodrigues et al., 2009) and raises questions

about the valitidy of the results of Davis et al. (2003) concerning the summer southern Europe surface temperature at 6 kyBP.

6. In order to gain more information on the origin of the incompatibilities between some reconstructions suggested by our experiments, it would be instructice to perform data assimilation separately for the surface temperature derived from Alkenones and the ones derived from other marine proxies.

CHAPTER 3

The impact of the volcanism on the Holocene climate

The volcanism is known to be one of the main natural climate forcings at annual to centennial timescales. As a consequence, this forcing is crucial to study the Holocene climate variability. To date, such an analysis has never been performed, because of the lack of an adequate forcing. Here the beta-version of a forcing obtained in the framework of Past4Future is implemented in the model LOVECLIM, and two Holocene simulations are performed: one that is driven by the volcanic forcing and one that is not. This study demonstrates that the volcanic forcing indeed influences the climate on yearly to multi-decadal time-scale, and that in theory it can therefore be used to explain some rapid fluctuations that are recorded by proxies. Nevertheless, our results are still very preliminary since we also have shown that the forcing is not realistic at this stage, mainly because of an overestimation of large eruptions when the methods applied currently for the last millenium are used over the whole Holocene.

3.1 Introduction

This chapter and the next one have been developped in parrallel and are connected by a common goal: studying the centennial and multi-centennial fluctuations that are superimposed on the long-term trends over the Holocene. Since the volcanism is known to be one of the main natural climate forcings at annual to centennial timescales, investigating its impact over the Holocene appears justified. Such an analysis has never been performed before, because of the lack of an adequate forcing. To date, Gao et al. (2008) have published the longest reconstruction of the past volcanic activities, i.e. covering the last 1500 years. This reconstruction has been widely used by the PMIP3 community to model the climate of the last millennium (Schmidt et al., 2012). In the present context, to study the impact of the volcanism on the Holocene with LOVECLIM, we have used the beta-version of a forcing that have been obtained in the framework of Past4Future and covers the last 10 kyBP.

This chapter is organised as follows. First, this introduction provides a brief overview of the link between volcanism and climate and how the past volcanism activity can be retrieved. Second, the section 3.2 describes how the forcing provided by Past4Future has been adapted into a forcing that can be used by LOVECLIM. Third, the objective of section 3.3 is to compare two Holocene simulations realized with LOVECLIM. One is driven by the volcanic forcing while the other is not. This section investigates the impact of the volcanism on the Holocene climate which is the objective of this chapter. Finally, the main findings of this study are summed up in the conclusion.

The links between climate and volcanism have been widely studied for a number of years now (e.g. Robock, 2000; Goosse and Renssen, 2004; Schmidt et al., 2004a; Jones et al., 2005; Robock et al., 2009; Schneider et al., 2009; Timmreck et al., 2010; McGregor and Timmermann, 2011; Driscoll et al., 2012; Zanchettin et al., 2013). In 2000, Alan Robock published one of the most complete review concerning volcanic eruptions and their impact on climate, which is the basis of the following description.

A volcanic eruption ejects magmatic material and emits gases (see Fig. 3.1). The magmatic material is solid or solidifies into large particles, called ash. Ash falls out of the atmosphere quickly; therefore, its impact on climate is limited. The principal emitted gases are H_2O, N_2 and CO_2. Although they are greenhouse gases, H_2O and CO_2 emitted by a single eruption do not have a significant impact on the radiative balance of the Earth, as their atmospheric concentrations are already large before the eruption and the quantities added by the eruption do not modify significantly this concentration.

The impact of the eruption on climate is mainly due to the injection of sulfur gases (SO_2). The SO_2 reacts with OH and H_2O to form H_2SO_4, the sulfuric acid. After several weeks, this process results in the formation of a cloud of H_2SO_4 aerosols. A cloud can be formed in the stratosphere or in the troposphere, depending on whether it is an explosive eruption or a quiescent eruption. The cloud e-folding decay time is the amount of time required to decrease the initial concentration of H_2SO_4 to e^{-1} of its initial value. Whether the cloud is formed in the troposphere or the stratosphere, its e-folding time will be respectively about 1 to 3 weeks or 1 to 3 years. The smaller the e-folding and the less time the cloud will affect the global climate.

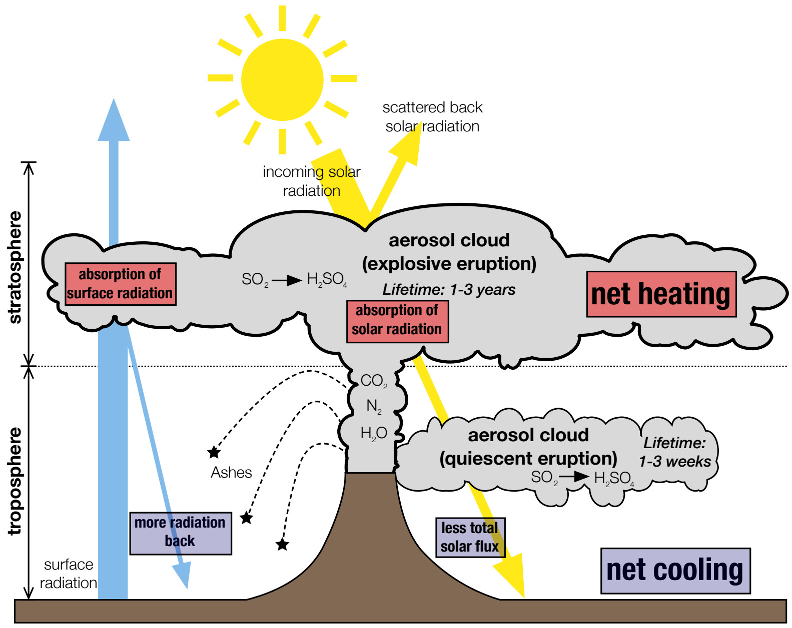

Figure 3.1: Simplified representation of volcanic inputs and their effects based on Plate 1 of Robock (2000).

Consequently, the only eruptions that affect global climate are the large explosive ones, which propel an aerosol cloud into the stratosphere. Once created, such a cloud travels around the globe. Its dispersion depends on winds at the time of the eruption. The cloud produces three major climate effects. First, some of the solar radiation is scattered back to space; this is the dominant radiative effect. It reduces the amount of solar energy that reaches the Earth's surface, which brings a net cooling at the surface. Second, more longwave radiation is emited back to Earth's surface, which attenuates the previous effect. Third, the H_2SO_4 aerosols absorb both solar and terrestrial radiations, which produces a net warming of the stratosphere.

A fraction of the sulfate emitted by the eruption is deposited and preserved in ice sheets. The ice cores are therefore suitable archives to reconstruct past volcanic activity. For each ice core, the sulfate concentration time series reveals the volcanic deposition signal, which is the amount of sulfate of volcanic origin deposited by km^2 (for more details, see for instance Gao et al. (2006)). The sulfate signal is highly dependent on precipitation (Gao et al., 2007), meaning that more sulfates are deposited in regions experiencing high precipitation. For a particular eruption, this leads to very high spatial variability in the deposition. For instance, for the large Tambora eruption of 1815 yAD, the spatial variations of the amount of sulfates measured in different ice cores reaches 45% of the total signal, for both the Greenland and Antarctic ice sheets (Gao et al., 2007). This indicates that multiple ice cores with a good spatial coverage should be used to reconstruct accurately the past volcanism.

Multiple techniques exist to derive the amount of sulfates initially injected by volcanic eruptions into the atmosphere from the measurements of sulfate deposition in ice cores (Gao et al., 2007). Among them, the technique based on nuclear bomb test debris assumes that the transport and deposition of the latter is similar to those of volcanic aerosols on a large scale. Specifically, this method assumes that the ratio between the total β activity (^{90}Sr+^{137}Cs) injected into the atmosphere and the total β activity measured in the ice core is the same than the ratio between the sulfates injected into the atmosphere and the sulfates measured into the ice core. The amount of sulfate injected by the different volcanic eruptions can then be derived from knowing the ratio for the bomb test and the sulfates measured into the ice core. Other techniques have confirmed the results of this methodology (e.g. Gao et al., 2007).

Ideally, as in the GCMs, the volcanic forcing should be take into account via an AOD, i.e. a local measurement of how opaque the atmosphere is in a single column. In the model LOVECLIM, the volcanism is taken into account as a negative anomaly of the TSI (Wm^{-2}). Therefore, it is necessary to first estimate the radiative forcing at the top of the atmosphere resulting from each explosive eruption in order to evaluate the effect of volcanism on climate in LOVECLIM. In 2008, Gao et al. have published a simple model to compute the atmospheric sulfate loadings, i.e. the amount of sulfates in the atmosphere as a function of time and latitude, as a function of the mass injected in the atmosphere by the volcano (hereafter referred to as the injection). This model is described in section 3.2.1.2. Once calculated, the sulfate loadings are converted into an equivalent TSI anomaly via the AOD by a linear scaling (see section 3.2.1.3 and equation 3.3).

This means that two of the three major climate effects induced by volcanism are not taken into account by LOVECLIM, i.e. (1) the resending of more terrestrial radiation that attenuates the surface cooling and (2) the net warming of the stratosphere. This has clear limitations on the model performance. For instance, the winter warming in Europe that follows some large tropical eruptions is not simulated by the model. As explained in Robock (2000), such a warming is triggered by a stronger stratospheric equator-pole temperature gradient that takes place because of the stronger warming of the tropical stratosphere. This is associated with a more powerful polar vortex (jet stream) that favors a positive North Atlantic Oscillation circulation pattern (Hurrell, 1995), producing more advection of the warm air of Atlantic origin over Europe. This generates a net warming that overwhelms the radiative cooling.

3.2 Methodology

Two groups of simulations have been performed with LOVECLIM. They represent the climate of the last 10 ky. Each simulation is composed of 12 members. They both use the same forcings, except that one includes the Holocene volcanic activity forcing described below, while the other does not. We will refer to these simulations as VOLC and NOVOLC simulations, respectively. The difference between both simulations will highlight the impact of the Holocene volcanic activity. The forcing in NOVOLC is the same as in Mathiot et al. (2013), Mairesse et al. (2013) and in Klein et al. (2014), except for the solar forcing, because the latter has only been provided by the Past4Future project recently (see section 1.3.2 for a graphical representation).

The orbital parameters follow Berger (1978). The greenhouse gas concentrations are based on the data of Flückiger et al. (2002). The Laurentide ice sheet topography and surface albedo have been adapted for LOVECLIM by Renssen et al. (2009) from the reconstruction of Peltier (2004). The freshwater fluxes coming from the Antarctic ice sheet are added in the Amundsen, the Bellingshausen and the western part of Weddell Seas, based on Pollard and DeConto (2009). For the Northern Hemisphere, the freshwater fluxes resulting from the melt of the Laurentide ice sheet are injected in the Labrador Sea and off the coast of the Gulf of Saint Lawrence (Renssen et al., 2009). The solar forcing is provided by the European project Past4Future (P4F), based on Steinhilber et al. (2009).

3.2.1 From the sulfate injection to the LOVECLIM forcing

3.2.1.1 Description of the unpublished volcanic injection data set

Bo Vinther, from the Centre for Ice and Climate of the University of Copenhagen, has built, in the framework of P4F, the first Holocene data set of the volcanic activity. This data set is still unpublished and at the beta-version stage. As we are involved in P4F, we are authorized to use it. But our work has to be considered as a first step in the understanding of the impact of volcanic activity on the Holocene climate and it will not be published before a final version of the data set is publicly available.

year (BP)	year (AD)	Southern Hemisphere injection (Tg)	Northern Hemisphere injection (Tg)	Global injection (Tg)
8651	-6701	63	469	532
8395	-6445	44	543	588
7591	-5641	139	441	580
7201	-5251	130	443	573
4885	-2935	131	126	258
2387	-437	195	88	283
692	1258	112	146	258

Table 3.1: The seven Holocene eruptions that inject more than 200 Tg of sulfate into the atmosphere at the global scale.

The data set consists in volcanic sulfate injections at the hemispherical scale (see Tab. 3.1), based on the measurements from two ice cores: the Antarctica EDML ice core and the Greenland GISP2 ice core. This data set spans the time -9545 to 720 yAD. Estimated volcanic injections have been scaled to conform to Gao et al. (2008) volcanic injection data that represent the last 1500 years. This scaling enables to reconstruct a stack constituted of the injections of Vinther from -8050 to 720 yAD and the injections of Gao et al. (2008) for 721 to 2000 yAD. As our Holocene simulation starts 10 ky ago, we do not use the first 1495 years provided by Bo Vinther.

The resulting injection data set contains 617 eruptions; 317 are measured in the GISP2 ice core only, 204 are found in the EDML ice core only and the signal of 96 of them is retrieved in both ice cores. More than half of Holocene eruptions (358) inject less than 10 Tg of sulfate in the atmosphere, while very few eruptions (22) inject more than 100 Tg (Fig. 3.2). Similarly, only 7 eruptions inject more than 200 Tg into the atmosphere (Tab. 3.1). Among them, the largest eruption of the last millennium, the 1258 yAD eruption, is the smallest.

The large uncertainties associated to this data set remain difficult to quantify. First, this reconstruction is still a beta-version and will be revised, especially the chronology of the eruptions. Second, only two ice cores intervene in the reconstruction, while huge variations in the deposition of sulfate exist between different ice cores in Greenland or in Antarctica (Gao et al., 2007). Third, it has been suggested that the sulfate record coming from ice cores located in central Greenland above 72°N, as it is the case for the GISP2 (72.58°N, 38.46°W) ice core, usually have less than average volcanic depositions (Gao et al., 2007).

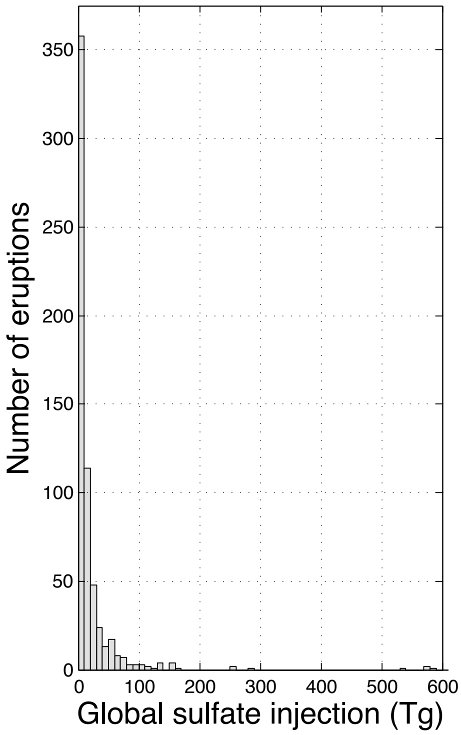

Figure 3.2: Histogram of the sulfate amount (in Tg) that is injected into the atmosphere at the global scale by volcanic eruptions during the last 10 ky.

3.2.1.2 The sulfate dispersion model of Gao et al. (2008)

The model published by Gao et al. (2008) is applied here to convert the annual sulfate injections per hemisphere in a monthly data set of loadings per latitude band. The lack of information on the past eruptions leads us to make the following three hypotheses, similar to the ones originally applied in Gao et al. (2008). First, each eruption starts presumably in April and injects sulfate during four months (April, May, June and July). Because the injection follows a linear law, the maximum amount of sulfate, due to a single eruption is reached at the end of July. Kravitz and Robock (2011) justify this timing choice as they found out that it is easier to detect the effect of an eruption that takes place during the summer. Second, there is only one eruption per year, which means that if that eruption was recorded in both hemispheres, it would have taken place in the tropics. Otherwise, the eruption happened in the mid-to-high latitudes of the hemisphere where it is detected in ice cores. Third, the Earth is divided into 16 equal-area latitude bands. Each hemisphere is composed of three bands for the tropics, four for the mid-latitudes and one for the high-latitudes.

Two models are used to describe the dispersion of sulfate: (1) a model of decay, based on an exponential decrease, and (2) an updated version of the Grieser and Schonwiese (1999) model that transports the stratospheric sulfates between the different latitude bands. Every two days both models are updated to comply with the time step chosen by Grieser and Schonwiese (1999) following the procedure below. Firstly, if there is an eruption during the time step, the amount of sulfates of the latitude bands where the eruption takes place are updated. For a hemispheric injection, the sulfate (Tg) is divided between the 5 bands representing the mid-to-high latitudes of the concerned hemisphere. For a global eruption, sulfates (Tg) are distributed amongst the six bands that represent the tropics. Secondly, the e-folding decay time model reduces the amount of sulfates of each latitude bands. Thirdly, sulfates are transported between the latitude bands by the parameterization of Grieser and Schonwiese (1999).

The e-folding decay time model

For each time step of two days and each latitude band, the following equation is applied to compute the atmospheric sulfate decay.

$$C_{(t)} = C_{t-1} \times \exp(-\frac{t}{\tau}) \tag{3.1}$$

where $C_{(t)}$ is the amount of sulfates in the atmosphere at the time step t, C_{t-1} is the amount of sulfate in the atmosphere at the previous time step and τ is the e-folding decay time in month, i.e. the number of months needed to decrease the initial quantity of sulfate by a factor e^{-1}. In the equation 3.1 τ is expressed in time step. The sulfate residence time in the atmosphere is proportional to the e-folding decay time (Fig. 3.3). The e-folding time is function of the latitude band and the period of the year, set to 36 months for the tropics and 12 months for the mid-latitudes. For the high-latitudes, it is fixed to 6 months all year long, except during winter, when it is 3 months, because of the sink mechanism links to the stratospheric aerosol (Gao et al., 2008).

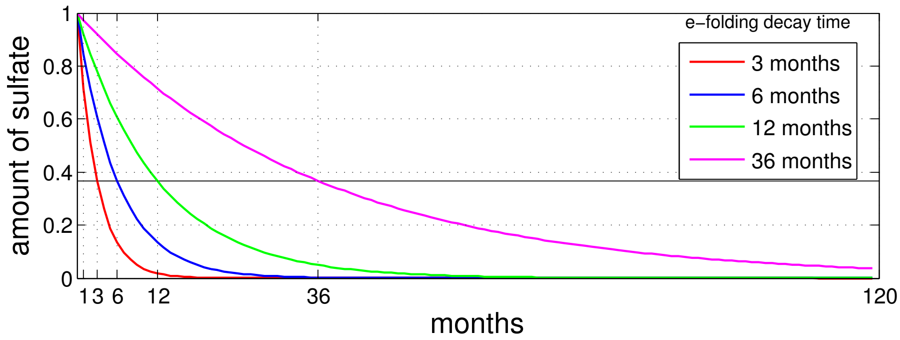

Figure 3.3: The evolution of the amount of atmospheric sulfate for different e-folding decay times. The black line shows the e^{-1} value.

Transport between the different latitude bands

In order to transport sulfate between the different latitude bands, two minor modifications are brought to the parameterization of Grieser and Schonwiese (1999) by Gao et al. (2008). First, there is no sulfate transport between both hemispheres because it is assumed that the ice cores provide accurate estimates of the hemispheric distribution. Second, the exchange coefficients between the different latitude bands, which depend on the latitude bands and the season, are slightly different (Tab. 3.2).

Direction of the transfer	coefficient
Tropics $\rightarrow$ tropics	91%
Tropics $\rightarrow$ mid-latitudes	50%
Mid-latitudes $\rightarrow$ tropics	7%
Mid-latitudes $\leftrightarrow$ mid-latitudes (winter & sping)	90%
Mid-latitudes $\leftrightarrow$ mid-latitudes (summer & fall)	70%
Mid-latitudes $\rightarrow$ high-latitudes (winter)	10%
Mid-latitudes $\rightarrow$ high-latitudes (summer)	70%
Mid-latitudes $\rightarrow$ high-latitudes (spring & fall)	40%
High-latitudes $\rightarrow$ mid-latitudes	4%

Table 3.2: Monthly exchange coefficients between the different regions.

For each time step, the exchange coefficients regulate the amount of sulfates that is exchanged between contiguous latitude bands. The amount of sulfates of a latitude band x at the end of a time step (S^x_{t+1}), taking into account the transport, is calculated as follows:

$$S_{t+1}^{x} = S_t^x - \left(S_t^x \times C^{tu}\right) - \left(S_t^x \times C^{td}\right) + \left(S_t^{x-1} \times C^{fd}\right) + \left(S_t^{x+1} \times C^{fu}\right) \quad (3.2)$$

where
- S_t^x is the amount of sulfates at the beginning of the time step in the latitude band x
- S_t^{x-1} is the amount of sulfates at the beginning of the time step in the latitude band southward of x
- S_t^{x+1} is the amount of sulfates at the beginning of the time step in the latitude band northward of x
- C^{tu} is the exchange coefficient from the band x to the band $x+1$
- C^{td} is the exchange coefficient from the band x to the band $x-1$
- C^{fu} is the exchange coefficient from the band $x+1$ to the band x
- C^{fd} is the exchange coefficient from the band $x-1$ to the band x

The model output for the eruption of 1258 yAD

The tropical eruption of 1258 yAD has injected 146 Tg of sulfate in the Northern Hemisphere and 112 Tg in the Southern Hemisphere. Fig. 3.4 shows the evolution of the atmospheric sulfate loadings resulting from this eruption. Between April and July of 1258 yAD, the amount of atmospheric sulfates increases in each hemisphere. The increase is nearly linear in the two tropics because the progressive sulfate injection is slowed down by the sulfate decay. As a consequence, the total loading in each hemisphere reaches its maximum after four months but is not as high as the 146 Tg and the 112 Tg. A fraction of the sulfates injected in the tropics is transported gradually to higher latitudes. This explains the slow increase of sulfate in the extra-tropics with a peak a bit less that one year after the beginning of the eruption. As there is no transfer between the two hemispheres, the amount of sulfate remains greater in the Northern extra-tropics than in the Southern extra-tropics.

3.2.1.3 From the sulfate loadings to the LOVECLIM forcing

As explained in section 1.3.2.3, volcanism is taken into account in LOVECLIM as a negative anomaly of the TSI (Wm^{-2}) and is defined for four equal-area latitude bands: from 90°S to 30°S, from 30°S to the equator, from the equator to 30°N, from 30°N to 90°N. For each of these four latitude bands the amount of sulfates (in Tg) is converted in AOD by dividing it by $\left(150 \times \frac{1}{4}\right)$. The 150 factor is the value that Stothers (1984) find for the Earth. The $\frac{1}{4} = \left(\frac{\text{band area}}{\text{Earth area}}\right)$ factor

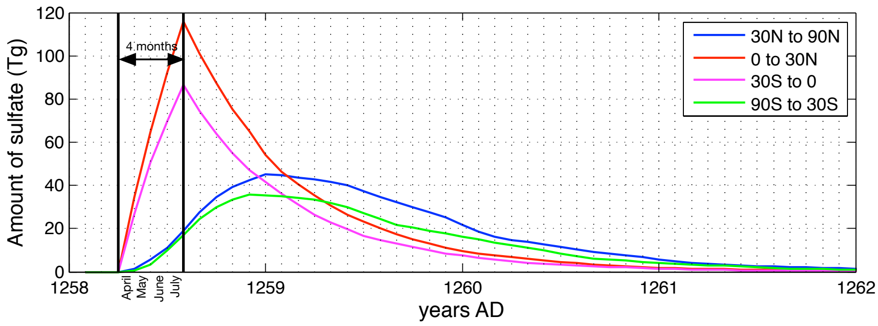

Figure 3.4: Evolution of the atmospheric sulfate loadings (in Tg) resulting from the eruption of 1258 yAD. The results are aggregated for the four equal-area latitude bands of LOVECLIM.

is therefore used to take into account the area of the considered band compared to the whole Earth. Then, according to Wigley et al. (2005), the AOD is multiply by -20 to obtain the radiative forcing at the top of the atmosphere. Finally, the result is multiplied by $\frac{4}{0.7}$ to obtain the TSI equivalent. This procedure is summarized by the following equation:

$$\text{TSI in Wm}^{-2} = \underbrace{\overbrace{\overbrace{\frac{\text{amount of sulfate in Tg}}{150 \times \left(\frac{\text{band area}}{\text{Earth area}}\right)}}^{\text{Optical depth (AOD)}} \times -20}^{\text{Radiative forcing at the top of the atmosphere (Wm}^{-2})} \times \frac{4}{0.7}}_{\text{TSI equivalent forcing (Wm}^{-2})} \qquad (3.3)$$

The comparison of the resulting LOVECLIM forcing (Fig. 3.5) for the eruption of 1258 yAD with the sulfate loadings (Fig. 3.4) clearly shows that the function to convert the amount of sulfates (in Tg) into a TSI forcing is linear. Up to date, it is considered that this function is adequate to calculate the forcing of the past 1500 years, since for instance its use is recommended in the framework of PMIP3 (Schmidt et al., 2011).

Using this linear function to calculate the forcing of the last 10 ky leads to estimated forcing values in TSI equivalent very close to the solar constant for the largest eruptions (Fig. 3.6). In other words, the impact of the four Holocene eruptions that injected the highest quantity of sulfates in the atmosphere would be similar to a nearly complete absence of solar radiation at the ground during

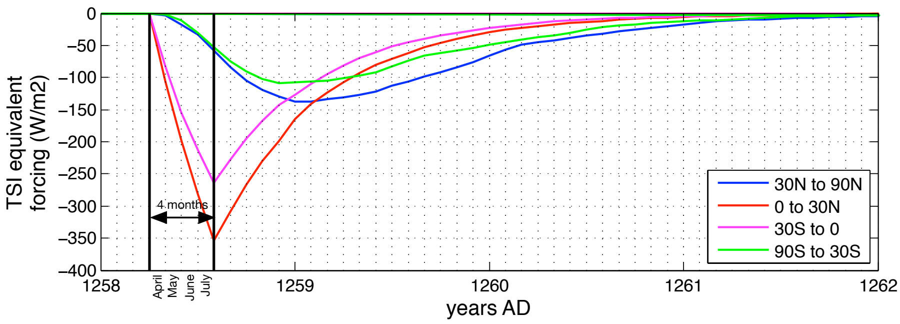

Figure 3.5: Evolution of the LOVECLIM TSI forcing resulting from the volcanic eruption of 1258 yAD.

few months. This is clearly not realistic because of the three reasons explained below. Nevertheless, as no consensus exists on a best way to evaluate the forcing from the atmospheric loading, this forcing is taken as such but the simulation driven by this forcing must be considered only as a sensitivity experiment, not as a realistic estimate of the impact of volcanic eruptions on Holocene climate.

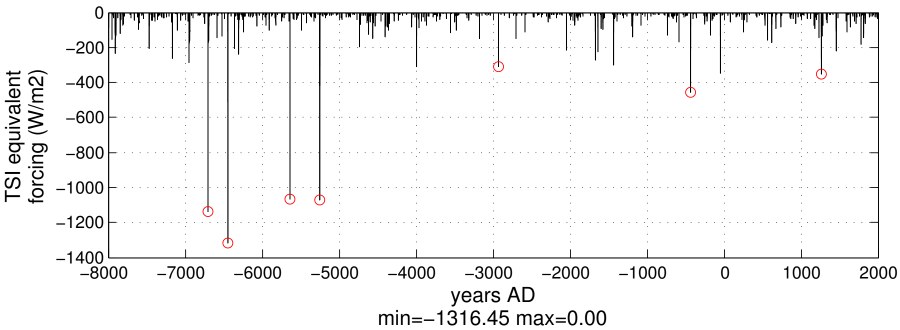

Figure 3.6: Monthly Holocene volcanic forcing in TSI equivalent (Wm^{-2}). The red circle highlights the 7 largest eruptions of last 10 kyBP displayed in the Tab. 3.1.

First, such major events would have led to a large signal in proxies having a high temporal resolution, in the environment as it would be associated to large death rate of plants and animals, as well as in some documents for the late ones. The amplitude of the signal that should be found in a proxy-based surface temperature reconstruction at centennial timescales can be estimated by filtering the global annual mean surface temperature of the simulation VOLC with a running mean (Fig. 3.7) at four different temporal resolutions: 101, 251, 501 and 1001 years. At a resolution of 100 years, the maximum effect of the

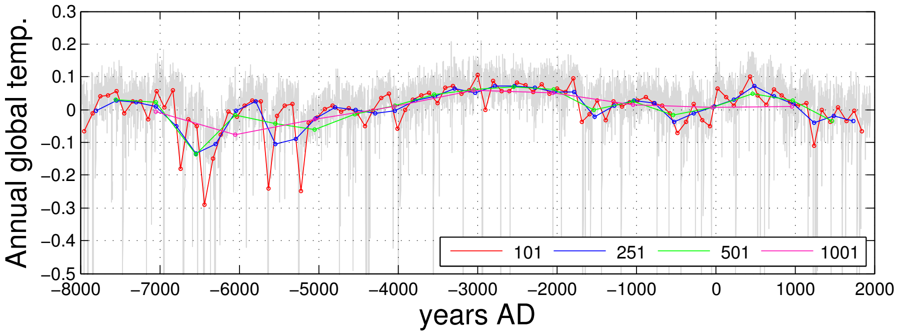

Figure 3.7: Global annual mean surface temperature difference between the simulation with and without (in grey) volcanism and the surface temperature filtered by a running mean of 101 (red), 251 (blue), 501 (green) and 1001 years (pink). Be aware that the vertical scale does not show the whole range of values. The annual global temperature difference peaks at 6°C. See Fig. 3.8 for the complete information.

volcanism on the global annual mean surface temperature is about 0.3°C. To date, such a signal can not be detected in a proxy-based reconstruction of surface temperature; i.e. because the associated uncertainty is often larger than 0.3°C, but the volcanic eruptions still let a significant imprint in the time series.

Second, the LOVECLIM TSI forcing is not an appropriate approximation of the effect of the largest eruptions. This could also be the case for smaller eruptions, but for a super eruption, Jones et al. (2005) have shown that the annual radiative forcing is of about 150 Wm^{-2} for the shortwave, while the increase of downward longwave radiations having a magnitude of about 90 Wm^{-2} compensates for the half. For a super-eruption, the net resulting radiative forcing is about 60 Wm^{-2}, which is therefore smaller than what is estimated for LOVECLIM because the latter does not take into account the effect of the changes.

Third, the scaling should not be linear between the loadings and the TSI forcing for large eruptions. Timmreck et al. (2010) suggest that the impact of huge volcanic eruptions is not proportional to the amount of sulfates injected in the atmosphere. Indeed, during super-eruptions, the concentration of sulfates is so high that the collision rates between the aerosols are higher, leading to bigger particle sizes and a more rapid falling out. A mitigating factor may be considered then to limit the forcing of huge eruptions. Yet, there is no consensus about the correction and the threshold that should be used.

3.3 Results and discussion

There are two standard ways to detect and estimate the impact of the volcanic forcing. The first is to compare the results of the simulation with the volcanic forcing (VOLC) and the one without it (NOVOLC). The ensemble means of each simulation are used. The second approach is to study the difference between the climates before and after each eruption, within the simulation VOLC. Both methods are used here.

For the second methodology, we are interested in looking at the effect of clearly separated eruptions to avoid attributing the impact of multiple eruptions to a single one. Presumably, the response to an eruption can be considered independent to other eruptions if the corresponding eruption occurs at least 20 years after the last eruption and before the next eruption. This period of 20 years is subjective but it is chosen in order to (1) keep enough eruptions for the study and (2) avoid to analyzing the signal of multiple eruptions, since the impact of most of the eruption does not last longer than 20 years, as it will be explained later (see Fig. 3.11). Moreover, we consider only the eruptions that inject very large amounts of sulfates in the atmosphere, i.e. at least 50 Tg, and therefore the impact of these independent eruptions will be easily detected. These hypotheses lead to select 10 target eruptions for the analysis (Tab. 3.3).

year (BP)	year (AD)	Southern Hemisphere injection (Tg)	Northern Hemisphere injection (Tg)	Global injection (Tg)	Amount of years without eruption before/after
9899	-7949	25	63	88	45/21
9790	-7840	9	50	59	25/33
8395	-6445	44	543	588	37/39
7437	-5487	0	51	51	41/24
7201	-5251	130	443	573	25/34
4885	-2935	131	126	258	104/40
4001	-2051	46	90	136	33/31
2535	-585	30	68	98	23/55
2127	-177	26	54	81	42/25
309	1641	18	34	52	22/32

Table 3.3: The 10 Holocene eruptions that inject more than 50 Tg of sulfate into the atmosphere at the global scale and for which the response has likely not been influenced by another eruption.

3.3.1 The surface temperature and atmospheric response

As expected, the impact of volcanism is detectable in the surface temperature difference between the simulations VOLC and NOVOLC. For the seven eruptions that inject the largest amount of sulfates in the atmosphere (Tab. 3.1), the annual global surface temperature drop is greater than 2°C (Fig. 3.8). The largest temperature decrease is around 6°C, which testifies of the strength of this volcanic forcing. For the Northern Hemisphere, the annual temperature drop reaches a maximum of about 10°C for the Holocene and 3°C for the last millennium. Concerning the last millennium, this temperature drop is slightly overestimated compared to the majority of the PMIP3 models (Berdahl and Robock, 2013). The magnitude of the volcanic forcing which is slightly higher here than in the recommended PMIP3 forcing, could be the reason of this overestimation of the cooling.

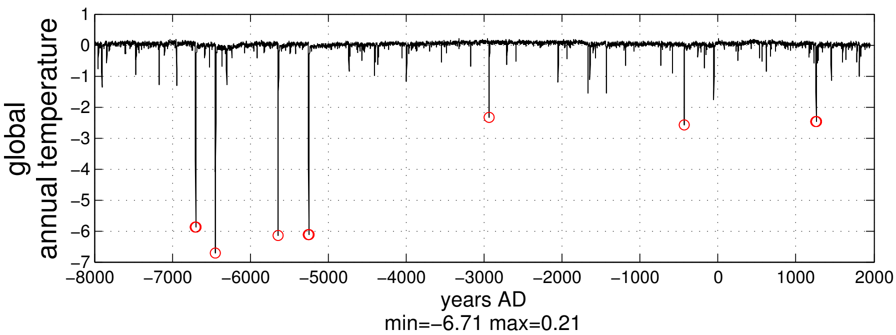

Figure 3.8: Global annual mean surface temperature difference (°C) between the simulation VOLC and NOVOLC. The red circles highlight the impact of the seven largest eruptions of the last 10 kyBP resume in the Tab. 3.1.

The comparison between the radiative forcing (Fig. 3.6) and the response of the annual air surface temperature (Fig. 3.8) suggests that a linear relation exists between these two variables. We investigate this relation on the basis of the ten independent eruptions (Fig. 3.9). Regarding the radiative forcing, the value we take is the biggest annual diminution over the four latitude bands used in LOVECLIM to compute the radiative forcing. For each of the ten eruptions, the temperature drop is maximal within the two years that follow the eruption. The temperature drop is therefore defined as the difference between the average global temperature of the two years after the eruption and the average global temperature of the 20 years before the eruption. A regression is applied to the data and confirms that the relationship between the temperature drop and the radiative forcing decrease is linear. According to Fig. 3.9, there is no evidence that this relation could be saturated for strong forcing or amplified as specific feedback mechanisms take place at large value. In other words, there is no indication that, at one point, a stronger forcing will no longer induce a bigger temperature drop or, on the contrary, that a shift to a different state is (temporarily) triggered above a particular threshold.

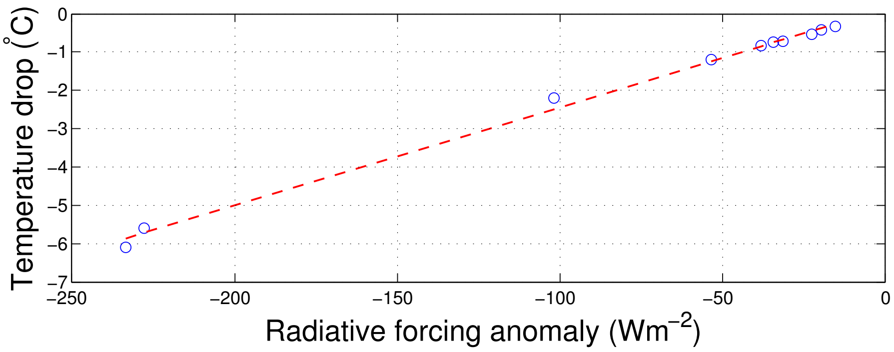

Figure 3.9: Temperature drop after the ten independent eruptions (Tab. 3.3) as a function of the biggest annual diminution of the radiative forcing over the four latitude bands used in LOVECLIM to compute the radiative forcing. The dotted line represents the linear regression between the two variables: $f(x) = 2.163 * x - 1.866$

The recovery timing is defined here as the number of years necessary for the global annual mean surface temperature to reach a value to the one before the eruption. To estimate this, we adopt a simple statistical methodology based on the following hypotheses. First, only the ten independent eruptions are considered. The black curve in the Fig. 3.10 illustrates the global annual temperature drop generated by the eruption of 7201 yBP. Jones et al. (2005) found a similar global annual temperature drop and recovery, using the HadCM3 model to simulate the response to an eruption that inject 100 times more sulfates in the atmosphere than the 1991 yAD Mount Pinatubo eruption, i.e. about 300 Tg of injection. Second, for each of these eruptions, we fit a gaussian distribution to the annual temperature of the 20 years before the eruption. The 95% range (2.5-97.5%) is displayed in red for the 20 years before the eruption in Fig. 3.10 and is extended to the years that follow the eruption. This predication interval means that without any volcanic injection, there is 95% chance that the annual global temperature of the next year will be within this interval.

The recovery time is then obtained by estimating the number of years between the eruption and the first year after the eruption when the annual global temperature is within the temperature range for the period preceding the eruption. Third, to avoid that an unusually warm or cold year that would follow the eruption has too much impact on this calculation, we fit an exponential model to the

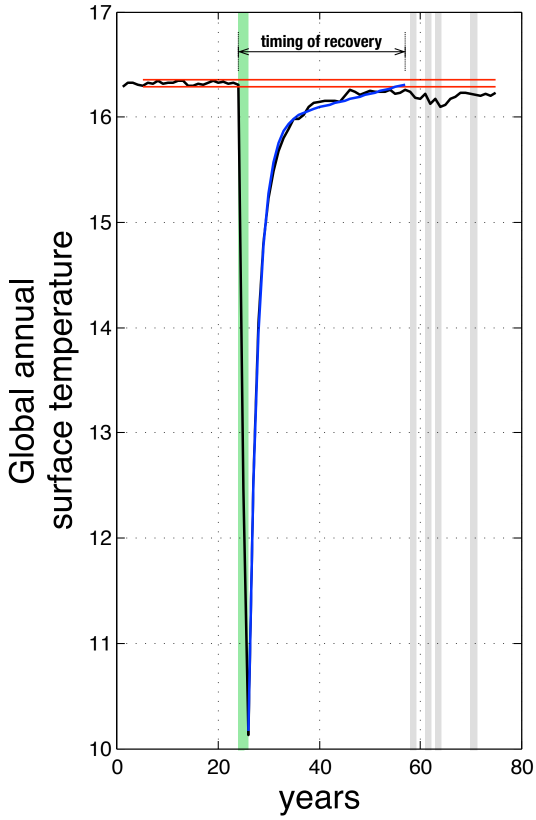

Figure 3.10: Global annual mean surface temperature (in black) for the period including the 7201 yBP eruption that injected 573 Tg of sulfates in the atmosphere. The green shaded area shows the decrease in temperature due to the eruption. The grey shaded areas show the timing of additional eruptions. The two red lines represent the 95% range of a gaussian distribution fitted to the temperatures of the 20 years preceding the eruption. The blue is the exponential fit of the 20 years after the eruption.

temperature of the years following the eruption during which no other eruption occurs. Depending on the eruption, this amount of years therefore range from 21 to 55 years (see last column of Tab. 3.3). Changing this amount to 15 or 25 years does not much modify the recovery time and does not change the conclusions that are derived below from the results of Fig. 3.11. The amount of years to recover is found when the exponential model is in the 95% range. The statistical model is in blue in Fig. 3.10 and has the form $a \times exp(b \times x) + c \times exp(d \times x)$, where x is the year and a,b,c and d are parameters.

The recovery time for the ten independent eruptions is shown with respect to the annual maximum decrease of the radiative forcing in Fig. 3.11. As expected, this demonstrates that the drop in global annual air surface temperature due to a volcanic eruption lasts longer if the amount of sulfates injected is bigger, resulting then in a stronger radiative forcing drop. The exponential fit highlights also a saturation phenomenon meaning that the number of years to recover does not increase linearly with the radiative forcing decrease.

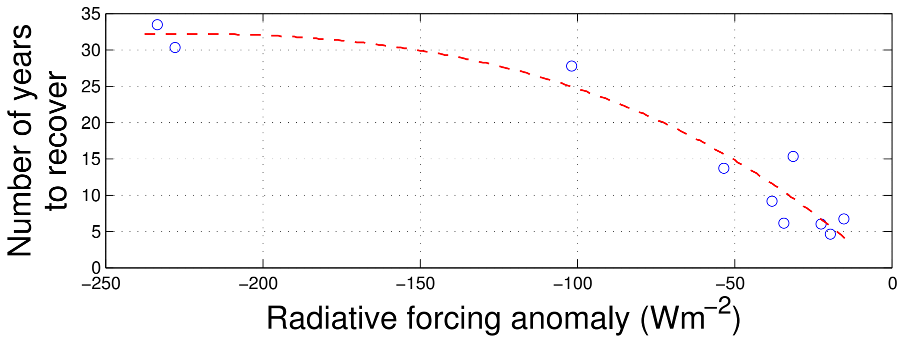

Figure 3.11: Number of years to recover the initial surface temperature in relation to the annual maximum decrease of the radiative forcing. This relation is based on the ten independent eruptions. The red dashed line is an exponential fit used to show the saturation phenomena.

Finally, Fig. 3.9 and 3.11 highlight that eruptions that inject a comparable amount of sulfate into the atmosphere generate a similar impact on the climate, no matter what is the initial state of the climate. Indeed, the eruptions that occur at three different times, in 309, 7437 and 9790 kyBP, produce the same global temperature drop of about 0.5°C (Fig. 3.9) and the same recovery timing of about 6 years (Fig. 3.11).

In order to understand better the mechanisms behind the propagation, the spatial distribution of the cooling could be analyzed. The discussion is focusing on the eruption 7201 yBP. It is one of the strongest eruption in Tab. 3.3. It injects more sulfates in the Northern Hemisphere than in the Southern one. The spatial pattern of the changes induced by this eruption are similar for the other tropical eruptions of Tab. 3.3. Of course, differences exist in the spatial pattern when analyzing eruptions that only inject aerosols in the Northern or in the Southern Hemisphere compared to tropical eruptions. This could be interesting to discuss these differences, but it will not be the subject of the present chapter.

The propagation of the cooling induced by the eruption of 7201 yBP can be visualized with several maps. Each map shows the difference in the annual air surface temperature between one of the 6 years after the eruption and the averaged 20 years before the eruption (Fig. 3.12). During the first year, the tropical eruption has mainly an impact on the tropical, the continental and the high-latitude areas (Fig. 3.12a). Over Sahara, the annual mean cooling locally reaches -25°C. This seems excessive and therefore, this is another argument in favor of a non-realistic forcing applied in this experiment (see above). In extra-tropical areas, the temperature of the air over the ocean is slightly reduced because the forcing is not very strong the first year in extra-tropical areas and because of the high thermal inertia of the ocean. The continental areas are highly impacted by the eruption because of the small land thermal inertia. Because of the strong forcing in the tropics, the lands of this area display a larger response than anywhere else. Finally, the Arctic also endures a strong cooling, a characteristics of many simulations associated with polar amplification (Masson-Delmotte et al., 2013). This is among other processes explained by the ice-albedo feedback. The increase of Arctic sea ice cover (Fig. 3.16), induced by the surface cooling, increases the albedo, which reduces the amount of solar radiation that is absorbed by the surface and therefore strengthens the initial cooling (see also section 3.3.2).

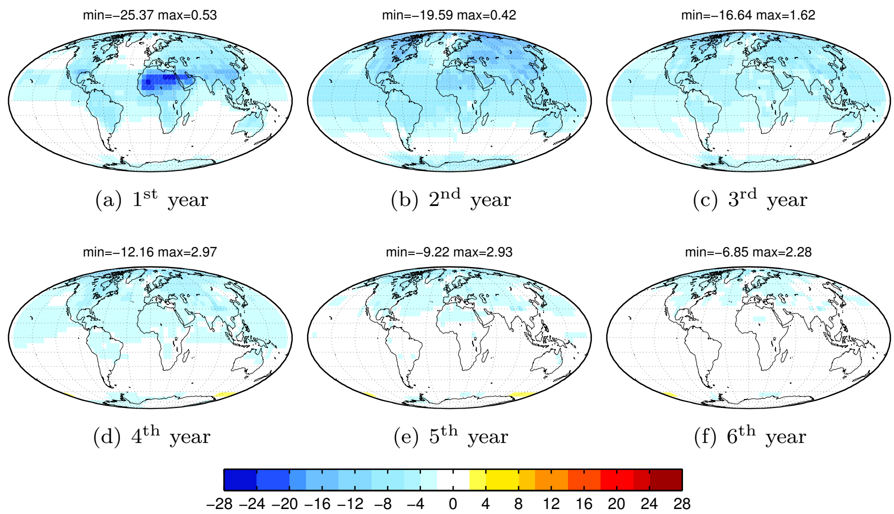

Figure 3.12: Annual mean surface temperature difference between the 1st to the 6th years after the eruption and the 20 years averaged air surface temperature before the 7201 yBP eruption.

During the second year after the eruption (Fig. 3.12b), the dispersion of sulfates is larger over the different latitude bands. This is illustrated by an almost homogeneous forcing (Fig. 3.5) that leads to a global cooling. The second year is also the coolest year after this eruption. In addition, one observes a spatial pattern characterized by more cooling in the Northern Hemisphere than in the Southern Hemisphere. This is because (1) there is no transport of the injection between the hemispheres, (2) there is less injection in the south (Tab. 3.1), leading to a smaller forcing in the Southern Hemisphere than in the Northern Hemisphere, and (3) there is more ocean in the Southern Hemisphere; the Southern Hemisphere response is therefore smaller since the oceanic reaction to many forcings is smaller than the one over continents because of the larger thermal inertia of the ocean and of various feedbacks (e.g., Boer, 2011; Joshi et al., 2013).

Afterwards, the cooling diminishes year after year and the signal disappears first from the Southern Hemisphere (because the forcing is stronger in the north) and then from the Northern Hemisphere (Fig. 3.12c-f). This characterized chain of events is similar for the ten independent eruptions listed in Tab. 3.3.

3.3.1.1 What is the effect of the volcanism on the atmospheric circulation?

During the first year after the 7201 yBP eruption, the air surface temperature cooling is strong over Antarctica (Fig. 3.12a). This leads to a higher surface pressure over this continent which weakens the westerlies and therefore results in a less intense atmospheric circulation around Antarctica (Fig. 3.13a). This situation persists two more years (Fig. 3.13b and c), until the almost total disappearance of the cooling over Antarctica, on the fourth year after the eruption (Fig. 3.12d and 3.13d).

For the Northern Hemisphere and the Atlantic sector in particular, the temperature gradient increases between the mid-latitudes and the North Pole. This may be the origin of the strengthening of the westerlies southward of 45°N, over the Atlantic. These stronger westerlies bring warmer air from the tropics over Southern Europe. This mechanism partially compensates the direct radiative cooling over Europe but is not sufficient to overwhelm it totally.

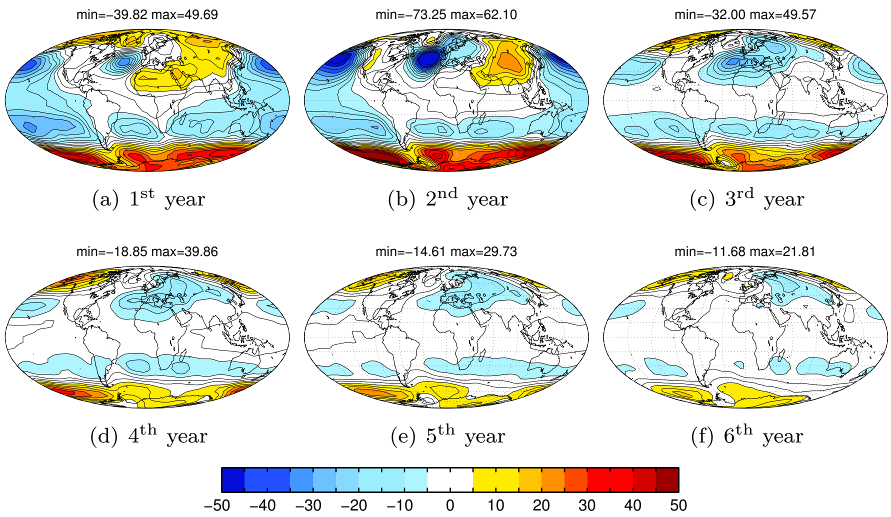

Figure 3.13: Annual 800hPa geopotential height (in m) difference between the 1st to the 6th years after the eruption and the 20 year averaged geopotential height before the 7201 yBP eruption.

3.3.2 The oceanic response

The oceanic response to a decrease in the solar irradiance is a cooling of the sea surface. For the 7201 yBP eruption, this cooling (Fig. 3.14) follows the same spatial pattern as the air surface temperature (Fig. 3.12).

During the first two years after the eruption, the temperature decreases and reaches, at the local scale, values as low as about -13°C in an annual average in comparison with the 20 year average that precede the eruption. As for the air surface temperature, the cooling propagates from the tropics to the high latitudes. After the second year, it follows the declining forcing. The sixth year after the eruption, the cooling greater than 2°C is almost only located at the high northern latitudes.

This surface temperature decrease, increases the density at surface and induces deeper convection in the areas of deep water formation. The cooling generates also an increase of the sea ice cover. According to Goosse and Renssen (2004), these two phenomena are associated with feedbacks that influence the Arctic and the North Atlantic region. They are detailed below.

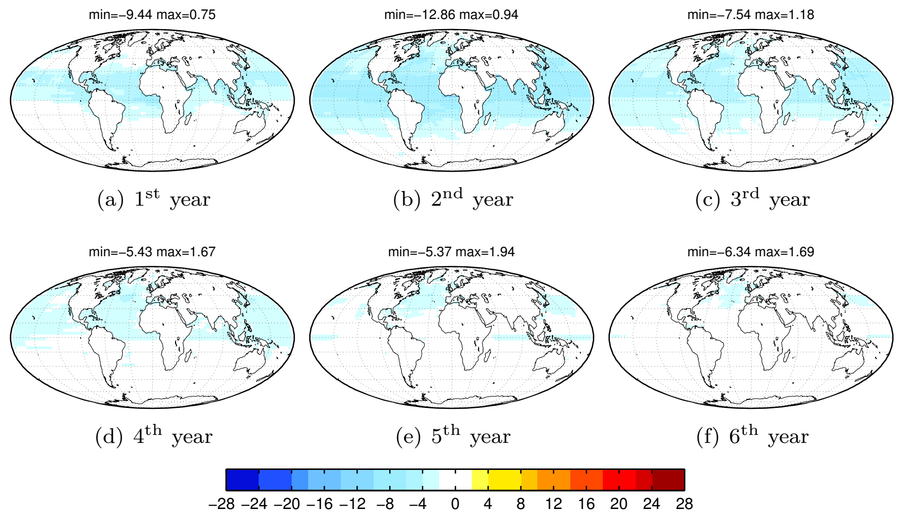

Figure 3.14: Difference in the annual mean sea surface temperature between the 1st to the 6th years after the eruption and the 20 year averaged air surface temperature before the 7201 yBP eruption.

The first one is a positive feedback, i.e. the chain of mechanisms induced by the decrease of the surface temperature, strengthens the initial surface cooling. It works as follows: the surface cooling generates the production of more sea ice in the North Atlantic and in the Barents Sea as shown in Fig. 3.15. Because the sea ice concentration is higher in the Barents Sea, the exchange between the ocean and atmosphere are more limited. This strengthens the surface cooling since less heat of the ocean is transferred to the atmosphere.

This higher sea ice concentration is associated with a larger sea ice extent. The sea ice extent is defined here as the total area covered by the model grids that contain a sea ice concentration of at least 15%. Compared to the 20 years before the 7201 yBP eruption, the additional annual sea ice extent, two years after the eruption, peaks at 4.7 $\times 10^6$km^2 for the Northern Hemisphere and 2.7 $\times 10^6$km^2 for the Southern Hemisphere. It is not surprising that the sea ice cover increases after large volcanic eruption. It has also been found in some PMIP3 models by Berdahl and Robock (2013), who have investigated the response of those models to the last millennium volcanic forcing.

The evolution of the sea ice extent during the Holocene in the simulation VOLC in comparison with the simulation NOVOLC demonstrates well the amplitude of the impact of the volcanism on the sea ice cover (Fig. 3.16). The differ-

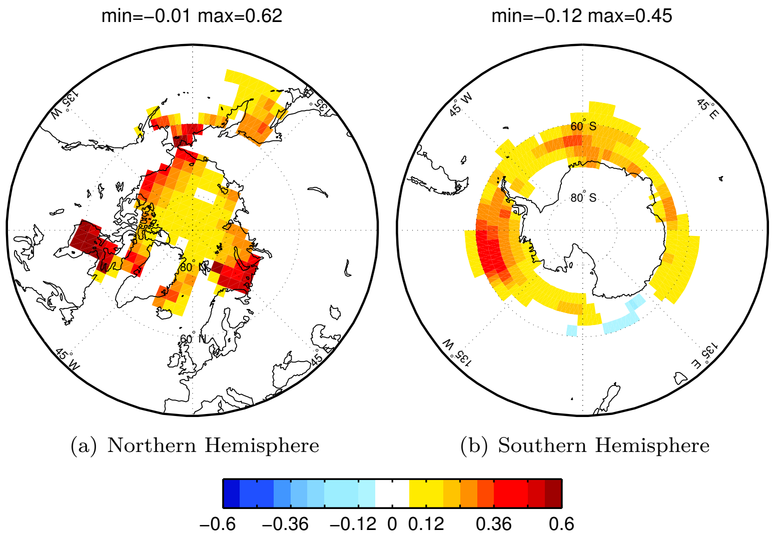

(a) Northern Hemisphere (b) Southern Hemisphere

Figure 3.15: Annual mean sea ice concentration difference (in %) between the average 20 years before the eruption 7201 yBP and for the 2nd year after the same eruption.

ence between the simulation VOLC and the simulation NOVOLC is maximum 5.67×10^6km^2 for the Northern Hemisphere and 3.05×10^6km^2 for the Southern Hemisphere in annual average. These variations are substantial knowing that the annual Holocene sea ice extent of the simulation NOVOLC ranges between 8 and 10×10^6km^2 for the Northern Hemisphere and 9 and 10×10^6km^2 for the Southern Hemisphere.

The variations are greater in the Northern Hemisphere than in the Southern because the volcanic activity, according to the forcing, is generally more active in the Northern Hemisphere. For the eruptions producing a stronger forcing in the Southern Hemisphere than in the Northern Hemisphere, greater changes in sea ice are simulated in the Southern Hemisphere, as it is the case for the -437 yAD eruption (Fig. 3.16 and Tab. 3.1).

The second feedback is negative and is triggered by the increase of the depth of convection due to the denser surface water after a volcanic eruption. This more dense surface water has two origins: the direct surface water cooling and the increase in salinity of the surface water. This second factor comes from (1) the larger sea ice formation and (2) the decrease in precipitation after the eruption, as in a colder climate, less water evaporates and therefore the

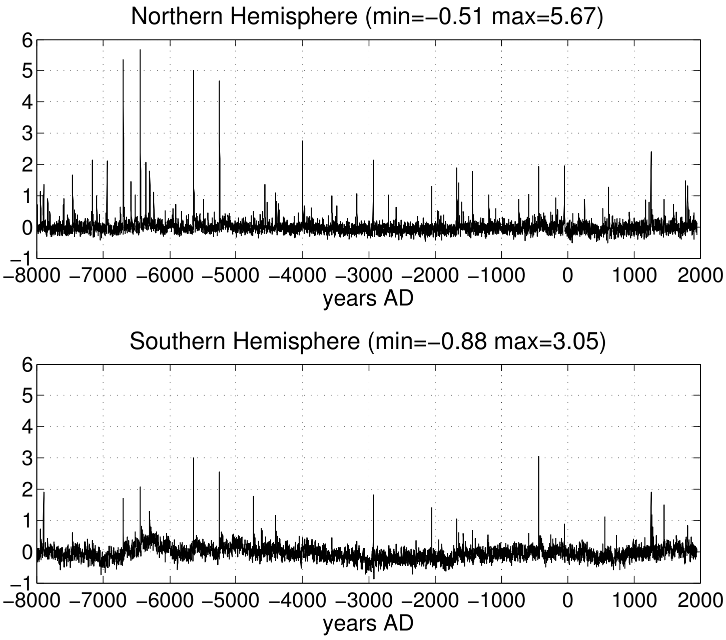

Figure 3.16: Differences in sea ice extent (in $10^6 km^2$) over the Holocene between the simulation VOLC and NOVOLC. The sea ice extent is defined as the area covered by at least 15% of sea ice.

atmosphere humidity is lower. This precipitation reduction that induce higher surface salinities after volcanic eruption is in agreement with the results of Iwi et al. (2012) and Iles et al. (2013), who performed last millennium simulations with the HadCM3 model.

For the 7201 yBP eruption, the depth of convection in the North Atlantic has increased at all the major deep convection sites in the model: the Labrador Sea, the Irminger Sea and the Norwegian Sea. The additional depth of convection reaches a maximum value of about 1000 m in the Norwegian Sea, during the 2nd year after the eruption (not shown). These changes in the depth of convection in the North Atlantic enhance the formation of the North Atlantic Deep Water (NADW) and directly influence the maximum of the Atlantic Meridional Overturning Circulation (AMOC) in the North (Fig. 3.17). As a result, four years after the eruption the value of the latter is increased by 11 Sv. Additionally, the overturning cell is deeper, reaching 4000 m instead of 3000 m 10 years after the eruption (compare Fig. 3.18a and 3.18g). It takes several years to have the maximum impact because of the response time of the ocean. The

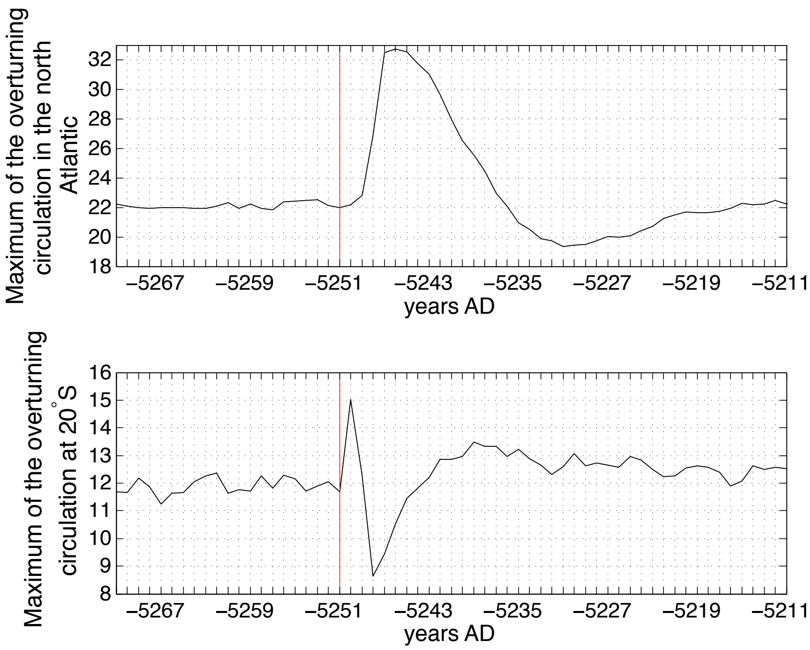

Figure 3.17: Maximum of the overturning circulation (Sv) in the north Atlantic (top panel) and at 20°S (bottom panel) for the simulation period that includes the 7201 yBP eruption. The vertical red line is the time of eruption.

displacement of the NADW forces the Antarctic Bottom Water (AABW) to retreat southward and the corresponding overturning cell is shifted by about 15° of latitude (compare Fig. 3.18a and 3.18g). The result is a warming of the bottom water in the North Atlantic basin since the NADW is warmer than the AABW.

Moreover, during the first year after the 7201 yBP eruption, the depth of convection has increased in the Atlantic Ocean, at around 30°N, by about 50 to 200 meters (not shown), due to the strong and rapid cooling of the sea surface temperature in this area during that same year (Fig. 3.14a). This is associated with a local ephemeral equatorial circulation (Fig. 3.18b). This local circulation in the Atlantic is found after the four largest tropical volcanic eruptions (see Tab. 3.1) and has a direct impact on the maximum of the overturning circulation at 20°S (Fig. 3.17). Indeed, its value, for the average 20 years before the 7201 yBP eruption is about 12 Sv. During the first year after the eruption, its value peaks at 15 Sv (Fig. 3.17), then decreases in only two years to about

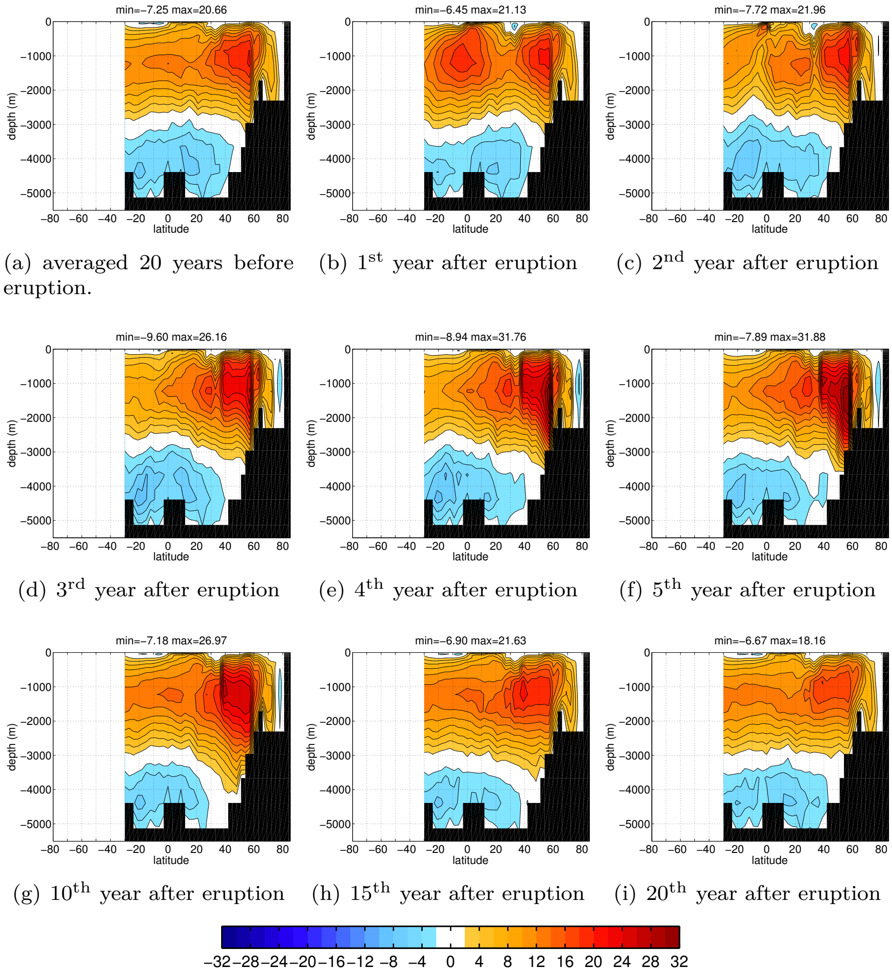

(a) averaged 20 years before eruption.

(b) 1st year after eruption

(c) 2nd year after eruption

(d) 3rd year after eruption

(e) 4th year after eruption

(f) 5th year after eruption

(g) 10th year after eruption

(h) 15th year after eruption

(i) 20th year after eruption

Figure 3.18: Evolution of the meridional overturning circulation (Sv) in the Atlantic and the Arctic Ocean for the 7201 yBP eruption. The circulation is clockwise for the positive values and counterclockwise for the negative values. $1\text{Sv} = 10^6\text{m}^3\text{s}^{-1}$

8.5 Sv and then increases again to reach 13.5 Sv in response to the changes in the North Atlantic, the 12th year after the eruption.

This amplified AMOC results in more meridional heat transport between the equator and the North Atlantic, up to 0.16 PW (Fig. 3.19) on the 12th year after the eruption. This strengthening of the AMOC is consistent with the findings of Stenchikov et al. (2009), who have studied the volcanic 1991 yAD and the 1815 yAD signals in ocean with a coupled climate model.

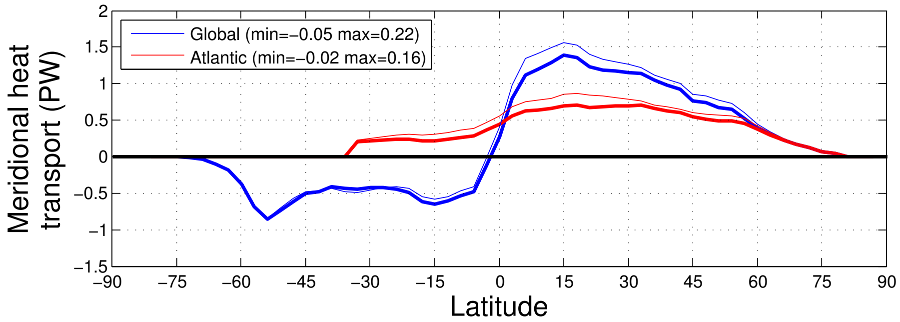

Figure 3.19: Meridional heat transport for the average 20 years before the 7201 yBP eruption (tick line) and the 12th year after the same eruption (thin line) for two different oceanic basins: the global basin (blue) and the Atlantic basin (red).

In contrary to the atmosphere and the surface ocean, the time delay for the whole ocean to recover from the forcing perturbation can be longer than centuries because of the high thermal inertia of the ocean and the slow rate of water mass renewal in the deep ocean. This is illustrated by the difference between the global oceanic temperatures of the simulations VOLC and NOVOLC (Fig. 3.20). Note that a difference of the ocean global temperature of 0.1°C corresponds to a difference of the sea level of about 5 cm.

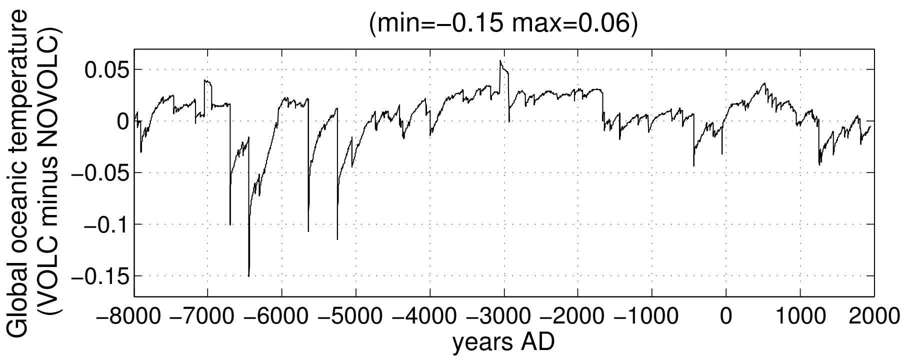

Figure 3.20: Difference between the global temperature of the ocean (°C) in the simulation VOLC and in the simulation NOVOLC.

Before launching the simulation VOLC, we wondered if it would be possible that such a large volcanic forcing produce irreversible changes in the meridional overturning circulation, or other major long-term shift in the system as speculated in some studies (e.g. Robock et al., 2009). It is not the case in our simulation over the Holocene despite the fact that we likely strongly overestimate the magnitude of the volcanic forcing.

Despite the fact that this analysis has mainly been focused on the volcanic eruption of 7201 yBP, the volcanism has a clear impact on the whole Holocene period. For instance, it produces at the millennial scale changes of about 0.1 to 0.2°C on the global mean surface temperature (Fig. 3.7). Also, this Fig. 3.7 shows that some single eruptions could have a bigger impact on the climate than clustered eruptions. This is likely related to the way the forcing has been implemented, since the forcing induced by super-eruption is overestimated. Testing if this is still the case with an uptdate version of the forcing will be an interesting perspective. Also, this Fig. 3.7 well illustrates that periods with less intense volcanism are at the global scale warmer than in the simulation without volcanism. This is because the forcing is implemented in LOVECLIM with a zero mean (see section 1.3.2.3), and therefore a less intense volcanic activity can engender warmer periods as it is the case, on average, between -3.5 to -2.5 kyAD.

3.4 Conclusion

The conclusions derived from our analysis can be summarized as follows.

- Even if the data set compiled by Bo Vinther is still at the beta-version stage, the periods when the volcanic forcing is strong are relatively clear. On the contrary, the forcing amplitude applied in our simulation is not well constrained because the linear scaling used to transform the aerosol injection from the strongest eruptions of the last 10 ky into a forcing usable by LOVECLIM likely leads to an overestimation of the amplitude of this forcing. Furthermore, the way volcanism is implemented in LOVECLIM, does not take into account two of the three major climate impacts generated by a volcanic cloud. This is why the VOLC simulation has to be considered as a sensibility experiment.

- One way to make this forcing more realistic is to apply a correction to the radiative forcing to take into account the effect of the downward longwave radiations. This correction should be proportional to the size of the eruption and, for instance, could consists in dividing the radiative forcing by 2.5 for an eruption corresponding to 100 times the one of the Pinatubo according to Jones et al. (2005).

- In the VOLC simulation, volcanism has an impact on the climate that is greater at short term and lasts up to a maximum of few decades (Fig. 3.11), except on the global temperature of the ocean (Fig. 3.20). Clustered eruptions can induce an additional influence of volcanism at multi-decadal to centennial timescales.

- In response to a volcanic eruption, the surface temperature drops (Fig. 3.10). The magnitude of this drop is linearly proportional to the amplitude of the volcanic eruption in LOVECLIM (Fig. 3.9), while it is not the case for the recovery timing which follows a saturation curve (Fig. 3.11).

- Moreover, even if the forcing used is strong, there is no long-term state shift in the simulation. We have taken an extreme case and volcanism has a clear impact on the climate system on periods of a few decades with maximum amplitude of global mean cooling of about 6°C on annual average (Fig. 3.8). Nevertheless, this kind of forcing cannot induce changes that last a few hundred years.

- The comparison of our results with the one of GCMs over the Holocene, the investigation of the vegetation response to the volcanic forcing and further analysis of the oceanic feedbacks, are interesting perspectives when the results of a new simulation driven by a more realisitic forcing will be available.

CHAPTER 4

The assimilation of the Holocene surface temperature multi-centennial variability

This chapter investigates the ability of LOVECLIM to reproduce the observed variations of surface temperature at the multi-centennial timescale. Following the procedure of Wanner et al. (2011), the signal assimilated is obtained by removing high- and low-frequency variability from the temporal series of surface temperature reconstructions derived from proxy records. In contrast to the simulations presented in chapter 2 that were using a constant forcing, the analysis of multi-centennial variability requires transient experiments. This chapter demonstrates that LOVECLIM can be driven by the data assimilation methodology to follow the multi-centennial signal depict by surface temperature proxy-based reconstructions. This has been shown by focussing on a cold period in the Arctic around 2.7 kyBP.

4.1 Introduction

This chapter and the previous one have been developped in parrallel and are connected by a common goal: studying the centennial and multi-centennial fluctuations that are superimposed on the long-term trends over the Holocene. In this chapter, the ability of LOVECLIM to reproduce the observed surface temperature variations at the multi-centennial timescale is investigated. Following the procedure of Wanner et al. (2011), the signal assimilated is obtained by removing high- and low-frequency variability to the temporal series of surface temperature reconstructions derived from proxy records.

This chapter builds on chapter 2 of this thesis in which we have demonstrated that the data assimilation can drive LOVECLIM to reproduce the long-term local climate response. Here, the goal is to explore if LOVECLIM can also be driven by the data assimilation to reproduce the observed variations at the centennial timescale.

Section 4.2 aims to describe and apply the methodology of Wanner et al. (2011) to this thesis database of proxy record. This section also details the different simulations realized and describes which proxy-based reconstructions are used by the data assimilation. In section 4.3, the results of the simulations conducted with data assimilation are presented and discussed. Particularly, it is established whether or not the main objective of this chapter is fulfilled, i.e. verify that the data assimilation methodology can be used to drive the LOVECLIM climate model to reproduce the multi-centennial variations of surface temperature. Finally, the main findings of this study are summed up in the conclusion.

4.2 Methodology

4.2.1 The procedure proposed by Wanner et al. (2011)

Wanner et al. (2011) used 46 surface temperature reconstructions and 35 humidity/precipitation time series based on various proxies. They also used 34 proxies defining glacier advances. The temperature and humidity records have been selected among more than 500 reconstructions. They were chosen on the basis of the following criteria. They have a precise site description, an average temporal resolution better than 160 years and a temporal coverage of at least 70% for the last 10 kyBP. Each temperature or humidity reconstruction, i.e. each time series, has been filtered to keep the multi-centennial variability by removing high- and low-frequency variability. Such filtering is done using a spline-fit with a cut-off frequency, respectively of 500 years for high-frequency variability and 3000 years for low-frequency. The result they obtained for one of the 46 proxy-based reconstructions of surface temperature is shown in the upper panel of Fig. 4.1.

The standardized difference between the two filtered time series, i.e. the result of the 500 year filter minus the result of the 3000 year filter, is the multi-centennial variability (lower panel of Fig. 4.1). A threshold of plus or minus one half of a standard deviation of the Holocene mean value defines the periods that substantially deviates from the 3000 year filter, i.e. the Holocene trend. With respect to the temperature time series, the periods above the threshold are considered as warmer than the Holocene trend, while the ones below are

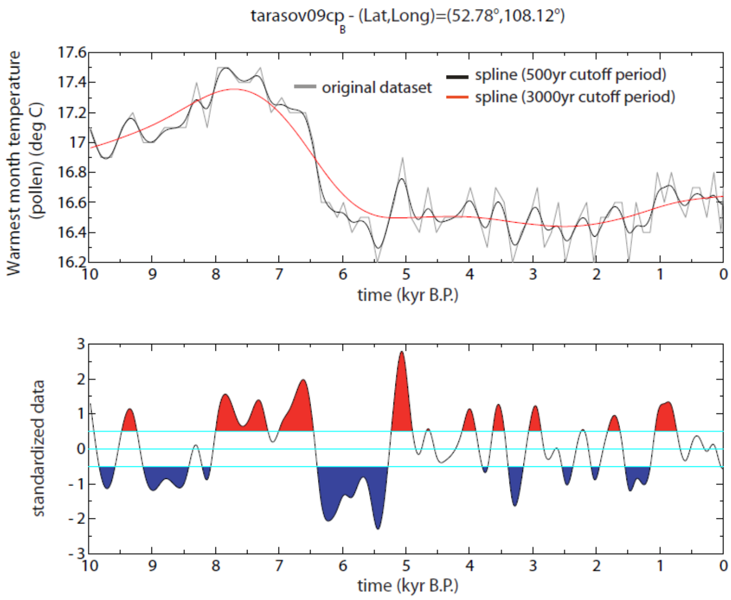

Figure 4.1: This figure comes from the Holocene Climate Atlas (HOCLAT) presented in Wanner et al. (2011). **Upper panel**: surface temperature reconstruction based on pollen retrieved in the Lake Baikal sediment core (grey curve). The smoothing splines with a cut-off frequency of 500 and 3000 years are shown in black and red, respectively. **Lower panel**: standard deviation between the spline with a cut-off frequency of 500 years and the spline with a cut-off frequency of 3000 years. The periods that are above and below one half of the standard deviation are considered as warm in red and cold in blue, respectively.

colder. Regarding the humidity reconstructions, the threshold defines more humid or dry periods.

The cold periods of each proxy-based reconstruction of surface temperature can be presented in function of the latitude (Fig. 4.2). In this figure, each blue horizontal bar represents a colder period. The length of the horizontal bar is the length of the cold period. For each reconstruction, this length is the amount of years below the threshold that define the colder periods. This provides information about the location and timing of the cold periods. To characterize the periods when several multi-centennial cold events occur simultaneously in different records, the sum of the cold events can be calculated as a function of time. In Fig. 4.3a, the sum is inversely weighted by the number of available proxy-based reconstructions at a given time and smoothed by a 50-year moving average. The same procedure is applied for the glacier advances (Fig. 4.3b).

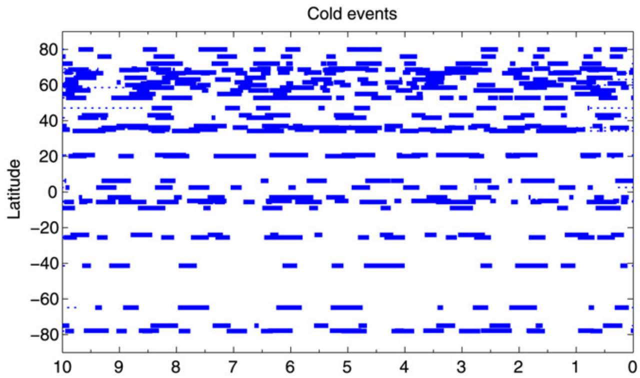

Figure 4.2: Fig. 2a of Wanner et al. (2011). The blue horizontal dashed lines represent the cold periods based on 46 time series of temperature shown as a function of latitude.

Additionally, for comparison purposes, the Bond cycles have been added to Fig. 4.3. These cycles, whose existence have been postulated by Bond et al. (1997,2001), are Holocene quasi-periodic cycles with an average length of about 1470±500 years that Bond et al. (2001) defined as follows: "A prominent feature of the North Atlantic's Holocene climate is a series of shifts in ocean surface hydrography during which drift ice and cooler surface waters in the Nordic and Labrador Seas were repeatedly advected southward and eastward, each time penetrating deep into the warmer strands of the subpolar circulation".

Then, based on the sum of the cold periods, on the Bond cycles and on the sum of the glacier advances, Wanner et al. (2011) have distinguished six remarkable cold events during the last 10 kyBP: at 8.2, 6.3, 4.7, 2.7, 1.55 and 0.55 kyBP. They are depicted in Fig. 4.3 by the blue vertical bars with a length of 200 years. We have added in Fig. 4.3 the pink vertical bars to show the length of the cold periods according to Tab. 5 of Wanner et al. (2011).

4.2.2 The procedure of Wanner et al. (2011) applied to the surface temperature data set of this thesis

The data set of the proxy-based surface temperature reconstruction used in this chapter is very similar to the one of chapter 2. The differences lie in the selection rules, which have slightly changed in order to keep more proxy-based reconstructions and to restrain the study area to the mid- to high-latitudes. Each selected reconstruction should (1) represent the air or sea surface temperature, (2) be located northward of 40°N, (3) be continuous between 6 kyBP

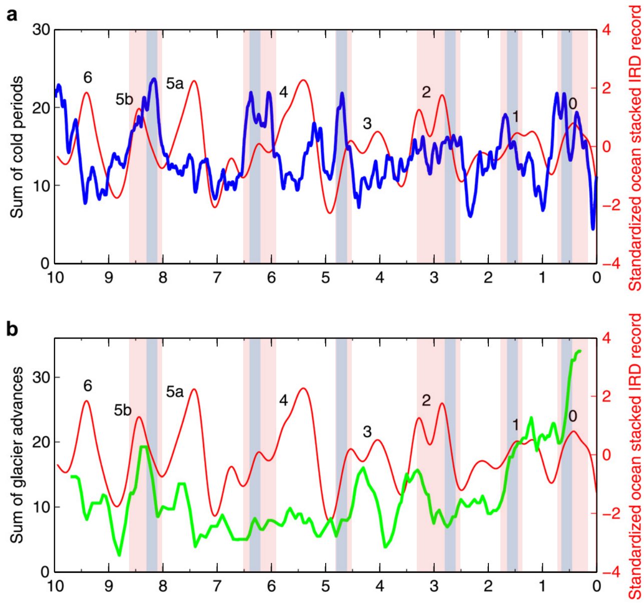

Figure 4.3: Fig. 3a,b of Wanner et al. (2011). (a) Weighted and smoothed curve (see the explanations in text) that represents the sum of cold periods (blue curve). (b) Same as (a) but for glacier advances (green curve). The red curves, added for comparison purposes, are the standardized ocean stacked ice rafted debris record representing the Bond events no. 0-6 (Bond et al., 2001). Blue vertical bars denote the time of the six remarkable cold events with a 200-year window length. The pink vertical bars represent the length of the cold periods according to Tab. 5 of Wanner et al. (2011).

and 1 kyBP, (4) have at least a temporal resolution of 250 years over the period 6 kyBP to 450 yBP and (5) be freely distributed. As in chapter 2, preference is given to the proxy-based reconstructions that represent seasonal information, instead of annual proxy-based reconstructions. Finally, we decided not to take into consideration the reconstructions based on ice cores that are not uplift-corrected, as they do not represent a surface temperature. The 48 reconstructions selected according to these rules are listed in Tab. 4.1. Their location is shown in Fig. 4.4, while the temporal series are displayed in appendix A. Within those 48 reconstructions, those used in chapter 2 are highlighted in Tab. 4.1. The three proxies northward of 40°N that were used in chapter 2 and have not been kept are: N3 and N4 (Tab. 2.1) because they are not freely distributed and N15 (Tab. 2.1) because it represents likely a subsurface signal rather than a sea surface temperature. For the simulations using data assimilation, proxies representing the same variable and the same season are merged

ID	Lat	Lon	Site or core name	Area	Archive type	Proxy-based reconstruction	Temporal interpretation	Reference
1	75.00	13.97	M23258	Barents slope	Alkenone - Uk37	SST	Summer	Marchal et al. (2002)
2	66.97	7.63	MD95-2011	Norwegian Sea	Alkenone - Uk37	SST	Summer	Calvo et al. (2002)
3	58.76	-25.96	MD95-2015	North Atlantic	Alkenone - Uk37	SST	Annual	Marchal et al. (2002)
4	43.88	-62.80	OCE326-GGC30	Northwest Atlantic	Alkenone - Uk37	SST	Annual	Sachs (2007)
5	43.48	-54.87	OCE326-GGC26	Northwest Atlantic	Alkenone - Uk37	SST	Annual	Sachs (2007)
6	66.60	-17.58	JR51-GC35	Nordic Seas	Alkenone - Uk37	SST	Annual	Bendle and Rosell-Melé (2007)
7	41.68	-124.93	ODP1019C	North Pacific	Alkenone - Uk37	SST	Annual	Barron et al. (2003)
8	44.53	145.00	MD01-2412	Okhotsk Sea	Alkenone - Uk37	SST	Autumn	Harada et al. (2006)
9	75.00	13.97	Kasten core 23258-2	Norwegian Sea	Forams (planktic)	SST	Summer	Sarnthein et al. (2003)
10	75.00	13.97	Kasten core 23258-2	Norwegian Sea	Forams (planktic)	SST	Winter	Sarnthein et al. (2003)
11	62.09	-17.82	RAPiD-12-1k	North Atlantic	Mg/Ca	SST	May, June	Thornalley et al. (2009)
12	61.00	-25.00	ODP 984	North Atlantic	Mg/Ca	SST	Winter	Came et al. (2007)
13	57.43	-27.90	MD99-2251	North Atlantic	Mg/Ca	SST	August	Farmer et al. (2008)
14	66.97	7.64	MD95-2011	Norwegian Sea	Radiolarian (polycystine)	SST	Summer	Dolven et al. (2002)
15	68.37	18.70	Lake Njulla	Sweden (Abisko valley)	Midges (chironomid)	ST	July	Larocque and Hall (2004)
16	62.35	-138.35	Hanging lake	Canada	Midges (chironomid)	ST	July	Kurek et al. (2009)
17	61.37	-143.60	Moose lake	Alaska	Midges (chironomid)	ST	July	Clegg et al. (2010)
18	61.48	26.07	Laihalampi lake	Southern Finland	Pollen	ST	Annual	Heikkilä and Seppä (2003)
19	69.20	21.47	Toskaljavri lake	Northern Finland	Pollen	ST	July	Seppä and Birks (2002)
20	68.68	22.08	Tsuolbmajavri lake	Northern Finland	Pollen	ST	July	Seppä and Birks (2001)
21	60.08	15.83	Stora Gilltjarnen	Sweden	Pollen	ST	Annual	Antonsson et al. (2006)
22	58.55	13.67	Lake Flarken	Sweden	Pollen	ST	Annual	Seppä et al. (2005)
23	74.47	98.63	Levinson-Lessing lake	Russia	Pollen	ST	Annual	Andreev et al. (2003)
24	58.58	26.65	Raigastvere lake	Estonia	Pollen	ST	Annual	Seppä and Poska (2004)
25	52.78	108.12	Kotokel lake	Russia	Pollen	ST	January	Tarasov et al. (2009)
26	52.78	108.12	Kotokel lake	Russia	Pollen	ST	July	Tarasov et al. (2009)
27	68.00	60.00	Khaipudurskaya Guba lake	Arctic Russia	Pollen	ST	January	Andreev and Klimanov (2000)
28	68.00	60.00	Khaipudurskaya Guba lake	Arctic Russia	Pollen	ST	July	Andreev and Klimanov (2000)
29	60.00	-57.50	Labrador region	Canada	Pollen	ST	January	Viau and Gajewski (2009)
30	60.00	-57.50	Labrador region	Canada	Pollen	ST	July	Viau and Gajewski (2009)
31	60.00	-72.50	Northern Quebec region	Canada	Pollen	ST	January	Viau and Gajewski (2009)
32	60.00	-72.50	Northern Quebec region	Canada	Pollen	ST	July	Viau and Gajewski (2009)
33	60.00	-100.00	Central Canada region	Canada	Pollen	ST	January	Viau and Gajewski (2009)
34	60.00	-100.00	Central Canada region	Canada	Pollen	ST	July	Viau and Gajewski (2009)
35	60.00	-130.00	MacKenzie region	Canada	Pollen	ST	January	Viau and Gajewski (2009)
36	60.00	-130.00	MacKenzie region	Canada	Pollen	ST	July	Viau and Gajewski (2009)
37	71.34	-113.78	KR02 lake	Canada	Pollen	ST	July	Peros and Gajewski (2008)
38	63.50	1.50	Northwest region	Europe	Pollen	ST	Winter	Davis et al. (2003)
39	63.50	1.50	Northwest region	Europe	Pollen	ST	Summer	Davis et al. (2003)
40	50.00	1.50	Centralwest region	Europe	Pollen	ST	Winter	Davis et al. (2003)
41	50.00	1.50	Centralwest region	Europe	Pollen	ST	Summer	Davis et al. (2003)
42	63.50	32.50	Northeast region	Europe	Pollen	ST	Winter	Davis et al. (2003)
43	63.50	32.50	Northeast region	Europe	Pollen	ST	Summer	Davis et al. (2003)
44	50.00	32.50	Centraleast region	Europe	Pollen	ST	Winter	Davis et al. (2003)
45	50.00	32.50	Centraleast region	Europe	Pollen	ST	Summer	Davis et al. (2003)
46	66.55	13.92	SG93	Norway	Speleothem	ST	Annual	Lauritzen and Lundberg (1999a)
47	80.70	-73.70	Agassiz Ice cap	Greenland	ice core - d18O	ST	Annual	Vinther et al. (2009)
48	71.27	-26.73	Renland Ice Cap	Greenland	ice core - d18O	ST	Annual	Vinther et al. (2009)

Table 4.1: List and description of the proxy-based surface temperature reconstructions used in this chapter. The light grey cells highlight the reconstructions that are also used in chapter 2. For the data assimilation, the following proxies have been merged because they represent the same information and are located in the same grid point of LOVECLIM: the n°19 (hereafter N19) and the N20 under the number N19. The N2 and the N14 under the number N2. The N1 and the N9 under the number N1.

if they are located in the same model grid. The resulting data set contains 45 reconstructions. The list of reconstructions that have been merged is added in Tab. 4.1.

The procedure developed by Wanner et al. (2011) has been applied to these 45 surface temperature reconstructions. The only change operated for practical reasons is the replacement of the spline filter by a LOWESS filter (MathWorks, 2014) using the same cut-off frequencies as in Wanner et al. (2011). The LOWESS filter is a method that uses locally weighted a linear regression to smooth data. The method is local because the smoothed value depends on the neighbors data points within the cut-off frequency. Fig. 4.5 shows the

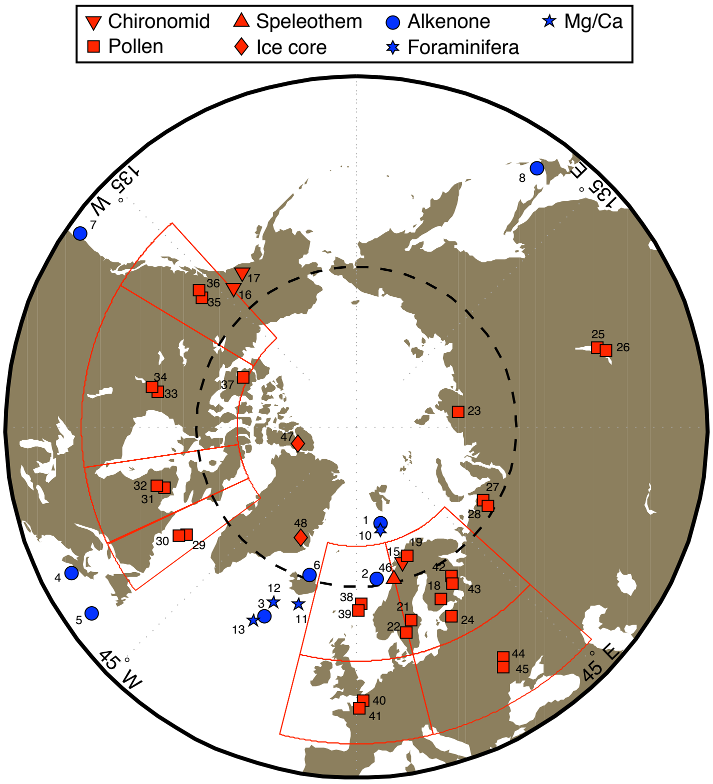

Figure 4.4: The proxy-based reconstructions used in this chapter. The numbers correspond to the reconstructions listed in Tab. 4.1. The black dashed line circle limits the Arctic (66°N-90°N). The red boxes display the areas that correspond to the proxy-based reconstructions of Davis et al. (2003) and Viau and Gajewski (2009). If more than one proxy-based reconstruction is given at the same location, the markers representing the proxy-based reconstructions are slightly shifted for improved readability.

result from the proxy-based reconstruction already described in Fig. 4.1. Comparing the two lower panels of these figures demonstrates that the choice of a LOWESS filter instead of a spline filter does not significantly modify the results even if the spline filter seems to be slightly more sensitive to the multi-centennial variations when comparing the events ~8.2 kyBP, ~4.6 kyBP and ~3.8 kyBP between the two figures.

The cold periods of the 45 temperature reconstructions are presented as a function of the latitude in Fig. 4.6. Additionally, the warm periods and the

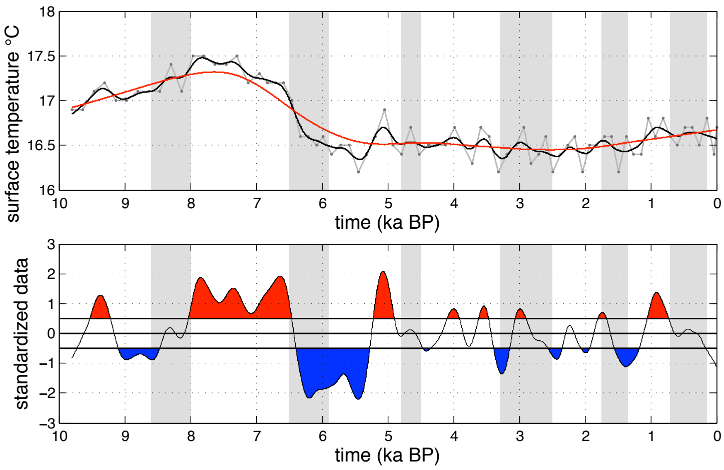

Figure 4.5: Upper panel: Surface temperature reconstruction based on pollen retrieved from the Lake Baikal sediment core (black dots linked by light gray curve), corresponding to reconstruction N26 in Tab. 4.1. The results of the LOWESS filter with a cut-off frequency of 500 and 3000 years are in black and red, respectively. **Lower panel**: the standardized difference between the two filters. The values beyond plus or minus one half of the standard deviation are shaded in red or blue and show the warmer or colder periods than the Holocene trend, respectively. The grey shaded vertical bar represents the cold period found by Wanner et al. (2011).

periods of transition between a warmer and a colder period, have been added to the same figure. Firstly, this figure confirms that these 45 reconstructions are marked by multi-centennial events, as the reconstructions selected by Wanner et al. (2011). Secondly, this figure demonstrates how difficult it is to clearly highlight the Holocene periods that are particularly warmer or colder than the Holocene trend.

Fig. 4.7b presents the sum of the colder, warmer and transition periods that have been inversely weighted by the number of available reconstructions (Fig. 4.7a) and filtered with a 50-year running mean. Fig. 4.7b also indicates that the colder periods discovered by Wanner et al. (2011) do not always coincide with those found with another data set. For instance, the period around 4.7 kyBP contains a greater number of warmer periods than colder periods. This demonstrates that the conclusion of Wanner et al. (2011) about a possible colder period at this time is highly dependent on the data set used. Moreover, for the periods around 2.7 kyBP and around 1.55 kyBP it is not clear that the area located northward of 40°N has experienced particularly cold periods. Besides, both data sets highlight cold periods around 8.2 kyBP,

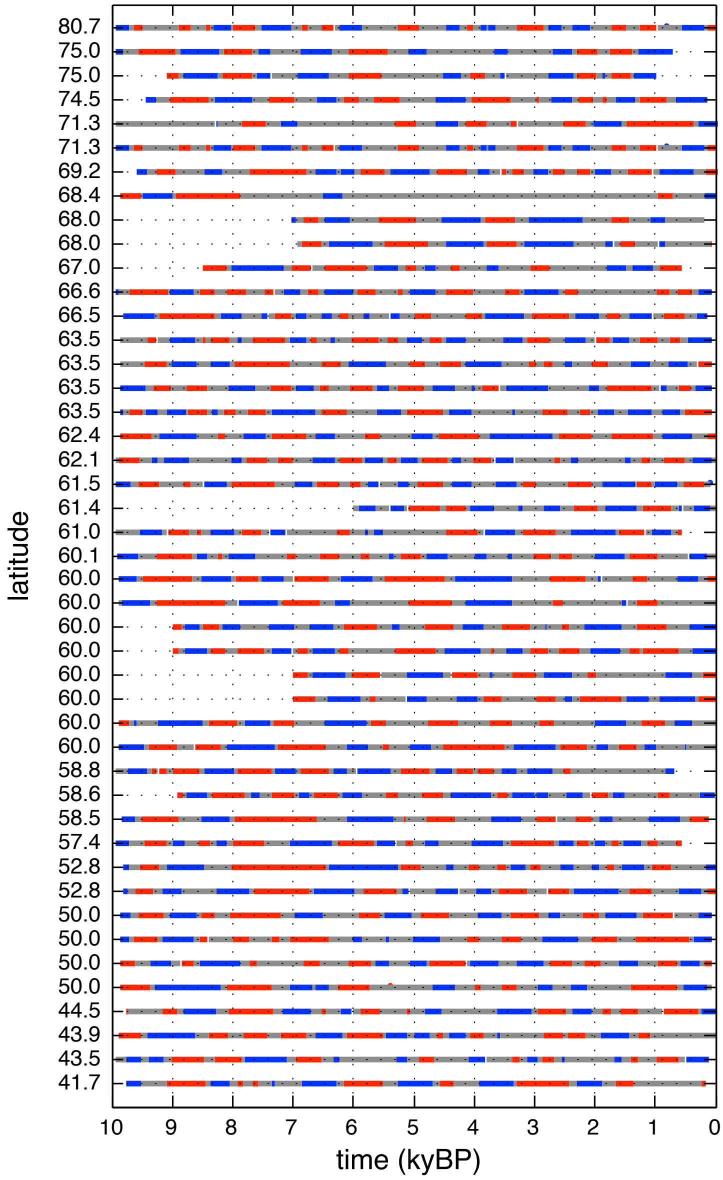

Figure 4.6: For each surface temperature reconstruction, the colder, the warmer or the transition periods are shown in blue, red or grey, respectively, at the latitude of the proxy, as a function of time. The latitude axis is not proportional.

6.3 kyBP and during the Little Ice Age (LIA). The potential origin of the discrepancies between our analysis and the one of Wanner et al. (2011) are investigated in the next section.

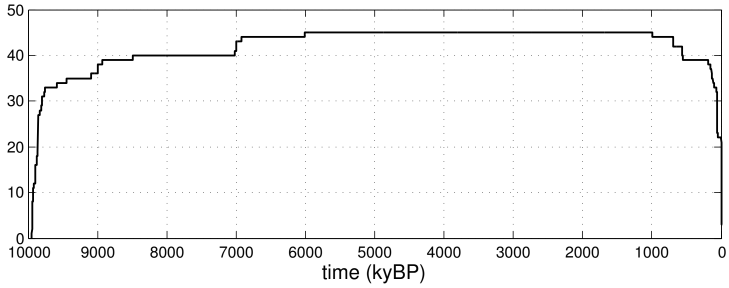

(a) Number of proxies

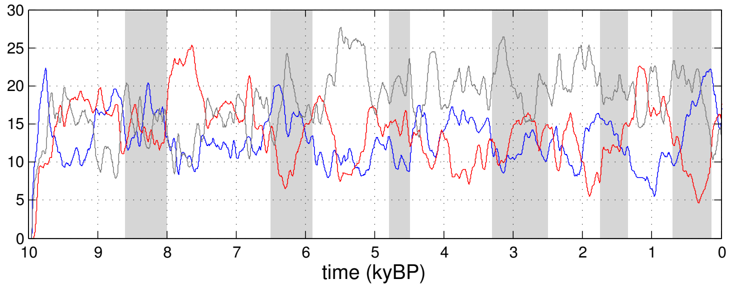

(b) Number of periods

Figure 4.7: (a) Number of available proxy-based reconstructions according to the selection criteria. **(b)**: the sum of cold (blue), warm (red) and transition (grey) events that have been inversely weighted by the number of available proxy-based reconstructions at the given time and smoothed by a 50-year moving average. The grey shaded vertical bar displays the cold period found by Wanner et al. (2011).

4.2.3 Comparison between the present results with the ones of Wanner et al. (2011)

To estimate the length of the cold periods (displayed in pink in Fig. 4.3), Wanner et al. (2011) have only used the number of cold periods as a function of time. Accordingly, the surface temperatures are assumed sufficient to find these cold periods and there is no need to use information from glacier advance or about humidity reconstructions. Hence, we will focus only on the difference between their selection of surface temperature and ours.

Our selection rules regarding the proxy records are different. Wanner et al. (2011) selected reconstructions with a higher temporal resolution and with a longer time coverage. But the rule that produces the main difference between our results and the ones of Wanner et al. (2011) is that we only select the reconstructions northward of 40°N, while they keep the surface temperature reconstructions located all over the globe to be as much as possible representative of the global scale.

The majority of the 46 temperature reconstructions used by Wanner et al. (2011) (more than 70%) are located in the Northern Hemisphere. From those reconstructions, two-thirds are derived from continental proxies, while one-third comes from oceanic archives. About a third of the Northern Hemispheric proxies used by Wanner et al. (2011) is also used in this chapter, in other words a quarter of the proxies is common.

Among the reconstructions selected by Wanner et al. (2011) located northward of 40°N, 10 are not in our selection. Specifically, Wanner et al. (2011) have included two oceanic reconstructions, four reconstructions based on pollens and four reconstructions derived from ice cores that we have not selected. Regarding the oceanic reconstructions, the first one is the SST reconstruction of Risebrobakken et al. (2003); that reconstruction likely represents a subsurface signal rather than a sea surface temperature. That is the reason why it does not appear in our selection. The oceanic reconstruction presented by Mayewski et al. (2004) is the second one; that data set was not available at the time of the database elaboration, which explains why we did not use it. The pollen-based reconstructions in Wanner et al. (2011) come from Viau et al. (2006) but we use the updated version published by Viau and Gajewski (2009). For the four reconstructions based on ice cores, as in chapter 2, we do not use the ice cores that are not uplift-corrected, explaining the difference compared to Wanner et al. (2011).

The reconstruction that are selected in the present work and that Wanner et al. (2011) have not used, have the following id in Tab. 4.1: N1 to N6, N8 to N13, N16, N17, N23, N27 to N45, N47 and N48.

As explained above, we have applied the methodology developed by Wanner et al. (2011), with the exception that the spline filter has been replaced by the LOWESS filter. As we demonstrated it before, the effect on the result is weak, which does not explain all the differences in the results of both studies.

To summarize, the procedure of Wanner et al. (2011) allows putting in evidence multi-centennial variations from an individual reconstruction. At a more global scale, i.e. using several reconstructions, the procedure is very sensitive to the reconstructions chosen to define periods during which a greater number of warmer or colder events took place. This must be kept in mind in the interpretation of our results.

4.2.4 Does the use of a volcanic forcing improve the consistency between the Holocene climate simulated by LOVECLIM and the cold periods of Wanner et al. (2011)?

Following the methodology of Wanner et al. (2011), the Holocene global surface temperature of the simulation VOLC, used in chapter 3, has been filtered with a LOWESS filter with a cut-off frequency of 500 years (hereafter LOWESS500) and a LOWESS filter with a cut-off frequency of 3000 years (hereafter LOWESS3000). The cold periods highlighted by the difference between these two filters are in black in Fig. 4.8. In the same figure, the six cold periods of Wanner et al. (2011) are shown in green. Additionally, the periods of intense volcanism, i.e. the periods during which volcanic eruptions inject at least 75 Tg of sulfate in the atmosphere, are shown in the same figure. We compare the cold periods of Wanner et al. (2011) with the ones found using the global temperature of the VOLC simulation since Wanner et al. (2011) postulate that their proxy-based data set is representative of the whole world.

This comparison proves that the volcanic forcing influences the occurence, the length and the timing of the cold periods. For instance, the cold period between 9 and 8 kyBP in the simulation VOLC is due to the cumulative effect of several major eruptions. This analysis shows that the volcanic forcing can also contribute to cold periods close to the 8.2 kyBP event. It also confirm, even if the volcanic forcing used is likely overestimated, that volcanoes have likely played a role in the onset of the LIA as suggested by Crowley et al. (2008), Miller et al. (2012) and Schleussner and Feulner (2013). For the other

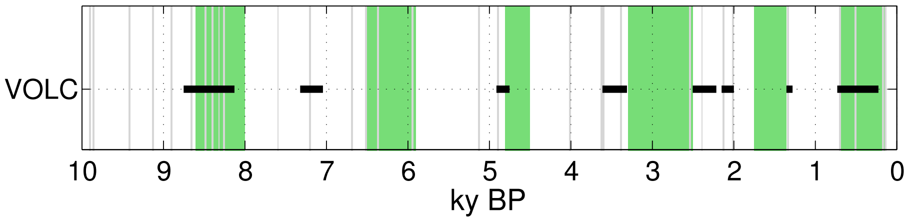

Figure 4.8: Timing and length of the cold periods of Wanner et al. (2011) (green) and of the VOLC simulation (black). The grey vertical bars show the volcanic eruptions used in chapter 3 that inject more than 75 Tg of sulfate in the atmosphere.

periods, the cold events in the simulation VOLC do not correspond to the ones described by Wanner et al. (2011).

4.2.5 Identification of a regional cold period

Fig. 4.7 highlights that no cold event is common in more than 50% of the proxies located north of 40°N. By restricting the domain considered, from 40°N-90°N to the Arctic (66°N-90°N), several particularly cold periods are more clearly defined during the Holocene (upper panel of Fig. 4.9). Two periods, during which at least two-thirds of the 13 Arctic proxy-based reconstructions, outline colder periods at 6.4 kyBP and 2.65 kyBP. Other periods as the one around 8.25 kyBP are also remarkable as approximately a third of the proxy-based reconstructions show a cold period, while very few show a warmer period. The same applies for the period around 4.45 kyBP. We choose to focus on the period around 2.65 kyBP (2.8-2.6 kyBP) (lower panel of Fig. 4.9). The 13 proxy-based reconstructions used to define this period are inside the dashed black circle in Fig. 4.4.

4.2.6 The experimental design

The experimental design is more complicated than in chapter 2 because here we establish the basis to perform transient data assimilation. The forcing used to represent the Holocene climate is the same as in chapter 3 with the exception that we use a random volcanic forcing with a magnitude of about ± 1 Wm^{-2} to represent the uncertainty in the transient forcing. The data assimilation technique has been explained in details in the introduction and in chapter 2. Here, we will only review the changes we have brought to allow the transient data assimilation.

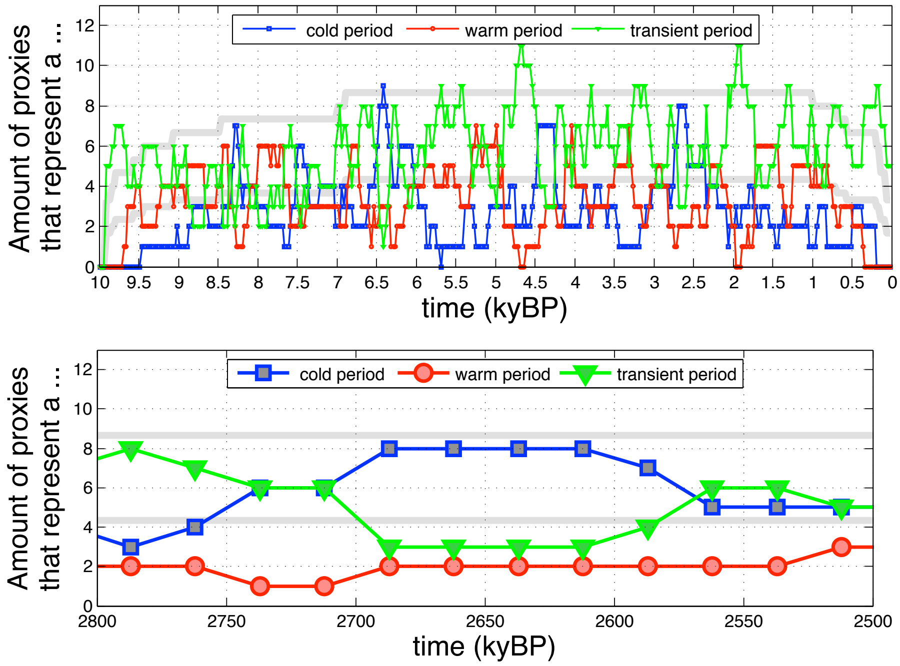

Figure 4.9: Number of proxy-based reconstructions of surface temperature that represent a cold, warm or transition period between warmer and colder periods. **Upper panel**: These numbers are calculated for each 25-year time slice taking into account the 13 Arctic reconstructions. **Lower panel**: zoom over the period 2.8 to 2.6 kyBP. The grey horizontal lines in each panel represent respectively one-third and two-thirds of the number of reconstructions used.

4.2.6.1 Modification of the data assimilation procedure

Compared to chapter 2, only two modifications are made. First, the variable that we assimilate is the difference of surface temperature between the result of the filter LOWESS500 and the result of LOWESS3000. The value of this multi-centennial variability evolves with time. Second, the model reference is no longer fixed. In this design, the reference also evolves with time and is equal to the results of an ensemble transient simulations driven by external forcing (as the NOVOLC simulation described in chapter 3), filtered by LOWESS3000. In other words, the anomalies of surface temperature are calculated with respect to the orbital forcing response, since at a multi-millennial timescale, the orbital forcing is the major one that influences climate. As a consequence, any bias in the long-term response does not have any impact on the model-data comparison at multi-centennial timescales

4.2.6.2 The different simulations

Because we have seen in chapter 2 that it is difficult to assimilate a signal that is not clear, we have moved forward step by step, beginning by the simplest possible case. At first, our objective is to provide, through data assimilation, a clear constrain to LOVECLIM in order to see how the model is behaving and to be sure that this new design of transient data assimilation works properly. The first simulation is therefore a simulation with data assimilation in which the selected assimilated proxy-based reconstructions all display a cold period between 2.8 and 2.6 kyBP. This concerns 11 of the 13 Arctic reconstructions. The values assimilated are constant, even if the simulation is transient, and represent the minimum value of each reconstruction over the cold period 2.8 to 2.6 kyBP. The simulation is therefore similar to a time slice simulation performed in the framework of a transient simulation. The simulation is performed with 96 particles and covers the period between 2.8 to 2.6 kyBP. This simulation is called DAMIN11 (Tab. 4.2). The second simulation, called DAMIN13, is the same as DAMIN11 except that the two remaining reconstructions that do not have a cold period between 2.8 and 2.6 kyBP are also assimilated. The values assimilated are still constant; they are the minimum values over the period 2.8 to 2.6 kyBP for all proxies as in DAMIN11. Finally, the third simulation, named DAMEAN13, is the same as DAMIN13 except that the mean values over the period 2.8 to 2.6 kyBP are assimilated.

For these three simulations with data assimilation, the reference model values used during the assimilation process should be the result of the LOWESS3000 from the 12 members NOVOLC simulation. Nevertheless, we have chosen to use the mean state of a 96 member simulation performed without data assimilation called REF, for simplicity. We can make this choice because the values assimilated are constant through time and, therefore, the reference can also be constant. The model reference approximation using the average of 96 members over 200 years is close to the average calculated over the 200 years of the LOWESS3000 from the NOVOLC simulation. Finally, because the values assimilated are the result of an average over 200 years, the uncertainties in the age model can be neglected.

This is not the first time that a transient data assimilation is performed with LOVECLIM. For instance, Goosse et al. (2012b) have assimilated over the last 1500 years the decadal mean large-scale surface temperature reconstruction of Mann et al. (2009). This reconstruction is mainly based on tree ring, ice core, coral, speleothem and sediment records and displays temperature fluctuations

Name	Description
REF	Simulation performed without data assimilation with 96 particles. The period covered is 2.8 to 2.6 kyBP.
DAMIN11	Simulation performed with data assimilation with 96 particles covering the same period than the simulation REF. The reconstructions that are assimilated, are the ones that display a colder period than the Holocene trend between 2.8 and 2.6 kyBP. For each proxy-based reconstruction, the value assimilated is constant and is the minimum value over the period 2.8 to 2.6 kyBP. The 11 reconstructions assimilated are the following: N1, N6, N10, N15, N19, N23, N27, N28, N37, N47 and N48.
DAMIN13	Same simulation that DAMIN11 except that two more reconstructions (N2 and N46) that display a warm period are assimilated. Their minimum value are assimilated.
DAMEAN13	Same simulation that DAMIN13 except that the mean value over the period 2.8 to 2.6 kyBP is assimilated.

Table 4.2: List and description of the simulations used in this chapter.

two to three times larger than the ones we use in this chapter. This is explained by the fact that proxy-based reconstructions have a higher resolution and therefore a higher variability over the last millennium than over the rest of the Holocene. In the simulation with data assimilation of Goosse et al. (2012b), the constraint is therefore stronger than the one we used here.

4.3 Results and discussion

To highlight the output of the data assimilation, Fig. 4.10 shows the agreement between model results and each proxy-based reconstruction. In this figure, the difference of surface temperature between the LOWESS500 result and the LOWESS3000 result is shown for each proxy-based reconstruction by the thick horizontal bar. Depending on the simulation, the proxy-based anomaly represented by the horizontal bar is colored differently: DAMIN11 in green, DAMIN13 in blue and DAMEAN13 in black. For each proxy-based reconstruction, its associated uncertainty is represented by the vertical bar, keeping the same color code. For these uncertainties, please refer to section 2.2.3 of the present thesis for more information.

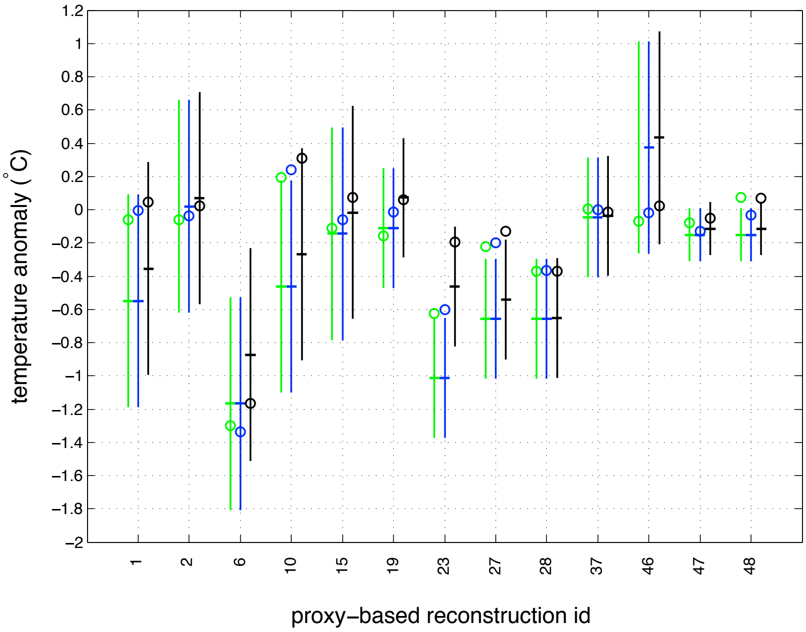

Figure 4.10: Reconstructed surface temperature anomalies (thick horizontal bar) that are assimilated in LOVECLIM. This is presented for each proxy-based reconstruction for the three simulations: DAMIN11 (in green), DAMIN13 (in blue) and DAMEAN13 (in black). For each proxy, the small circle is the model anomaly (see in the text for more information) and the vertical lines represent the estimated uncertainty.

In Fig. 4.10, the model anomaly is indicated by a small circle. Specifically, the circle represents the difference between the mean result provided by simulation with data assimilation (DAMIN11 or DAMIN13 or DAMEAN13) over the period 2.8-2.6 kyBP and the corresponding reference value, i.e. the ensemble average over the 200 years of the simulation REF. In this study, the proxy-based reconstructions N2 and N46 are not used for the simulation DAMIN11, which explains the absence of a horizontal green bar. Indeed, these two reconstructions are not colder during the period 2.8-2.6 kyBP.

Fig. 4.10 outlines that, as required by the experimental design, the values of the 11 proxy-based reconstructions used to constrain the simulation DAMIN11 are negative. Concerning the simulation DAMIN13, the two additional reconstructions used are positive (N2 and N46). For the simulation DAMEAN13, the proxy-based anomalies are smaller than the ones used in the two other simulations. This is because the anomalies represent the average of the 200 years period and not the minimum value of this period. Moreover, in this last simulation, the anomaly of N19 becomes positive. The second column of Tab. 4.3 summarizes this information. The constraint, imposed by the data set on the LOVECLIM model simulation throughout the data assimilation process, is therefore strongest in the case of DAMIN11 and weakest in DAMEAN13. The third column of Tab. 4.3 shows clearly that LOVECLIM is more locally constrained if the signal of the data set used is stronger and homogeneous. This column shows, for each simulation performed with data assimilation, the mean model anomaly signal at locations where the reconstructions are available. The stronger the constraint, i.e. the clearer the signal of the proxy-based reconstruction, the stronger the impact on the model.

simulation name	signal of the proxy-based reconstruction (°C)	signal of the simulation with data assimilation (°C) at the location of the proxies
DAMIN11	-0.51	-0.31
DAMIN13	-0.38	-0.26
DAMEAN13	-0.23	-0.15

Table 4.3: Mean of the proxy-based reconstructions data set used in the simulations with data assimilation (2^{nd} column). The 3^{rd} column shows the corresponding value in the simulations with data assimilation providing a measure of the constrain imposed by the data assimilation.

In Fig. 4.10, the LOVECLIM simulation is consistent with a particular proxy-based reconstruction if the model result (the small circle) is close to the reconstruction (thick horizontal bar) or at least if the model anomaly (the small circle) falls within the estimated uncertainty of the proxy-based reconstruction (vertical bar). This is the case for almost all the proxy-based reconstructions, which means that the LOVECLIM model can manage to be consistent with the forcing and the proxy-based reconstructions used. Pay attention to the fact that the proxy-based reconstruction signal is weak compared to the uncertainty. This plays a role in the agreement between the model and the proxy-based reconstruction.

The larger and clearer the signal to assimilate, in other words the more coherent the proxy-based reconstructions, the higher the constraint on the model. Let's illustrate this with the following example. The reconstruction N1 signal of -0.55°C drives the DAMIN11 and DAMIN13 simulations to have this difference with simulation REF (Fig. 4.10), at the location of the reconstruction N1. The result is that the model difference is -0.06°C for the simulation DAMIN11 and -0.006°C for DAMIN13. The difference in these results is due to the constraint which is stronger in simulation DAMIN11 in comparison to DAMIN13 (see second column of Tab. 4.3). A stronger total constraint therefore leads to obtain locally a better coherence between DAMIN11 simulation and the proxy-based reconstruction N1, than between the same proxy-based reconstruction and simulation DAMIN13. The same applies for simulation DAMIN11 with respect to DAMEAN13 simulation or for the DAMIN13 simulation compared to the DAMEAN13 simulation. This difference between the three simulations is clearly seen in Fig. 4.10 for the proxy-based reconstructions N1, N15, N19, N23 and N27.

Fig. 4.10 also informed us that taking into account the information given by the data set used to constrain simulation DAMIN11 (i.e. the reconstructions N1, N6, N10, N15, N19, N23, N27, N28, N37, N47 and N48), the LOVECLIM physics combined to the forcing provide a slightly negative anomaly where the reconstructions N2 and N46 (see green circles) are located. If the signal of these two reconstructions is taken into account (in DAMIN13 and DAMEAN13 simulations), the model tries to find a way to obtain a positive anomaly where these two proxy-based reconstruction (N2 and N46) are located. The model performs well for reconstruction N2, since its signal is very small and therefore not so inconsistent with the other surrounding proxy-based reconstructions over Northern Europe. For reconstruction N46, it is difficult for the model to get a positive anomaly of about 0.4°C on an annual average in Norway, while the surrounding proxies suggest a negative one. LOVECLIM therefore does its best by providing a very small positive anomaly.

For N28 and N37, the other proxy-based reconstructions used in the process of data assimilation do not influence the way data assimilation is able to force the LOVECLIM results to be more consistent with these reconstructions. Indeed, there is no difference in the results provided by the three simulations regarding those two reconstructions (Fig. 4.10).

For reconstruction N10, data assimilation does not succeed to drive LOVECLIM results to a negative anomaly. Nevertheless, the anomaly is more positive in DAMEAN13 than in DAMIN13 and DAMIN11.

Before analyzing the spatial patterns of the simulated changes, we can conclude that the results of three very simple simulations, performed with data assimilation, are coherent. The more LOVECLIM is constrained by an inhomogeneous reconstruction data set, the closer the results and the conclusion of this study will be to those obtained in chapter 2. Besides, these three simulations have proven that the transient data assimilation framework works properly and is ready for longer simulations.

4.3.1 Spatial patterns of surface temperature and geopotential height

The data assimilation process brings changes to the model results that are not confined to the local area where the proxy-based reconstructions are located. This is illustrated by the average difference between the surface air temperature of each simulation using data assimilation and the REF simulation. In Fig. 4.11, this difference is shown in annual mean and for July and January as at least one reconstruction is assimilated for those periods. These changes are also shown in Fig. 4.12 for sea surface temperature.

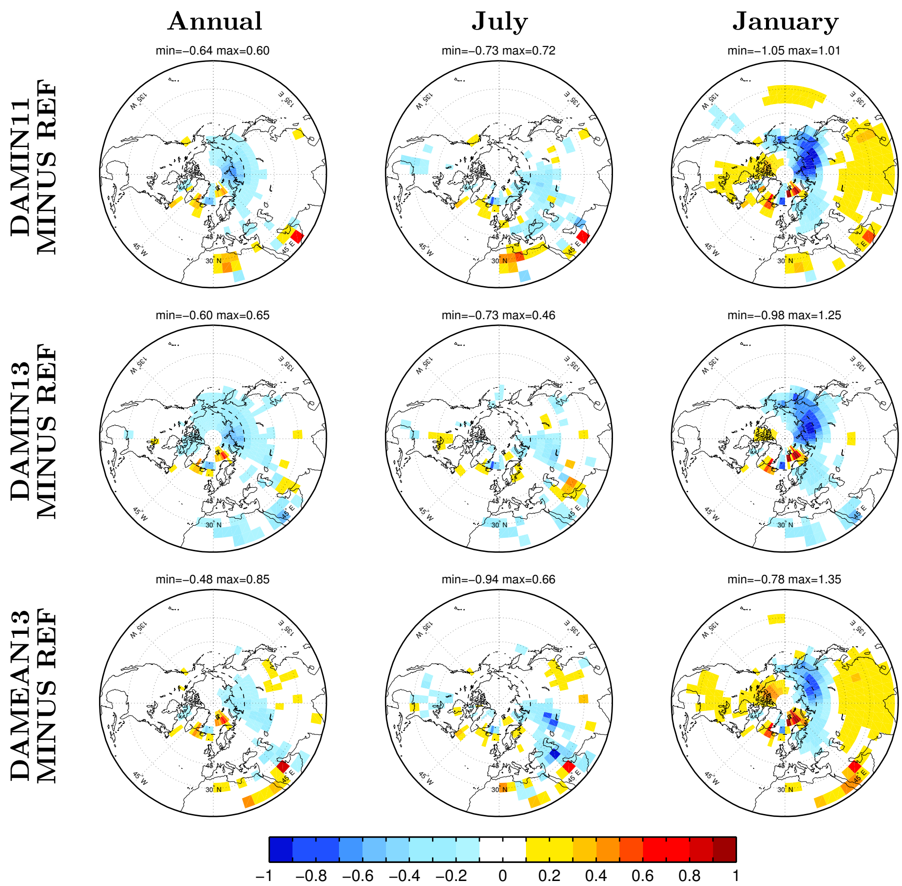

Figure 4.11: Average 200 year surface air temperature difference between the simulation DAMIN11 and REF for different months (upper panel). The same difference for DAMIN13 simulation (middle panel) and DAMEAN13 simulation (lower panel).

As expected, for the surface air temperature, the main change in the simulation with data assimilation compared to REF is a net cooling of the surface in North Asia and in Northern Europe (Fig. 4.11). This cooling is centered between the Laptev Sea and the Kara Sea at the location of the reconstruction N23. For several reasons, we can conclude that the amplitude of this cooling is highly influenced by reconstruction N23. First of all, this reconstruction is annual and influences throughout the year its surroundings with a highly negative anomaly (in DAMIN11 and DAMIN13 simulations) compared to the closest reconstructions N27 and N28 (Fig. 4.4 and 4.10). Second, the maximum cooling in the simulations with data assimilation is proportional to the anomaly of the reconstruction N23. Indeed, in DAMIN11 and DAMIN13 simulations, the anomaly of reconstruction N23 is -1°C (Fig. 4.10) and the maximum cooling in the simulations is -0.64°C (DAMIN11) and -0.60°C (DAMIN13), respectively (Fig. 4.11). When the anomaly of reconstruction N23 is about -0.5°C (in DAMEAN13), the maximum cooling is -0.48°C.

Surface air temperature changes are more widespread than the changes in sea surface temperature, the oceanic variations being much weaker in LOVECLIM (compare Fig. 4.11 and 4.12). Nevertheless, the changes at the local scale for the SST (Fig. 4.12) are similar in magnitude to those of surface air temperature (compare minimum and maximum of Fig. 4.11 and 4.12). Likewise, for both variables, the changes in the signal are mainly located in the Northern Hemisphere where the proxy-based reconstructions are assimilated. More particularly concerning SST, the changes are almost only located in areas where a proxy-based reconstruction of the SST used in the assimilation is located (Fig. 4.12).

Data assimilation also drives the LOVECLIM model to produce warming in some areas (Fig. 4.11). These warmings have the same magnitude as the cooling. As a result, the annual global surface temperature of DAMIN11 simulation is almost not impacted by the data assimilation (upper panel of Fig. 4.13). The same applies for the two other simulations with data assimilation. At the regional scale, the data assimilation can therefore push LOVECLIM towards the proxy-based reconstructions (Fig. 4.10), but at the global scale the changes are almost not discernible (see DAMIN13 or DAMEAN13 simulation on the upper panel of Fig. 4.13) or not discernible at all (see DAMIN11 simulation in the upper panel of Fig. 4.13). Nevertheless, over a smaller area as the Arctic, the assimilation of 11 to 13 proxy-based reconstructions produces a net annual cooling of the surface in comparison to REF (lower panel of Fig. 4.13). This cooling is larger in DAMIN11 and DAMIN13 simulations than in the DAMEAN13 simulation since the signal of the proxy-based reconstruction is stronger in these two simulations (Tab. 4.3). The same conclusion applies for the SST because

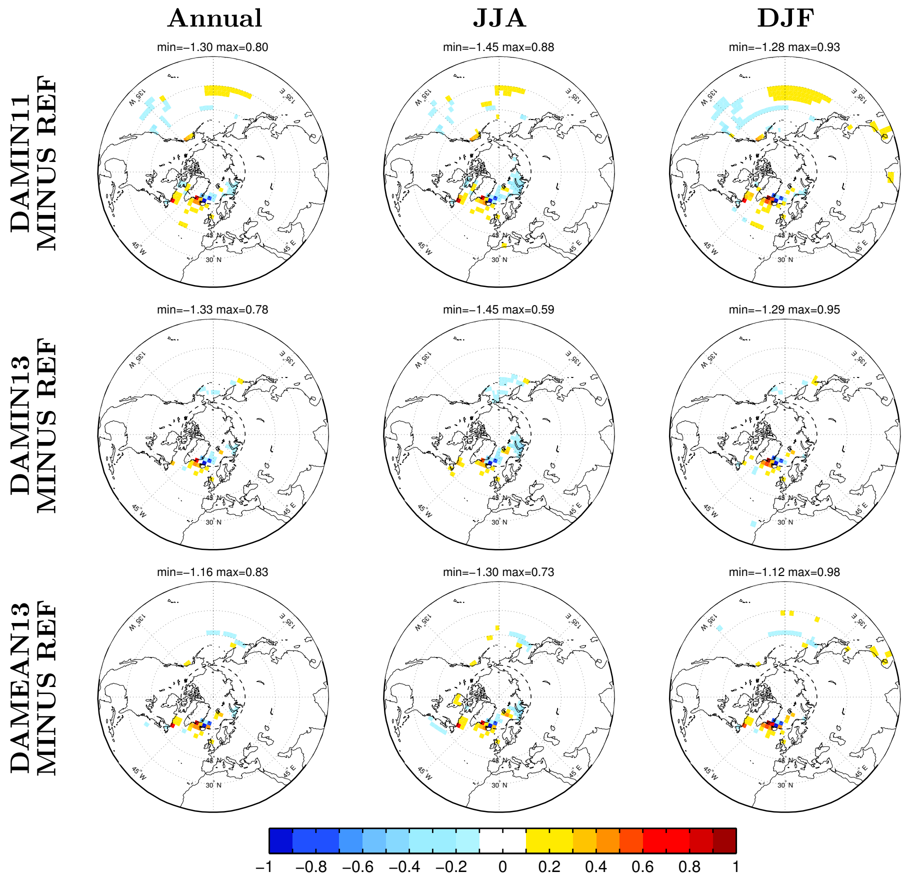

Figure 4.12: Average 200 year sea surface temperature difference between DAMIN11 simulation and REF for different months (upper panel). The same difference for DAMIN13 simulation (middle panel) and DAMEAN13 simulation (lower panel).

the Arctic SST is cooled in the simulation with data assimilation, while the global SST changes are not detectable (not shown).

To summarize, the proxy-based reconstructions have highlighted a cooler period in the Arctic. The objective to drive LOVECLIM towards this Arctic cooling using these 11 to 13 reconstructions through data assimilation is met in the three simulations (lower panel of Fig. 4.13). Nevertheless, this general cooling of the Arctic does not prevent local Arctic area from being warmer (Fig. 4.14). The Arctic cooling is therefore mainly created by the cooling of Northern Asia. This cooling is due to an attenuation of the Atlantic westerlies (Fig. 4.14), which

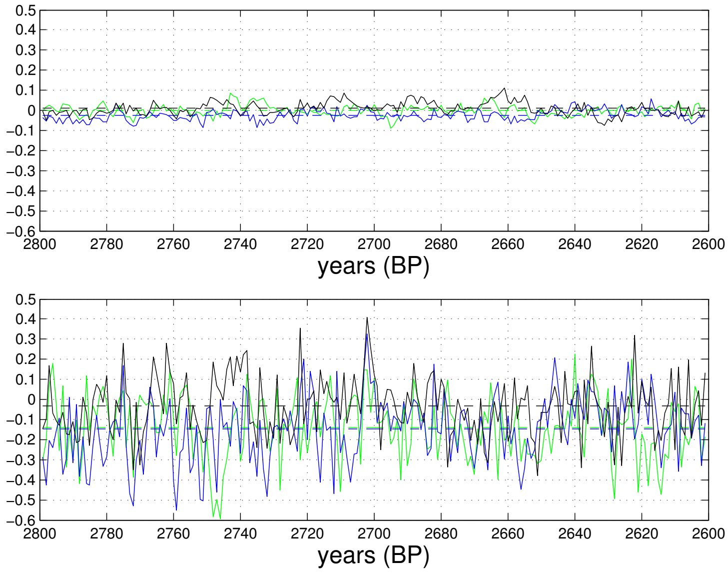

Figure 4.13: Annual global (**upper panel**) and average of the Arctic (**lower panel**) surface air temperature difference (°C) between the simulations with data assimilation and the reference simulation without data assimilation: DAMIN11-REF (green), DAMIN13-REF (blue) and DAMEAN13-REF (black). The dashed lines on both panels represent the average value over the period 2.8 to 2.6 kyBP.

prevent the warm southern mass of air from warming up the Northern Asia. The spatial heterogeneity of the spatial patterns simulated by LOVECLIM stresses once more the importance of the distribution of proxies in determining cold periods. A cooling in one region is not necessarily associated with a global event.

Our results also outline some limitations of LOVECLIM. For instance, in DAMIN11 simulation, the annual N6 surface temperature reconstruction drives LOVECLIM to obtain a strong cooling in the north of Iceland. To obtain such a cooling, it is natural for LOVECLIM to warm up the air over the Barents Sea. LOVECLIM tends indeed to produce a dipole in the surface temperature between the North Iceland and the Barents Sea. This is a well known mode of variability of LOVECLIM described in Goosse et al. (2002). The dipole is clearly visible for the three simulations with data assimilation in Fig. 4.11 and is the strongest during winter. Unfortunately, the two proxy-based reconstructions N1 and N10 also try to push LOVECLIM towards a more negative anomaly, while they are located in the area that LOVECLIM tends to warm because of its mode of variability triggered by the negative anomaly of N6.

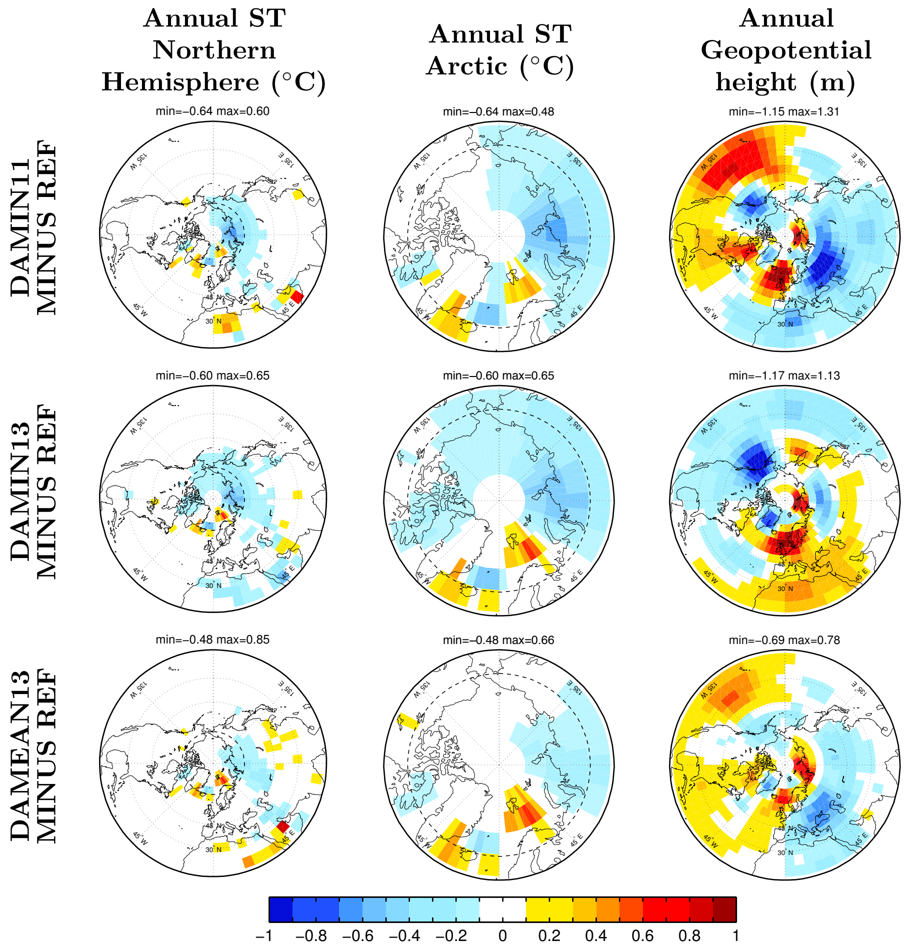

Figure 4.14: Annual surface air temperature (°C) and geopotential height (m) difference between the DAMIN11 simulation and REF (upper panel). The surface air temperature difference is shown for the Northern Hemisphere and for the Arctic. The middle panel shows the same for DAMIN13 simulation. The lower panel shows the results for DAMEAN13 simulation. The first column has already been shown in the Fig. 4.11 and is included here to facilitate the comparison.

Reconstructions N1 and N10 could not force LOVECLIM to display a cooling at this location (Fig. 4.11). Besides, Renssen et al. (2014) have demonstrated that both areas can be colder at the same time if the forcing is strong enough but it is not the case in our experiments. Moreover, the warmer the anomaly between the north Iceland and the Barents Sea, the larger the warming in the Barents Sea.

Such a dipole is also present in the GCM CCSM2, but it is shifted and affects the Labrador and the Barents Sea (Goosse and Holland, 2005). In agreement with observations which has a clear impact on the simulations with data assimilation, LOVECLIM therefore tends to pack the dipole. This is a bias of the model.

4.4 Conclusion

As a conclusion, we will review the main findings of our analysis.

- Wanner et al. (2011) developed an interesting methodology to highlight the multi-centennial variability over long periods such as the Holocene.
- Many of the cold periods identified by Wanner et al. (2011) can not been found north of 40°N using a different set of proxies. The conclusions of Wanner et al. (2011) are thus sensitive to the dataset selected.
- By applying this procedure to our surface temperature data set, we have been able to identify multiple periods during which the Arctic was colder than the Holocene trend. One of these periods, around about 2.65 kyBP, has been chosen to perform a transient simulation in which Holocene proxy-based temperature reconstructions are assimilated. LOVECLIM is able to reproduce this cold period over the Arctic. This means that the LOVECLIM model can be driven by the data assimilation method to reproduce the multi-centennial climate variability observed in surface temperature data.
- The three simulations with data assimilation confirm that the procedure, i.e. the experimental design, is ready to run a long transient simulation with data assimilation.
- Finally, the forcings used here, in the four simulations performed for this chapter, are subject to uncertainties. This means that the data assimilation results might be different if other forcings are used. The same applies to all the simulations performed within this thesis, with data assimilation. Those uncertainties could be estimated by performing additional sensitivity studies, as done for instance in Mathiot et al. (2013), but it is out of the scope of the present study.

CHAPTER 5

Conclusions

This doctoral thesis is one of the first modeling studies that focus on the Holocene climate using a data assimilation method, combining the model results, the proxy-based reconstructions and the forcings. Here we conclude the thesis, sum up the most important findings and perspectives, and we provide answers to the questions asked in the section 1.6 of the introduction. We first remind why there was a need to combine models and proxy-based reconstructions. Afterward, the main results brought by this work are reviewed. Then we explain some of the difficulties encountered. Finally, we provide perspectives for future work.

Even though multi-centennial variability is clearly present during the Holocene, as illustrated by Fig. 4.6, these climate fluctuations are relatively weak compared to the glacial-interglacial changes or the abrupt events occurring during the deglaciation. As a consequence, the magnitudes of the proxy-based reconstructions of surface temperature are often close to the uncertainties of the reconstructions themselves. For instance, we have shown in chapter 2 that the change of surface temperature between 6 kyBP and the first half of the last millennium is on average about 1.6°C. This has been obtained using surface temperature reconstructions derived both from marine and continental archives that are located northward of 20°N and have at least a multi-centennial resolution. Moreover, the uncertainties associated with proxy-based reconstructions are difficult to estimate in an objective way. When this information is available, it is often an upper limit that needs to be interpreted with care in the context of data assimilation. In the framework of this thesis, this has been a major issue because if the proxies have a signal of the same order of the uncertainty, the constrain brought by data assimilation is very weak. To overcome this problem, we have deliberately chosen low values for these uncertainties. The precise choice of the value selected affects weakly the spatial patterns but influences the magnitude of the changes induced by the data assimilation processes. This has been taken into account in the interpretation of the results of our experiments.

Regarding uncertainties, we have shown that the Earth system model of intermediate complexity LOVECLIM has also its own biases. Its performance have been assessed in section 1.3.1.5. Additionally, specific information on LOVECLIM limitations are also provided in each chapter of this thesis. For instance, its simplified physics has been identified in chapter 2 as a limiting factor to follow simultaneously the signal off all the proxy-based reconstructions. In chapter 3, we have been forced to consider the simulation VOLC as a sensitivity experiment, one of the main reasons being that LOVECLIM does not take into account two of the three major climate impacts generated by a volcanic cloud. In chapter 4 we have demonstrated that, because of a mode of internal variability that creates a dipole in the surface temperature between the North Iceland and the Barents Sea, it is difficult for the model to assimilate two proxy-based reconstructions that have a signal of the same sign and are located in those two areas. The answer to the question raised in the introduction "Do the model limitations affect the reconstruction of the past climate that is produced with and without the data assimilation method?" is thus clearly yes and our analyses illustrate where those limitations have likely the largest impact on our results.

Because of these uncertainties, these two independent sources of informations about past climate, namely proxy-based reconstructions and model results, are not always consistent when basic model-data comparisons are performed. We have proven this in chapter 2 by showing that the model-data agreement is low at local/regional scale for the mid-Holocene and that the models agree much better between themselves than with the proxy-based reconstructions. This is not only valid for LOVECLIM but has also been demonstrated for three state-of-the-art general circulation models.

At the onset of this PhD thesis, we hoped that the data assimilation methodology can be used to solve this problem and one of the goal of this thesis was to produce a climate reconstruction covering the whole Holocene that is both consistent with proxy-based reconstructions and the physics of a climate model. For the last millennium, Goosse et al. (2010b, 2012b) produced such reconstructions but the issues are different for the Holocene. The proxy-based reconstructions are less numerous and have a lower temporal resolution. The resulting data set is therefore less homogeneous and presents lower variations. It therefore produces a weaker influence on the model results through the data assimilation process and leads to larger uncertainties. Consequently, the data assimilation methodology has thus been more used here to understand whether the models and the proxy-based reconstructions of surface temperature can be consistent.

The first main result of this thesis is that the assimilation of a simple data set provides a clear constraint to the model, even if the data set contains very few reconstructions. The term "simple" stands here for a data set that contains very clear informations, covering adequately the region of interest, that the model is in theory able to reproduce. This has been highlighted in chapter 4 in which LOVECLIM has been driven to simulate colder conditions in the Arctic between 2.8 and 2.6 kyBP with only 11 surface temperature reconstructions that are well distributed in space. This first result also illustrates that a cooling in one region is not necessarily associated with a global event, which underlines the importance of a good spatial distribution of the proxies. Because of this, we consider that it may be helpful to point out several areas northward of 20°N, where proxy-based reconstructions of surface temperature are lacking, although it might be difficult to fill in those gaps for various reasons (see Fig. A.1): the southern Asia (between 45°E and 135°E) and the central Pacific and Arctic Oceans.

The second result is that the data assimilation process can be used to explain the variations recorded by proxies. In other words, the mechanisms selected by the model to produce the results through the data assimilation constraint provide reasonable ways to explain the proxy-based fluctuations. For instance, all the simulations of chapter 2 have shown that to warm up the northern Europe, the model strengthens its westerlies at mid-latitudes. Chapter 4 demonstrates that to obtain a cooling of the northern Asia, weaker Atlantic westerlies are required.

The third major result is that the data assimilation is a valuable tool to objectively identify the proxy-based reconstructions that are incompatible with the model physics or with other reconstructions. This has been found in chapter 2, by performing a simulation without data assimilation (NODATA) and three simulations with data assimilation driven by different proxy-based records: i.e. the reconstructions derived from the continental proxies (in simulation CON), the oceanic archives (in simulation OCE) and both type of informations (in simulation ALL). For instance, if a continental proxy-based reconstruction is more consistent with the results of the simulation CON than with the results of NODATA, but less consistent with the results of the simulation ALL, it indicates that the signal of this continental reconstruction is incompatible with the signal of at least one oceanic reconstruction according to the LOVECLIM physics. Moreover, if another continental reconstruction is never more consistent with the LOVECLIM results in the simulation CON or ALL than with the results of the simulation NODATA, this means that the signal derived from the proxy is not compatible with the physics of LOVECLIM. This can also mean that the signal of this proxy is not well interpreted if it is believed that the LOVECLIM physics must be sufficient to explain the variations of this kind of proxy-based reconstruction. In particular, the LOVECLIM physics is not compatible with the 6 kyBP summer temperature gradient obtained in the pollen-based surface temperature reconstructions of Davis et al. (2003), which indicates a colder southern Europe and a warmer northern Europe (Fig. 2.6).

A last major result is that a volcanic forcing covering the Holocene is not yet ready to be used by climate models that take into account the volcano's climatic influence through a modification of the radiative forcing, such as LOVECLIM. It has been shown in chapter 3 that such a forcing indeed influences the climate on yearly to multi-decadal time-scale, and that in theory it can therefore be used to explain some rapid fluctuations that are recorded by proxies. Nevertheless, our results are still very preliminary since we also have demonstrated that the forcing is not realistic at this stage, mainly because of an overestimation of large eruptions when the methods applied currently for the last millenium are used over the whole Holocene. To make this forcing more realistic, the easier way is to apply a correction to the radiative forcing to take into account the effect of the downward longwave radiations. This correction should be proportional to the size of the eruption and, for instance, could consists in dividing the radiative forcing by 2.5 for an eruption corresponding to 100 times the one of the Pinatubo according to Jones et al. (2005).

Limitations

The data assimilation method as also limitations. The most important are reviewed here. First, a right balance must be found between the number of observations used to constrain the model results and the number of particles that is affordable. As explained in the introduction the more complex is the target described by the proxy-based reconstructions, the larger the ensemble of particles needed for the data assimilation process. Since the number of particles that composed this ensemble is not infinite due to computing costs, a reasonable amount of data should be choosen to provide a target to data assimilation that well represents the dominant features of the past climate. The quality of the data is therefore more important than the quantity, as discussed below in the perspectives. To conclude, if the data set is composed of reconstructions derived from lots of different archives types, that have been processed by different scientists, as it is the case within this thesis, the climate target provided by the data set is likely very complex, and therefore I recommend to not use more than about 50 proxy-based reconstructions for 96 particles.

Second, there is no guarantee that the interpretation of the proxy-based reconstructions used in the assimilation process is valid. In other words, it is not because the model surface temperature is compared to the proxy signal that the latter really represents this variable. The same applies for the period of the year that the proxy represents. There is also no guarantee that the LOVECLIM grid is well representative of the area that had an influence on the proxy signal.

Furthermore, if the data assimilation works and drives the LOVECLIM results towards the proxy-based reconstructions, it is not sure that it is for the right reasons. LOVECLIM may not represent well the physical processes that explain the variations of the proxy-based reconstruction or is maybe not able to reproduce the mechanisms that are responsible for the reconstructed changes.

In addition, using an Earth system model of intermediate complexity with a very simplified atmospheric circulation is a limiting factor because of the limited number of ways LOVECLIM is able to produce a cooling or a warming in a region. For instance, in the three simulations with data assimilation of chapter 2, the mechanism underlined to warm up northern Europe is a strengthening of the mid-latitudes westerlies, despite the fact that the data set used in the three simulations are different. A similar pattern was also found in Goosse et al. (2012b) for the Medieval Climate Anomaly. This demonstrates that the data assimilation method highlights the same mechanism to explain a particular phenomenon. This might indicate the importance of westerlies for northern Europe climate but this importance is maybe overestimated because of the simplified physics of the model. Indeed, the model underestimates the potential role of other mechanisms that could also warm up the northern Europe.

Finally, data assimilation can attenuate the influence of some model biases but cannot correct all of them. This is because the data assimilation technique implemented here does not modify the physics of the model or the model parameters. The bias compensation should therefore stay in the range of the model results that are coherent with its own physics.

Perspectives

Many results of this thesis can be improved by further work. Some suggestions are presented below.

The first suggestion is to review the information brought by the proxies. To my point of view, one of the main weaknesses of the present work is related to the way the proxy data are applied in the data assimilation process. We use a standard direct and simple interpretation of those proxies, while any biases in this interpretation have considerable consequences on our results. Ideally the following questions should be answered for each data in order to characterize them and to facilitate their use in the data assimilation process. Which months does the proxy represents? Does the proxy-based reconstruction represent a physical variable of the climate model that will be used for data assimilation? If not, is it possible to create a corresponding variable in the model? What is the area that is representative of the proxy-based reconstruction? Is this area smaller than the model grid? If yes, can we adapt the proxy signal to be representative of the model grid? What is the uncertainty linked to this reconstruction? Does the reconstruction still provide useful information taking into account the value of the uncertainty? Is it possible, from a single archive, as a marine core for instance, to provide multiple reconstructions of the same physical variable based on different proxies? If yes, do the multiples reconstructions agree with each other? If not, why? And in this case what reconstruction should we select for data assimilation? All of these questions are very specific and it is not straightforward to answer them. They should be considered as a basis of reflexion for the scientists that are interested in producing a paleoclimate reconstruction based on proxies, if they want this reconstruction to be useful for the model data comparison or for the data assimilation method.

Additionally, data assimilation can be a tool to interpret the proxies, if it is supposed that the model physics and the forcings are correct. For instance, to determine if a proxy-based reconstruction corresponds more to the summer or winter months, two simulations should be performed: one in which the model is driven to be as close as possible to the summer data, and one in which the model is driven towards the winter data. The final interpretation, summer or winter, is the one that maximize the agreement between the model and the data. In this particular case, the new interpretated data can not be used anymore in the simulation with data assimilation, in order to avoid a circular process.

In the same vein, the data assimilation can be used to select the forcings that are the most suitable, according to the model physics and the surface temperature reconstructions. This has already been done in Mathiot et al. (2013) for the Early-Holocene freshwater fluxes and this could be done for the forcings used within this thesis. This can help to reduce the uncertainties that are linked to the forcings. Indeed, within this thesis, we have not considered any uncertainties on forcings, while some are obviously present. For instance, the TSI forcing used in the chapters 3 and 4 is relatively weak in comparison to the one used in Renssen et al. (2006).

Another perspective is to assimilate other proxy-based reconstructions, to verify the robustness of our conclusions. This could be done for instance with the regional and a global Holocene temperatures reconstruction of Marcott et al.

(2013). This reconstruction has not been used in this thesis as it has been released to late to be included in our simulations with data assimilation.

To complete the work presented in chapter 4, a longer transient simulation with data assimilation could be performed. Such a simulation has not yet been done because of the time required. Indeed, a minimum of 500 to 1000 years of simulation should be performed to detect any change because of the low resolution of the proxies. Additionally, another perspective of this work is to compare our results with the very recent Arctic Holocene proxy climate database of Sundqvist et al. (2014). They gathered a large number of peer-reviewed proxy-based reconstructions that are not available through on-line archives. This database focuses on the Arctic and includes several different physical variables. Performing simulation with data assimilation based on the information of this database would also be very instructive.

One more suggestion is to perform data assimilation of the same data set with different climate models that have different physics. Indeed, it is not intended to modify the fundamental model assumptions that cause the biases in LOVECLIM, in order to preserve the philosophy behind the model development (Goosse et al., 2010a). Using other models will therefore provide a panel of mechanisms that are able to explain the assimilated data set. This will also provide a range of model reconstructions that describe the past climate. In particular, it would be instructive to perform data assimilation over the Holocene using a general circulation model instead of a Earth system model of intermediate complexity. This should probably be done on short periods because of the computer costs. Indeed, the used of a complex model with an elaborate physics will likely allow to explain more proxy-based reconstructions variations. Thus, the more complex the model, the more you can be confident that two proxy-based reconstructions used in the data assimilation process are incompatible if the model physics cannot explain them together. To summarize, in order to minimize the probability that two proxy-based reconstructions are considered incompatible with each other because of a too simple physics, we advice to use more complex models that most likely incorporate the physics able to explain the proxy variations.

Furthermore, instead of performing data assimilation of a reconstructed variable as the surface temperature, the raw observed data can be directly assimilated to reduce the uncertainty associated with the interpretation of the data assimilated. For instance, the $\delta^{18}O$ can be directly used in the process of assimilation instead of using the surface temperature derived from it. This will require a complete model of the oxygen isotope coupled to LOVECLIM (Roche, 2013; Roche and Caley, 2013; Caley and Roche, 2013).

APPENDIX A

The proxy-based reconstructions database

This appendix contains all the proxy-based reconstructions of surface air (ST) and sea surface (SST) temperature that are used within this thesis. They are listed in the table A.1 that provides the correspondance between the id used in the chapter 2 and 4. The temperature series are shown after Fig. A.1. In each figure, the raw data are displayed by the grey dots, while the grey lines are linear interpolation between those values. In chapter 4, these temperature series have been filtered to keep the multi-centennial variability, removing high- and low-frequency variability. Such filtering have been performed using a LOWESS filter with a cut-off frequency, respectively of 500 years for high-frequency variability (black curve in figures below) and 3000 years for low-frequency (red curve). The LOWESS filter is a method that uses a locally weighted linear regression to smooth data. The method is local because the smoothed value depends on the neighbors data points within the cut-off frequency.

Table A.1: Surface air (ST) and sea surface (SST) Holocene temperature proxy-based reconstructions (hereafter in the table, Proxy. recons.) used within this thesis. The columns Id2 and Id4 provide the correspondance between the Id used in the chapter 2 (Tab. 2.1) and chapter 4 (Tab. 4.1), respectively. In these two columns, the "X" letter is used if the proxy has not been used in the chapter corresponding to the column. The column's name "Temporal interp." stands for Temporal interpretation. Winter corresponds to December–February (DJF) and summer to June–August (JJA).

Id	Id2	Id4	Lat	Lon	Site or core name	Area	Archive type	Proxy. recons.	Temporal interp.	Reference
1	25	X	20.12	117.38	GIK17940-2	South China Sea	Alkenone - Uk37	SST	Annual	Pelejero et al. (1999)
2	18	X	20.75	-18.58	ODP658C	Northwest Africa Sea	Forams (planktic)	SST	August	deMenocal et al. (2000)
3	19	X	20.75	-18.58	ODP658C	Northwest Africa Sea	Forams (planktic)	SST	February	deMenocal et al. (2000)
4	9	X	30.85	-11.50	GeoB 6007-02	Northwest Africa	Alkenone - Uk37	SST	Annual	Kim et al. (2007)
5	20	X	31.48	128.52	Core B-3GC	Northwestern Pacific Ocean	Forams (planktic)	SST	Summer	Jian et al. (2000)
6	21	X	31.48	128.52	Core B-3GC	Northwestern Pacific Ocean	Forams (planktic)	SST	Winter	Jian et al. (2000)
7	24	X	36.03	141.78	KR02-06 St.A MC/GC & MD01-2421	Northwestern Pacific	Alkenone - Uk37	SST	Summer	Isono et al. (2009)
8	42	X	37.50	1.50	Southwest region	Europe	Pollen	ST	January	Davis et al. (2003)
9	43	X	37.50	1.50	Southwest region	Europe	Pollen	ST	July	Davis et al. (2003)
10	48	X	37.50	32.50	Southeast region	Europe	Pollen	ST	January	Davis et al. (2003)
11	49	X	37.50	32.50	Southeast region	Europe	Pollen	ST	July	Davis et al. (2003)
12	7	X	37.56	-10.14	MD01-2444	Iberian Margin	Alkenone - Uk37	SST	Annual	Martrat et al. (2007)
13	10	X	38.63	-9.45	D13882	Iberian Margin	Alkenone - Uk37	SST	Annual	Rodrigues et al. (2009)
14	4	X	40.50	4.03	Minorca	Mediterranean sea (Menorca)	Alkenone - Uk37	SST	Annual	Martrat (2007)
15	17	7	41.68	-124.93	ODP1019C	North Pacific	Alkenone - Uk37	SST	Annual	Barron et al. (2003)
16	6	5	43.48	-54.87	OCE326-GGC26	Northwest Atlantic	Alkenone - Uk37	SST	Annual	Sachs (2007)
17	5	4	43.88	-62.80	OCE326-GGC30	Northwest Atlantic	Alkenone - Uk37	SST	Annual	Sachs (2007)
18	36	8	44.53	145.00	MD01-2412	Okhotsk Sea	Alkenone - Uk37	SST	Autumn	Harada et al. (2006)
19	40	40	50.00	1.50	Centralwest region	Europe	Pollen	ST	January	Davis et al. (2003)

Continued on next page

Table A.1 – continued from previous page

Id	Id2	Id4	Lat	Lon	Site or core name	Area	Archive type	Proxy. recons.	Temporal interp.	Reference
20	41	41	50.00	1.50	Centralwest region	Europe	Pollen	ST	July	Davis et al. (2003)
21	46	44	50.00	32.50	Centraleast region	Europe	Pollen	ST	January	Davis et al. (2003)
22	47	45	50.00	32.50	Centraleast region	Europe	Pollen	ST	July	Davis et al. (2003)
23	26	25	52.78	108.12	Kotokel lake	Russia	Pollen	ST	January	Tarasov et al. (2009)
24	27	26	52.78	108.12	Kotokel lake	Russia	Pollen	ST	July	Tarasov et al. (2009)
25	3	X	55.65	-13.98	ENAM9606 & M200309	North Atlantic (Feni Drift)	Alkenone - Uk37	SST	Annual	Esparza (2005)
26	X	13	57.43	-27.90	MD99-2251	North Atlantic	Mg/Ca	SST	August	Farmer et al. (2008)
27	14	22	58.55	13.67	Lake Flarken	Sweden	Pollen	ST	Annual	
28	23	24	58.58	26.65	Raigastvere lake	Estonia	Pollen	ST	Annual	Seppä and Poska (2004)
29	X	3	58.76	-25.96	MD95-2015	North Atlantic	Alkenone - Uk37	SST	Annual	Marchal et al. (2002)
30	30	29	60.00	-57.50	Labrador region	Canada	Pollen	ST	January	Viau and Gajewski (2009)
31	31	30	60.00	-57.50	Labrador region	Canada	Pollen	ST	July	Viau and Gajewski (2009)
32	32	33	60.00	-100.00	Central Canada region	Canada	Pollen	ST	January	Viau and Gajewski (2009)
33	33	34	60.00	-100.00	Central Canada region	Canada	Pollen	ST	July	Viau and Gajewski (2009)
34	34	35	60.00	-130.00	MacKenzie region	Canada	Pollen	ST	January	Viau and Gajewski (2009)
35	35	36	60.00	-130.00	MacKenzie region	Canada	Pollen	ST	July	Viau and Gajewski (2009)
36	X	31	60.00	-72.50	Northern Quebec region	Canada	Pollen	ST	January	Viau and Gajewski (2009)
37	X	32	60.00	-72.50	Northern Quebec region	Canada	Pollen	ST	July	Viau and Gajewski (2009)
38	12	21	60.08	15.83	Stora Gilltjarnen	Sweden	Midges (chironomid)	ST	Annual	Antonsson et al. (2006)
39	13	X	60.58	24.08	Lake Arapisto	Finland	Pollen	ST	Annual	
40	X	12	61.00	-25.00	ODP 984	North Atlantic	Mg/Ca	SST	Winter	Came et al. (2007)
41	X	17	61.37	-143.60	Moose lake	Alaska	Midges (chironomid)	ST	July	Clegg et al. (2010)
42	1	18	61.48	26.07	Laihalampi lake	Southern Finland	Pollen	ST	Annual	Heikkilä and Seppä (2003)
43	11	11	62.09	-17.82	RAPiD-12-1k	Subpolar North Atlantic	Mg/Ca	SST	May, June	Thornalley et al. (2009)
44	X	16	62.35	-138.35	Hanging lake	Canada	Midges (chironomid)	ST	July	Kurek et al. (2009)
45	38	38	63.50	1.50	Northwest region	Europe	Pollen	ST	January	Davis et al. (2003)

Continued on next page

Table A.1 – continued from previous page

Id	Id2	Id4	Lat	Lon	Site or core name	Area	Archive type	Proxy. recons.	Temporal interp.	Reference
46	39	39	63.50	1.50	Northwest region	Europe	Pollen	ST	July	Davis et al. (2003)
47	44	42	63.50	32.50	Northeast region	Europe	Pollen	ST	January	Davis et al. (2003)
48	45	43	63.50	32.50	Northeast region	Europe	Pollen	ST	July	Davis et al. (2003)
49	22	46	66.55	13.92	SG93	Norway	Speleothem	ST	Annual	Lauritzen and Lundberg (1999a)
50	8	6	66.60	-17.58	JR51-GC35	Nordic Seas	Alkenone - Uk37	SST	Annual	Bendle and Rosell-Melé (2007)
51	15	X	66.97	7.63	JM97-948/2A & MD95-2011	Norwegian Sea	Forams (planktic)	SST	August	Risebrobakken et al. (2003)
52	X	2	66.97	7.63	MD95-2011	Norwegian Sea	Alkenone - Uk37	SST	Summer	Calvo et al. (2002)
53	X	14	66.97	7.64	MD95-2011	Norwegian Sea	Radiolarian (polycystine)	SST	Summer	Dolven et al. (2002)
54	X	27	68.00	60.00	Khaipudurskaya Guba lake	Arctic Russia	Pollen	ST	January	Andreev and Klimanov (2000)
55	X	28	68.00	60.00	Khaipudurskaya Guba lake	Arctic Russia	Pollen	ST	July	Andreev and Klimanov (2000)
56	X	15	68.37	18.70	Lake Njulla	Sweden (Abisko valley)	Midges (chironomid)	ST	July	Larocque and Hall (2004)
57	2'	20	68.68	22.08	Tsuolbmajavri lake	Northern Finland	Pollen	ST	July	Seppä and Birks (2001)
58	2	19	69.20	21.47	Toskaljavri lake	Northern Finland	Pollen	ST	July	Seppä and Birks (2002)
59	29	48	71.27	-26.73	Renland Ice Cap	Greenland	ice core - d18O	ST	Annual	Vinther et al. (2009)
60	37	37	71.34	-113.78	KR02 lake	Victoria Island (Canada)	Pollen	ST	July	Peros and Gajewski (2008)
61	16	23	74.47	98.63	Levinson-Lessing lake	Russia	Pollen	ST	Annual	Andreev et al. (2003)
62	X	1	75.00	13.97	M23258	Barents slope	Alkenone - Uk37	SST	Summer	Marchal et al. (2002)
63	X	9	75.00	13.97	Kasten core 23258-2	Norwegian Sea	Forams (planktic)	SST	Summer	Sarnthein et al. (2003)
64	X	10	75.00	13.97	Kasten core 23258-2	Norwegian Sea	Forams (planktic)	SST	Winter	Sarnthein et al. (2003)
65	28	47	80.70	-73.70	Agassiz Ice cap	Greenland	ice core - d18O	ST	Annual	Vinther et al. (2009)

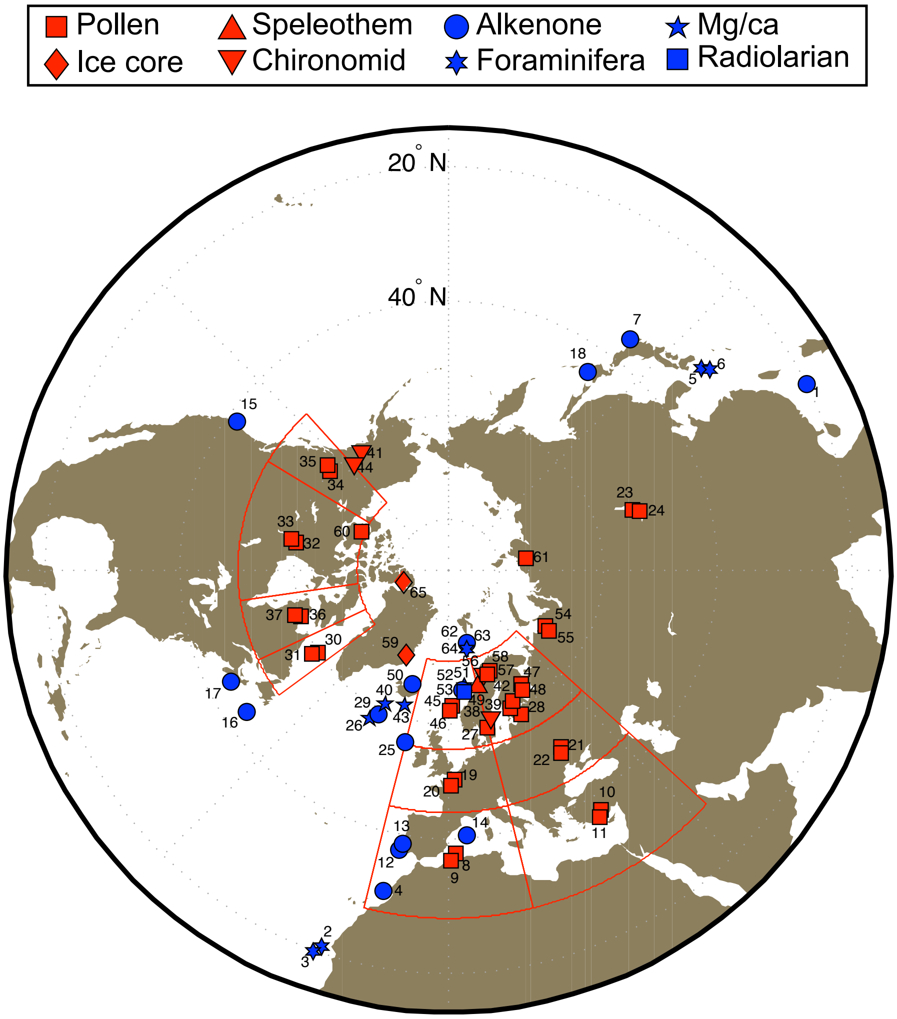

Figure A.1: Location of the proxy-based reconstructions used within this thesis. The numbers refer to the reconstructions listed in Tab. A.1. The red boxes display the areas that correspond to the proxy-based reconstructions of Davis et al. (2003) and Viau and Gajewski (2009). If more than one proxy-based reconstruction is given at the same location, the markers representing the proxy-based reconstructions are slightly shifted for improved readability.

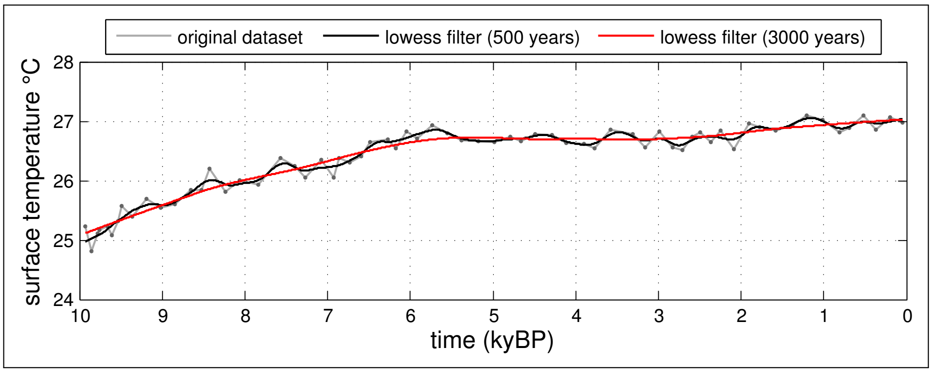

(1) Annual SST (South China Sea), Pelejero et al. (1999)

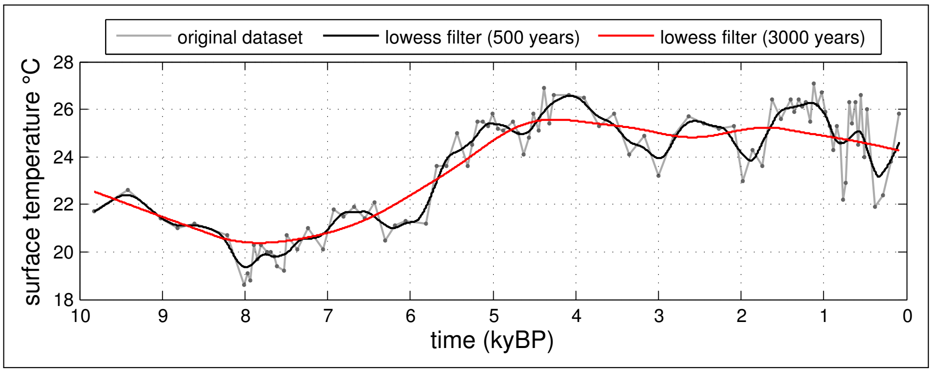

(2) August SST (Northwest Africa Sea), deMenocal et al. (2000)

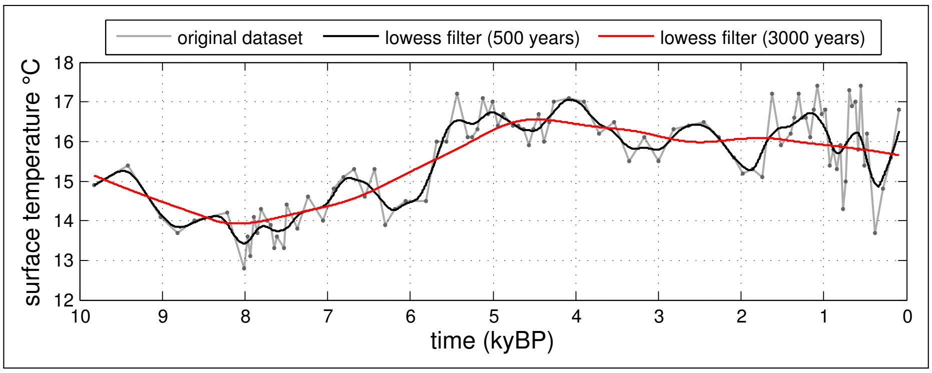

(3) February SST (Northwest Africa Sea), deMenocal et al. (2000)

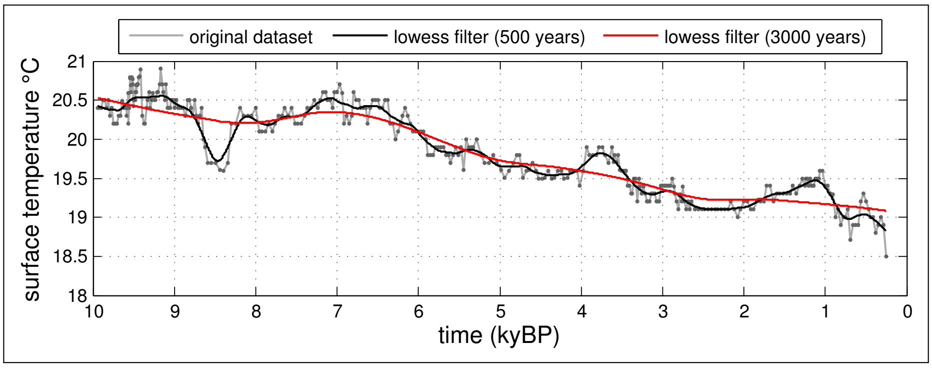

(4) Annual SST (Northwest Africa), Kim et al. (2007)

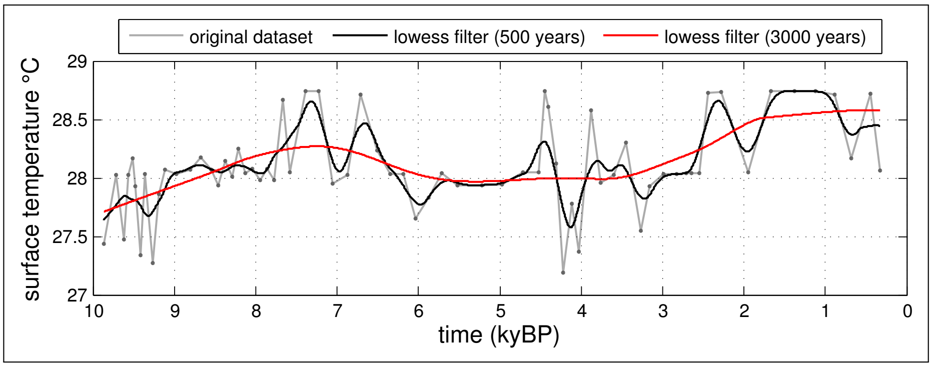

(5) Summer SST (Northwestern Pacific Ocean), Jian et al. (2000)

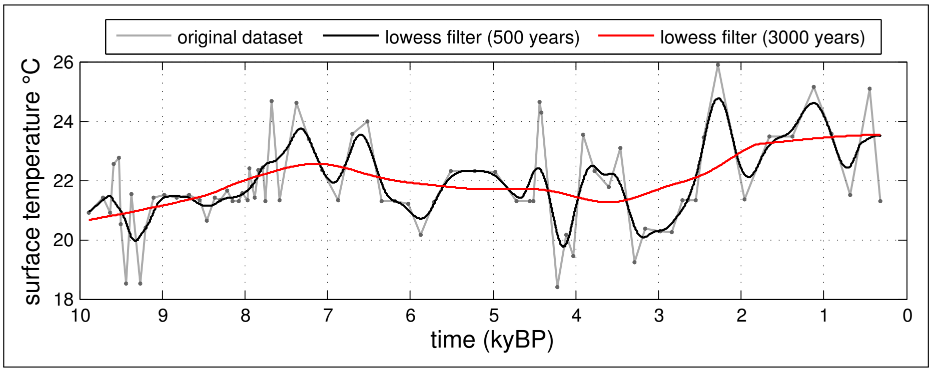

(6) Winter SST (Northwestern Pacific Ocean), Jian et al. (2000)

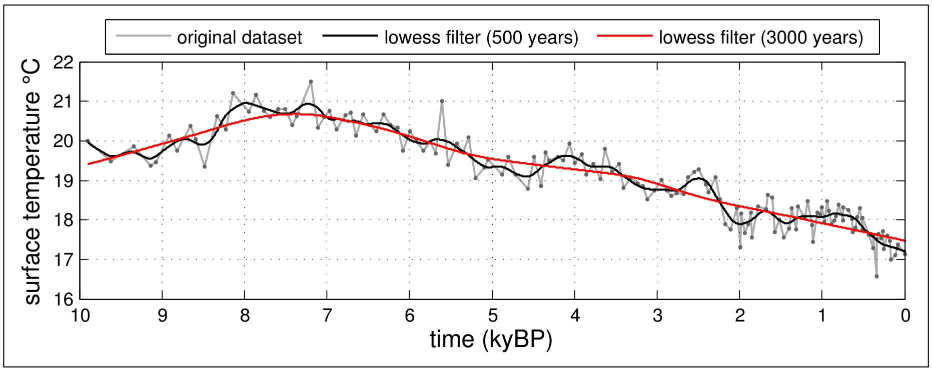

(7) Summer SST (Northwestern Pacific), Isono et al. (2009)

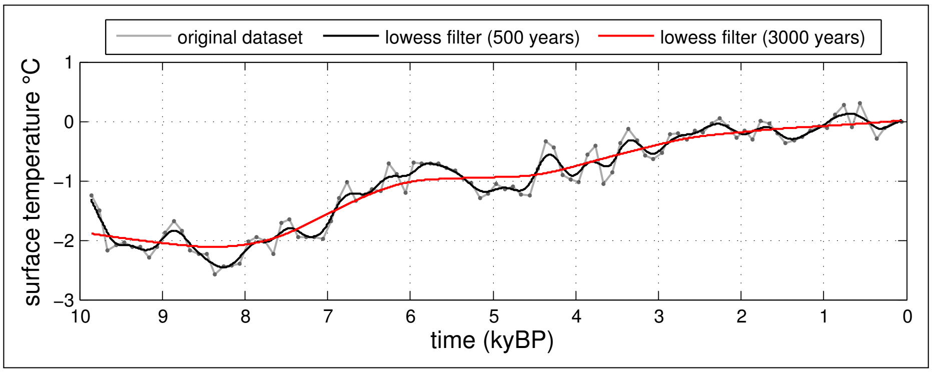

(8) January ST (Europe), Davis et al. (2003)

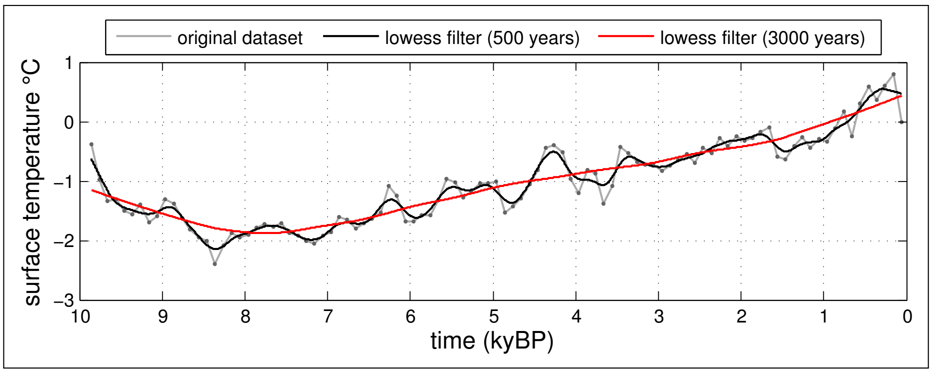

(9) July ST (Europe), Davis et al. (2003)

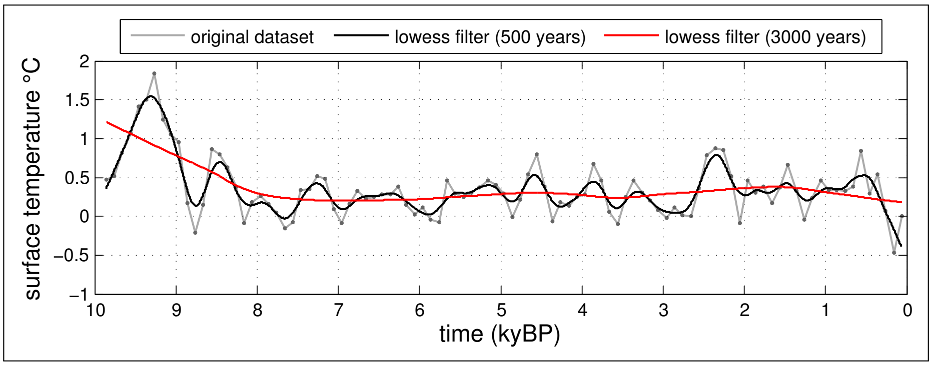

(10) January ST (Europe), Davis et al. (2003)

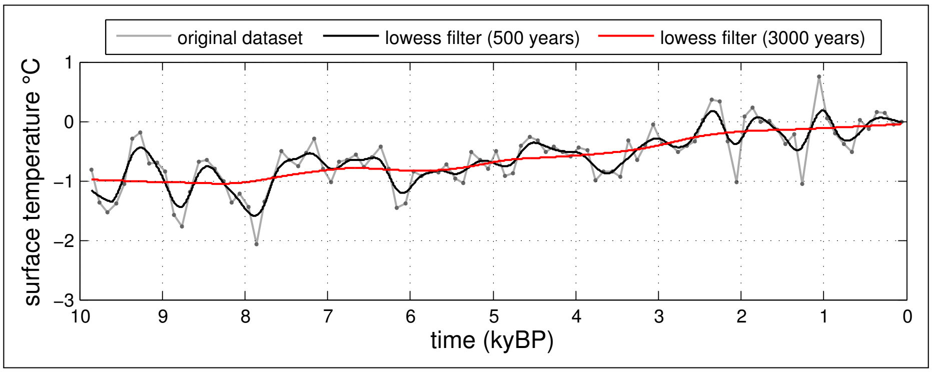

(11) July ST (Europe), Davis et al. (2003)

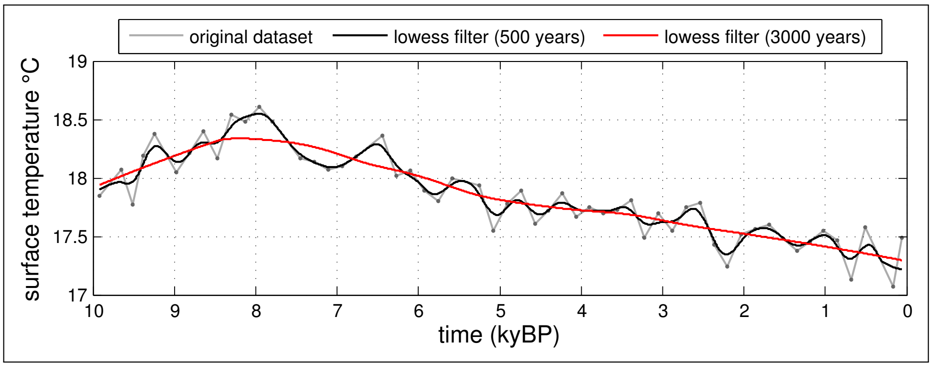

(12) Annual SST (Iberian Margin), Martrat et al. (2007)

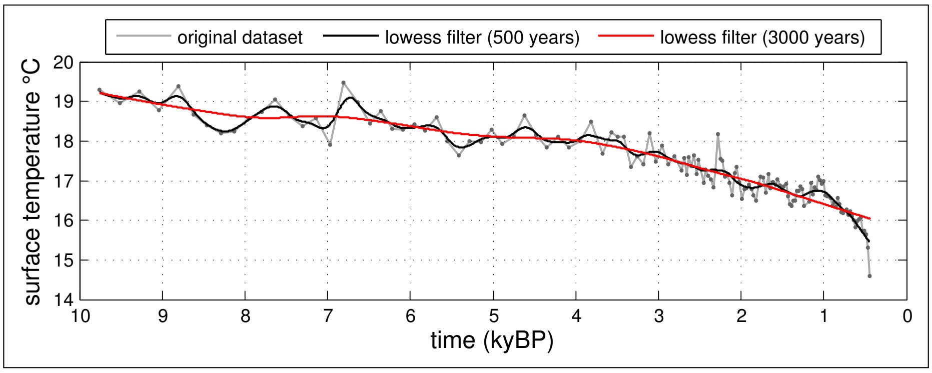

(13) Annual SST (Iberian Margin), Rodrigues et al. (2009)

This data is not freely distributed.

(14) Annual SST (Mediterranean sea (Menorca)), Martrat (2007)

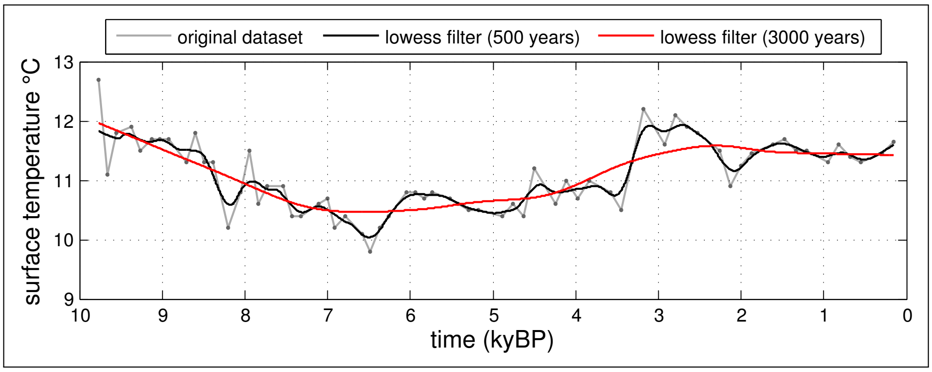

(15) Annual SST (North Pacific), Barron et al. (2003)

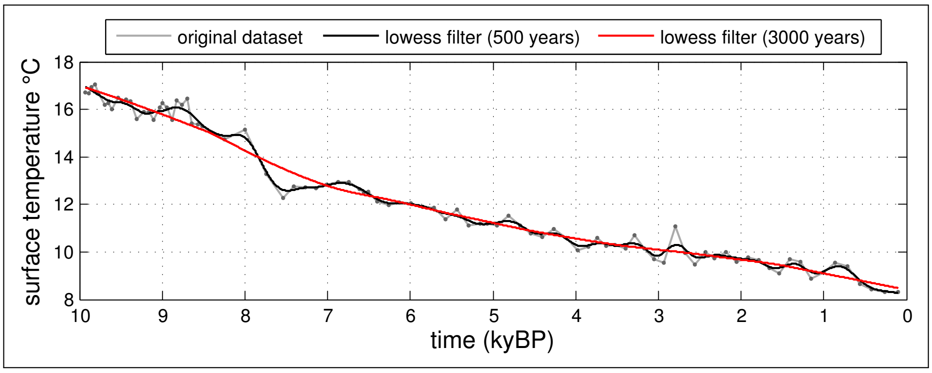

(16) Annual SST (Northwest Atlantic), Sachs (2007)

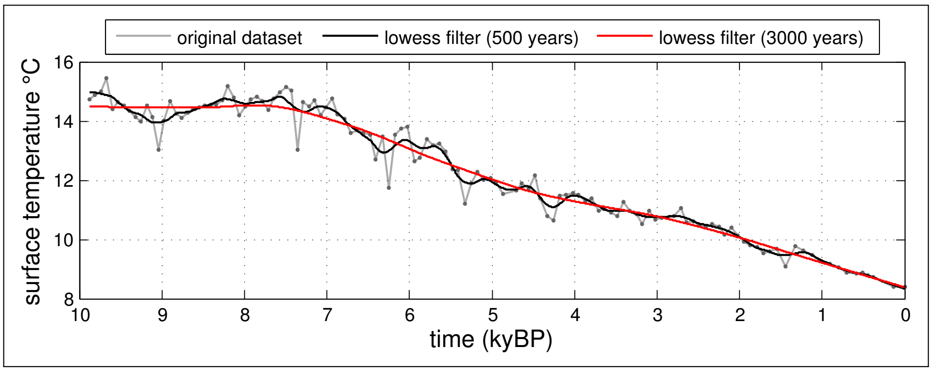

(17) Annual SST (Northwest Atlantic), Sachs (2007)

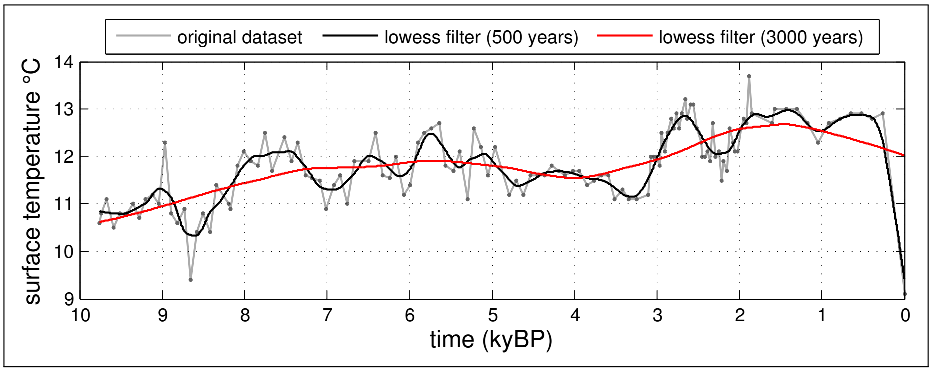

(18) Autumn SST (Okhotsk Sea), Harada et al. (2006)

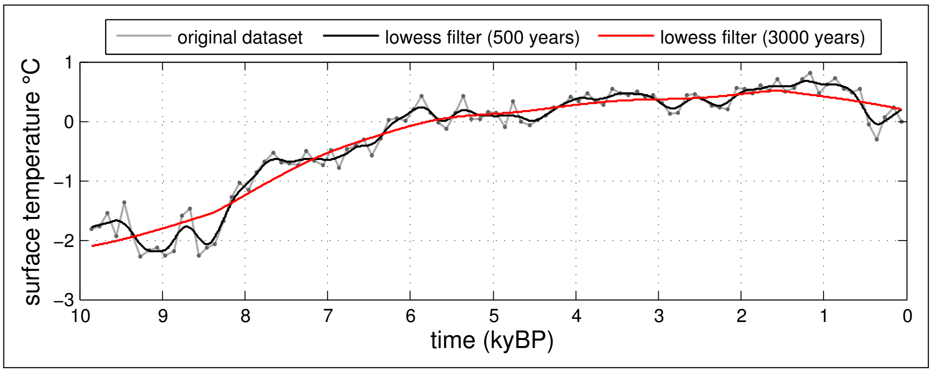

(19) January ST (Europe), Davis et al. (2003)

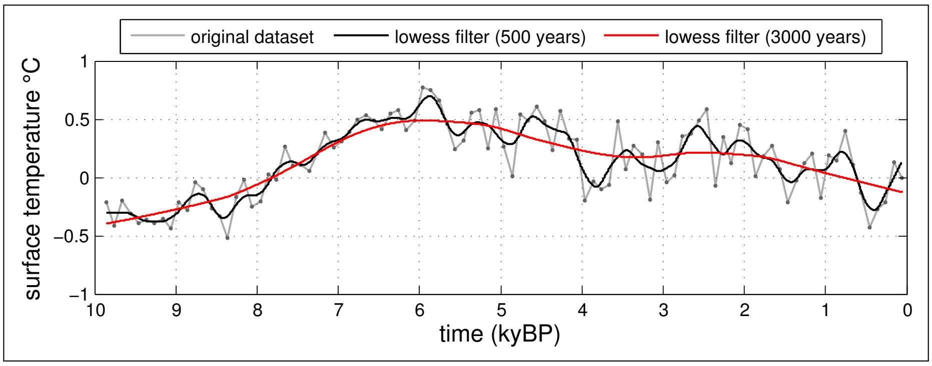

(20) July ST (Europe), Davis et al. (2003)

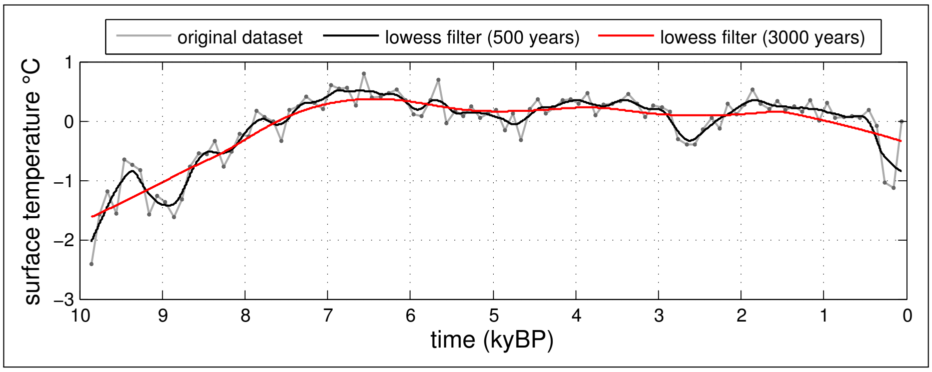

(21) January ST (Europe), Davis et al. (2003)

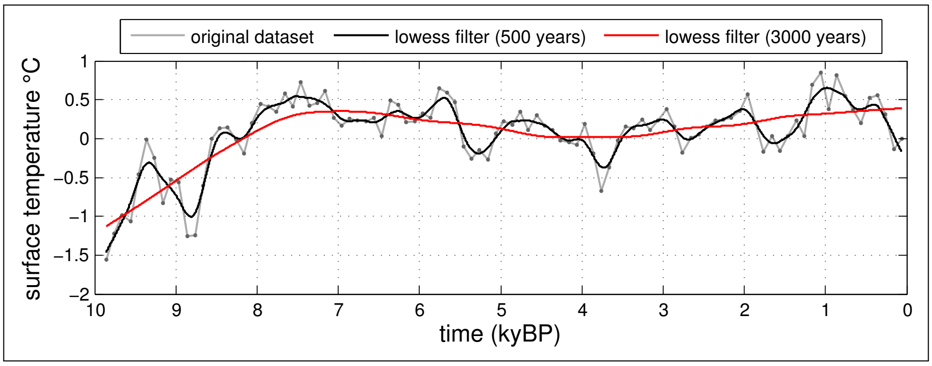

(22) July ST (Europe), Davis et al. (2003)

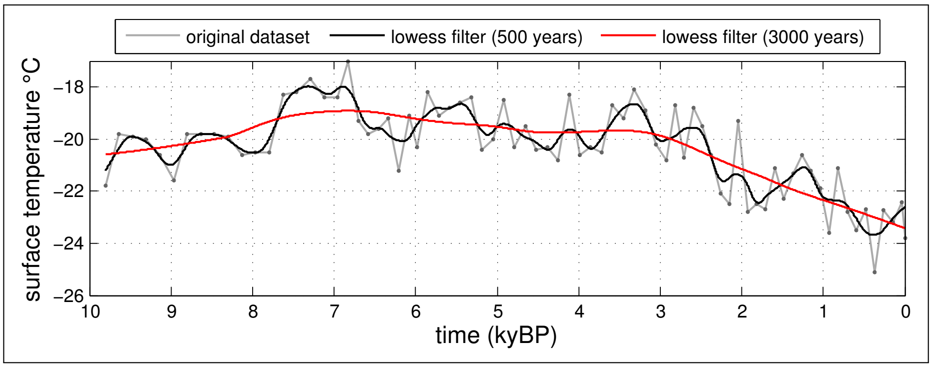

(23) January ST (Russia), Tarasov et al. (2009)

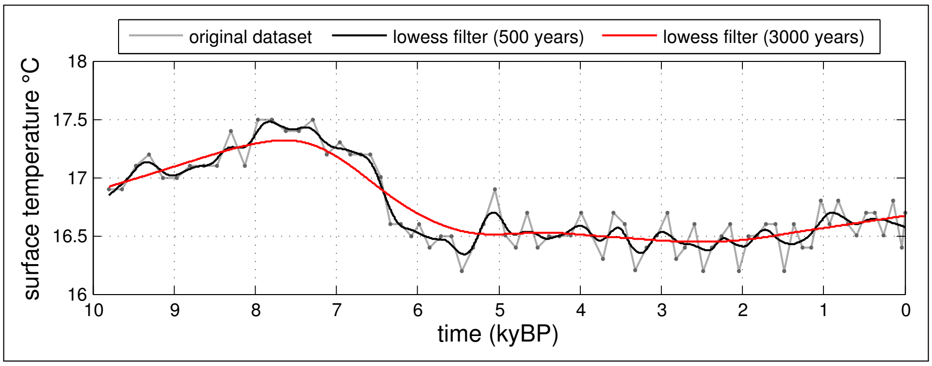

(24) July ST (Russia), Tarasov et al. (2009)

This data is not freely distributed.

(25) Annual SST (North Atlantic (Feni Drift)), Esparza (2005)

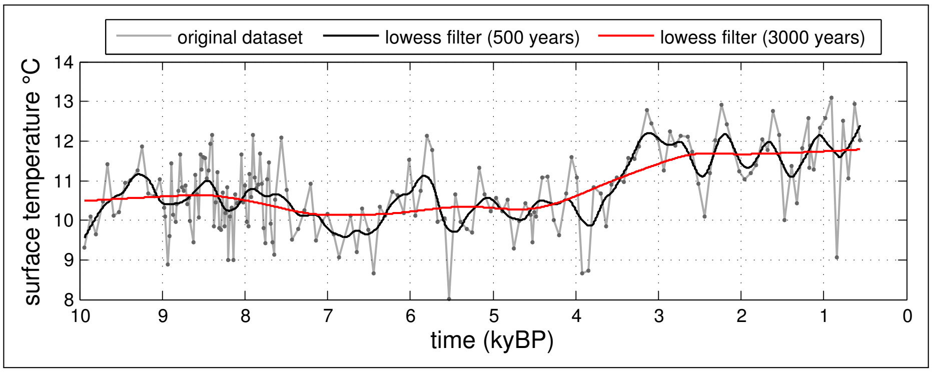

(26) August SST (North Atlantic), Farmer et al. (2008)

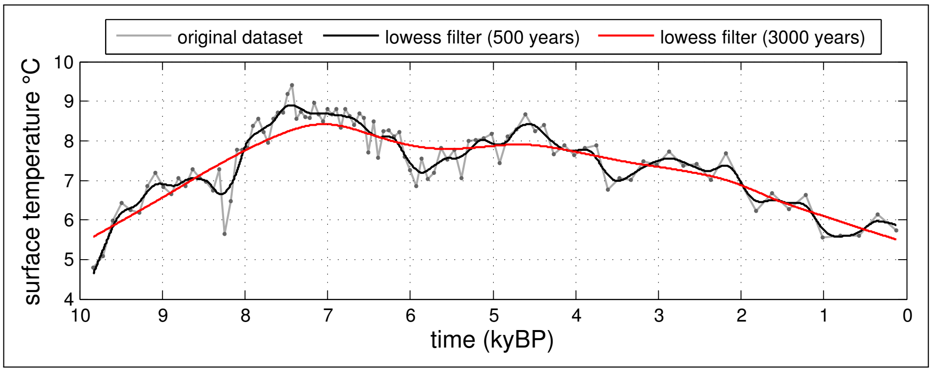

(27) Annual ST (Sweden),

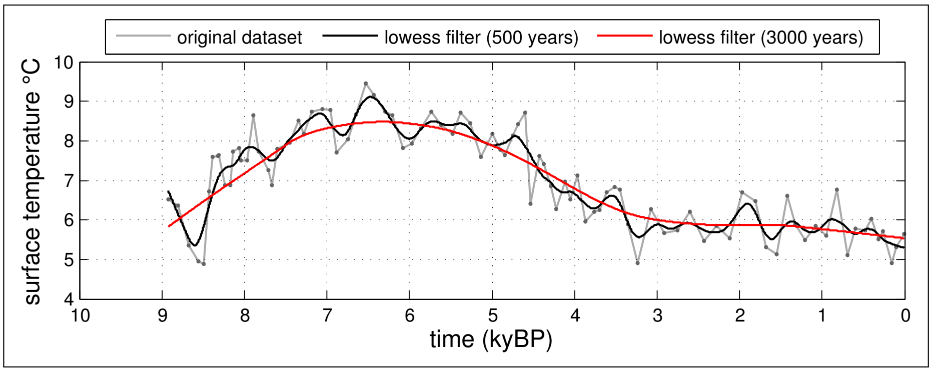

(28) Annual ST (Estonia), Seppä and Poska (2004)

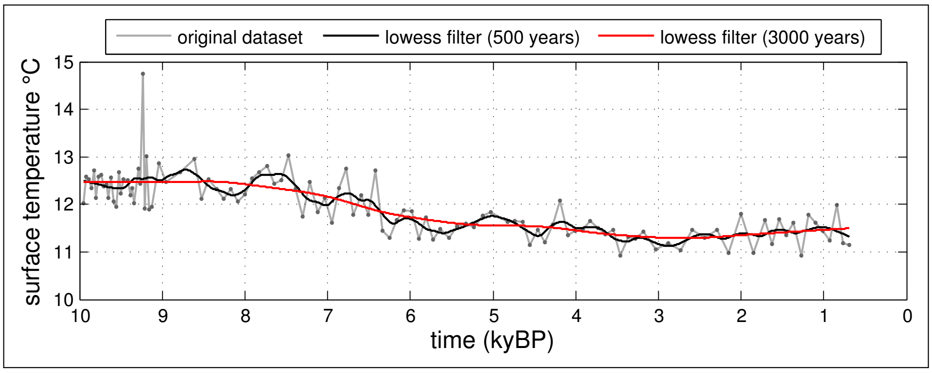

(29) Annual SST (North Atlantic), Marchal et al. (2002)

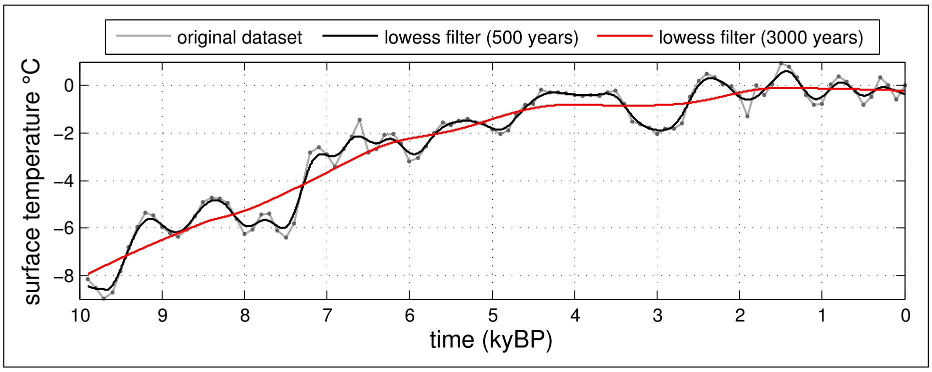

(30) January ST (Canada), Viau and Gajewski (2009)

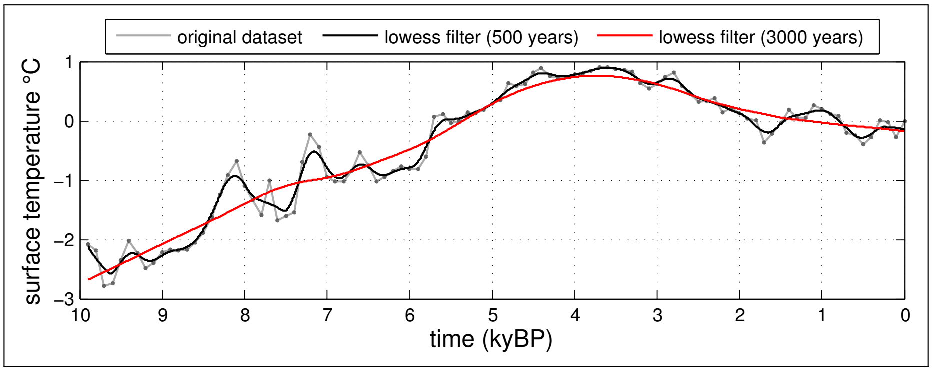

(31) July ST (Canada), Viau and Gajewski (2009)

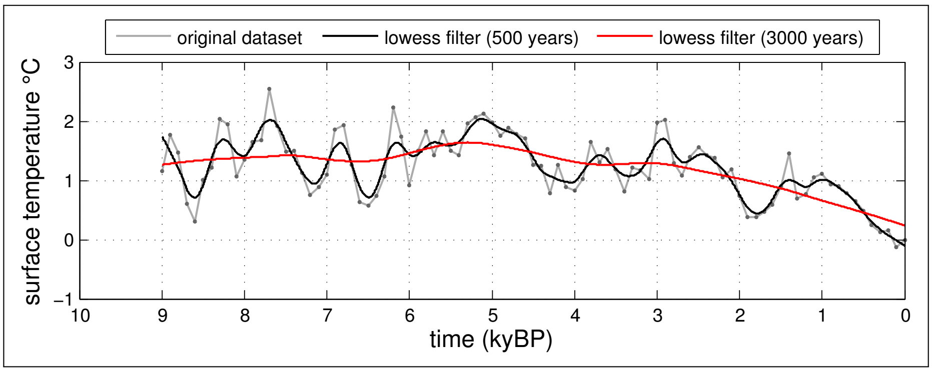

(32) January ST (Canada), Viau and Gajewski (2009)

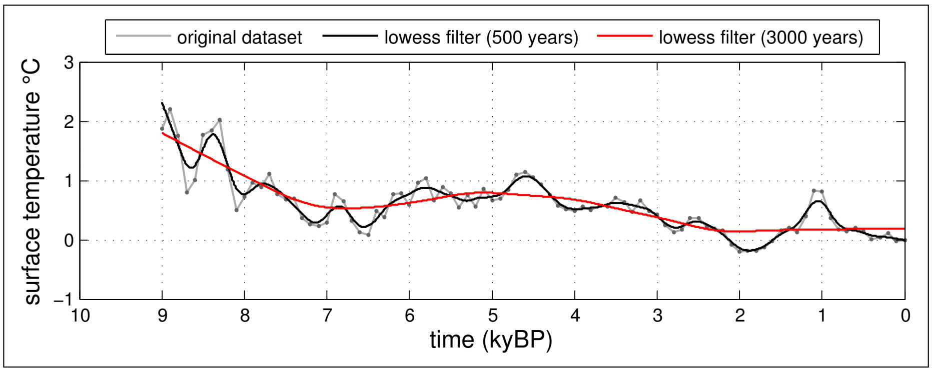

(33) July ST (Canada), Viau and Gajewski (2009)

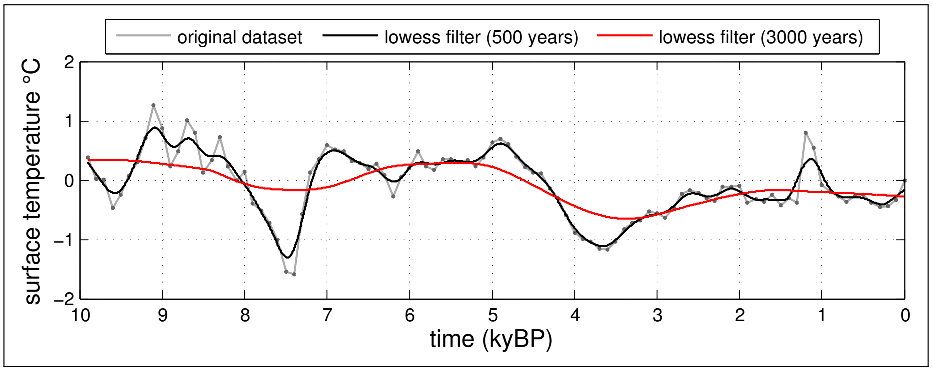

(34) January ST (Canada), Viau and Gajewski (2009)

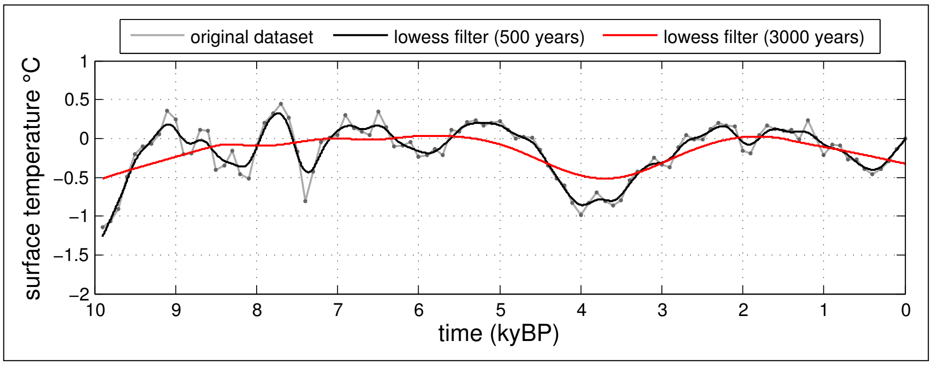

(35) July ST (Canada), Viau and Gajewski (2009)

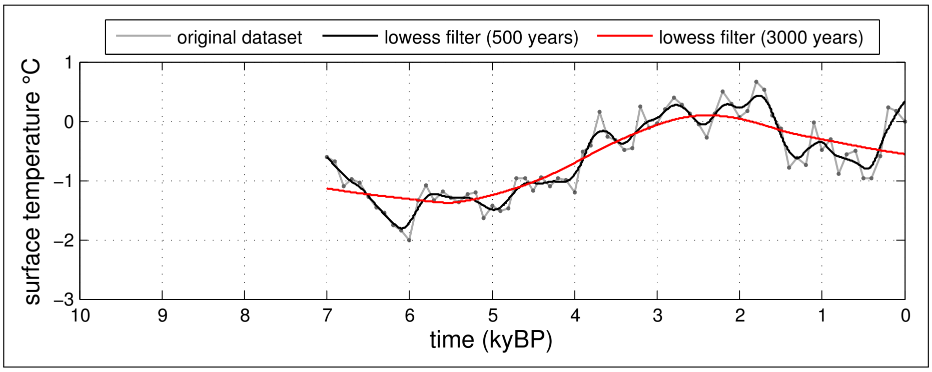

(36) January ST (Canada), Viau and Gajewski (2009)

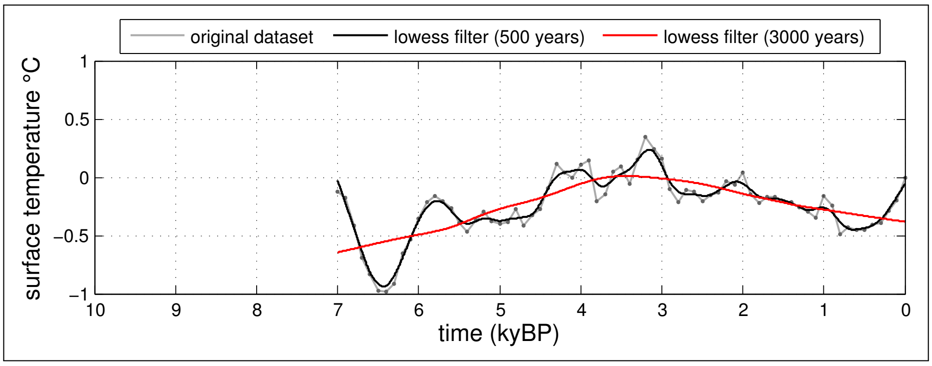

(37) July ST (Canada), Viau and Gajewski (2009)

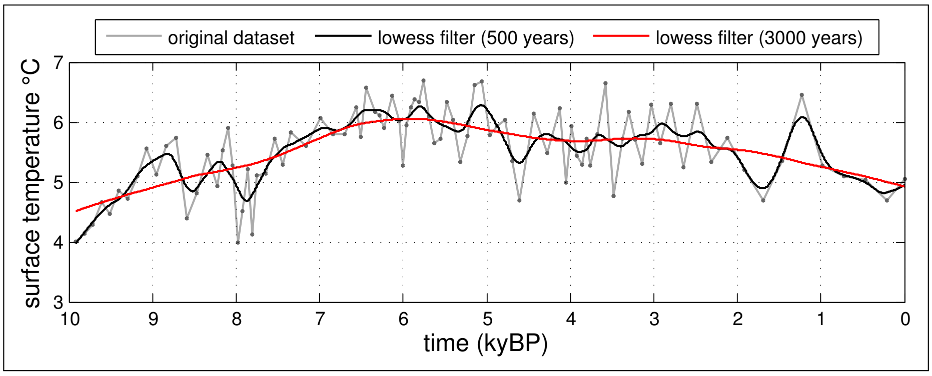

(38) Annual ST (Sweden), Antonsson et al. (2006)

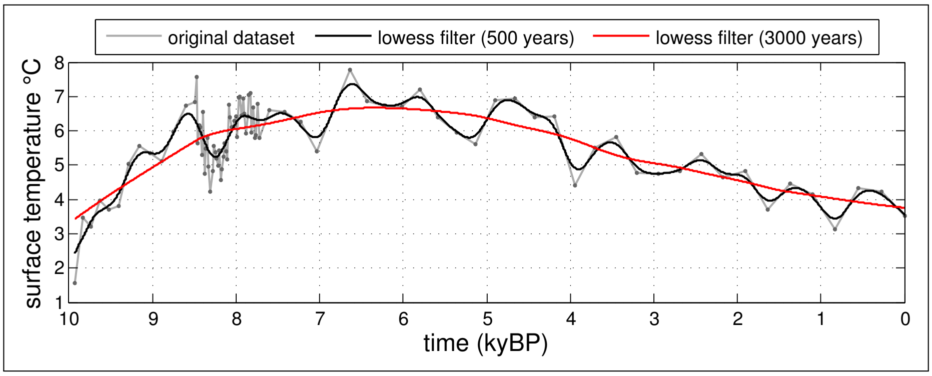

(39) Annual ST (Finland),

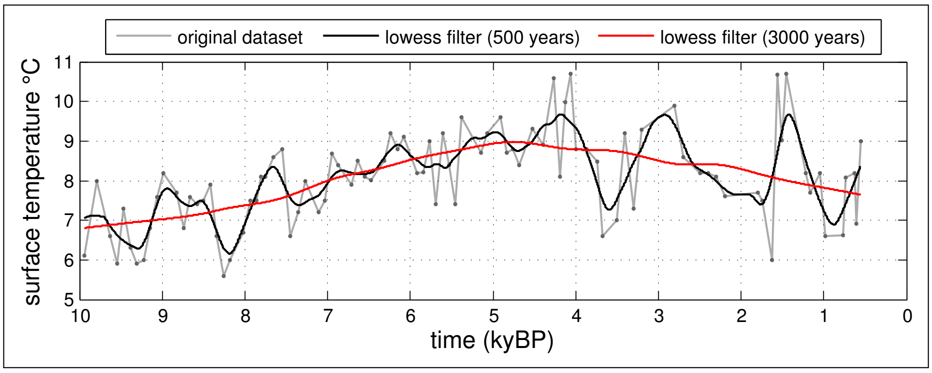

(40) Winter SST (North Atlantic), Came et al. (2007)

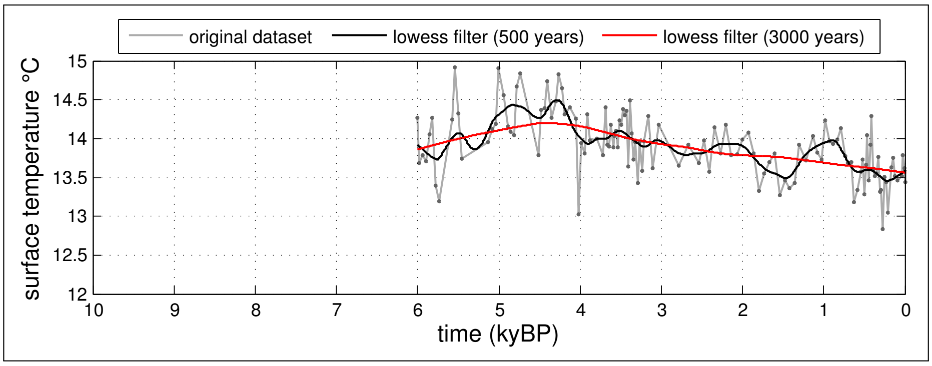

(41) July ST (Alaska), Clegg et al. (2010)

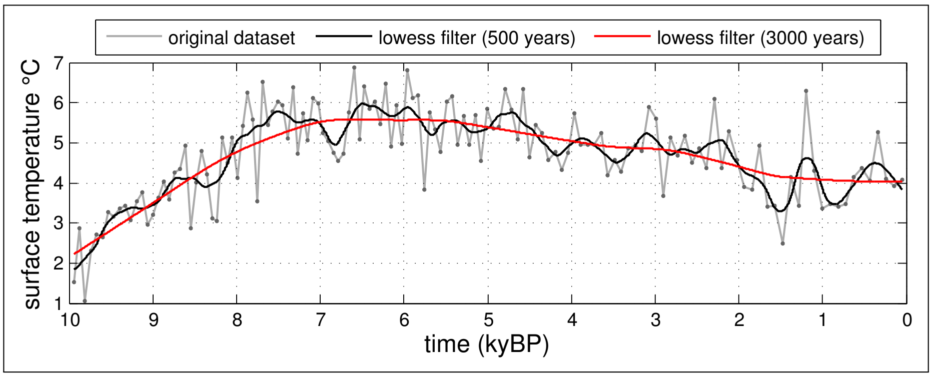

(42) Annual ST (Southern Finland), Heikkilä and Seppä (2003)

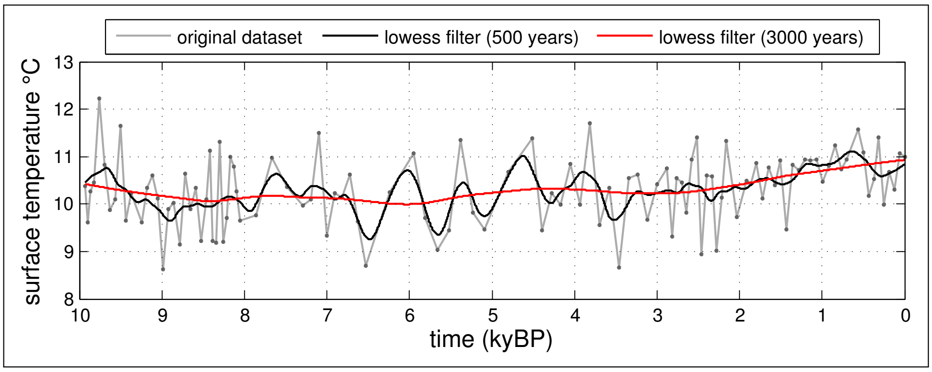

(43) May, June SST (Subpolar North Atlantic), Thornalley et al. (2009)

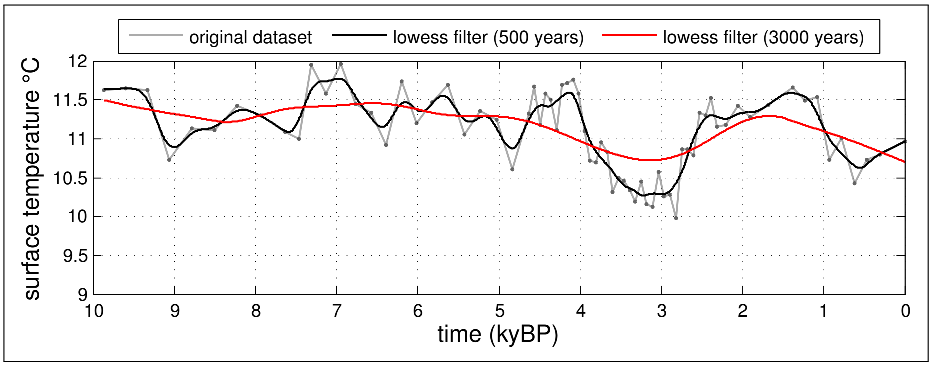

(44) July ST (Canada), Kurek et al. (2009)

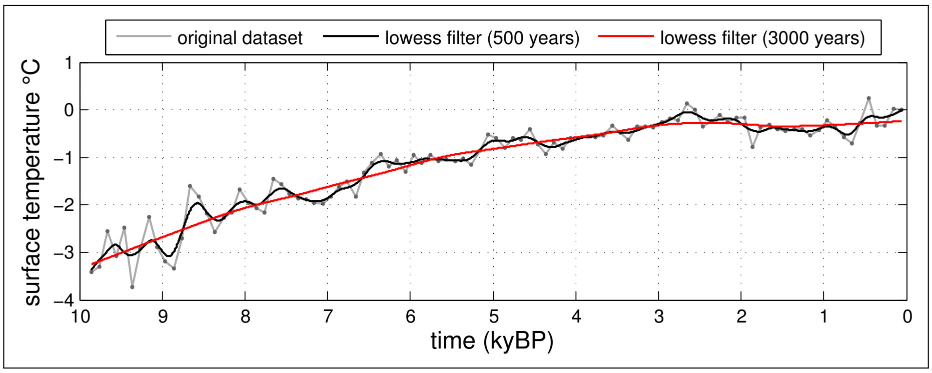

(45) January ST (Europe), Davis et al. (2003)

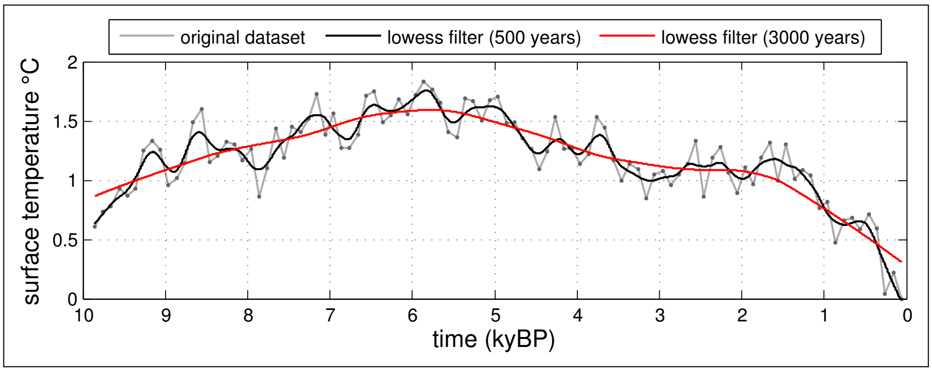

(46) July ST (Europe), Davis et al. (2003)

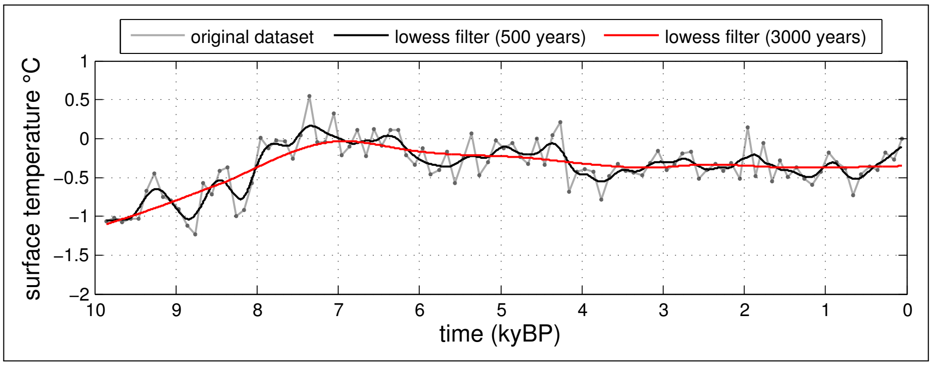

(47) January ST (Europe), Davis et al. (2003)

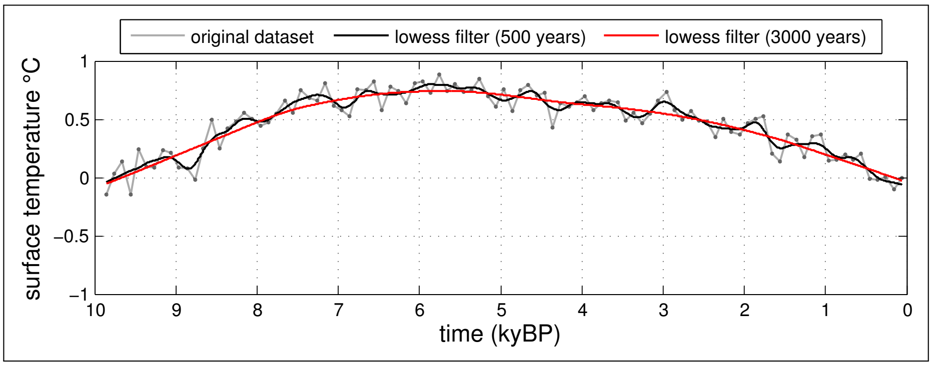

(48) July ST (Europe), Davis et al. (2003)

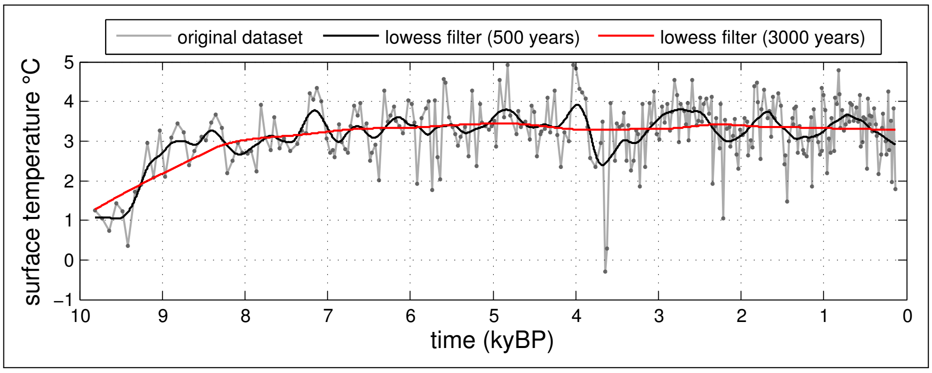

(49) Annual ST (Norway), Lauritzen and Lundberg (1999a)

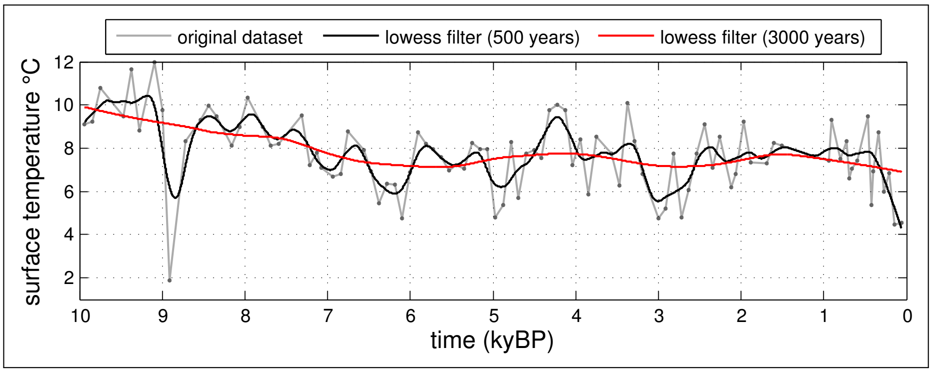

(50) Annual SST (Nordic Seas), Bendle and Rosell-Melé (2007)

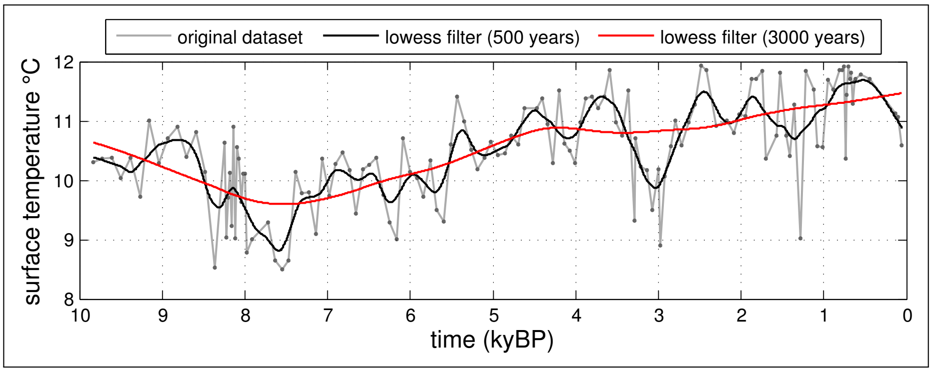

(51) August SST (Norwegian Sea), Risebrobakken et al. (2003)

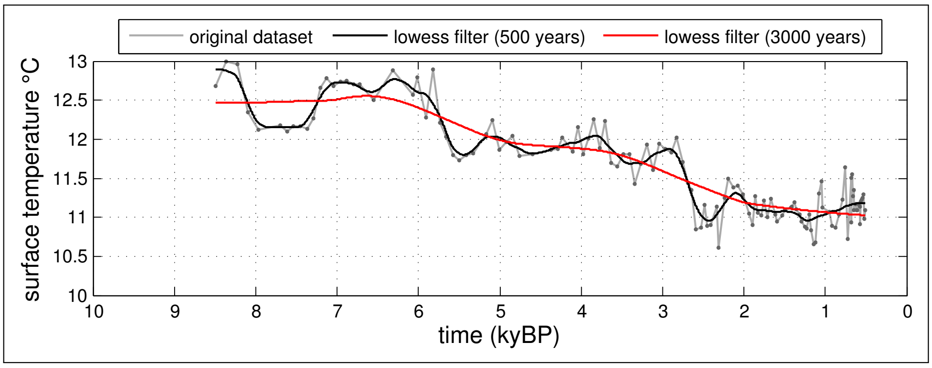

(52) Summer SST (Norwegian Sea), Calvo et al. (2002)

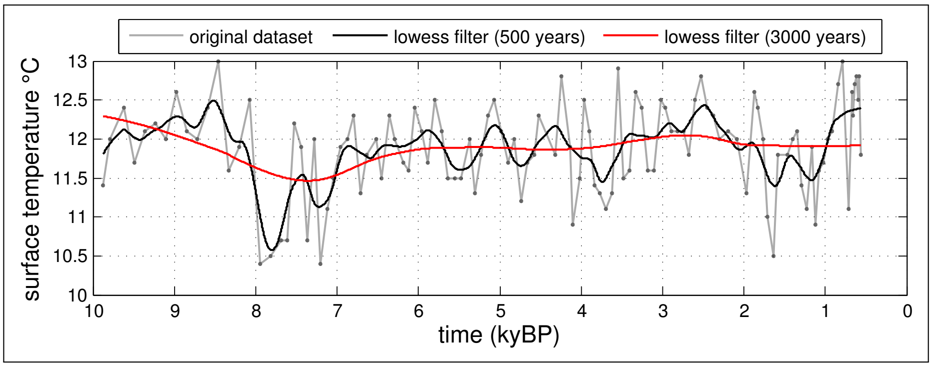

(53) Summer SST (Norwegian Sea), Dolven et al. (2002)

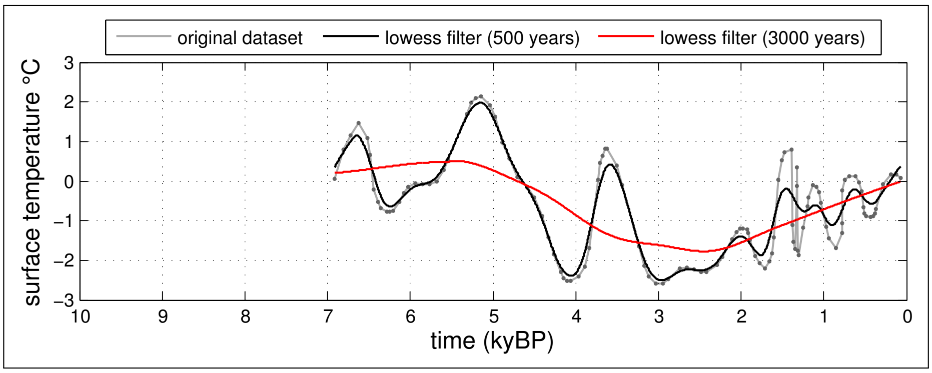

(54) January ST (Arctic Russia), Andreev and Klimanov (2000)

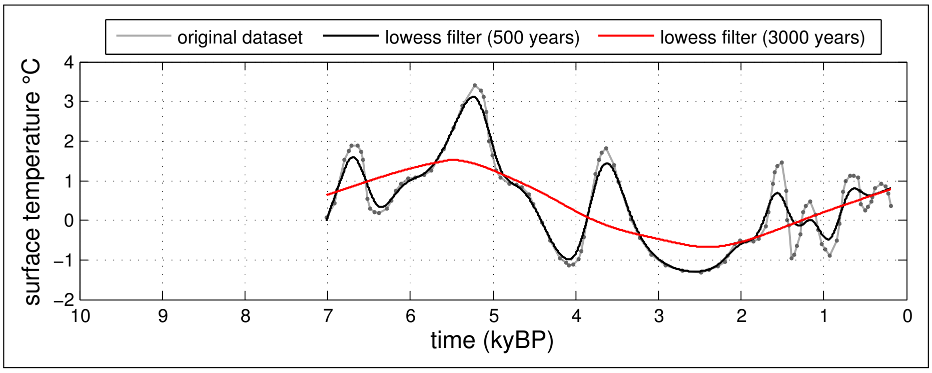

(55) July ST (Arctic Russia), Andreev and Klimanov (2000)

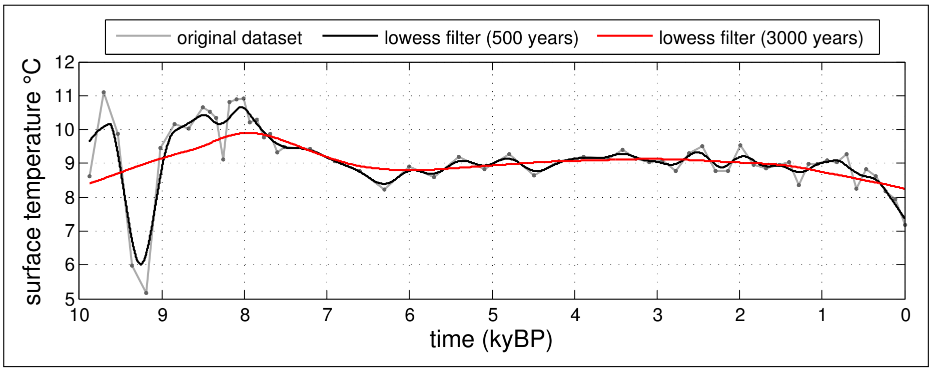

(56) July ST (Sweden (Abisko valley)), Larocque and Hall (2004)

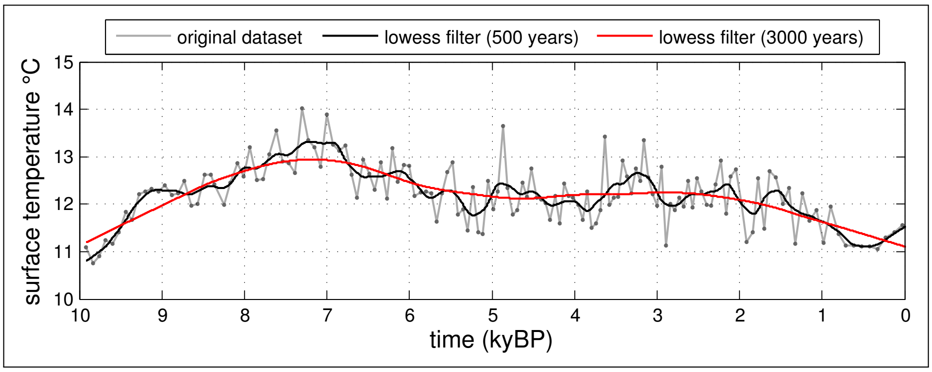

(57) July ST (Northern Finland), Seppä and Birks (2001)

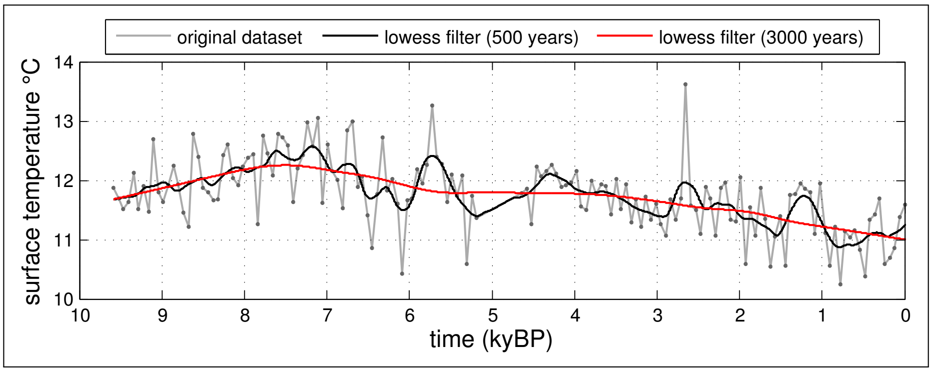

(58) July ST (Northern Finland), Seppä and Birks (2002)

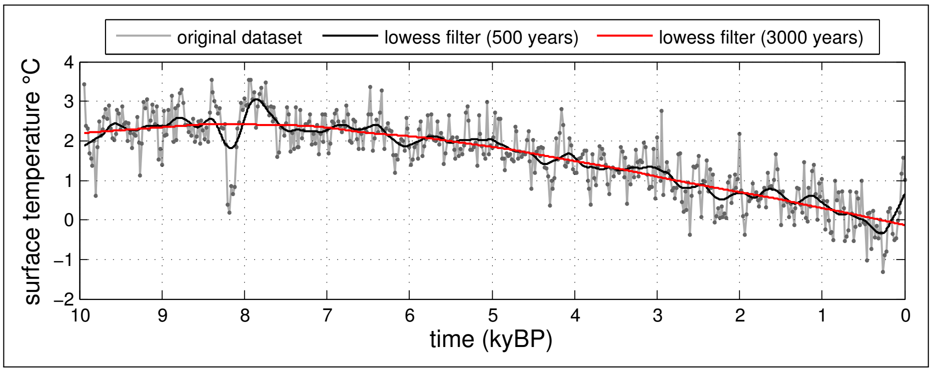

(59) Annual ST (Greenland), Vinther et al. (2009)

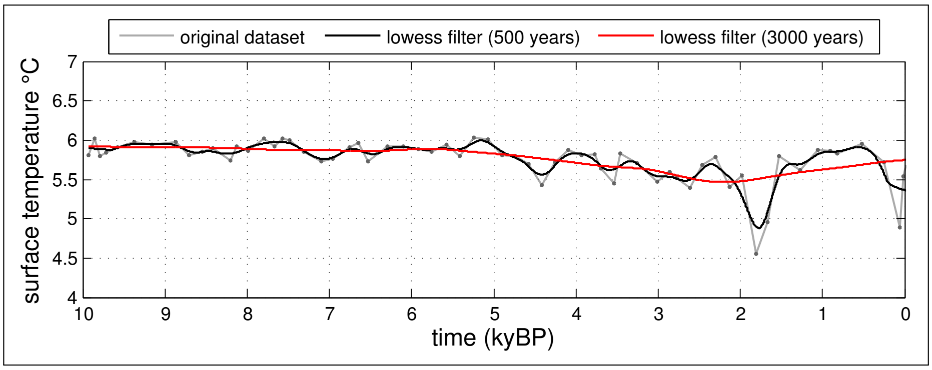

(60) July ST (Victoria Island (Canada)), Peros and Gajewski (2008)

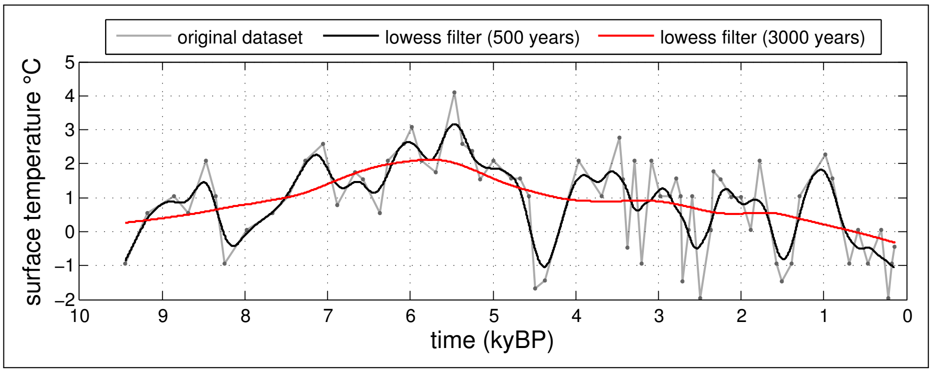

(61) Annual ST (Russia), Andreev et al. (2003)

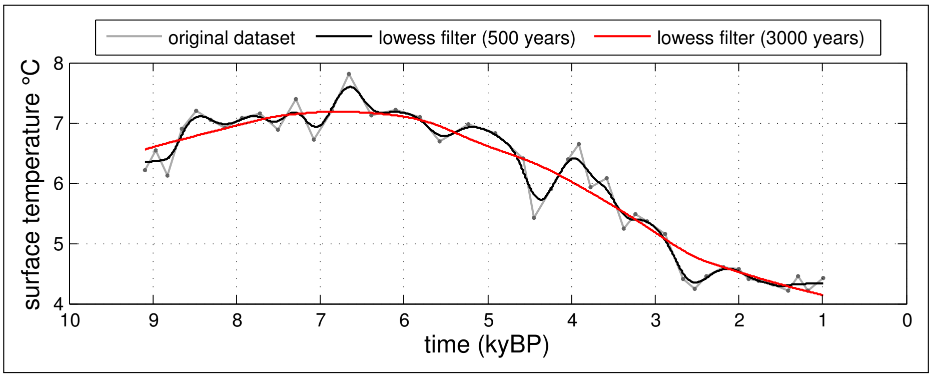

(62) Summer SST (Barents slope), Marchal et al. (2002)

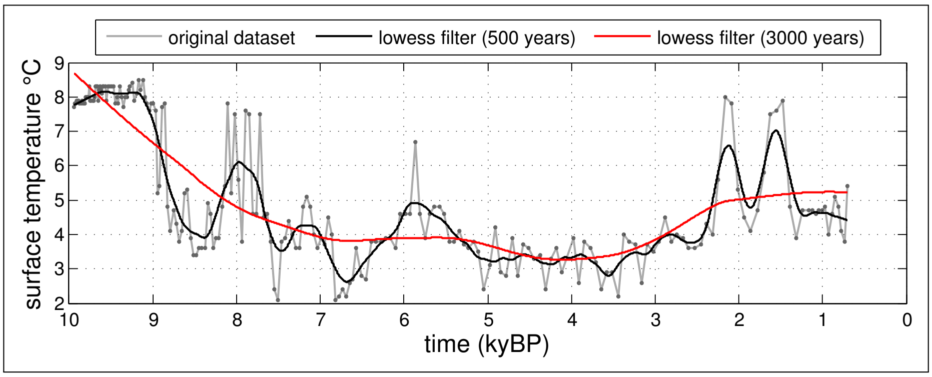

(63) Summer SST (Norwegian Sea), Sarnthein et al. (2003)

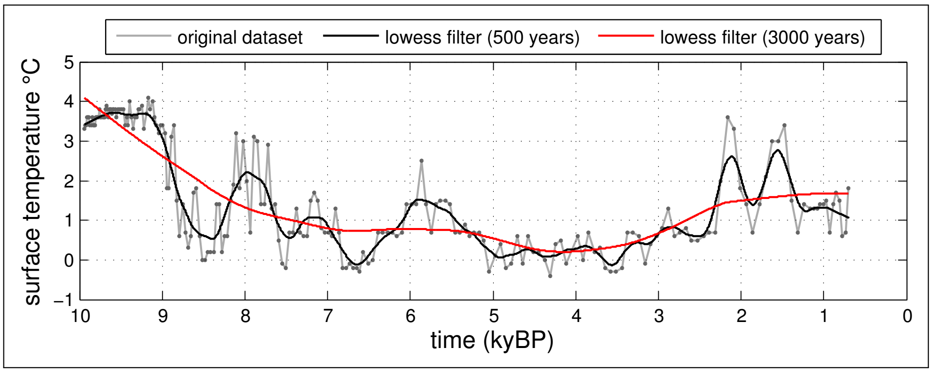

(64) Winter SST (Norwegian Sea), Sarnthein et al. (2003)

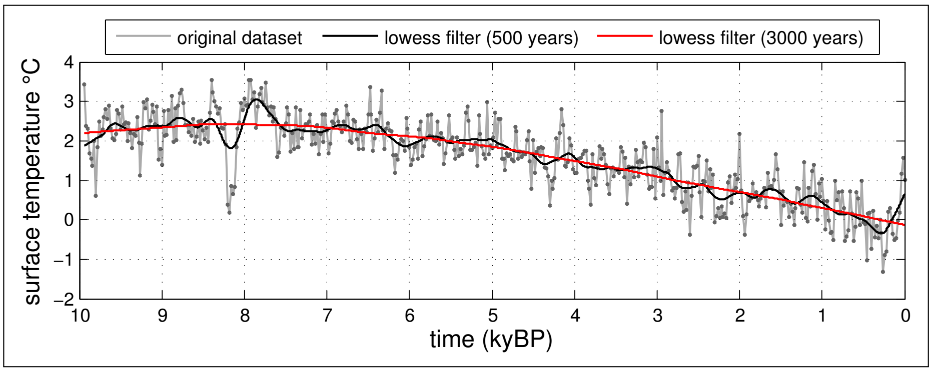

(65) Annual ST (Greenland), Vinther et al. (2009)

References

Andreev, A. A. and Klimanov, V. (2000). Quantitative Holocene climatic reconstruction from Arctic Russia. *Journal of Paleolimnology*, 24(1):81–91. Cited in pages 96, 128, 147, and 148.

Andreev, A. A., Tarasov, P. E., Siegert, C., Ebel, T., Klimanov, V. A., Melles, M., Bobrov, A. A., Dereviagin, A. Y., Lubinski, D. J., and Hubberten, H.-W. (2003). Late pleistocene and holocene vegetation and climate on the northern taymyr peninsula, arctic russia. *Boreas*, 32(3):484–505. Cited in pages 36, 41, 96, 128, and 150.

Antonsson, K., Brooks, S. J., Seppä, H., Telford, R. J., and Birks, H. J. B. (2006). Quantitative palaeotemperature records inferred from fossil pollen and chironomid assemblages from lake gilltjärnen, northern central sweden. *Journal of Quaternary Science*, 21(8):831–841. Cited in pages 40, 96, 127, and 142.

Bakker, P., Masson-Delmotte, V., Martrat, B., Charbit, S., Renssen, H., Gröger, M., Krebs-Kanzow, U., Lohmann, G., Lunt, D., Pfeiffer, M., Phipps, S., Prange, M., Ritz, S., Schulz, M., Stenni, B., Stone, E., and Varma, V. (2014). Temperature trends during the present and last interglacial periods – a multi-model-data comparison. *Quaternary Science Reviews*, 99(0):224 – 243. Cited in page 15.

Barber, D., Dyke, A., Hillaire-Marcel, C., Jennings, A., Andrews, J., Kerwin, M., Bilodeau, G., McNeely, R., Southon, J., Morehead, M., et al. (1999). Forcing of the cold event of 8,200 years ago by catastrophic drainage of laurentide lakes. *Nature*, 400(6742):344–348. Cited in page 2.

Barkan, E. and Luz, B. (2005). High precision measurements of 17o/16o and 18o/16o ratios in h2o. *Rapid Communications in Mass Spectrometry*, 19(24):3737–3742. Cited in page 11.

Barron, J., Heusser, L., Herbert, T., and Lyle, M. (2003). High-resolution climatic evolution of coastal northern california during the past 16,000 years. *Paleoceanography*, 18(1):n/a–n/a. Cited in pages 41, 96, 126, and 134.

Bartlein, P., Hostetler, S., and Alder, J. (2014). Paleoclimate. In Ohring, G., editor, *Climate Change in North America*, Regional Climate Studies, pages 1–51. Springer International Publishing. Cited in page 6.

Bartlein, P. J., Harrison, S. P., Brewer, S., Connor, S., Davis, B. A. S., Gajewski, K., Guiot, J., Harrison-Prentice, T. I., Henderson, A., Peyron, O., Prentice, I. C., Scholze, M., Seppä, H., Shuman, B., Sugita, S., Thompson, R. S., Viau, A. E., Williams, J., and Wu, H. (2011). Pollen-based continental climate reconstructions at 6 and 21 ka: a global synthesis. *Climate dynamics*, 37(3):775–802. Cited in pages 13 and 36.

Bendle, J. and Rosell-Melé, A. (2007). High-resolution alkenone sea surface temperature variability on the North Icelandic Shelf: implications for Nordic Seas palaeoclimatic development during the Holocene. *The Holocene*, 17(1):9–24. Cited in pages 9, 39, 40, 96, 128, and 146.

Berdahl, M. and Robock, A. (2013). Northern Hemispheric cryosphere response to volcanic eruptions in the Paleoclimate Modeling Intercomparison Project 3 last millennium simulations. *Journal of Geophysical Research: Atmospheres*, 118(22):12,359–12,370. Cited in pages 75 and 82.

Berger, A. (1978). Long-term variations of daily insolation and quaternary climatic changes. *Journal of Atmospheric Sciences*, 35:2362–2367. Cited in pages 2, 15, 17, 23, 46, and 65.

Birks, H., Heiri, O., Seppä, H., and Bjune, A. (2010). Strengths and weaknesses of quantitative climate reconstructions based on late-quaternary biological proxies. *Open Ecology Journal*, 3:68–110. Cited in page 39.

Birks, H. J. B. (2007). Quantitative palaeoenvironmental reconstructions. In Maddy, D. and Brew, J. S., editors, *Statistical Modelling of Quaternary Science Data*. Technical guide 5, Quaternary Research Association, Cambridge. Cited in page 12.

Blum, P. (1997). Physical properties handbook: a guide to the shipboard measurement of physical properties of deep-sea cores. Technical report, ODP Tech. Note. Cited in page 7.

Boer, G. (2011). The ratio of land to ocean temperature change under global warming. *Climate Dynamics*, 37(11-12):2253–2270. Cited in pages 50 and 80.

Bond, G., Kromer, B., Beer, J., Muscheler, R., Evans, M., Showers, W., Hoffmann, S., Lotti-Bond, R., Hajdas, I., and Bonani, G. (2001). Persistent solar influence on north atlantic climate during the holocene. *Science*, 294(5549):2130–2136. Cited in pages 94 and 95.

Bond, G., Showers, W., Cheseby, M., Lotti, R., Almasi, P., Priore, P., Cullen, H., Hajdas, I., Bonani, G., et al. (1997). A pervasive millennial-scale cycle in north atlantic holocene and glacial climates. *science*, 278(5341):1257–1266. Cited in page 94.

Bonfils, C., de Noblet-Ducoudre, N., Guiot, J., and Bartlein, P. (2004). Some mechanisms of mid-holocene climate change in europe, inferred from comparing pmip models to data. *Climate dynamics*, 23(1):79–98. Cited in page 14.

Braconnot, P., Harrison, S., Kageyama, M., Bartlein, P., Masson-Delmotte, V., Abe-Ouchi, A., Otto-Bliesner, B., and Zhao, Y. (2012). Evaluation of climate models using palaeoclimatic data. *Nature Climate Change*, 2(6):417–424. Cited in pages 14, 28, and 36.

Braconnot, P., Otto-Bliesner, B., Harrison, S., Joussaume, S., Peterchmitt, J.-Y., Abe-Ouchi, A., Crucifix, M., Driesschaert, E., Fichefet, T., Hewitt, C. D., Kageyama, M., Kitoh, A., Laîné, A., Loutre, M.-F., Marti, O., Merkel, U., Ramstein, G., Valdes, P., Weber, S. L., Yu, Y., and Zhao, Y. (2007a). Results of PMIP2 coupled simulations of the Mid-Holocene and Last Glacial Maximum – Part 1: experiments and large-scale features. *Climate of the Past*, 3(2):261–277. Cited in pages 14, 29, 36, and 46.

Braconnot, P., Otto-Bliesner, B., Harrison, S., Joussaume, S., Peterchmitt, J.-Y., Abe-Ouchi, A., Crucifix, M., Driesschaert, E., Fichefet, T., Hewitt, C. D., Kageyama, M., Kitoh, A., Loutre, M.-F., Marti, O., Merkel, U., Ramstein, G., Valdes, P., Weber, S. L., Yu, Y., and Zhao, Y. (2007b). Results of PMIP2 coupled simulations of the Mid-Holocene and Last Glacial Maximum – Part 2: feedbacks with emphasis on the location of the ITCZ and mid and high latitudes heat budget. *Climate of the Past*, 3(2):279–296. Cited in pages 14 and 29.

Bradley, R. (1999). *Paleoclimatology: reconstructing climates of the Quaternary*. Academic Press. Cited in pages 3, 11, and 12.

Brewer, S., Guiot, J., and Barboni, D. (2007a). Pollen Methods and Studies : Use of Pollen as Climate Proxies. In Elias, S. A., editor, *Encyclopedia of Quaternary Science*, pages 2497–2508. Elsevier, Oxford. Cited in pages 12 and 39.

Brewer, S., Guiot, J., and Torre, F. (2007b). Mid-holocene climate change in europe: a data-model comparison. *Climate of the Past*, 3(3):499–512. Cited in pages 29 and 36.

Brook, E. J. (2007). Ice Core Methods : Overview. In Elias, S. A., editor, *Encyclopedia of Quaternary Science*, pages 2497–2508. Elsevier, Oxford. Cited in pages 10 and 39.

Brovkin, V., Bendtsen, J., Claussen, M., Ganopolski, A., Kubatzki, C., Petoukhov, V., and Andreev, A. (2002). Carbon cycle, vegetation, and climate dynamics in the holocene: Experiments with the climber-2 model. *Global Biogeochemical Cycles*, 16(4):86–1. Cited in page 15.

Brovkin, V., Ganopolski, A., and Svirezhev, Y. (1997). A continuous climate-vegetation classification for use in climate-biosphere studies. *Ecological Modelling*, 101(2-3):251–261. Cited in pages 15, 18, 19, and 37.

Caley, T. and Roche, D. M. (2013). δ^{18}o water isotope in the iloveclim model (version 1.0) – part 3: A palaeo-perspective based on present-day dataâ“model comparison for oxygen stable isotopes in carbonates. *Geoscientific Model Development*, 6(5):1505–1516. Cited in page 123.

Calvo, E., Grimalt, J., and Jansen, E. (2002). High resolution UK37 sea surface temperature reconstruction in the norwegian sea during the holocene. *Quaternary Science Reviews*, 21(12-13):1385 – 1394. Cited in pages 56, 96, 128, and 147.

Came, R. E., Oppo, D. W., and McManus, J. F. (2007). Amplitude and timing of temperature and salinity variability in the subpolar north atlantic over the past 10 k.y. *Geology*, 35(4):315–318. Cited in pages 8, 9, 96, 127, and 143.

Charney, J., Stone, P. H., and Quirk, W. J. (1975). Drought in the sahara: a biogeophysical feedback mechanism. *Science*, 187:434–435. Cited in page 2.

Chou, C. and Neelin, J. D. (1996). Linearization of a longwave radiation scheme for intermediate tropical atmospheric models. *Journal of Geophysical Research: Atmospheres*, 101(D10):15129–15145. Cited in page 17.

Claussen, M. (2005). Table of emics (earth system models of intermediate complexity). Technical report, PIK Report 98, Potsdam-Institut fur Klimafolgenforschung, Potsdam, Germany. Cited in page 13.

Claussen, M., Kubatzki, C., Brovkin, V., Ganopolski, A., Hoelzmann, P., and Pachur, H. (1999). Simulation of an abrupt change in saharan vegetation in the mid-holocene. *Geophysical Research Letters*, 26(14):2037–2040. Cited in page 36.

Claussen, M., Mysak, L., Weaver, A., Crucifix, M., Fichefet, T., Loutre, M., Weber, S., Alcamo, J., Alexeev, V., Berger, A., et al. (2002). Earth system models of intermediate complexity: closing the gap in the spectrum of climate system models. *Climate Dynamics*, 18(7):579–586. Cited in page 13.

Clegg, B. F., Clarke, G. H., Chipman, M. L., Chou, M., Walker, I. R., Tinner, W., and Hu, F. S. (2010). Six millennia of summer temperature variation based on midge analysis of lake sediments from alaska. *Quaternary Science Reviews*, 29(23-24):3308 – 3316. Cited in pages 36, 96, 127, and 143.

COHMAP-Members (1988). Climatic changes of the last 18,000 years: Observations and model simulations. *Science*, 241:1043–1052. Cited in page 14.

Craig, H. (1961). Standard for reporting concentrations of deuterium and oxygen-18 in natural waters. *Science*, 133(3467):1833–1834. Cited in page 11.

Crespin, E., Goosse, H., Fichefet, T., Mairesse, A., and Sallaz-Damaz, Y. (2013). Arctic climate over the past millennium: Annual and seasonal responses to external forcings. *The Holocene*, 23(3):321–329. Cited in pages 14, 15, and 45.

Crespin, E., Goosse, H., Fichefet, T., and Mann, M. E. (2009). The 15th century arctic warming using coupled model simulations with data assimilation. *Climate of the Past*, 5:389–401. Cited in page 31.

Crowley, T., Zielinski, G., Vinther, B., Udisti, R., Kreutz, K., Cole-Dai, J., and Castellano, E. (2008). Volcanism and the little ice age. *PAGES news*, 16(2):22–23. Cited in pages 24 and 102.

Crucifix, M. (2008). Modelling the climate of the holocene. In *R. W. Battarbee and H. Binney, editors, Natural climate variability and global warming: a Holocene perspective*, pages 98–122. Wiley-Blackwell, Singapore. Cited in page 36.

Crucifix, M., Loutre, M. F., Tulkens, P., Fichefet, T., and Berger, A. (2002). Climate evolution during the Holocene: a study with an Earth system model of intermediate complexity. *Climate Dynamics*, 19(1):43–60. Cited in page 15.

Cullen, H. M. and deMenocal, P. B. (2000). North atlantic influence on tigris–euphrates streamflow. *International Journal of Climatology*, 20(8):853–863. Cited in page 3.

Davis, B. A. S., Brewer, S., Stevenson, A. C., and Guiot, J. (2003). The temperature of europe during the holocene reconstructed from pollen data. *Quaternary Science Reviews*, 22(15-17):1701 – 1716. Cited in pages 13, 34, 36, 42, 43, 44, 59, 60, 96, 97, 120, 126, 127, 128, 129, 132, 133, 136, 137, 144, and 145.

Davis, M. (2000). Palynology after y2k-understanding the source area of pollen in sediments. *Annual Review of Earth and Planetary Sciences*, 28(1):1–18. Cited in page 11.

Delaygue, G. and Bard, E. (2009). Solar forcing based on Be-10 in Antarctica ice over the past millennium and beyond. In *EGU2009-6943 keynote*. Cited in page 23.

Deleersnijder, E., Beckers, J.-M., Campin, J.-M., El Mohajir, M., Fichefet, T., and Luyten, P. (1997). Some mathematical problems associated with the development and use of marine models. In *The mathematics of models for climatology and environment*, pages 39–86. Springer. Cited in page 17.

Demenocal, P., Ortiz, J., Guilderson, T., Adkins, J., Sarnthein, M., Baker, L., and Yarusinsky, M. (2000). Abrupt onset and termination of the african humid period:: rapid climate responses to gradual insolation forcing. *Quaternary science reviews*, 19(1):347–361. Cited in page 2.

deMenocal, P., Ortiz, J., Guilderson, T., and Sarnthein, M. (2000). Coherent high- and low-latitude climate variability during the holocene warm period. *Science*, 288(5474):2198–2202. Cited in pages 41, 126, and 130.

deMenocal, P. B. (2001). Cultural responses to climate change during the late holocene. *Science*, 292(5517):667–673. Cited in page 3.

Dickinson, R. E., Kennedy, P., and Henderson-Sellers, A. (1993). *Biosphere-atmosphere transfer scheme (BATS) version 1e as coupled to the NCAR community climate model.* National Center for Atmospheric Research, Climate and Global Dynamics Division. Cited in page 19.

Dolven, J., Cortese, G., and Bjørklund, K. (2002). A high-resolution radiolarian-derived paleotemperature record for the Late Pleistocene-Holocene in the Norwegian Sea. *Paleoceanography.* Cited in pages 96, 128, and 147.

Dowsett, H. J. (2007). Paleoceanography, Biological Proxies : Planktic foraminifera. In Elias, S. A., editor, *Encyclopedia of Quaternary Science*, pages 1678 – 1682. Elsevier, Oxford. Cited in pages 7 and 8.

Driscoll, S., Bozzo, A., Gray, L. J., Robock, A., and Stenchikov, G. (2012). Coupled Model Intercomparison Project 5 (CMIP5) simulations of climate following volcanic eruptions. *Journal of Geophysical Research: Atmospheres*, 117(D17):n/a–n/a. Cited in page 62.

Dubinkina, S., Goosse, H., Sallaz-damaz, Y., Crespin, E., and Crucifix, M. (2011). Testing a particle filter to reconstruct climate changes over past centuries. *International Journal of Bifurcation and Chaos*, 21(12):3611–3618. Cited in pages 29, 31, 37, 38, and 39.

Elderfield, H. and Ganssen, G. (2000). Past temperature and δ^{18}o of surface ocean waters inferred from foraminiferal Mg/Ca ratios. *Nature*, 405(6785):442–445. Cited in page 8.

Esparza, M. (2005). Estudi de la variabilitat climàtica de l'oceà Atlàntic nord durant l'holocè mitjançant biomarcadors moleculars. Master's thesis, Autonomous University of Barcelona. Faculty of Sciences. Cited in pages 40, 127, and 138.

Farmer, E., Chapman, M., and Andrews, J. (2008). Centennial-scale Holocene North Atlantic surface temperatures from Mg/Ca ratios in Globigerina bulloides. *Geochemistry Geophysics Geosystems*, 9(12):Q12029. Cited in pages 96, 127, and 138.

Fichefet, T., Huybrechts, P., Decleir, H., and Munhoven, G. (2007). *Modelling the evolution of climate and sea level during the third millennium (MILMO)*, volume 2 - Global Change. Ecosystem and Biodiversity - Atmosphere and Climate. Belgian Science Policy. Cited in page 18.

Fichefet, T. and Morales Maqueda, M. A. (1997). Sensitivity of a global sea ice model to the treatment of ice thermodynamics and dynamics. *Journal of Geophysical Research: Oceans*, 102(C6):12609–12646. Cited in page 18.

Flato, G., Marotzke, J., Abiodun, P., Braconnot, P., Chou, S., Collins, P. C., Driouech, F., Emori, S., Eyring, V., Forest, C., Gleckler, E., Guilyardi, E., Jakob, C., Kattsov, V., Reason, C., and Rummukainen, M. (2013). Evaluation of Climate Models. In *Climate Change 2013: The Physical Science Basis. Contribution of Working Group I to the Fifth Assessment Report of the Intergovernmental Panel on Climate Change [Stocker, T.F., D. Qin, G.-K. Plattner, M. Tignor, S.K. Allen, J. Boschung, A. Nauels, Y. Xia, V. Bex and P.M. Midgley (eds.)]*. Cambridge University Press, Cambridge, United Kingdom and New York, NY, USA. Cited in page 21.

Flückiger, J., Monnin, E., Stauffer, B., Schwander, J., Stocker, T. F., Chappellaz, J., Raynaud, D., and Barnola, J.-M. (2002). High-resolution holocene n2o ice core record and its relationship with ch4 and co2. *Global Biogeochemical Cycles*, 16(1):10–1–10–8. Cited in pages 22, 25, 26, 46, and 65.

Fraile, I., Mulitza, S., and Schulz, M. (2009). Modeling planktonic foraminiferal seasonality: Implications for sea-surface temperature reconstructions. *Marine Micropaleontology*, 72(1–2):1 – 9. Cited in page 8.

Gao, C., Oman, L., Robock, A., and Stenchikov, G. L. (2007). Atmospheric volcanic loading derived from bipolar ice cores: Accounting for the spatial distribution of volcanic deposition. *Journal of Geophysical Research: Atmospheres (1984–2012)*, 112(D9). Cited in pages 63, 64, and 66.

Gao, C., Robock, A., and Ammann, C. (2008). Volcanic forcing of climate over the past 1500 years: An improved ice core-based index for climate models. *Journal of Geophysical Research: Atmospheres*, 113(D23):n/a–n/a. Cited in pages 10, 22, 24, 61, 64, 66, 67, 68, and 69.

Gao, C., Robock, A., Self, S., Witter, J. B., Steffenson, J. P., Clausen, H. B., Siggaard-Andersen, M.-L., Johnsen, S., Mayewski, P. A., and Ammann, C. (2006). The 1452 or 1453 a.d. kuwae eruption signal derived from multiple ice core records: Greatest volcanic sulfate event of the past 700 years. *Journal of Geophysical Research: Atmospheres*, 111(D12):n/a–n/a. Cited in page 63.

Gibbons, A. (1993). How the akkadian empire was hung out to dry. *Science (New York, NY)*, 261(5124):985. Cited in page 3.

Gladstone, R., Ross, I., Valdes, P., Abe-Ouchi, A., Braconnot, P., Brewer, S., Kageyama, M., Kitoh, A., Legrande, A., Marti, O., Otto-Bliesner, B., Peltier, W. R., and Vettoretti, G. (2005). Mid-holocene NAO: a PMIP2 model intercomparison. *Geophysical Research Letters*, 32(16):L16707. Cited in pages 14 and 46.

Goelzer, H., Huybrechts, P., Raper, S., Loutre, M.-F., Goosse, H., and Fichefet, T. (2012). Millennial total sea-level commitments projected with the earth system model of intermediate complexity loveclim. *Environmental Research Letters*, 7(4):045401. Cited in page 16.

Goosse, H., Braida, M., Crosta, X., Mairesse, A., Masson-Delmotte, V., Mathiot, P., Neukom, R., Oerter, H., Philippon, G., Renssen, H., Stenni, B., van Ommen, T., and Verleyen, E. (2012a). Antarctic temperature changes during the last millennium: evaluation of simulations and reconstructions. *Quaternary Science Reviews*, 55(0):75 – 90. Cited in page 15.

Goosse, H., Brovkin, V., Fichefet, T., Haarsma, R., Huybrechts, P., Jongma, J., Mouchet, A., Selten, F., Barriat, P.-Y., Campin, J.-M., Deleersnijder, E., Driesschaert, E., Goelzer, H., Janssens, I., Loutre, M.-F., Morales Maqueda, M. A., Opsteegh, T., Mathieu, P.-P., Munhoven, G., Pettersson, E. J., Renssen, H., Roche, D. M., Schaeffer, M., Tartinville, B., Timmermann, A., and Weber, S. L. (2010a). Description of the earth system model of intermediate complexity LOVECLIM version 1.2. *Geoscientific Model Development*, 3(2):603–633. Cited in pages 15, 16, 17, 18, 21, 37, 45, and 123.

Goosse, H., Campin, J.-M., Deleersnijder, E., Fichefet, T., Mathieu, P.-P., Morales Maqueda, M. A., and Tartinville, B. (2000). *Description of the CLIO model version 3.0.* Cited in pages 17 and 18.

Goosse, H., Crespin, E., de Montety, A., Mann, M. E., Renssen, H., and Timmermann, A. (2010b). Reconstructing surface temperature changes over the past 600 years using climate model simulations with data assimilation. *J. Geophys. Res.*, 115(D9). Cited in pages 31 and 118.

Goosse, H., Crespin, E., Dubinkina, S., Loutre, M.-F., Mann, M. E., Renssen, H., Sallaz-Damaz, Y., and Shindell, D. (2012b). The role of forcing and internal dynamics in explaining the "medieval climate anomaly". *Climate Dynamics*, 39(12):2847–2866. Cited in pages 31, 34, 39, 44, 105, 106, 118, and 121.

Goosse, H. and Fichefet, T. (1999). Importance of ice-ocean interactions for the global ocean circulation: a model study. *Journal of Geophysical Research*, 104(C10):23337–23355. Cited in pages 15, 17, and 37.

Goosse, H., Guiot, J., Mann, M. E., Dubinkina, S., and Sallaz-Damaz, Y. (2012c). The medieval climate anomaly in Europe: Comparison of the summer and annual mean signals in two reconstructions and in simulations with data assimilation. *Global and Planetary Change*, 84 - 85(0):35 – 47. Cited in page 31.

Goosse, H. and Holland, M. M. (2005). Mechanisms of decadal arctic climate variability in the community climate system model, version 2 (ccsm2). *Journal of climate*, 18(17):3552–3570. Cited in page 115.

Goosse, H., Lefebvre, W., de Montety, A., Crespin, E., and Orsi, A. H. (2009). Consistent past half-century trends in the atmosphere, the sea ice and the ocean at high southern latitudes. *Climate Dynamics*, 33(7-8):999–1016. Cited in page 31.

Goosse, H. and Renssen, H. (2004). Exciting natural modes of variability by solar and volcanic forcing: idealized and realistic experiments. *Climate dynamics*, 23(2):153–163. Cited in pages 62 and 81.

Goosse, H., Renssen, H., Timmermann, A., Bradley, R., and Mann, M. E. (2006). Using paleoclimate proxy-data to select optimal realisations in an ensemble of simulations of the climate of the past millennium. *Climate Dynamics*, 27(2):165–184. Cited in pages 31 and 38.

Goosse, H., Selten, F., Haarsma, R., and Opsteegh, J. (2001). Decadal variability in high northern latitudes as simulated by an intermediate-complexity climate model. *Annals of Glaciology*, 33(1):525–532. Cited in page 16.

Goosse, H., Selten, F., Haarsma, R., and Opsteegh, J. (2002). A mechanism of decadal variability of the sea-ice volume in the northern hemisphere. *Climate dynamics*, 19(1):61–83. Cited in pages 16 and 113.

Grieser, J. and Schonwiese, C. (1999). Parameterization of spatio-temporal patterns of volcanic aerosol induced stratospheric optical depth and its climate radiative forcing. *Atmosfera*, 12(2). Cited in pages 68 and 69.

Grimalt, J. and Lopez, J. (2007). Paleoceanography, Biological Proxies : Alkenone Paleothermometry from Coccoliths. In Elias, S. A., editor, *Encyclopedia of Quaternary Science*, pages 1610 – 1618. Elsevier, Oxford. Cited in pages 9 and 39.

Guiot, J., Boreux, J.-J., Braconnot, P., and Torre, F. (1999). Data-model comparison using fuzzy logic in paleoclimatology. *Climate dynamics*, 15(8):569–581. Cited in page 51.

Guiot, J. and de Vernal, A. (2007). Transfer functions: methods for quantitative paleoceanography based on microfossils. *Developments in marine geology*, 1:523–563. Cited in page 6.

Harada, N., Ahagon, N., Sakamoto, T., Uchida, M., Ikehara, M., and Shibata, Y. (2006). Rapid fluctuation of alkenone temperature in the southwestern okhotsk sea during the past 120 ky. *Global and Planetary Change*, 53(1-2):29 – 46. Cited in pages 42, 96, 126, and 135.

Hargreaves, J. C., Annan, J. D., Ohgaito, R., Paul, A., and Abe-Ouchi, A. (2013). Skill and reliability of climate model ensembles at the last glacial maximum and mid-holocene. *Climate of the Past*, 9(2):811–823. Cited in pages 36 and 51.

Hartmann, D., Tank, A. K., Rusticucci, M., Alexander, L., Brönnimann, S., Charabi, Y., Dentener, F., Dlugokencky, E., Easterling, D., Kaplan, A., Soden, B., Thorne, P., Wild, M., and Zhai, P. (2013). Observations: Atmosphere and surface. In *Climate Change 2013: The Physical Science Basis. Contribution of Working Group I to the Fifth Assessment Report of the Intergovernmental Panel on Climate Change [Stocker, T.F., D. Qin, G.-K. Plattner, M. Tignor, S.K. Allen, J. Boschung, A. Nauels, Y. Xia, V. Bex and P.M. Midgley (eds.)]*. Cambridge University Press, Cambridge, United Kingdom and New York, NY, USA. Cited in page 3.

Hedges, J. I., Hu, F. S., Devol, A. H., Hartnett, H. E., Tsamakis, E., and Keil, R. G. (1999). Sedimentary organic matter preservation: a test for selective degradation under oxic conditions. *American Journal of Science*, 299(7-9):529–555. Cited in page 11.

Heikkilä, M. and Seppä, H. (2003). A 11,000 yr palaeotemperature reconstruction from the southern boreal zone in finland. *Quaternary Science Reviews*, 22(5-7):541 – 554. Cited in pages 34, 40, 43, 96, 127, and 143.

Herbert, T. (2003). Alkenone paleotemperature determinations. In Holland, H. D. and Turekian, K. K., editors, *Treatise on Geochemistry*, pages 391 – 432. Pergamon, Oxford. Cited in pages 9 and 39.

Hönisch, B. and Hall, J. (2007). Paleoceanography, Physical and Chemical Proxies : Carbon cycle proxies. In Elias, S. A., editor, *Encyclopedia of Quaternary Science*, pages 1699 – 1710. Elsevier, Oxford. Cited in page 9.

Hurrell, J. W. (1995). Decadal trends in the north atlantic oscillation: Regional temperatures and precipitation. *Science*, 269(5224):676–679. Cited in page 65.

Huybrechts, P. (2002). Sea-level changes at the LGM from ice-dynamic reconstructions of the Greenland and Antarctic ice sheets during the glacial cycles. *Quaternary Science Reviews*, 21(1–3):203 – 231. Cited in page 16.

Iles, C. E., Hegerl, G. C., Schurer, A. P., and Zhang, X. (2013). The effect of volcanic eruptions on global precipitation. *Journal of Geophysical Research: Atmospheres*, 118(16):8770–8786. Cited in page 84.

IPCC (2007). Glossary of terms used in the IPCC fourth assessment report, Working Group I. Technical report, IPCC. Cited in pages 23 and 25.

Isono, D., Yamamoto, M., Irino, T., Oba, T., Murayama, M., Nakamura, T., and Kawahata, H. (2009). The 1500-year climate oscillation in the midlatitude North Pacific during the Holocene. *Geology*, 37(7):591. Cited in pages 41, 126, and 132.

Iwi, A. M., Hermanson, L., Haines, K., and Sutton, R. T. (2012). Mechanisms Linking Volcanic Aerosols to the Atlantic Meridional Overturning Circulation. *Journal of Climate*, 25(8):3039–3051. Cited in page 84.

Jacobson Jr, G. L. and Bradshaw, R. H. (1981). The selection of sites for paleovegetational studies. *Quaternary Research*, 16(1):80–96. Cited in page 11.

Jian, Z., Wang, P., Saito, Y., Wang, J., Pflaumann, U., Oba, T., and Cheng, X. (2000). Holocene variability of the kuroshio current in the okinawa trough, northwestern pacific ocean. *Earth and Planetary Science Letters*, 184(1):305 – 319. Cited in pages 41, 126, and 131.

Jones, G. S., Gregory, J. M., Stott, P. a., Tett, S. F. B., and Thorpe, R. B. (2005). An AOGCM simulation of the climate response to a volcanic supereruption. *Climate Dynamics*, 25(7-8):725–738. Cited in pages 62, 73, 76, 88, and 120.

Joshi, M., Lambert, F., and Webb, M. (2013). An explanation for the difference between twentieth and twenty-first century land–sea warming ratio in climate models. *Climate Dynamics*, 41(7–8):1853–1869. Cited in pages 50 and 80.

Joussaume, S. and Duplessy, J.-C. (2013). *Paléoclimatologie, enquête sur les climats anciens: trouver, dater et interpreter les indices - tome 1*, volume 1, chapter Le système climatique : son fonctionnement et son histoire. EDP Sciences / CNRS Editions. Cited in page 1.

Joussaume, S., Taylor, K. E., Braconnot, P., Mitchell, J. F. B., Kutzbach, J. E., Harrison, S. P., Prentice, I. C., Broccoli, A. J., Abe-Ouchi, A., Bartlein, P. J., Bonfils, C., Dong, B., Guiot, J., Herterich, K., Hewitt, C. D., Jolly, D., Kim, J. W., Kislov, A., Kitoh, A., Loutre, M. F., Masson, V., McAvaney, B., McFarlane, N., de Noblet, N., Peltier, W. R., Peterschmitt, J. Y., Pollard, D., Rind, D., Royer, J. F., Schlesinger, M. E., Syktus, J., Thompson, S., Valdes, P., Vettoretti, G., Webb, R. S., and Wyputta, U. (1999). Monsoon changes for 6000 years ago: Results of 18 simulations from the paleoclimate modeling intercomparison project (pmip). *Geophysical Research Letters*, 26(7):859–862. Cited in pages 14 and 15.

Jouzel, J., Masson-Delmotte, V., Cattani, O., Dreyfus, G., Falourd, S., Hoffmann, G., Minster, B., Nouet, J., Barnola, J. M., Chappellaz, J., Fischer, H., Gallet, J. C., Johnsen, S., Leuenberger, M., Loulergue, L., Luethi, D., Oerter, H., Parrenin, F., Raisbeck, G., Raynaud, D., Schilt, A., Schwander, J., Selmo, E., Souchez, R., Spahni, R., Stauffer, B., Steffensen, J. P., Stenni, B., Stocker, T. F., Tison, J. L., Werner, M., and Wolff, E. W. (2007). Orbital and millennial antarctic climate variability over the past 800,000 years. *Science*, 317(5839):793–796. Cited in pages 4 and 10.

Juggins, S. (2013). Quantitative reconstructions in palaeolimnology: new paradigm or sick science? *Quaternary Science Reviews*, 64(0):20 – 32. Cited in page 39.

Kim, J., Meggers, H., Rimbu, N., Lohmann, G., Freudenthal, T., Müller, P., and Schneider, R. (2007). Impacts of the North Atlantic gyre circulation on Holocene climate off northwest Africa. *Geology*, 35(5):387. Cited in pages 40, 126, and 131.

Klein, F., Goosse, H., Mairesse, A., and de Vernal, A. (2014). Model data comparison and data assimilation of mid-holocene arctic sea ice concentration. *Climate of the Past*, 10(3):1145–1163. Cited in pages 15, 32, and 65.

Kravitz, B. and Robock, A. (2011). Climate effects of high-latitude volcanic eruptions: Role of the time of year. *Journal of Geophysical Research*, 116(D1):D01105. Cited in page 67.

Kucera, M. (2007). Planktonic foraminifera as tracers of past oceanic environments. *Developments in marine geology*, 1(6):213–262. Cited in pages 7, 8, and 9.

Kucera, M., Rosell-Melé, A., Schneider, R., Waelbroeck, C., and Weinelt, M. (2005). Multiproxy approach for the reconstruction of the glacial ocean surface (MARGO). *Quaternary Science Reviews*, 24(7):813–819. Cited in page 13.

Kurek, J., Cwynar, L. C., and Vermaire, J. C. (2009). A late quaternary paleotemperature record from hanging lake, northern yukon territory, eastern beringia. *Quaternary Research*, 72(2):246 – 257. Cited in pages 96, 127, and 144.

Kutzbach, J. and Liu, Z. (1997). Response of the african monsoon to orbital forcing and ocean feedbacks in the middle holocene. *Science*, 278(5337):440–443. Cited in page 2.

Larocque, I. and Hall, R. I. (2004). Holocene temperature estimates and chironomid community composition in the abisko valley, northern sweden. *Quaternary Science Reviews*, 23(23-24):2453 – 2465. Cited in pages 96, 128, and 148.

Lauritzen, S.-E. (1998). SPEP: the speleothem record in the pole-equator-pole transects. In Gasse, F., Oldfield, F., and Kroepelin, S., editors, *PEP III: The Pole-Equator-Pole transect through Europe and Africa*, pages 37–43, Bern: PAGES. Cited in page 12.

Lauritzen, S.-E. and Lundberg, J. (1999a). Calibration of the speleothem delta function: an absolute temperature record for the Holocene in northern Norway. *The Holocene*, 9(6):659. Cited in pages 12, 41, 96, 128, and 146.

Lauritzen, S.-E. and Lundberg, J. (1999b). Speleothems and climate: a special issue of the holocene. *The Holocene*, 9(6):643–647. Cited in page 12.

Leduc, G., Schneider, R., Kim, J.-H., and Lohmann, G. (2010). Holocene and eemian sea surface temperature trends as revealed by alkenone and Mg/Ca paleothermometry. *Quaternary Science Reviews*, 29(7-8):989 – 1004. Cited in page 36.

Lieth, H. (1975). *Primary Productivity of the Biosphere*, volume 14 of *Ecological Studies*, chapter Modeling the primary productivity of the world. Springer Berlin Heidelberg. Cited in page 19.

Lohmann, G., Pfeiffer, M., Laepple, T., Leduc, G., and Kim, J.-H. (2013). A model-data comparison of the holocene global sea surface temperature evolution. *Climate of the Past*, 9(4):1807–1839. Cited in pages 29, 36, and 49.

Lorenz, S. J., Kim, J.-H., Rimbu, N., Schneider, R. R., and Lohmann, G. (2006). Orbitally driven insolation forcing on holocene climate trends: Evidence from alkenone data and climate modeling. *Paleoceanography*, 21(1):n/a–n/a. Cited in page 36.

Lorenz, S. J. and Lohmann, G. (2004). Acceleration technique for milankovitch type forcing in a coupled atmosphere-ocean circulation model: method and application for the holocene. *Climate dynamics*, 23(7-8):727–743. Cited in page 15.

Loutre, M. F., Mouchet, A., Fichefet, T., Goosse, H., Goelzer, H., and Huybrechts, P. (2011). Evaluating climate model performance with various parameter sets using observations over the recent past. *Climate of the Past*, 7(2):511–526. Cited in page 16.

Mairesse, A., Goosse, H., Mathiot, P., Wanner, H., and Dubinkina, S. (2013). Investigating the consistency between proxy-based reconstructions and climate models using data assimilation: a mid-holocene case study. *Climate of the Past*, 9(6):2741–2757. Cited in pages 15, 32, 35, and 65.

Mann, M., Zhang, Z., Hughes, M., Bradley, R., Miller, S., Rutherford, S., and Ni, F. (2008). Proxy-based reconstructions of hemispheric and global surface temperature variations over the past two millennia. *Proceedings of the National Academy of Sciences*, 105(36):13252–13257. Cited in page 31.

Mann, M. E., Zhang, Z., Rutherford, S., Bradley, R. S., Hughes, M. K., Shindell, D., Ammann, C., Faluvegi, G., and Ni, F. (2009). Global signatures and dynamical origins of the little ice age and medieval climate anomaly. *Science*, 326(5957):1256–1260. Cited in page 105.

Marchal, O., Cacho, I., Stocker, T. F., Grimalt, J. O., Calvo, E., Martrat, B., Shackleton, N., Vautravers, M., Cortijo, E., van Kreveld, S., et al. (2002). Apparent long-term cooling of the sea surface in the northeast atlantic and mediterranean during the holocene. *Quaternary Science Reviews*, 21(4):455–483. Cited in pages 96, 127, 128, 139, and 150.

Marcott, S. A., Shakun, J. D., Clark, P. U., and Mix, A. C. (2013). A reconstruction of regional and global temperature for the past 11,300 years. *Science*, 339(6124):1198–1201. Cited in pages 13, 36, and 122.

Marsland, S., Haak, H., Jungclaus, J., Latif, M., and Röske, F. (2003). The max-planck-institute global ocean/sea ice model with orthogonal curvilinear coordinates. *Ocean Modelling*, 5(2):91 – 127. Cited in page 45.

Martrat, B. (2007). *Studies of sedimentary organic matter to infer rapid climatic changes at the Barents and Iberian continental margins on centennial time resolution over the past four climate cycles of the Quaternary (ca. 420,000 years)*. PhD thesis, UPC, CSIC. Cited in pages 40, 59, 126, and 134.

Martrat, B., Grimalt, J., Shackleton, N., de Abreu, L., Hutterli, M., and Stocker, T. (2007). Four climate cycles of recurring deep and surface water destabilizations on the iberian margin. *Science*, 317(5837):502–507. Cited in pages 4, 34, 40, 43, 59, 126, and 133.

Masson-Delmotte, V. and Guiot, J. (2013). *Paléoclimatologie, enquête sur les climats anciens: trouver, dater et interpreter les indices - tome 1*, volume 1, chapter Comment reconstruire la physique et la circulation de l'atmosphère. EDP Sciences / CNRS Editions. Cited in pages 3, 5, and 6.

Masson-Delmotte, V., Hou, S., Ekaykin, A., Jouzel, J., Aristarain, A., Bernardo, R., Bromwich, D., Cattani, O., Delmotte, M., Falourd, S., et al. (2008). A review of antarctic surface snow isotopic composition: Observations, atmospheric circulation, and isotopic modeling. *Journal of Climate*, 21(13). Cited in page 11.

Masson-Delmotte, V., Schulz, M., Abe-Ouchi, A., Beer, J., Ganopolski, A., González Rouco, J., Jansen, E., Lambeck, K., Luterbacher, J., Naish, T., Osborn, T., Otto-Bliesner, B., Quinn, T., Ramesh, R., Rojas, M., Shao, X., and Timmermann, A. (2013). Information from Paleoclimate Archives. In *Climate Change 2013: The Physical Science Basis. Contribution of Working Group I to the Fifth Assessment Report of the Intergovernmental Panel on Climate Change [Stocker, T.F., D. Qin, G.-K. Plattner, M. Tignor, S.K. Allen, J. Boschung, A. Nauels, Y. Xia, V. Bex and P.M. Midgley (eds.)]*. Cambridge University Press, Cambridge, United Kingdom and New York, NY, USA. Cited in page 79.

Mathiot, P., Goosse, H., Crosta, X., Stenni, B., Braida, M., Renssen, H., Van Meerbeeck, C. J., Masson-Delmotte, V., Mairesse, A., and Dubinkina, S. (2013). Using data assimilation to investigate the causes of southern hemisphere high latitude cooling from 10 to 8 ka bp. *Climate of the Past*, 9(2):887–901. Cited in pages 15, 32, 34, 38, 39, 43, 45, 46, 65, 115, and 122.

MathWorks (2014). Curve Fitting Toolbox: Filtering and Smoothing Data. *http://www.mathworks.nl/help/curvefit/smoothing-data.html*, Last checked: 26th August 2014. Cited in page 96.

Mayewski, P. A., Rohling, E. E., Curt Stager, J., Karlén, W., Maasch, K. A., David Meeker, L., Meyerson, E. A., Gasse, F., van Kreveld, S., Holmgren, K., et al. (2004). Holocene climate variability. *Quaternary Research*, 62(3):243–255. Cited in page 101.

McGregor, S. and Timmermann, A. (2011). The Effect of Explosive Tropical Volcanism on ENSO. *Journal of Climate*, 24(8):2178–2191. Cited in page 62.

Miller, G. H., Geirsdóttir, Á., Zhong, Y., Larsen, D. J., Otto-Bliesner, B. L., Holland, M. M., Bailey, D. A., Refsnider, K. A., Lehman, S. J., Southon, J. R., et al. (2012). Abrupt onset of the little ice age triggered by volcanism and sustained by sea-ice/ocean feedbacks. *Geophysical Research Letters*, 39(2). Cited in page 102.

Mock, C. J. (2007). Paleoclimate : Introduction, Why Study Paleoclimatology ? In Elias, S. A., editor, *Encyclopedia of Quaternary Science*, pages 1867–1872. Elsevier. Cited in pages 28 and 36.

Mouchet, A. and François, L. (1996). Sensitivity of a global oceanic carbon cycle model to the circulation and to the fate of organic matter: Preliminary results. *Physics and Chemistry of the Earth*, 21(5–6):511 – 516. Cited in page 16.

Muller, P. J., Kirst, G., Ruhland, G., von Storch, I., and Rosell-Melé, A. (1998). Calibration of the alkenone paleotemperature index u37k based on core-tops from the eastern south atlantic and the global ocean (60 °n-60 °s). *Geochimica et Cosmochimica Acta*, 62(10):1757 – 1772. Cited in pages 4, 9, 34, and 44.

Nikolova, I., Yin, Q., Berger, A., Singh, U. K., and Karami, M. P. (2013). The last interglacial (eemian) climate simulated by loveclim and ccsm3. *Climate of the Past*, 9(4):1789–1806. Cited in page 16.

Ohlwein, C. and Wahl, E. (2011). Review of probabilistic pollen-climate transfer methods. *Quaternary Science Reviews*, 31(0):17 – 29. Cited in pages 34 and 43.

Opsteegh, J. D., Haarsma, R. J., Selten, F. M., and Kattenberg, A. (1998). ECBILT : a dynamic alternative to mixed boundary conditions in ocean models. *Tellus. Series A, Dynamic meteorology and oceanography*, 50(3):348–367. Cited in pages 15, 16, and 37.

Ortiz, J. D. (2007). Paleoceanography, Biological Proxies : Temperature Proxies, Census Counts. In Elias, S. A., editor, *Encyclopedia of Quaternary Science*, pages 1692–1699. Elsevier, Oxford. Cited in page 39.

Pelejero, C., Grimalt, J., Heilig, S., Kienast, M., and Wang, L. (1999). High-resolution UK37 temperature reconstructions in the South China Sea over the past 220 kyr. *Paleoceanography*, 14(2):224–231. Cited in pages 41, 126, and 130.

Peltier, W. (2004). Global glacial isostasy and the surface of the ice-age earth: the ICE-5G (VM2) model and GRACE. *Annu. Rev. Earth Planet. Sci.*, 32:111–149. Cited in pages 22, 26, 46, and 65.

Peros, M. and Gajewski, K. (2008). Holocene climate and vegetation change on Victoria Island, western Canadian Arctic. *Quaternary Science Reviews*, 27(3-4):235–249. Cited in pages 42, 96, 128, and 149.

Petit, J.-R., Jouzel, J., Raynaud, D., Barkov, N. I., Barnola, J.-M., Basile, I., Bender, M., Chappellaz, J., Davis, M., Delaygue, G., et al. (1999). Climate and atmospheric history of the past 420,000 years from the vostok ice core, antarctica. *Nature*, 399(6735):429–436. Cited in pages 4 and 10.

Phipps, S. J., Rotstayn, L. D., Gordon, H. B., Roberts, J. L., Hirst, A. C., and Budd, W. F. (2011). The csiro mk3l climate system model version 1.0 – part 1: Description and evaluation. *Geoscientific Model Development*, 4(2):483–509. Cited in page 45.

Pohl, F. (1937). *Die Pollenerzeugung der Windblütler: eine vergleichende Untersuchung mit Ausblicken auf den Bestäubungshaushalt tierblütiger Gewächse, und die pollen-analytische Waldgeschichtsforschung*. C. Heinrich. Cited in page 11.

Pollard, D. and DeConto, R. (2009). Modelling West Antarctic ice sheet growth and collapse through the past five million years. *Nature*, 458(7236):329–332. Cited in pages 22, 27, 28, 46, and 65.

Pongratz, J., Reick, C., Raddatz, T., and Claussen, M. (2008). A reconstruction of global agricultural areas and land cover for the last millennium. *Global Biogeochemical Cycles*, 22(3). Cited in page 25.

Prahl, F. and Wakeham, S. (1987). Calibration of unsaturation patterns in long-chain ketone compositions for palaeotemperature assessment. *Nature*. Cited in page 9.

Prahl, F. G., Muehlhausen, L. A., and Zahnle, D. L. (1988). Further evaluation of long-chain alkenones as indicators of paleoceanographic conditions. *Geochimica et Cosmochimica Acta*, 52(9):2303 – 2310. Cited in page 9.

Prentice, C. (1988). Records of vegetation in time and space: the principles of pollen analysis. In Huntley, B. and Webb, T., I., editors, *Vegetation history*, volume 7, pages 17–42. Springer Netherlands. Cited in page 11.

Raddatz, T., Reick, C., Knorr, W., Kattge, J., Roeckner, E., Schnur, R., Schnitzler, K.-G., Wetzel, P., and Jungclaus, J. (2007). Will the tropical land biosphere dominate the climate–carbon cycle feedback during the twenty-first century ? *Climate Dynamics*, 29(6):565–574. Cited in page 45.

Ramankutty, N. and Foley, J. (1999). Estimating historical changes in global land cover: Croplands from 1700 to 1992. *Global Biogeochemical Cycles*, 13(4):997–1027. Cited in page 25.

Renssen, H., Brovkin, V., Fichefet, T., and Goosse, H. (2003). Holocene climate instability during the termination of the african humid period. *Geophysical Research Letters*, 30(4). Cited in pages 2 and 16.

Renssen, H., Goosse, H., and Fichefet, T. (2002). Modeling the effect of freshwater pulses on the early Holocene climate: The influence of high-frequency climate variability. *Paleoceanography*, 17(2):1020. Cited in page 28.

Renssen, H., Goosse, H., Fichefet, T., Brovkin, V., Driesschaert, E., and Wolk, F. (2005). Simulating the holocene climate evolution at northern high latitudes using a coupled atmosphere-sea ice-ocean-vegetation model. *Climate Dynamics*, 24(1):23–43. Cited in pages 15, 16, and 46.

Renssen, H., Goosse, H., and Muscheler, R. (2006). Coupled climate model simulation of Holocene cooling events: oceanic feedback amplifies solar forcing. *Climate of the Past*, 2(2):79–90. Cited in page 122.

Renssen, H., Mairesse, A., Goosse, H., Mathiot, P., and Roche, D. M. (2014). The cause of the Younger Dryas cold event. in preparation. Cited in pages 32 and 114.

Renssen, H., Seppä, H., Crosta, X., Goosse, H., and Roche, D. (2012). Global characterization of the holocene thermal maximum. *Quaternary Science Reviews*, 48(0):7 – 19. Cited in page 36.

Renssen, H., Seppä, H., Heiri, O., Roche, D., Goosse, H., and Fichefet, T. (2009). The spatial and temporal complexity of the holocene thermal maximum. *Nature Geoscience*, 2(6):411–414. Cited in pages 22, 26, 28, 46, and 65.

Rimbu, N., Lohmann, G., Kim, J.-H., Arz, H. W., and Schneider, R. (2003). Arctic/north atlantic oscillation signature in holocene sea surface temperature trends as obtained from alkenone data. *Geophysical Research Letters*, 30(6):1280. Cited in page 57.

Risebrobakken, B., Jansen, E., Andersson, C., Mjelde, E., and Hevrøy, K. (2003). A high-resolution study of Holocene paleoclimatic and paleoceanographic changes in the Nordic Seas. *Paleoceanography*, 18(1):1017. Cited in pages 40, 48, 56, 101, 128, and 146.

Robock, A. (2000). Volcanic eruptions and climate. *Reviews of Geophysics*, 38(2):191–219. Cited in pages 62, 63, and 64.

Robock, A., Ammann, C. M., Oman, L., Shindell, D., Levis, S., and Stenchikov, G. (2009). Did the Toba volcanic eruption of 74 ka B.P. produce widespread glaciation? *Journal of Geophysical Research*, 114(D10):D10107. Cited in pages 62 and 88.

Roche, D. M. (2013). δ^{18}o water isotope in the iloveclim model (version 1.0) – part 1: Implementation and verification. *Geoscientific Model Development*, 6(5):1481–1491. Cited in page 123.

Roche, D. M. and Caley, T. (2013). δ^{18}o water isotope in the iloveclim model (version 1.0) – part 2: Evaluation of model results against observed î^{18}o in water samples. *Geoscientific Model Development*, 6(5):1493–1504. Cited in page 123.

Roche, D. M., Dokken, T. M., Goosse, H., Renssen, H., and Weber, S. L. (2007). Climate of the last glacial maximum: sensitivity studies and model-data comparison with the loveclim coupled model. *Climate of the Past*, 3(2):205–224. Cited in page 16.

Rodrigues, T., Grimalt, J., Abrantes, F., Flores, J., and Lebreiro, S. (2009). Holocene interdependences of changes in sea surface temperature, productivity, and fluvial inputs in the iberian continental shelf (tagus mud patch). *Geochemistry, Geophysics, Geosystems*, 10(7):n/a–n/a. Cited in pages 40, 59, 126, and 134.

Rostek, F., Ruhland, G., Bassinot, F., Müller, P., Labeyrie, L., Lancelot, Y., and Bard, E. (1993). Reconstructing sea surface temperature and salinity using and alkenone records. *Nature*, 364:319–321. Cited in page 8.

Sachs, J. P. (2007). Cooling of northwest atlantic slope waters during the holocene. *Geophysical Research Letters*, 34(3):L03609. Cited in pages 40, 96, 126, and 135.

Samtleben, C. and Bickert, T. (1990). Coccoliths in sediment traps from the norwegian sea. *Marine Micropaleontology*, 16:39 – 64. Cited in page 39.

Sarmaja-Korjonen, K. and Seppä, H. (2007). Abrupt and consistent responses of aquatic and terrestrial ecosystems to the 8200 cal. yr cold event: a lacustrine record from Lake Arapisto, Finland. *The Holocene*, 17(4):457–467. Cited in page 40.

Sarnthein, M., Van Kreveld, S., Erlenkeuser, H., Grootes, P. M., Kucera, M., Pflaumann, U., and Schulz, M. (2003). Centennial-to-millennial-scale periodicities of holocene climate and sediment injections off the western barents shelf, 75 degrees n. *Boreas*, 32(3):447–461. Cited in pages 96, 128, 150, and 151.

Schleussner, C. F. and Feulner, G. (2013). A volcanically triggered regime shift in the subpolar North Atlantic Ocean as a possible origin of the Little Ice Age. *Climate of the Past*, 9(3):1321–1330. Cited in page 102.

Schmidt, G., Shindell, D., Miller, R., Mann, M., and Rind, D. (2004a). General circulation modelling of holocene climate variability. *Quaternary Science Reviews*, 23(20-22):2167–2181. Cited in page 62.

Schmidt, G. A., Jungclaus, J. H., Ammann, C. M., Bard, E., Braconnot, P., Crowley, T. J., Delaygue, G., Joos, F., Krivova, N. A., Muscheler, R., Otto-Bliesner, B. L., Pongratz, J., Shindell, D. T., Solanki, S. K., Steinhilber, F., and Vieira, L. E. A. (2011). Climate forcing reconstructions for use in pmip simulations of the last millennium (v1.0). *Geoscientific Model Development*, 4(1):33–45. Cited in pages 22, 25, 26, and 71.

Schmidt, G. A., Jungclaus, J. H., Ammann, C. M., Bard, E., Braconnot, P., Crowley, T. J., Delaygue, G., Joos, F., Krivova, N. A., Muscheler, R., Otto-Bliesner, B. L., Pongratz, J., Shindell, D. T., Solanki, S. K., Steinhilber, F., and Vieira, L. E. A. (2012). Climate forcing reconstructions for use in pmip simulations of the last millennium (v1.1). *Geoscientific Model Development*, 5(1):185–191. Cited in pages 22, 25, and 62.

Schmidt, M., Spero, H., and Lea, D. (2004b). Links between salinity variation in the Caribbean and North Atlantic thermohaline circulation. *Nature*, 428(6979):160–163. Cited in page 8.

Schneider, B., Leduc, G., and Park, W. (2010). Disentangling seasonal signals in holocene climate trends by satellite-model-proxy integration. *Paleoceanography*, 25(4):n/a–n/a. Cited in page 36.

Schneider, D. P., Ammann, C. M., Otto-Bliesner, B. L., and Kaufman, D. S. (2009). Climate response to large, high-latitude and low-latitude volcanic eruptions in the Community Climate System Model. *Journal of Geophysical Research*, 114(D15):D15101. Cited in page 62.

Seppä, H. (2007). Pollen Analysis, Principles: Introduction. In Elias, S. A., editor, *Encyclopedia of Quaternary Science*, pages 2497–2508. Elsevier, Oxford. Cited in pages 11 and 12.

Seppä, H. and Birks, H. (2001). July mean temperature and annual precipitation trends during the Holocene in the Fennoscandian tree-line area: pollen-based climate reconstructions. *The Holocene*, 11(5):527–539. Cited in pages 34, 36, 40, 44, 96, 128, and 148.

Seppä, H. and Birks, H. (2002). Holocene climate reconstructions from the Fennoscandian tree-line area based on pollen data from Toskaijavri. *Quaternary Research*, 57(2):191–199. Cited in pages 36, 40, 96, 128, and 149.

Seppä, H., Hammarlund, D., and Antonsson, K. (2005). Low-frequency and high-frequency changes in temperature and effective humidity during the Holocene in south-central Sweden: implications for atmospheric and oceanic forcings of climate. *Climate Dynamics*, 25(2):285–297. Cited in pages 40 and 96.

Seppä, H. and Poska, A. (2004). Holocene annual mean temperature changes in Estonia and their relationship to solar insolation and atmospheric circulation patterns. *Quaternary Research*, 61(1):22–31. Cited in pages 41, 96, 127, and 139.

Shi, F., Yang, B., Mairesse, A., von Guten, L., Li, J., Bräuning, A., Yang, F., and Xiao, X. (2013). Northern hemisphere temperature reconstruction during the last millennium using multiple annual proxies. *Climate Research*, 56:231–244. Cited in page 15.

Steig, E. J., Ding, Q., White, J. W., Küttel, M., Rupper, S. B., Neumann, T. A., Neff, P. D., Gallant, A. J., Mayewski, P. A., Taylor, K. C., et al. (2013). Recent climate and ice-sheet changes in west antarctica compared with the past 2,000 years. *Nature Geoscience*, 6(5):372–375. Cited in page 10.

Steinhilber, F., Beer, J., and Fröhlich, C. (2009). Total solar irradiance during the holocene. *Geophysical Research Letters*, 36(19). Cited in pages 22, 23, and 65.

Stenchikov, G., Delworth, T. L., Ramaswamy, V., Stouffer, R. J., Wittenberg, A., and Zeng, F. (2009). Volcanic signals in oceans. *Journal of Geophysical Research*, 114(D16):D16104. Cited in page 87.

Stothers, R. B. (1984). The great tambora eruption in 1815 and its aftermath. *Science*, 224(4654):1191–1198. Cited in pages 24 and 70.

Sundqvist, H. S., Kaufman, D. S., McKay, N. P., Balascio, N. L., Briner, J. P., Cwynar, L. C., Sejrup, H. P., Seppä, H., Subetto, D. A., Andrews, J. T., Axford, Y., Bakke, J., Birks, H. J. B., Brooks, S. J., de Vernal, A., Jennings, A. E., Ljungqvist, F. C., Rühland, K. M., Saenger, C., Smol, J. P., and Viau, A. E. (2014). Arctic holocene proxy climate database ndash; new approaches to assessing geochronological accuracy and encoding climate variables. *Climate of the Past*, 10(4):1605–1631. Cited in page 123.

Tarasov, P. E., Bezrukova, E. V., and Krivonogov, S. K. (2009). Late glacial and holocene changes in vegetation cover and climate in southern siberia derived from a 15 kyr long pollen record from lake kotokel. *Climate of the Past*, 5(3):285–295. Cited in pages 41, 96, 127, and 137.

Tartinville, B., Campin, J.-M., Fichefet, T., and Goosse, H. (2001). Realistic representation of the surface freshwater flux in an ice–ocean general circulation model. *Ocean Modelling*, 3(1–2):95 – 108. Cited in page 18.

Telford, R. and Birks, H. (2005). The secret assumption of transfer functions: problems with spatial autocorrelation in evaluating model performance. *Quaternary Science Reviews*, 24(20-21):2173 – 2179. Cited in page 39.

Thomsen, C., Schulz-Bull, D., Petrick, G., and Duinker, J. (1998). Seasonal variability of the long-chain alkenone flux and the effect on the uk37-index in the norwegian sea. *Organic Geochemistry*, 28(5):311 – 323. Cited in page 39.

Thornalley, D., Elderfield, H., and McCave, I. (2009). Holocene oscillations in temperature and salinity of the surface subpolar North Atlantic. *Nature*, 457(7230):711–714. Cited in pages 40, 96, 127, and 144.

Timm, O. and Timmermann, A. (2007). Simulation of the last 21 000 years using accelerated transient boundary conditions. *Journal of Climate*, 20(17). Cited in page 15.

Timmreck, C., Graf, H.-F., Lorenz, S. J., Niemeier, U., Zanchettin, D., Matei, D., Jungclaus, J. H., and Crowley, T. J. (2010). Aerosol size confines climate response to volcanic super-eruptions. *Geophysical Research Letters*, 37(24):n/a–n/a. Cited in pages 62 and 73.

van Leeuwen, P. J. (2009). Particle filtering in geophysical systems. *Monthly Weather Review*, 137(12):4089–4114. Cited in pages 29 and 30.

Varma, V., Prange, M., Merkel, U., Kleinen, T., Lohmann, G., Pfeiffer, M., Renssen, H., Wagner, A., Wagner, S., and Schulz, M. (2012). Holocene evolution of the southern hemisphere westerly winds in transient simulations with global climate models. *Climate of the Past*, 8(2):391–402. Cited in page 15.

Viau, A., Gajewski, K., Sawada, M., and Fines, P. (2006). Millennial-scale temperature variations in north america during the holocene. *Journal of Geophysical Research: Atmospheres (1984–2012)*, 111(D9). Cited in page 101.

Viau, A. E. and Gajewski, K. (2009). Reconstructing millennial-scale, regional paleoclimates of boreal canada during the holocene. *Journal of Climate*, 22(2):316–330. Cited in pages 13, 34, 36, 41, 42, 43, 44, 96, 97, 101, 127, 129, 139, 140, 141, and 142.

Vinther, B., Buchardt, S., Clausen, H., Dahl-Jensen, D., Johnsen, S., Fisher, D., Koerner, R., Raynaud, D., Lipenkov, V., and Andersen, K. (2009). Holocene thinning of the Greenland ice sheet. *Nature*, 461(7262):385–388. Cited in pages 11, 36, 41, 96, 128, 149, and 151.

Waelbroeck, C., Paul, A., Kucera, M., Rosell-Melé, A., Weinelt, M., Schneider, R., Mix, A., Abelmann, A., Armand, L., Bard, E., et al. (2009). Constraints on the magnitude and patterns of ocean cooling at the last glacial maximum. *Nature Geoscience*, 2(2):127–132. Cited in page 13.

Walker, M., Johnsen, S., Rasmussen, S. O., Popp, T., Steffensen, J.-P., Gibbard, P., Hoek, W., Lowe, J., Andrews, J., Björck, S., Cwynar, L. C., Hughen, K., Kershaw, P., Kromer, B., Litt, T., Lowe, D. J., Nakagawa, T., Newnham, R., and Schwander, J. (2009). Formal definition and dating of the gssp (global stratotype section and point) for the base of the holocene using the greenland ngrip ice core, and selected auxiliary records. *Journal of Quaternary Science*, 24(1):3–17. Cited in page 1.

Walker, M. J. C., Berkelhammer, M., Björck, S., Cwynar, L. C., Fisher, D. A., Long, A. J., Lowe, J. J., Newnham, R. M., Rasmussen, S. O., and Weiss, H. (2012). Formal subdivision of the Holocene Series/Epoch: a Discussion Paper by a Working Group of INTIMATE (Integration of ice-core, marine and terrestrial records) and the Subcommission on Quaternary Stratigraphy (International Commission on Stratigraphy). *Journal of Quaternary Science*, 27(7):649–659. Cited in page 1.

Wang, Y., Lean, J., Sheeley, N., et al. (2005). Modeling the sun's magnetic field and irradiance since 1713. *The Astrophysical Journal*, 625:522. Cited in page 23.

Wanner, H., Beer, J., Bütikofer, J., Crowley, T., Cubasch, U., Flückiger, J., Goosse, H., Grosjean, M., Joos, F., Kaplan, J., Küttel, M., Müller, S., Prentice, I., Solomina, O., Stocker, T., Tarasov, P., Wagner, M., and Widmann, M. (2008). Mid-to Late Holocene climate change: an overview. *Quaternary Science Reviews*, 27(19-20):1791–1828. Cited in page 46.

Wanner, H., Solomina, O., Grosjean, M., Ritz, S., and Jetel, M. (2011). Structure and origin of holocene cold events. *Quaternary Science Reviews*. Cited in pages vi, 91, 92, 93, 94, 95, 96, 98, 100, 101, 102, 103, and 115.

Weiss, H., Courty, M.-A., Wetterstrom, W., Guichard, F., Senior, L., Meadow, R., and Curnow, A. (1993). The genesis and collapse of third millennium north mesopotamian civilization. *SCIENCE-NEW YORK THEN WASHINGTON-*, 261:995–995. Cited in page 3.

Widmann, M., Goosse, H., van der Schrier, G., Schnur, R., and Barkmeijer, J. (2010). Using data assimilation to study extratropical northern hemisphere climate over the last millennium. *Climate of the Past*, 6(201):627—644. Cited in page 29.

Wigley, T., Ammann, C., Santer, B., and Raper, S. C. (2005). Effect of climate sensitivity on the response to volcanic forcing. *Journal of Geophysical Research: Atmospheres (1984–2012)*, 110(D9). Cited in pages 24 and 71.

Winter, A., Jordan, R., and Roth, P. (1994). Biogeography of living coccolithophores in ocean waters. In Winter, A. and Siesser, W. G., editors, *Coccolithophores*, pages 161–177. Cambridge University Press, Cambridge, UK. Cited in page 9.

Zanchettin, D., Timmreck, C., Bothe, O., Lorenz, S. J., Hegerl, G., Graf, H.-F., Luterbacher, J., and Jungclaus, J. H. (2013). Delayed winter warming: A robust decadal response to strong tropical volcanic eruptions? *Geophysical Research Letters*, 40(1):204–209. Cited in page 62.

Zhao, Y., Braconnot, P., Marti, O., Harrison, S., Hewitt, C., Kitoh, A., Liu, Z., Mikolajewicz, U., Otto-Bliesner, B., and Weber, S. (2005). A multi-model analysis of the role of the ocean on the african and indian monsoon during the mid-holocene. *Climate Dynamics*, 25(7-8):777–800. Cited in page 36.